Università degli Studi di Milano
Facoltà di Scienze Matematiche, Fisiche e Naturali.
Dipartimento di Matematica

Dottorato di Ricerca in Matematica e Statistica per le Scienze Computazionali
MASSC, XXIII ciclo

Non-overlapping domain decomposition methods for three-dimensional cardiac reaction-diffusion models and applications.

MAT/08

Candidate
Stefano Zampini

Advisor
Prof. Luca F. Pavarino

Ph.D. Program Coordinator
Prof. Vincenzo Capasso

Academic Year
2009/2010

To my parents,
to my Heart.

Contents

Introduction

Recent advances in biotechnology and the availability of ever more powerful computers have led to the formulation of increasingly complex models at all levels of life sciences, in particular of cardiac electrophysiology. Multiscale modeling of the bioelectric activity of the heart, taking into account macroscopic (fiber architecture and anisotropy) and microscopic (cellular) features of the tissue, aim to develop predictive tools for future drug design and patient-specific therapies, using detailed and efficient three-dimensional solvers for the governing equations of tissue electrophysiology.

At the microscopic level, models of cellular electrophysiology are built up via an iterative interaction between experiment and theory. The sequential activation of depolarizing and repolarizing currents carried by ion channels, specified proteins located across the cell membrane, give rise to cardiac action potentials, which describe the pointwise excitation of the tissue. Action potential waveforms are distinct in different regions of the hearth owing to differences in channels' expression. In the first chapter of this thesis, after a brief introduction on cellular electrophysiology and the underlying mathematical modeling techniques, we will provide a review of the experimental results related to the cellular heterogeneity of the canine left ventricle and, starting from a recently published model of canine epicardial cell represented by a stiff nonlinear system of 29 ODEs, we will then derive and validate a model of canine LV cellular heterogeneity based on available published experimental data.

At the macroscopic level, the cardiac tissue can be represented as the superimposition of two anisotropic continuous media, the intra- (i) and extra- (e) cellular media, coexisting at every point of the tissue and separated by a distributed continuous cellular membrane; the cardiac Bidomain model consists of a system of two nonlinear Reaction-Diffusion equations for the intra- and extra-cellular potentials u_i and u_e

$$\begin{cases} \partial_t v - \text{div}(D_i \nabla u_i) + I_{ion}(v,w,c) = 0 & \text{in } \Omega \times (0,T) \\ -\partial_t v - \text{div}(D_e \nabla u_e) - I_{ion}(v,w,c) = -I^e_{app} & \text{in } \Omega \times (0,T) \\ \mathbf{n}^T D_{i,e} \nabla u_{i,e} = 0 & \text{in } \partial\Omega \times (0,T)\,, \\ \partial_t w - R(v,w) = 0,\ \partial_t c - S(v,w,c) = 0 & \text{in } \Omega \times (0,T) \\ v(\mathbf{x},0) = v_0(\mathbf{x}), w(\mathbf{x},0) = w_0(\mathbf{x}), c(\mathbf{x},0) = c_0(\mathbf{x}) & \text{in } \Omega \end{cases}$$

where $v = u_i - u_e$ is the transmembrane potential, I_{ion} the ionic current per unit volume,

I^e_{app} the applied extracellular stimulus, D_i and D_e the anisotropic diffusion tensors of the two media accounting for fiber rotation and tissue anisotropy. This degenerate parabolic system of PDEs is coupled with the stiff ionic model where w are the gating variables of the ionic channels and c the intracellular ionic concentrations. The Monodomain model, a single parabolic Reaction-Diffusion equation for the transmembrane potential, is usually derived in literature by assuming equal anisotropy ratio of the two media. In this thesis, the anisotropic Monodomain model will be derived from the Bidomain model by assuming that the major source of electrical flux is directed along the fibers. Both models are discretized by the finite element method with Q1 elements in the three dimensional space and a semi-implicit IMEX method in time; for the Bidomain model shown above, we then obtain the following iteration matrix

$$\frac{1}{\delta_t}\begin{bmatrix} \mathrm{M} & -\mathrm{M} \\ -\mathrm{M} & \mathrm{M} \end{bmatrix} + \begin{bmatrix} \mathrm{A}_i & 0 \\ 0 & \mathrm{A}_e \end{bmatrix},$$

where A_i and A_e are the stiffness matrices related to the elliptic diffusion part of the PDEs, M the mass matrix and δ_t is the time step. In Chapter two, we will thus introduce the differential formulation of both the models, and we will show how the Monodomain can be derived from the Bidomain model. The variational formulations at the semidiscrete level will be also shown and we will describe in details the splitting of the time operator. Additional details related to the variational formulation of the elliptic stationary problems will be given in order to provide additional results needed in the following chapters.

For the three-dimensional solvers considered in this thesis, the main computational costs at each time step are associated with the solution of a large and sparse linear system. Since both the Bidomain or the Monodomain iteration matrices are symmetric positive semidefinite (Monodomain matrix is positive definite), we will use the Preconditioned Conjugate Gradient method (PCG), which efficiency depends on the choice of the initial guess and on the preconditioner. Namely, at the mth iteration of the method the well known formula for error reduction holds

$$||\mathbf{y} - \mathbf{y}_m||_A \leq 2||\mathbf{y} - \mathbf{y}_0||_A \left(\frac{\sqrt{\kappa_2(M^{-1}A)} - 1}{\sqrt{\kappa_2(M^{-1}A)} + 1} \right)^m,$$

where $\mathbf{y}$ is the exact solution vector of the linear system, $\mathbf{y}_0$ the PCG initial guess, $\mathbf{y}_m$ the m-th iterate of the PCG, A the iteration matrix, M the preconditioner and $\kappa_2(M^{-1}A)$ the condition number of the preconditioned system. The choice of the PCG initial guess can thus produce a gain in the iterative solution process lowering the initial residual, though it will not be as substantial as using an optimal preconditioner. However, the latter can be designed independently from the choice of the initial guess. In Chapter three, we will thus analyze different strategies for the choice of the PCG initial guess for the the cardiac Monodomain and Bidomain models, only using the solutions obtained in the previous time

steps: namely, we will study the efficiency of lagrangian interpolations in time of the previous solutions and some projection-based techniques, such the Fischer's algorithms and the Proper Ortoghonal Decomposition (POD) combined with a usual Galerkin technique. Finally, since the most recent models used to reproduce cellular reaction are very sensible to the initial ionic concentrations, we will introduce and validate a useful technique, based on an offline simulation of a one-dimensional fiber, to obtain suitable initial values for the ionic concentrations in order to reduce the necessary number of heart beats in the three dimensional context. Numerical results on the influence of transmural cellular heterogeneity on repolarization patterns in the tissue will be also provided for the Monodomain model.

In Chapter four of the thesis, we will introduce and analyze non-overlapping Domain Decomposition preconditioners of Neumann-Neumann (NN) type for the Monodomain and Bidomain models. After introducing the discrete bilinear forms of their Schur complements and additional results of upper bounds for finite element functions defined at the interface of the non-overlapping partition, we will explicitly construct such preconditioners and we will provide theoretical estimates. In particular, for the Monodomain model, we will construct and analyze the one-level multisubdomain NN preconditioner and we will be able to prove that the condition number of the preconditioned Monodomain operator will be independent of the number of subdomains of the non-overlapping partition and can be bounded by

$$\kappa_2(M_{NN}^{-1}\widehat{S}_\Gamma) \leq C\frac{\sigma_M\delta_t + H^2}{\min\{H^2, \sigma_m\delta_t\}}(1+\log(H/h))^2,$$

where $\widehat{S}_\Gamma$ is the Schur complement matrix of the Monodomain model, h is the discretization step, H the characteristic size of the non-overlapping partition, σ_M and σ_m the continuity and coercivity parameters of the Monodomain stiffness matrix and δ_t is the time step. For the Bidomain model we will consider the two-level hybrid Balancing version of the NN preconditioner (BNN), since the NN preconditioner itself cannot be directly applicable to the Bidomain model due to the singularity of the local problems involved in the application of the preconditioner. We will consider two choices for the balancing coarse space; in particular, we will be able to prove that the condition number of the preconditioned Bidomain operator using a minimal coarse space, needed to assure balancing, will be independent of the number of subdomains and bounded from above by

$$\kappa_2(M_{BNN}^{-1}\widehat{S}_\Gamma) \leq C\frac{\sigma_M\delta_t + H^2}{\min\{H^2, \sigma_m\delta_t\}}(1+\log(H/h))^2,$$

where now $\sigma_M = \max\{\sigma_M^i, \sigma_M^e\}$ and $\sigma_m = \min\{\sigma_m^i, \sigma_m^e\}$ where $\sigma_M^{i,e}$ and $\sigma_m^{i,e}$ are the continuity and the coercivity parameters of the elliptic part of the Bidomain iteration matrix. Using a suitable enriched coarse space we will prove that the condition number of the preconditioned Bidomain operator will be independent of the number of subdomains and bounded from above by

$$\kappa_2(M_{BNN}^{*^{-1}}\widehat{S}_\Gamma) \leq C \max_{\bullet=i,e}\left(\max_{j=1,\ldots,N}\frac{\sigma_M^{\bullet^{(j)}}\delta_t + H^2}{\sigma_m^{\bullet^{(j)}}\delta_t}\right)(1+\log(H/h))^2,$$

where now $\sigma_M^{i,e^{(j)}}$ and $\sigma_m^{i,e^{(j)}}$ are the maximum and minimum eigenvalues of the diffusion tensors of the jth subdomain. Numerical results will sharply confirm the theoretical estimates.

In Chapter five, we will introduce and analyze the recent Balancing Domain Decomposition by Constraints (BDDC) preconditioner for the Bidomain model; BDDC is a two-level additive preconditioner based on a non-overlapping partition of the spatial domain, and which is the dual of the FETI-DP preconditioner using the same set of primal constraints. Two BDDC formulations present in the literature will be introduced: a first one based on Lagrange multipliers and a second one which implements a change of basis of the underlying finite element space. Theoretical estimates and parallel results will be provided, showing the robustness of such a preconditioner for the cardiac Bidomain model in the presence of jumps in the coefficients of the stiffness matrix. In particular, using a special change of basis, we will be able to prove that the condition number of the preconditioned Bidomain operator will be independent of the number N of subdomains and can be bounded from above as

$$\kappa_2(M_{BDDC}^{-1}\widehat{S}_\Gamma) \leq C \max_{\bullet=i,e}\left(\max_{j=1,\ldots,N}\frac{\sigma_M^{\bullet^{(j)}}\delta_t + H^2}{\sigma_m^{\bullet^{(j)}}\delta_t}\right)(1+\log(H/h))^2.$$

Experimental results will improve the latter estimate for small values of δ_t showing a sigmoidal dependence of the condition number of the BDDC operator from the time step. Results will be also provided combining the BDDC preconditioner and the POD technique for the choice of the initial guess.

In Chapter six, we will introduce the inexact formulation of the BDDC preconditioner for the Bidomain model in order to deal with the intrinsic computational limitations of all non-overlapping preconditioners. In particular, since the main limitations of memory consumption are associated with the factorizations of the subdomain Dirichlet and Neumann problems involved in the application of the preconditioner, we will replace such problems with the application of Algebraic MultiGrid (AMG) preconditioners in order to exploit their optimal complexity and their spectral equivalence with the original local problems of the Bidomain model. After introducing in details the formulation of the inexact BDDC preconditioner, which relies on the original formulation of BDDC based on Lagrange multipliers, we will provide a theoretical link between the exact and inexact formulations; numerical results will fully confirm the theoretical results. Finally, we will provide parallel large scale numerical results regarding the scalability of the inexact BDDC method considered.

The parallel codes have been developed in Fortran90 using the MPI standard for message passing and different pre-existing high-performance libraries like PETSc, LAPACK, UMFPACK, MUMPS, SLEPc and HYPRE. Code developing has been performed using the

clusters Ulisse and Nemo located at the Math department; large numerical simulations (up to 576 computing cores) have been performed with the Linux cluster BCX and IBM machine SP6 (a power6) of CINECA (see http://hpc.cineca.it), and the Linux cluster MATRIX of CASPUR (see http://hpc.caspur.it). The BDDC code has been also used to validate a theoretical study (submitted for publication) on the solution of the three-dimensional linear elasticity system in the almost compressible case using Gauss-Lobatto-Legendre spectral elements, in collaboration with Prof. Luca F. Pavarino (University of Milan) and Prof. Olof B. Widlund (Courant Institute, NY).

Chapter 1

Cellular models of cardiac electrophysiology

1.1 Cellular electrophysiology

The mechanical functioning of the mammalian heart depends on its proper electrical functioning, reflected in the sequential activation of cells in specialized pacemakers regions of the heart and the propagation of activity through the ventricles. Myocardial cellular electrical activity is attributed to the generation, in response to an overthreshold stimulus, of action potentials (AP). The propagation of activity and the coordination of the electromechanical functioning of the ventricles also depend on electrical coupling between cells, mediated by gap junctions. The exciting wave is initiated in specialized self-depolarizing cells located in the sinoatrial (SA) node that acts as pacemakers (see figure 1.1). The wave is then propagated through the atria to the AV node; following a brief pause in the AV node, excitation spreads in the ventricles through the right and left bundle branches. Ramifications of the bundle branches give rise to the subendocardial network of the Purkinje fibers, that transmit the electrical impulse into the working myocardium. The heart is then activated from apex to base, from endocardium to epicardium, and his normal coordinated electrical functioning is readily detected in surface electrocardiograms (ECG in figure 1.1). The P wave indicates atrial excitation, the QRS complex ventricular contraction and the following T wave the subsequent ventricular relaxation.

The generation of myocardial APs reflects the sequential activation and inactivation of ion channels that conduct depolarizing (inward Na^+ and Ca^{2+}) currents, and repolarizing (outward K^+) currents. The waveforms of APs in different regions of the heart are distinct, owing to differences in the expression and/or the properties of the underlying ion channels; moreover, waveforms of cardiac APs are different among the animal species. Regional differences contribute to the normal unidirectional propagation of excitation through myocardium and to the generation of normal cardiac rhythms. Changes in the properties or the functional expression of myocardial ion channels can results from inherited mutations in

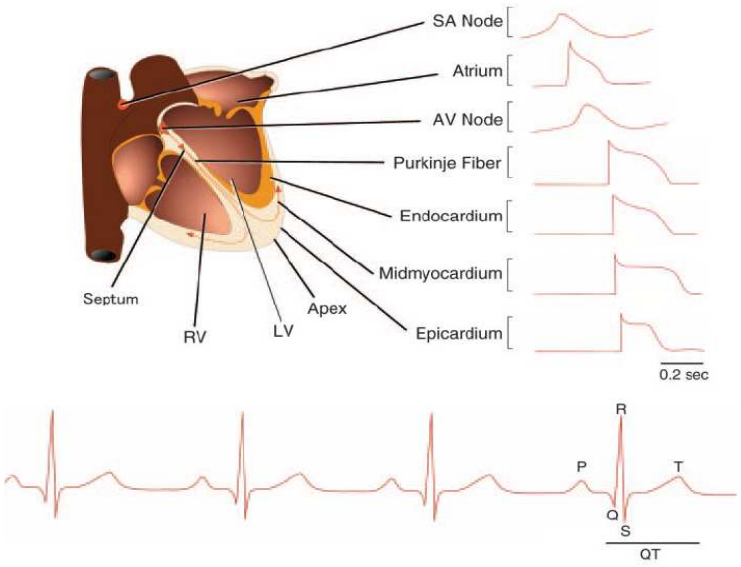

Figure 1.1: Electrical activity in the myocardium. Top: schematic of a human heart with illustration of typical action potential waveforms recorded in different regions. Bottom: schematic of a surface electrocardiogram; three sequential beats are displayed (redrawn from [97]).

the genes encoding these channels, from myocardial disease or from drug administration: these changes can lead to changes in APs waveforms, synchronization and propagation, thereby predisposing the hearth to potentially life-threatening arrhythmias.

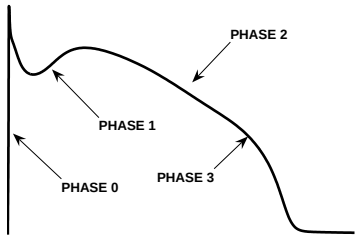

Figure 1.2: A ventricular action potential

In the following we will concentrate on canine left ventricular APs; for a review to whole heart regional and species differences see [97]. AP upstroke (phase 0 in figure 1.2) is rapid, resulting from the rapidly activation (and inactivation) of voltage-gated sodium channels underlying the fast inward sodium current I_{Na}. Phase 0 is followed by a transient repolarization (phase 1 or $notch$), reflecting sodium channels inactivation and the activation of the fast transient voltage-gated outward potassium current I_{to1} and the transient calcium dependent chloride current I_{to2}. Membrane depolarization also activates voltage-gated calcium current I_{CaL} through L-type calcium channels during the $plateau$ (phase 2): this current is the main trigger for excitation contraction coupling in the working myocardium. During the plateau phase, the driving force for potassium efflux is high and, as

the calcium channels inactivate, the outward potassium currents predominate, resulting in repolarization (phase 3), bringing the transmembrane voltage back to the resting potential. Although sodium channels inactivation is rapid, some channels reopen later during phase 3; this late sodium current is called I_{NaL}. In contrast to Na^+ and Ca^{2+} channels, there are multiple types of K^+ channels that contribute to AP repolarization: voltage-gated channels underlying the delayed rectifier currents I_{Ks} and I_{Kr} during phase 3, and non-voltage gated channels underlying the inward rectifier I_{K1} current that anchors the transmembrane potential to its resting value (late phase 3).

1.2 Evidences of left ventricular transmural heterogeneities

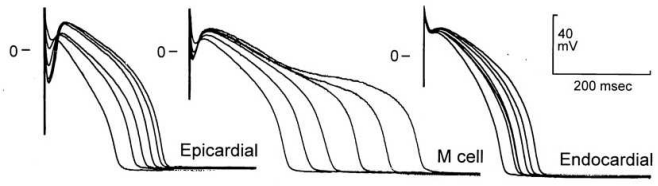

Figure 1.3: Superimposed APs recorded in isolated cells from different regions of the canine heart at different BCLs (redrawn from [83])

Until approximately twenty years ago, the cellular composition of the ventricular wall was thought to be largely homogeneous. Recent advances in our understanding of the electrophysiology and pharmacology of the ventricular myocardium have revealed at least three distinct ventricular types of isolated cells: epicardial (Epi), midmyocardial (M) and endocardial (Endo) cells (see figure 1.3). Differences in the expression patterns of a number of ion channels and in the pharmacologic profiles of these three myocardial cell types have been described in the dog, guinea pig, rabbit and human ventricles [2]. Recently ion channels' gene expression in the non-diseased human heart has been screened, showing statistical relevant differences among different regions of the heart, confirmed by the analysis of the protein levels [39].

The principal feature of the M cell is the ability of its action potential to prolong more than that of epicardium or endocardium with slowing of pacing rate ([82], [83]). In figure 1.4 experimental AP duration (at dynamical steady state) of isolated cells, measured at 90% of repolarization (APD_{90}), is plotted versus the basic cycle length of stimulation (BCL): a transmural gradient is evident with the longest APD_{90} in M cells and the shortest in Epi and Endo cells.

A review of canine LV transmural heterogeneities is given in the following; deeper descriptions with experimental data and related simulations will be given in the next sections. Properties of sodium currents expressed in different cell types from the same species, are

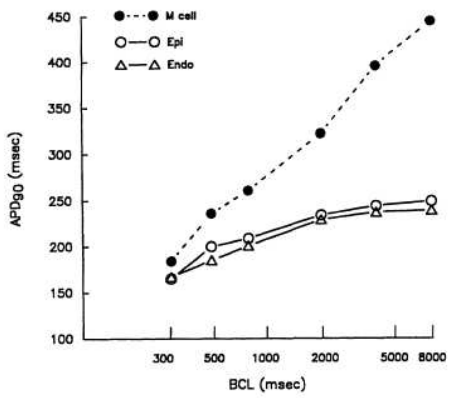

Figure 1.4: APD_{90} rate relationship from different regions of the canine heart (redrawn from [82])

similar [97]. Kinetic properties of L-type calcium channels are quite similar in different cell types too ([23], [76], [7]), even if an experimental study reports a transmural gradient in channel density [149]. Since this disparate results may be related to differences in experimental conditions or in cells' gender [150], we choose to assume the same channel densities and kinetic parameters for I_{CaL} in all types of cells considered. Also I_{K1} current has been considered the same among the three cell types [82]. The ionic currents that are known to exhibit transmural heterogeneities in the LV include the transient outward potassium current I_{to1} ([82], [76], [139]), the two components of the delayed rectifier potassium currents I_{Ks} and I_{Kr} [83], the late sodium current I_{NaL} ([156], [143]), the sodium-calcium exchanger (NCX) current I_{NaCa} ([155], [151]), the sodium-potassium pump (NaK) current I_{NaK} [41] and the sarcoplasmic reticulum pump current I_{up} [73].

I_{to1} : Channel density of I_{to1} varies transmurally in isolated cells from different regions of the LV whereas the time- and voltage-dependent properties of are similar. Differences in channel density influence AP shape, causing the observed *notch* of isolated cells from epicardium and midmyocardium ([82], [139], [76]).

I_{Ks} : As for the transient outward current, the time- and voltage-dependent properties of I_{Ks} in isolated cells from different regions of the LV are similar whereas the channel density varies transmurally: the lowest density of channels has been measured in M cells, and this contributes importantly to the longest APD of M cells (see [83])

I_{Kr} : The rapidly activating delayed rectifier potassium current I_{Kr} is almost the same with respect to his kinetics parameters, but a minimal difference in channel density exists ([83]).

I_{NaL} : Late sodium current contributes to maintaining the AP plateau in the different cell types across the wall of the canine LV; the existing regional differences are due to variations in channel density, with the greatest current reported in M cells, the lowest in Endo and Epi cells ([156], [143]).

I_{CaT} : In cells isolated from endocardium is expressed a different class of calcium channels, together with L-type channels, called T-type channels [149]. These channels (also known as low voltage calcium channels) are mainly expressed in cells of the conducting system, in which they play a role in pacemaking. They activate at relatively hyperpolarized potentials and does not contribute to excitation contraction coupling (maybe because they are located far away from T-tubules).

I_{NaCa} : A significant transmural gradient of I_{NaCa} is present in LV ([155],[151]): differences in protein levels have been measured, with the Epi layer exhibiting the greatest level compared with M and Endo layers. Yet, transmural differences in the current produced by the exchanger has been reported, with the greatest measured current in Epi cells, the lowest in Endo cells [151]. In a different experiment ([155]), the greatest current was found in M cells but this article alone cannot distinguishes whether transmural differences in I_{NaCa} result from a smaller density of channels, nonuniform sarcoplasmatic reticulum (SR) loading, or some factor limiting SR calcium release in the proximity of endocardial exchanger [155].

I_{NaK} : Transmural heterogeneities in the sodium-potassium pump have been published in [41], reporting a transmural gradient in the corresponding current: the latter larger in Epi cells than in Endo cells, with M cells being intermediate.

I_{up} : Transmural differences in canine calcium handling has been observed in wedge preparations [73] and in isolated cells [23]. Both studies reported a slower (larger time constant) calcium transient decay and a greater calcium transient duration in endocardium compared with epicardium. In [73] a reduced expression of the protein encoding the channels has been measured in the midmyocardial and endocardial layers compared with the epicardial layer. These facts suggests that the transmural heterogeneity of calcium handling reported is probably an intrinsic property of the cells, because activation sequence (endocardial versus epicardial pacing) did not influence the results [73].

1.3 Mathematical modeling of isolated cells

The first mathematical model designed to describe accurately AP waveform, the associated permeability changes of the cellular membrane and tissue conduction was proposed by Alan Lloyd Hodgkin and Andrew Fielding Huxley in 1952 [48]; for their pioneering and seminal work they received (sharing it with John C. Eccles for his works on synapsis and motoneurons) the Nobel Prize in medicine in 1963. Their formalism, developed to describe the AP of neurons has been used later in many models describing cardiac AP: for review of published computational models and the relative interaction between experiment and theory on cardiac cell (roughly speaking, the *state of the art*) see [117], [99], [110]. Since in this section whole cellular models will be introduced together with a sketch of implementation of experimental techniques, we refer the reader to the next section for a more complete

derivation of the Hodgkin-Huxley formalism from the more general statistical point of view of Markov chains.

Different ionic concentrations, between outside and inside the cell, build up a potential difference (an electrochemical gradient) across the cellular membrane and thus the latter acts as a capacitor. Specified proteins located on the cellular membrane are responsible for the diffusion of ions (ionic currents) between inside and outside the cell: ionic channels (pores of the membrane), pumps and exchangers. Ions flow through ionic channels along their electrochemical gradient (passive transport) whereas the trafficking of ions through pump and exchangers is made against the electrochemical gradient (active transport): pumps use energy derived from the metabolism (ATP hydrolysis), whereas exchangers exploit the diffusion energy of other ions. Different types of ionic channels, pumps and exchangers exist, each type made up by a population of identical proteins. The contractile function of the cell is a complex system involving different subcellular compartments for calcium handling. Hence the quantity of interest to reproduce cellular electrophysiology are the transmembrane potential v, the gating variables of ionic channels

$$w = (w_1, \dots, w_M),$$

and the ionic intracellular and subcellular concentration variables

$$c = (c_1, \dots, c_P).$$

Ionic currents acts as built in parallel with the capacitor behavior of the membrane: the total transmembrane current per unit area i_m (measured in $\mu A/cm^2$) is therefore the sum between capacity current and ionic current:

$$i_m = c_m \frac{dv}{dt} + i_{ion}, \tag{1.1}$$

where c_m is the surface capacitance (measured in $\mu F/cm^2$), $\frac{dv}{dt}$ the capacity current and i_{ion} the ionic current per unit area. When an external overthreshold conservative stimulus i_{app} is applied (see [64] for a mathematical analysis of the excitation process in the phases space), the *all-or-none* cellular response is the AP and the variation of transmembrane voltage for isolated cells is described by the equation:

$$\frac{dv}{dt} = -\frac{1}{c_m}(i_{ion} + i_{app}). \tag{1.2}$$

The right hand side of the latter equation can be viewed as composed by an autonomous system (represented by i_{ion} and the associated system of ODEs) and a forcing term i_{app} applied every fixed time T (referred to in cardiac literature as Basic Cycle Length, BCL); problems of this type can be classified as impulsive ODEs [4].

The transmembrane ionic current per unit area has the following general structure:

$$i_{ion}(v,c,w) = \sum_{k=1}^{N} G_k(v,c)(\prod_{j=1}^{M_k} w_{k_j}^{p_{k_j}})\Phi_k(v) + i_{pumps}(v,c), \tag{1.3}$$

where N is the number of different types of ionic currents and i_{pumps} is the total time independent (thus algebraic functions) ionic flux through pumps and exchangers. As a convention, an outward current is considered positive and therefore acts to reduce the transmembrane voltage, whereas an inward current is considered negative and thus raise up the transmembrane voltage. The current through the k-th population of ionic channels is characterized by a specific membrane conductance G_k that account for the whole number of channels of the population (i.e. channel density, measured in $\mu A/cm^2$), an instantaneous current voltage relation $\Phi_k(v)$ that account for the instantaneous current through a single channel of the population, and M_k dimensionless variables $w_{k_j}^{p_{k_j}}$ accounting for different gating mechanism of the k-th population. p_{k_j} is an integer representing the number of identical and independent subunits of the j-th gate for the k-th current; the opening probability of each subunit is described by a nonlinear ODE having the following structure

$$\begin{cases} \dfrac{dw_{k_j}}{dt} = \alpha_{k_j}(v)(1 - w_{k_j}) - \beta_{k_j}(v)w_{k_j} = R_{k_j}(v,w) \\ 0 \leq w_{k_j}(0) = w_{k_j}^0 \leq 1 \end{cases}, \tag{1.4}$$

where $a_{k_j}(v)$ and $b_{k_j}(v)$ (measured in s^{-1}) are positive functions representing voltage-dependent transition rates (from closed to open state and from open to closed state respectively) for each subunit of the j-th gate of the k-th current. All the p_{k_j} subunits must be in the conductive state to open the j-th gate, therefore the probability that the j-th gate is open is $w_{k_j}^{p_{k_j}}$, and $\prod_{j=1}^{M_k} w_{k_j}^{p_{k_j}}$ is the probability that the k-th channel is open (or equivalently the proportion of open channels of k-th population as it will be shown in the next section).

Experiments on ionic currents (see [47]) are mainly conducted controlling the transmembrane voltage; briefly, in *voltage clamp* (VC) and *patch clamp* (PC) conditions the transmembrane voltage is held fixed (i.e. dv/dt = 0 in (1.1)), whereas in *voltage ramp* (VR) conditions time derivative of transmembrane voltage is held fixed: ionic currents are measured as the transmembrane current necessary to maintain the conditioning (or clamped) potential. VC and PC techniques are principally used analyzing currents through ion channels, VR studying time independent currents through pumps and exchangers; in any case it is possible to isolate, with specific pharmacological aid (i.e. channel blockers or ion-free extracellular and/or intracellular conditions), each component of the ionic current. Differences between VC and PC exist: VC measures the total deterministic current across the membrane, PC isolates a little part of the membrane and measures the stochastic current through a single channel (we refer the interested reader to [47] for a deeper explanation). However, with these experimental techniques the voltage is fixed and therefore it is possible to analytically solve equation (1.4) and consequently infer the values of the transition rates.

Solutions of (1.4) at a given voltage $\overline{v}$ are characterized by the following two quantities:

$$w_{k_j,\infty}(\overline{v}) = \frac{\alpha_{k_j}(\overline{v})}{\alpha_{k_j}(\overline{v}) + \beta_{k_j}(\overline{v})}$$
$$\tau_{w_{k_j}}(\overline{v}) = \frac{1}{\alpha_{k_j}(\overline{v}) + \beta_{k_j}(\overline{v})},$$

where the dimensionless variable $w_{k_j,\infty}(\overline{v})$ is called *steady state availability* and $\tau_{w_{k_j}}(\overline{v})$ the *time constant* (measured in s) of the j-th gate of the k-th current at $\overline{v}$.

Instantaneous current voltage relation can be of two types:

$$\Phi_{LIN}(v) = v - E_c \tag{1.5}$$
$$\Phi_{GHK}(v) = \frac{z^2 v F^2}{RT} \frac{c_i e^{zFv/RT} - c_e}{e^{zFv/RT} - 1}, \tag{1.6}$$

where E_c is the Nerst potential of the ion c, z is the valence of ion c, F the Faraday constant, R the gas constant, T the absolute temperature and c_i and c_e the internal and external concentration of ion c. Both formulas are derived for electrodiffusion theories and are the results of two distinct limits for channel length: equation (1.5) (long-channel limit) is linear with transmembrane voltage, whereas equation (1.5) (short-channel limit) is the *constant field equation*, otherwise referred to as GHK equation; in both cases, the reversal potential is the so called Nerst potential

$$E_c = \frac{RT}{F} \log \frac{c_e}{c_i},$$

which can be derived from a statistical mechanics point of view (for mathematical derivations of these standard formulas, the reader is referred to [64]).

The dynamics of each intracellular concentration variable is tracked considering ionic and diffusion fluxes. The instantaneous flux J_k of a single ionic current $i_k(v, w)$ across the cellular membrane is described by the formula [28]:

$$J_k = -\frac{i_k(v, w) A_{cap}}{V z F}, \tag{1.7}$$

where V is the intracellular volume, A_{cap} is the capacitive membrane area, z is the valence of the ion and F is the Faraday constant. The minus sign appear taking into account the convention on the currents. The diffusion flux J_{DIFF} between one subcellular compartment with volume V_1 and local concentration c_1 to another compartment with volume V_2 and local concentration c_2 can be linearly approximated as

$$J_{DIFF} = -\frac{c_2 - c_1}{\tau_{12}} \frac{V_1}{V_2},$$

where τ_{12} is an experimental diffusion constant (measured in s) between V_2 and V_1. Each

concentration variable thus obeys the ODE:

$$\begin{cases} \dfrac{dc_j}{dt} = S_j(v, w, c) \\ c_j(0) = c_j^0 \end{cases}, \tag{1.8}$$

where $S_j(v, w, c)$ is the sum of all ionic and diffusive fluxes carrying ion c_j; the total flux of the j-th ion in the time interval $[t_0, t_1]$ can be computed as:

$$\int_{t_0}^{t_1} S_j(v, w, c)dt.$$

For sake of completeness, the conservative stimulus current is added in the computation of intracellular concentrations [53]: it is assumed equal to $-80\mu A/cm^2$, lasting for 1 ms and composed equally by potassium and chloride ions.

The whole nonlinear system of ODEs describing cellular electrophysiology is made up by equation (1.2) (where i_{ion} is given by equation (1.3)), coupled with M ($= \sum_k M_k$, i.e the number of gating variables) equation of type (1.4), P (number of intracellular and subcellular ionic concentrations) equation of type (1.8). Since different time scales exist during an AP (see figure 1.2), the cellular model must be solved with implicit methods designed for stiff problems. For these models, an usual choice in literature is the Matlab variable-order solver $ode15s$ (see also [126]).

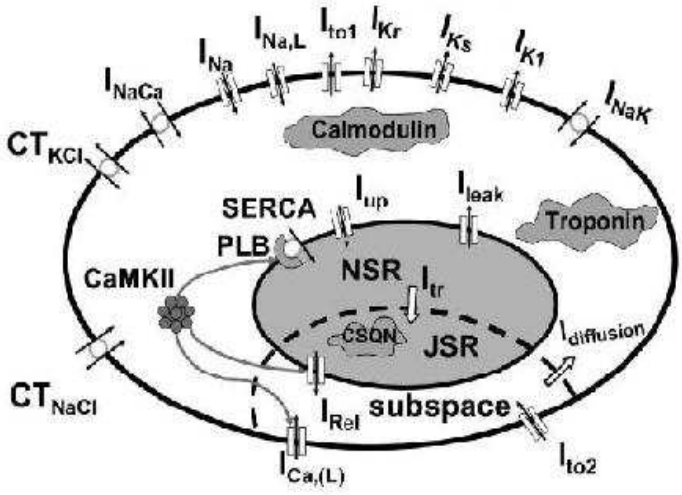

Figure 1.5: Schematic diagram of HRd2007 (redrawn from [81])

In the following we will consider the most recent published version [81] of the Hund-Rudy model [54] (HRd2007), designed for LV epicardial canine cells; see figure 1.5 for a schematic diagram of the model. Hrd2007's nonlinear system of ODEs has dimension twenty-eight: ionic currents considered are I_{Na}, I_{NaL}, I_{CaL}, I_{to1}, I_{to2}, I_{Ks}, I_{Kr}, I_{Kp} and I_{K1}, pumps and exchangers currents are I_{NaK}, I_{NaCa} and I_{pCa}. The latter current is the calcium sarcolemmatic pump that extrudes calcium ions from the cell. We elimi-

nate the plateau potassium current I_{Kp} from the original formulation because there is no evidence confirming its presence in canine ventricular cells ([97]). Dynamical intracellular ionic concentrations are sodium, potassium, calcium and chloride; subcellular calcium concentrations have been considered in the network sarcoplasmatic reticulum (NSR), in the junctional sarcoplasmatic reticulum (JSR) and in the dyadic space (subspace) with the associated diffusion fluxes. Since chloride concentrations are taken into account, the sodium-chloride cotransporter CT_{NaCl} and the potassium chloride cotransporter CT_{KCl} are included into the model. In the dyadic space, the calcium inward current through L-type channels interact in a phenomenological way with the ryanodine receptors (RyRs) to account for the excitation contraction coupling and I_{Rel} is resulting the calcium release current from JSR. Calcium buffers modeled in the intracellular volume are calmodulin and troponin, whereas in the JSR the calsequestrin is considered; each of these buffer mechanisms is assumed to be instantaneous. A protein kinase (CaMKII) is also taken into account and it interacts with calcium influx via L-type channels, calcium release trough RyRs and calcium uptake through SERCA2a pump. The interested reader is referred to [81] and references therein for a deeper description of the features and limitations of the HRd2007 model together with the complete set of model's equations.

1.4 Hodgkin-Huxley formalism and continuous time Markov chains

Although the current through the entire population of ionic channels of a species can be assumed deterministic, the current through a single channel is stochastic: deterministic models are useful tools to account for the whole species behavior but, since most properties of ion channels are best studied with single channel data [96], these models fail to reproduce physiological states of the constitutive proteins of ion channels. Proteins are typically composed of one or more pore-forming α-subunits that can be modulated by accessory subunits [97]. Each subunit contains sensors that can undergo conformational changes and must be in the activated position to open the channel. Markov state models are the natural framework to deal with this kind of complexity and they were applied after the stochastic nature of the single channel current was revealed in 1976 by Neher and Sakmann ([95], Nobel Prize in 1991), more than twenty years before Hodgkin and Huxley's work, further emphasizing the quality of their formalism.

The gating behavior of a single channel is assumed to be described by a semi-Markov process, i.e. a collection of random variables $\{X(t)|t \in \mathbb{R}^+\}$, with values in a finite *state space* $\mathcal{S} = \{1, \ldots, N\}$ in which states are visited according to an (homogeneus) continuous time *Markov chain*, i.e. $\forall s, t \geq 0, \forall 0 \leq u \leq s$ and $i, j, x(u) \in \mathcal{S}$ holds that [115]

$$P_{ij}(t) = \text{Prob}\,\{X(t+s) = j | X(s) = i\} = \text{Prob}\,\{X(t+s) = j | X(s) = i, X(u) = x(u)\}, \tag{1.9}$$

where the line brackets denote the conditioning probability. In other words, a continuous

time Markov chain is a process with no memory of the past: in fact, indicating with T_i the time spent by the system in state i (*dwell time*), from (1.9) follows that

$$\text{Prob}\,\{T_i > s + t | T_i > s\} = \text{Prob}\,\{T_i > t\}$$

$\forall s, t \geq 0$. Therefore the random variable T_i is memoryless and it must be necessarily exponentially distributed, i.e.

$$\text{Prob}\,\{T_i \leq t\} = 1 - e^{-\lambda_i t},$$

for some $\lambda_i \in \mathbb{R}^+$. Noting that $< T_i >= \lambda_i^{-1}$, where $< \cdot >$ denote the mean of a random variable, the parameter λ_i can be interpreted as the *exit rate* from state i. Let us define, $\forall i \neq j$

$$q_{ij} = \lambda_i P_{ij} \tag{1.10}$$

the *transition rate* from state i to state j; note that $q_{ij} = 0$ if states i and j are unlinked. Markov chains generally have several loops in the model that must satisfy *microscopic reversibility*. Microscopic reversibility is derived from the law of conservation of energy and states that the product of transition rate when traversing a loop clockwise must be equal to the product when traversing the same loop counterclockwise [47].

Supposing that, in an infinitesimal time interval dt, the probability that two transition occurs is $o(dt)$ (i.e. $o(dt)/dt \to 0$ if $dt \to 0$) holds that

$$\lim_{dt \to 0} \frac{1 - P_{ii}(dt)}{dt} = \lambda_i \tag{1.11}$$

$$\lim_{dt \to 0} \frac{P_{ij}(dt)}{dt} = q_{ij} \tag{1.12}$$

$\forall i \neq j$; therefore

$$\lambda_i = \sum_{j \neq i} q_{ij}, \tag{1.13}$$

i.e. the exit rate from state i is the sum of the transition rates from linked states. From assumptions (1.11) and (1.13) follows the so called *forward Kolmogorov equations* [144]:

$$\frac{d}{dt} P_{ij}(t) = -\lambda_i P_{ij}(t) + \sum_{k \neq i} q_{ik} P_{kj}(t) \tag{1.14}$$

$\forall t \in \mathbb{R}^+$ and $\forall i, j \in \mathcal{S}$.

The system of stochastic differential equations (1.14) describe the temporal behavior of the transition probabilities for a continuous time Markov chain, and exact stochastic trajectories of the process can be computed with standard Monte Carlo methods. Drawing two random numbers r_1 and r_2 uniformly distributed in $[0, 1]$ and supposing that the system is in state i, dwell times are computed as

$$T_i = -\log r_1 / \lambda_i,$$

since they are exponentially distributed with parameter λ_i. At the end of the dwell time, the next state k of the system is chosen if $r_2 \in I_k$, where I_k ($k \in \mathcal{S}, k \neq i$) is a subinterval of $[0, 1]$ of amplitude q_{ik}/λ_i.

Hodgkin and Huxley formalism can be derived analyzing the deterministic behavior of the system. We will denote with $x_i(t)$ the probability that a channel is in state i at time t: noting that the Kolmogorov equations (1.14) provide the temporal behavior of the transition probabilities not of the occupancy probabilities, and defining the set of states from whose the system can reach state i as

$$R_i = \{j \in \mathcal{S} | q_{ji} \neq 0\},$$

holds that [144]:

$$\frac{dx_i}{dt} = \sum_{k \in R_i} q_{ki} x_k(t) - \lambda_i x_i(t).$$

Therefore the vector of occupancy probabilities $\mathbf{x}(t) = (x_1(t), \ldots, x_N(t))^T$ obeys the linear system of stochastic differential equations

$$\frac{d}{dt}\mathbf{x}(t) = \mathbf{Q} \cdot \mathbf{x}, \tag{1.15}$$

where the *transition matrix* $\mathbf{Q}$ is

$$\begin{bmatrix} -\lambda_1 & q_{21} & \ldots & q_{n1} \\ q_{12} & -\lambda_2 & \ldots & q_{n2} \\ \vdots & \ddots & \ddots & \vdots \\ q_{1n} & q_{2n} & \ldots & -\lambda_N \end{bmatrix}. \tag{1.16}$$

Most ion channel models have distinct eigenvalues of transition matrix $\mathbf{Q}$ given in eq. (1.16), with one being zero, since the sum of each column of $\mathbf{Q}$ is zero for equation (1.13), and the others negative [22].

Supposing to have a large populations of independent channels $X_1, \ldots, X_M$, each of them obeying (1.15) (i.e. X_i are independent and equally distributed random variables), and defining the random variable

$$Y_{k,i}(t) = \begin{cases} 1 & \text{if } X_k(t) = i \\ 0 & \text{otherwise} \end{cases}$$

$\forall i \in \mathcal{S}$, from the laws of large numbers follows that

$$< \lim_{M \to \infty} \frac{1}{M} \sum_{k=1}^{M} Y_{k,i}(t) >= x_i(t),$$

and thus $x_i(t)$ describes the proportion of channels of the population occupying state i at a given time t. Therefore, since thousands of channels exist for each species, we can treat

deterministically system (1.15) in order to describe the average behavior of the whole population of a species.

Single activating subunit model. The simplest model is given by assuming that one subunit determines the opening and closure of the channel. The Hodgkin-Huxley formalism can be schematized as

$$\mathrm{C} \underset{\beta(v)}{\overset{\alpha(v)}{\rightleftharpoons}} \mathrm{O} \tag{1.17}$$

where C and O denotes closed and open state, $\alpha(v)$ and $\beta(v)$ are subunit's positive voltage dependent transition rates from closed to open state and from open to closed state respectively. The nonlinear system of differential equations is thus

$$\begin{cases} \dfrac{dC}{dt} = -\alpha(v)C(t) + \beta(v)O(t) \\ \dfrac{dO}{dt} = \quad \alpha(v)C(t) - \beta(v)O(t) \end{cases},$$

and the markovian matrix is

$$\mathbf{Q} = \begin{bmatrix} -\alpha & \beta \\ \alpha & -\beta \end{bmatrix}.$$

Since $\forall t \in \mathbb{R}^+$ must be $C(t) + O(t) = 1$, after some algebra the latter system can be reduced to a nonlinear differential equation

$$\frac{dO}{dt} = \frac{O_\infty(v) - O}{\tau_O(v)} \tag{1.18}$$

where

$$O_\infty(v) = \frac{\alpha(v)}{\alpha(v) + \beta(v)}$$
$$\tau_O(v) = \frac{1}{\alpha(v) + \beta(v)}.$$

Assuming that v is constant and equal to $\overline{v}$ (as in VC and PC experimental conditions) and that $O(0) = \overline{O}$, the solution of (1.18) is

$$O(t) = O_\infty(\overline{v}) - (O_\infty(\overline{v}) - \overline{O})e^{-\dfrac{t}{\tau_O(\overline{v})}}. \tag{1.19}$$

Therefore, for the simple gating schema given in eq. (1.17), if $\overline{O} < O_\infty(\overline{v})$ the channels open and the qualitative behavior of the solution is $1 - e^{-t/\tau_O(\overline{v})}$; otherwise, if $\overline{O} > O_\infty(\overline{v})$ the channels close and the solution behaves as $e^{-t/\tau_O(\overline{v})}$. Since equation (1.19) tends to $O_\infty(\overline{v})$ this quantity is called *steady state availability* of the gate; moreover, since it holds that

$$\frac{O(t + \tau_O(\overline{v})) - O(t)}{O_\infty(\overline{v}) - O(t)} = \frac{e-1}{e} \tag{1.20}$$

$\forall t \in \mathbb{R}^+$, $\tau_O(\overline{v})$ is called *time constant* of the gate. Greater time constants imply a slower

approach to steady state availability: in fact, assuming the same initial condition and steady state availability, from eq. (1.20) follows that $O(\tau_O(\overline{v}))$ is a constant function of the time constant (see Figure 1.6 and its caption).

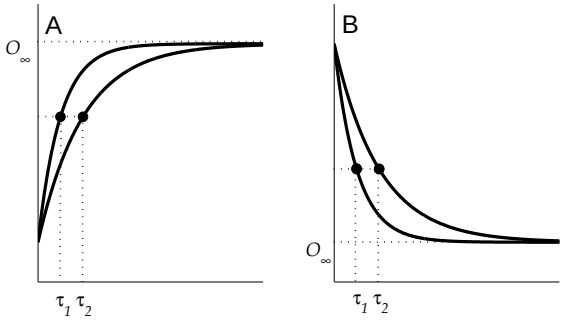

Figure 1.6: Simple gating mechanisms with same steady state availability and different time constants. Panel A: opening gates. Panel B: closing gates. For each panel, steady state availability (O_∞) and time constants ($\tau_1 < \tau_2$) are shown.

Multiple activating subunit model. Supposing that K independent and identical subunits regulate channel activation and denoting with C_j the state of a channel with $0 \leq j \leq K$ subunits in the opening position (i.e. the open state is C_K), we can deduce the following schema

$$
\begin{aligned}
&\mathrm{C}_0 \quad \underset{\beta(v)}{\overset{K\alpha(v)}{\rightleftharpoons}} \mathrm{C}_1 \\
&\mathrm{C}_1 \quad \underset{2\beta(v)}{\overset{(K-1)\alpha(v)}{\rightleftharpoons}} \mathrm{C}_2 \\
&\mathrm{C}_2 \quad \underset{3\beta(v)}{\overset{(K-2)\alpha(v)}{\rightleftharpoons}} \mathrm{C}_3 \\
&\dots \\
&\mathrm{C}_{K-2} \underset{(K-1)\beta(v)}{\overset{2\alpha(v)}{\rightleftharpoons}} \mathrm{C}_{K-1} \\
&\mathrm{C}_{K-1} \underset{K\beta(v)}{\overset{\alpha(v)}{\rightleftharpoons}} \mathrm{C}_K \quad .
\end{aligned}
$$

The system in state C_j can move to state C_{j+1} opening one of its $K - j$ subunit in closing position (with transition rate $(K - j)\alpha(v)$, where $\alpha(v)$ is the opening transition rate of each identical subunit), or to state C_{j-1} closing one of its j subunit (with transition rate $j\beta(v)$, where $\beta(v)$ is the closing transition rate of each identical subunit). In this case, the markovian matrix becomes a tridiagonal matrix where the main diagonal is given by

$$(-K\alpha, -(K-1)\alpha - \beta, \dots, -\alpha - (K-1)\beta, -K\beta),$$

the upper diagonal by

$$(\beta, 2\beta, \dots, K\beta),$$

and the lower diagonal by

$$(K\alpha, (K-1)\alpha, \ldots, \alpha).$$

It is possible to show that the occupancy probability of state C_j for a channel of this type is (see [64]):

$$C_j = \binom{K}{j} O^j (1-O)^{K-j}, \tag{1.21}$$

where $\binom{\cdot}{\cdot}$ is the binomial coefficient and O obeys the differential equation (1.18). With multiple subunits, open state probability shows an initial delay (S shaped behavior in panel A of figure 1.7) because each subunit must undergo an opening transition to open the channel, whereas channel closure is faster than in the simple gating mechanism because one subunit is enough to close the channel; with K subunits the time constant of the gate is approximately K times lower than a single subunit model as it can be seen in panel B of figure 1.7.

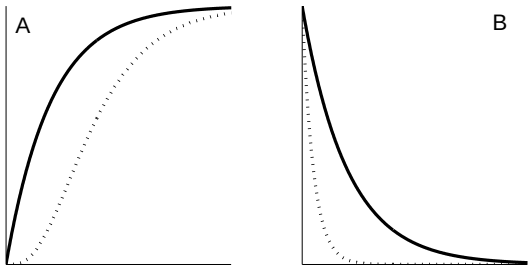

Figure 1.7: Qualitative comparison between opening (panel A) and closure (panel B) of a channel with 1 subunit (continuous lines) and 4 subunits (dotted lines).

Multiple activating and inactivating subunits model. The models constructed above doesn't account for the inactivation of channels (in time) at the same constant potential value. This can be achieved considering two different kind of subunits, one type regulating activation and one regulating inactivation. Denoting with $C_{i,j}$ the state of a channel with $0 \leq i \leq K$ independent and identical activating subunits (with forward and backward transition rates $\alpha(v)$ and $\beta(v)$ respectively) in opening positions and $0 \leq j \leq M$ independent and identical inactivating subunits (with forward and backward transition rates $\gamma(v)$ and $\delta(v)$ respectively) in opening position, the open state probability $C_{K,M}$ is (see [64])

$$C_{K,M} = O_A^K O_I^M \tag{1.22}$$

where O_A and O_I are the open state probability of an activating and inactivating subunit respectively, i.e they obeys

$$\begin{cases} \dfrac{dO_A}{dt} = \alpha(v)(1-O_A(t)) - \beta(v)O_A(t) \\ \dfrac{dO_I}{dt} = \gamma(v)(1-O_I(t)) - \delta(v)O_I(t) \end{cases}. \tag{1.23}$$

Figure 1.8 shows the open probability of a channel (continuous line) that can inactivate in time together with the opening probabilities of the activating subunits (dotted line) and inactivating ones (dashed lines).

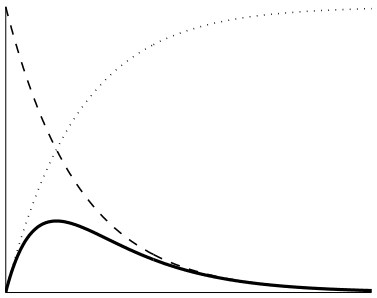

Figure 1.8: Opening probability (continuous line) of a channel that can inactivate as the product of the opening probability of one activating particle (dotted line) and one inactivating particle (dashed line).

As we have seen, Hodgkin-Huxley formalism can be derived from the more general framework of Markov chains when considering the independence and identity of subunits composing the channels. Although the Hodgkin-Huxley formalism is a powerful tool capable to reproduce the macroscopic observed features of the currents, more complex Markov chains can account for more physiological models of channels and provide useful insights into their mutations [117]. They are now widely used as accepted as the gold standard of ion channel modeling and extensively used for detailed cellular simulations (see for example [44], [35], [38]). However, the HRd2007 model has been chosen because it retains much of the complexity observed in a cardiac cell without the help of markovian models: clearly, a much simpler representation of the cell's mechanisms will loose accuracy in reproducing biophysical observations, but inserting markovian models with their multiple states and small time sclaes in tridimensional mathematical representation of the cardiac tissue would result in computationally untractable problems.

1.5 Modeling transmural cellular heterogeneities

In this section we will present the changes applied to HRd2007 in order to fit experimental data related to LV transmural heterogeneities. We will refer to this modified model as HHRd (Hetero HRd). Other models of ventricular heterogeneity have been published ([38], [10], [124]): [124] has been developed from the Priebe- Beuckelmann model [109] based on human data, [38] from the canine ventricular markovian model of Winslow and Greenstein [44] whereas [10] has been assembled from the Hund-Rudy model [54] and published in the meanwhile HHRd was developed. Qualitative differences and similarities exist between the HHRd model and the model published in [10], and they will be shown here and in the next sections. Results for Epi cells will be shown in red, for M cells in blue

and for Endo cells in green. Cell geometry and capacitance is assumed equal among the three types of cells [82].

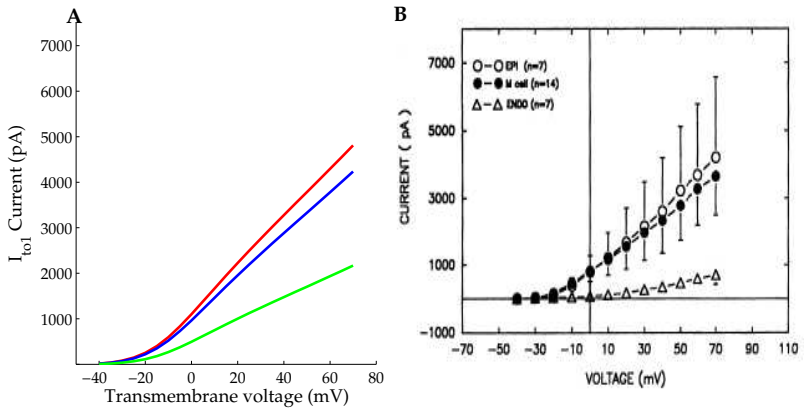

Figure 1.9: Panel A: Peak current voltage relations for I_{to1} in the three cell types. Panel B: Experimental values (redrawn from [82]).

Transient outward potassium current I_{to1} varies transmurally because of different channel densities; therefore we scale the maximum conductance of the current to reproduce the observed heterogeneity. With voltage clamp techniques, the greatest peak current has been measured in Epi and M cells, the lowest in Endo ([82], [76], [139]). The percentage of reduction from Epi to Endo cells vary among studies, from 80% ([82], [139]) to 50% [76]. The contribution of this current has been evaluated with the same VC protocol used in [82], setting $[K^+]_e = 6.0$ mM: from an holding potential of -80 mV, the cell is depolarized to different test potentials and peak of the current is measured. In figure 1.9 is provided a comparison between experimental [82] and simulated peaks at clamped potentials: the simulated current in Endo cells is greater than that measured in [82] and [76], but the ratio between Epi and Endo currents is in accordance with [139]. This choice has been made in order to get a more physiological AP waveform for endocardial cells as in [10]. In the heterogeneous model published in [38], this issue was overcame augmenting the maximum conductance of the chloride transient outward current I_{to2}: further experimental investigations are mandatory to resolve this point.

Channel densities of delayed rectifier potassium currents I_{Ks} and I_{Kr} vary transmurally. evaluating the tail currents (i.e. peak of current in response to repolarizing steps) in voltage clamp experiments, the greatest I_{Ks} current has been measured in Epi and Endo cells, the lowest in M cells ([83]). Regarding I_{Kr}, a minimal difference in channel density can be enlightened evaluating the tail currents [83]. Although a calmodulin mediated calcium dependence of I_{Ks} exists [125], we eliminate the calcium dependence of I_{Ks} from the original formulation (as in the model published in [44]) because it is based on guinea pig data [153]; further investigations, outside the scope of this study, are required to model this potentially important mechanism of functional regulation of I_{Ks}. Focusing on cellular heterogeneities, the contribution of delayed rectifier potassium currents has been assessed measuring *tail current densities* with a VC protocol setting $[K^+]_e = 6.0$ mM (see [83]):

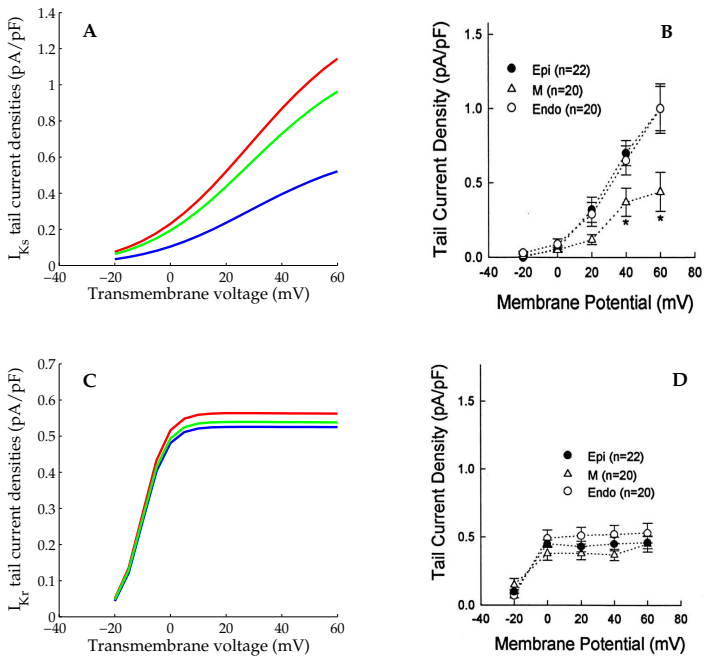

Figure 1.10: Heterogeneity of delayed rectifier potassium currents. Panel A: Tail current voltage relations for I_{Ks} in the three cell types. Panel B: I_{Ks} experimental data. Panel C: Tail current voltage relation for I_{Kr}. Panel D: I_{Ks} experimental data. (Experimental panels redrawn from [83]).

from an holding potential of -40 mV, the cell is depolarized for 5 seconds to different test potentials, ranging from -20 to 60 mV, and then stepped back to -40 mV (tail current densities are instantaneous peaks of the current during the step back); figure 1.10 shows a comparison between experimental and simulated tail currents densities versus the test potentials.

Late sodium current I_{NaL} varies transmurally [156]. We simulated the same experimental VC protocol ($[K^+]_e = 0$ mM, $[Cl^-]_e = 0$ mM and $[Na^+]_i = 10$ mM): from an holding potential of -130 mV, the cell is clamped for 1 second to different test potentials ranging from -40 to 0 mV. The mean current density during intervals of 30-35 ms (Panel A in figure 1.11) and 295-300 (Panel B) ms after the start of the depolarizing pulse has been simulated and compared in figure with experimental data. Time constant of inactivation was modified from the original constant value of 600 ms according to the formula

$$\tau = c_1 \exp(c_2 V)$$

where V is the potential and the constant values for the different cell types are listed in Table 1.1, in better agreement with canine data published in [86].

T-type calcium channels are present in Endo cells only; until now, they are not considered in any of the ventricular canine models present in literature. The formulation of the gating variables, together with time constant of activation, is from [34]. Time constant

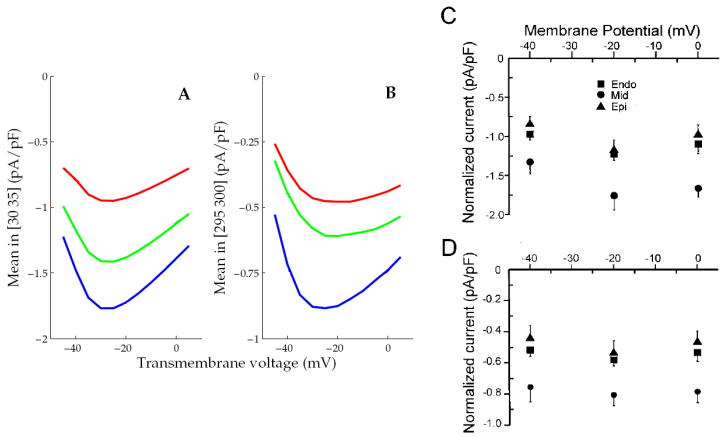

Figure 1.11: Mean of simulated I_{NaL} current density (panels A and B) and experimental data (panels C and D, redrawn from [156]) during 30-35 ms interval (panels A and C) and during 295-300 ms interval (panels B and C) after the start of the depolarizing pulse.

	Epi	M	Endo
c_1	495.1	426.9	387
c_2	9.185E-3	3.334E-3	7.898E-3

Table 1.1: Constants defining the time constant of inactivation of the Late Sodium current with the HHRd model. See text for details.

and steady state of inactivation are from canine data published in [149]. Steady state of activation has been assessed to reproduce observed peak current voltage relationship [149]. In figure 1.12 simulated (solid line) and experimental (filled circles) peak current voltage relationship have been compared; in order to perform simulation at physiological temperatures (experimental data are at 29 Celsius degrees) we assume a Q_{10} factor of 2.5 for the maximum conductance of the current.

Since a significant transmural gradient in NCX protein levels exists [151], a scaling parameter is introduced to the maximum current produced by the exchanger. The relative contribution of I_{NaCa} is evaluated performing the same experimental protocol described in [151] ($[K^+]_e = [K^+]_i = 0$ mM): the cell is initially clamped for several minutes at -40 mV to allow adequate internal dialysis of calcium and then a descending VR from 80 to -100 mV in 360 ms ($dV/dt = 0.5$) is applied. In figure 1.5 is shown a comparison between simulated (Panel A) and experimental (Panel B) currents plotted against transmembrane voltage: maxima and minima of current densities are in closely agreement with experimental values as well as the characteristic crossing of data at about -40 mV.

A transmural gradient of I_{NaK} and associated variations in intracellular calcium has been recently published [41] for isolated canine ventricular cells; we therefore introduce a

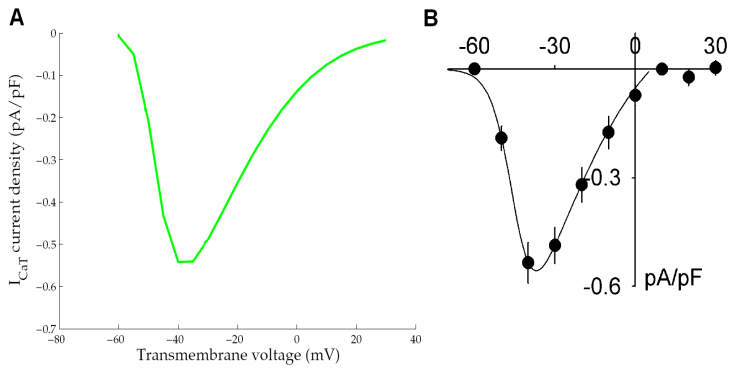

Figure 1.12: Simulated (panel A) and experimental (panel B, redrawn from [149]) peak current voltage relation of I_{CaT} in Endo cells at 29.

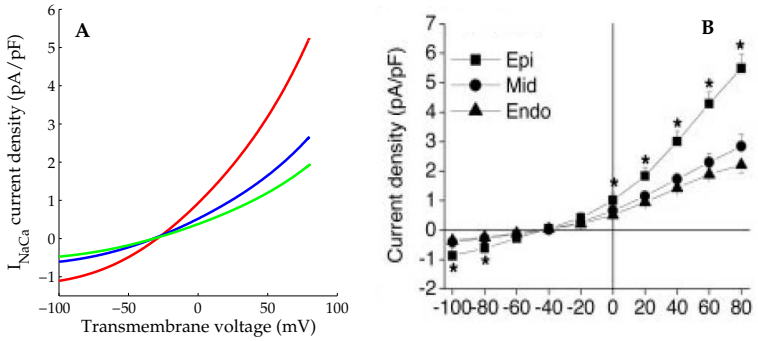

Figure 1.13: Simulated end experimental I_{NaCa} in different regions of the heart. Experimental figure has been redrawn from [151]

scaling parameter to the maximum current produced by the pump in order to qualitatively reproduce the experimental results. From an holding potential of 0 mV and with $[Na^+]_i = 60$ mM, a descending VR, from $+50$ mV to -100 mV in 4 seconds ($dV/dt = 3/80$), is applied. In figure 1.5 simulated (continuous lines) and experimental data (dotted lines) are compared: although simulated and experimental curves don't match, the transmural gradient is qualitatively preserved, with the highest current in Epi cells, the lowest in Endo ones.

A significant transmural gradient in SERCA2a protein levels exists [73]; a scaling parameter is thus introduced to the maximum uptake current I_{up}. Experimental values of protein level in M and Endo cells is 66% and 61% of Epi cells, computational percentages used for simulations are 67% and 50% respectively. Since a direct measurement of this current doesn't exist in literature, a validation can be made only analyzing his effects on whole cell calcium transients.

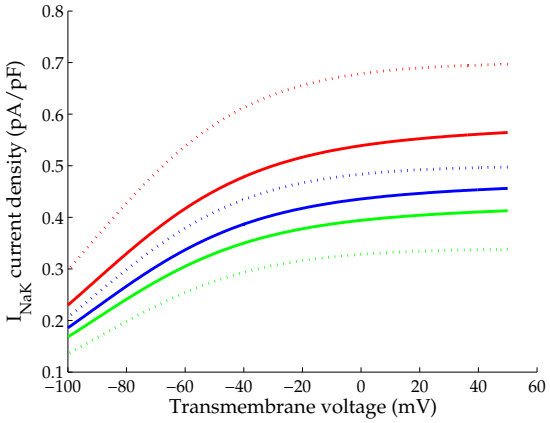

Figure 1.14: Simulated (continuous lines) end experimental (dotted lines) I_{NaK} in different regions of the heart.

	I_{Ks}	I_{Kr}	I_{to1}	I_{NaL}	I_{NaCa}	I_{NaK}	I_{up}	I_{CaT}
Epi	1.72	1.00	1.10	1.77	2.70	1.30	1.50	0.00
M	0.80	0.95	1.00	3.30	1.30	1.05	1.00	0.00
Endo	1.47	0.97	0.50	2.69	0.90	0.95	0.75	0.40

Table 1.2: Summary of scaling factors for maximum conductances of the HHRd model with respect to the original formulation.

1.6 Validations of the HHRd model

Dynamical steady state. The HHRd model has been simulated for thousands of beats from original (HRd2007) initial conditions until it will reach a dynamical (long term) steady state [53], here defined when the maximum absolute value of the difference between two consecutive vectors of initial conditions is less than 0.0001, i.e.

$$||\boldsymbol{x_0}^N - \boldsymbol{x_0}^{N+1}||_\infty < 0.0001 \tag{1.24}$$

where $\boldsymbol{x_0}^N$ is the vector of initial conditions for the N-th beat. All variables influences AP waveform: gating variables reach their dynamical steady state values within tens of beats, subcellular and intracellular calcium concentrations in hundreds of beats whereas other sarcoplasmatic ionic concentrations (sodium, potassium and chloride) reach their steady state values in thousands of beats with a biexponential time course of the type

$$x_0 + x_1 e^{-t/\tau_1} + x_2 e^{-t/\tau_2} \tag{1.25}$$

where x_0 is the dynamical steady state value. In figure 1.6 is shown a representative behaviour of the beat-varying intracellular ionic concentrations for Epi cells: sodium concentrations reach their steady state values within the simulations, whereas potassium and

chloride concentrations reach their long term steady state values after the simulated beats because the stimulus current is injected at every beat. We choose to maintain the cut-off value (1.24) since long term experimental concentrations of sodium have been already published [41], whereas potassium and chloride concentrations haven't been published yet.

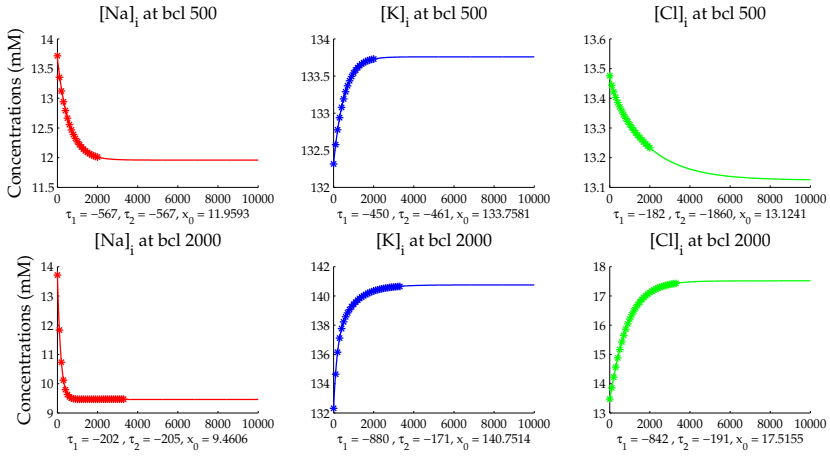

Figure 1.15: Initial values of intracellular ionic concentrations for Epi cells (asterisks) plotted against beat number; continuous line are the biexponential fittings. Below each panel the principal features of the fitting are summarized consistently with the notation used in eq. (1.25). Sodium concentrations are shown in red, potassium concentrations in blue and chloride concentrations in green

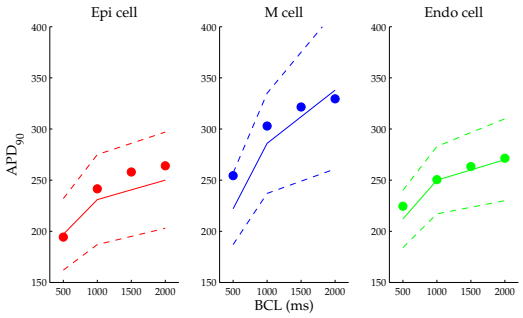

Figure 1.16: APD rate relationship for the HHRd model (filled circles) and experimental values (mean ± SD) at $[K^+]_e = 6.0$ mM [83].

APD rate relationship. Since the HHRd model was built up to analyze transmural dispersion of repolarization (TDR, maximum APD minus minimum APD among cell types at fixed BCL) in heterogeneous tissues, a validation of the ionic currents' balance should be based upon experimental data of steady state APD_{90} rate relationship: we choose the data published in [83] since they were used to validate the other models of left ventricular heterogeneity. Differently from other computational studies of cellular heterogeneity ([38], [10], [124]), we set $[K^+]_e = 6.0$ mM to more closely reproduce experimental conditions: simulated (filled circles) and experimental values (continuous line is for mean, dashed lines for mean ± standard deviation) are in agreement as shown in figure 1.16. Physiological

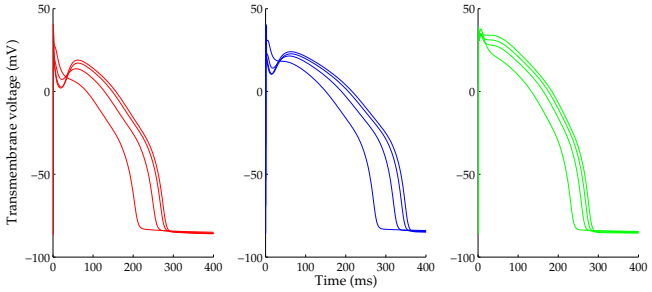

Figure 1.17: Steady state APs simulated with HHrd for BCLs ranging from 500 to 2000 ms in different regions of the heart.

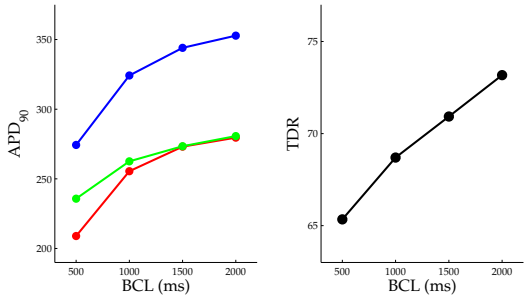

Figure 1.18: APD_{90} rate relationship in different regions of the heart.

($[K^+]_i = 5.4$ mM) steady state APs at different BCLs, ranging from 500 to 2000 ms in 500 ms step, are shown in figure 1.17 whereas in figure 1.18 is shown APD_{90} rate relationship for the three cell types together with the TDR. Observed APs are well reproduced by the HHRd model (see figure 1.3). The simulated APD_{90} rate relationships preserve the transmural gradient observed in most of experimental studies ([83], [5], [139], [138]), with Endo APD_{90} longest than that of Epi cells as in the model [38], even if some other experimental studies reports the opposite configuration ([82], [76], [127]) as predicted by the model published in [10]. Moreover, since the maximum conductance of I_{Kr} current is directly proportional to the square root of extracellular potassium, the HHRd model predicts longer APs at physiological concentrations of extracellular potassium (with values varying from 15 to 25 ms) than that used to validate it.

Diastolic concentrations. Dynamical steady states of diastolic intracellular concentrations of sodium and calcium are shown in figure 1.19. Diastolic intracellular sodium is higher at lower BCLs (a feature already reproduced by HRd2007 model) for each type of cell; moreover HHRd model predicts higher concentrations of sodium in Endo cells rather than Epi cells, in closely agreement with experimental values [41]. The greater heterogeneity of sodium flux across the membrane is through the sodium-calcium exchanger and the sodium potassium pump. In fact, total sodium flux through NCX (J^{Na}_{NCX}) is positive for each type of cells at every BCL simulated, and thus NCX pumps sodium into the cell; moreover, at dynamical steady state, the flux of the exchanger is an increasing function of the

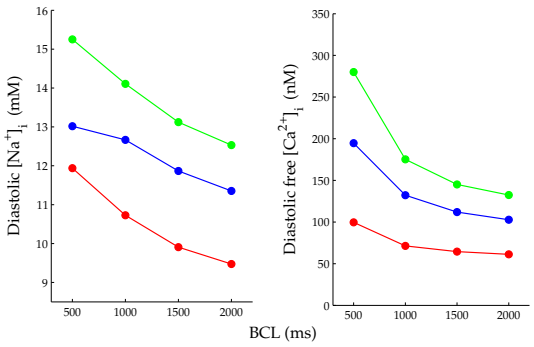

Figure 1.19: Heterogeneity of diastolic intracellular sodium and calcium concentrations at steady state simulated by the HHrd model as functions of BCL.

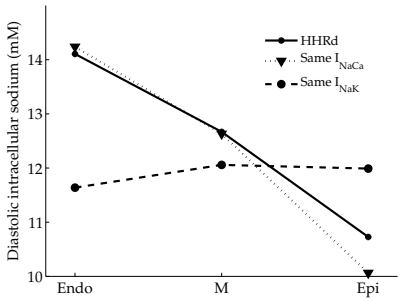

Figure 1.20: Transmural gradient in diastolic intracellular sodium concentration at 1 Hz: control conditions (continuous line), with the same I_{NaK} for all cells (dotted line) and with the same I_{NaCa} for all cells (dashed line)

BCL. NaK extrudes sodium ions from the cell (i.e the flux $J^{Na}_{NaK} < 0$) and it is a decreasing function of the BCL at dynamical steady state. The computational sum $J^{Na}_{NCX} + J^{Na}_{NCX}$ results in a negative decreasing function of the BCL, indicating that NaK has the major role in intracellular sodium handling. To enlight this point, dynamical steady states at 1 Hz have been simulated with the same density of I_{NaK} or with the same density of I_{NaCa} (chosen equal to the mean of densities in HHRd model) for each type of cell (see figure 1.20): the results show how heterogeneity in NaK is necessary to build up the intracellular sodium gradient observed in isolated cells, while I_{NaCa} heterogeneity doesn't influence intracellular sodium concentration heterogeneity. Regarding to diastolic intracellular free calcium concentration at dynamical steady state, HHRd model predicts higher concentrations in Endo cells rather than in Epi cells as observed experimentally in rat cells [29].

Systolic calcium concentration. Since tension development in cardiac cells is a function of peak intracellular calcium concentration, another important feature of LV transmural heterogeneity is the frequency dependence of calcium transients during an AP. In figure 1.21 calcium transients are plotted for the same cell type at different BCLs (see legend), whereas in figure 1.22 is shown the frequency-dependence of $\Delta[Ca^{2+}]_i$ (panel A) and of the peak of CaMKII activity (panel B). It must be noted that the model published in [10]

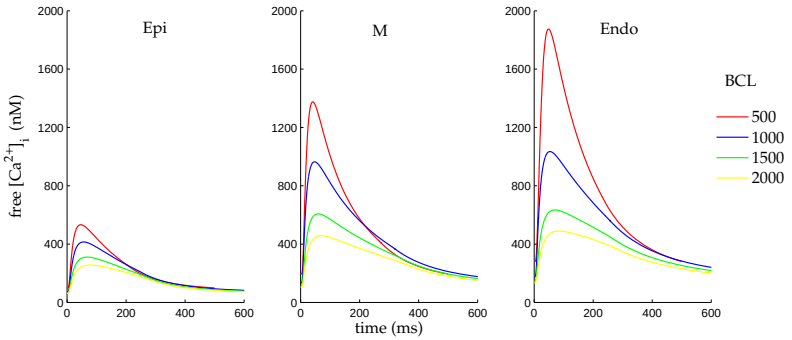

Figure 1.21: Calcium transients at different BCLs of stimulation (see legend) in different cell types.

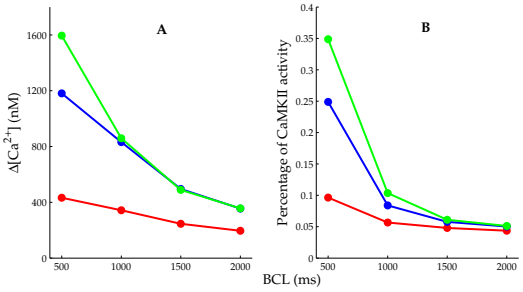

Figure 1.22: Heterogeneity of $\Delta[Ca^{2+}]_i$ (panel A) and CaMKII activity (panel B) simulated by the HHRd model.

doesn't account for a positive force frequency relationship (higher calcium peak at higher frequency) for Epi cells.

Chapter 2

Cardiac reaction-diffusion models

2.1 Governing partial differential equations

2.1.1 The Bidomain model

In the following, we will denote by Ω the volume of cardiac tissue considered, by v the transmembrane potential, i.e. the potential jump across the cellular membrane

$$v = u_i - u_e,$$

with u_i and u_e the intra- and extra-cellular electrical potentials, respectively. The macroscopic Bidomain model represents the cardiac tissue as a syncytium, i.e. the superimposition of two anisotropic continuous media, the intra- (i) and extra- (e) cellular media, coexisting at every point of the tissue and separated by a distributed continuous cellular membrane; see [98] and [107] for a derivation of the Bidomain model from homogenization of cellular models. The cardiac ventricular tissue can be modeled as an arrangement of cardiac fibers which rotate counterclockwise (CCW) from epi- to endocardium ([134]) and which has a laminar organization modeled as a set of muscle sheets running radially from epi- to endocardium ([75]). Therefore, at every point $\mathbf{x}$ it is possible to identify a triplet of orthonormal principal axes, $\mathbf{a}_l(\mathbf{x})$, $\mathbf{a}_t(\mathbf{x})$ and $\mathbf{a}_n(\mathbf{x})$, with $\mathbf{a}_l(\mathbf{x})$ parallel to the local fiber direction, $\mathbf{a}_t(\mathbf{x})$ and $\mathbf{a}_n(\mathbf{x})$ respectively tangent and orthogonal to the radial laminae, and both being trasversal to the fiber axis. Recently, the development of the Diffusion Tensor Magnetic Resonance Imaging (DT-MRI) has produced non-invasive information about the anatomic structure of the myocardium, which further supports the concept of a laminar structure, bringing about an orthotropic anisotropy of the myocardial tissue (see [52] for a recent numerical and experimental validation on this subject).

Denoting by $\sigma_l^{i,e}$, $\sigma_t^{i,e}$ and $\sigma_n^{i,e}$ the conductivity coefficients in the intra- and extracellular media measured along the corresponding directions $\mathbf{a}_l(\mathbf{x})$, $\mathbf{a}_t(\mathbf{x})$ and $\mathbf{a}_n(\mathbf{x})$, the anisotropic conductivity tensors $D_i(\mathbf{x})$ and $D_e(\mathbf{x})$ related to orthotropic anisotropy of the

	Intracellular	Extracellular	Unity measure
σ_l	$3 \cdot 10^{-3}$	$2 \cdot 10^{-3}$	$\Omega^{-1}cm^{-1}$
σ_t	$3.1525 \cdot 10^{-4}$	$1.3514 \cdot 10^{-3}$	$\Omega^{-1}cm^{-1}$
σ_n	$3.1525 \cdot 10^{-5}$	$6.757 \cdot 10^{-4}$	$\Omega^{-1}cm^{-1}$

Table 2.1: Conductivity coefficients

media are given by

$$D_{i,e}(\mathbf{x}) = \sigma_l^{i,e}\mathbf{a}_l(\mathbf{x})\mathbf{a}_l^T(\mathbf{x}) + \sigma_t^{i,e}\mathbf{a}_t(\mathbf{x})\mathbf{a}_t^T(\mathbf{x}) + \sigma_n^{i,e}\mathbf{a}_n(\mathbf{x})\mathbf{a}_n^T(\mathbf{x}). \tag{2.1}$$

In this thesis, domain Ω will be a three-dimensional slab (i.e. a parallelepiped) of cardiac tissue described in the usual cartesian coordinate system $(\boldsymbol{e}_x, \boldsymbol{e}_y, \boldsymbol{e}_z)$, in order to reproduce the experimental setting of the *arterially-perfused left ventricular wedge* of Antzelevitch [152]; the fibers rotate intramurally linearly proceeding CCW from epicardium to endocardium. Noting that $\mathbf{a}_l(\mathbf{x})$, $\mathbf{a}_t(\mathbf{x})$ and $\mathbf{a}_n(\mathbf{x})$ form an orthonormal triplet $\forall \mathbf{x} \in \Omega$, it follows that the diffusion tensors (2.1) can be expressed as

$$D_{i,e}(\mathbf{x}) = \sigma_t^{i,e} I + (\sigma_l^{i,e} - \sigma_t^{i,e})\mathbf{a}_l(\mathbf{x})\mathbf{a}_l^T(\mathbf{x}) + (\sigma_n^{i,e} - \sigma_t^{i,e})\mathbf{a}_n(\mathbf{x})\mathbf{a}_n^T(\mathbf{x}),$$

therefore only two orthogonal vectors are required to define the conductivity tensors. Considering $\mathbf{a}_n(\mathbf{x}) = \mathbf{e}_z$ (i.e. fibers lie in the (x,y) plane) and denoting with l_z the thickness of the tissue, we thus define a complete orthonormal triplet with a total amount of rotation $\alpha_0\pi$ by setting:

$$\begin{cases} \mathbf{a}_l(\mathbf{x}) = \mathbf{e}_x \cos\alpha(z) + \mathbf{e}_y \sin\alpha(z) \\ \alpha(z) = \alpha_0\pi\dfrac{l_z - z}{l_z} - \dfrac{\pi}{4} \qquad\qquad 0 \le z \le l_z \end{cases}.$$

We assume that both the intracellular coupling and the extracellular matrix are uniform, i.e. the intra- and extracellular conductivity coefficients along and across fibers are independent of position. Their values are given in table 2.1.1: for their validation, the interested reader is referred to [21].

Denoting by χ the ratio of membrane surface area per tissue volume, then from eq. (1.2) the transmembrane current per unit volume is given by $I_{ion} = \chi i_{ion}$ and the surface capacitance per unit volume is $C_m = \chi c_m$. In our simulations, the ratio of membrane area per tissue volume is assumed equal to 1E3 whereas the cell capacitance equal to 1E-3; therefore in the following we will assume $C_m = 1$. Imposing the conservation of currents, i.e. the interchange between the two media must balance the membrane current flow per unit volume, one derives a reaction-diffusion system for cardiac tissue. More specifically, denoted by $J_i = -D_i\nabla u_i$ and $J_e = -D_e\nabla u_e$ the intra- and extracellular current densities in terms of the intra and extracellular potentials, due to the current conservation law we have $\nabla \cdot J_i = -I_{ion}$ and $\nabla \cdot J_e = I_{ion} - I_{app}^e$ (I_{app}^e is a suitable applied extracellular

current per unit volume) with $\nabla\cdot$ the usual divergence operator, i.e. in three dimensions

$$\nabla \cdot u = \sum_{i=1}^{3} \frac{\partial u}{\partial x_i}.$$

Then the Bidomain model in the unknowns $u_i(\mathbf{x},t), u_e(\mathbf{x},t)$ and $v(\mathbf{x},t)$, coupled with the cellular model, can be written as:

$$\begin{cases} \partial_t v - \nabla\cdot(D_i\nabla u_i) + I_{ion}(v,w,c) = 0 & \text{on } \Omega\times(0,T) \\ -\partial_t v - \nabla\cdot(D_e\nabla u_e) - I_{ion}(v,w,c) = -I^e_{app} & \text{on } \Omega\times(0,T) \\ \partial_t w - R(v,w) = 0,\ \partial_t c - S(v,w,c) = 0 & \text{on } \Omega\times(0,T) \\ \boldsymbol{n}^T D_{i,e}\nabla u_{i,e} = 0 & \text{on } \partial\Omega\times(0,T) \\ v(\mathbf{x},0) = v_0(\mathbf{x}), w(\mathbf{x},0) = w_0(\mathbf{x}), c(\mathbf{x},0) = c_0(\mathbf{x}) & \text{on } \Omega \end{cases} \tag{2.2}$$

where the nonlinear functions $R(v,w)$ and $S(v,w,c)$ account for the gating and ionic cellular system (see Chapter 1). Since we have imposed insulated Neumann boundary conditions, we must impose the following compatibility condition for the system (2.2) in order to be solvable

$$\int_\Omega I^e_{app} = 0. \tag{2.3}$$

The Bidomain system uniquely determines v, while the potentials u_i and u_e are defined only up to a same additive time-dependent constant relating to the reference potential. This potential is chosen to be the average extracellular potential in the cardiac volume by imposing

$$\int_\Omega u_e \,\mathrm{dx} = 0. \tag{2.4}$$

2.1.2 The Monodomain model

It is well known that the Bidomain system reduces to the Monodomain model assuming equal anisotropy ratio of the two media [64]. For simulating purposes, we introduce another interesting derivation which does not make such an assumption (see also [62] and [15]) and that we will still call Monodomain model. Denoting by $J_{tot} = J_i + J_e$ the total current flowing in the two media, since $J_{tot} = -D_i\nabla u_i - D_e\nabla u_e$ and substituting $u_i = v + u_e$, we get

$$D\nabla u_e = -D_i\nabla v - J_{tot} \tag{2.5}$$

with $D = D_i + D_e$. Since the tensors $D_{i,e}$ are symmetric positive definite (see eq. (2.1) and Section 2.4), the second equation in (2.2) can be rewritten as

$$-\partial_t v + \nabla\cdot(D_e D^{-1} D_i\nabla v) + \nabla\cdot(D_e D^{-1} J_{tot}) - I_{ion}(v,w,c) = -I^e_{app} \tag{2.6}$$

and, omitting the dependence of principal axes from **x**, we obtain

$$D_e D^{-1} = \mu_l^e I + (\mu_t^e - \mu_l^e)\mathbf{a}_t\mathbf{a}_t^T + (\mu_n^e - \mu_l^e)\mathbf{a}_n\mathbf{a}_n^T \tag{2.7}$$

with $\mu_{l,t,n}^e = \sigma_{l,t,n}^e/(\sigma_{l,t,n}^e + \sigma_{l,t,n}^i)$. Assuming constant conductivity coefficients and taking into account that $\nabla \cdot J_{tot} = -I_{app}^e$, we have

$$\nabla\cdot(D_e D^{-1} J_{tot}) = -\mu_l^e I_{app}^e + (\mu_t^e - \mu_l^e)\nabla\cdot(\mathbf{a}_t\mathbf{a}_t^T J_{tot}) + (\mu_n^e - \mu_l^e)\nabla\cdot(\mathbf{a}_n\mathbf{a}_n^T)J_{tot}). \tag{2.8}$$

From (2.5) it follows that $-D_e D^{-1} D_i \nabla v = D_e D^{-1} J_{tot} + D_e \nabla u_e$; hence we have the flux relationship

$$\mathbf{n}^T(D_e D^{-1}\nabla v) = \mathbf{n}^T D_e D^{-1} J_{tot} + \mathbf{n}^T D_e \nabla u_e. \tag{2.9}$$

Using the split form (2.7) the first term on the right hand side can be written as

$$\mathbf{n}^T(D_e D^{-1} J_{tot}) = \mu_l^e \mathbf{n}^T J_{tot} + (\mu_t^e - \mu_l^e)(\mathbf{n}^T\mathbf{a}_t)(\mathbf{a}_t^T J_{tot}) + (\mu_n^e - \mu_l^e)(\mathbf{n}^T\mathbf{a}_n)(\mathbf{a}_n^T J_{tot}).$$

The insulating conditions $\mathbf{n}^T J_i = \mathbf{n}^T J_e = 0$ trivially imply that $\mathbf{n}^T J_{tot} = 0$, i.e. J_{tot} is tangent to $\partial\Omega$, and assuming that fibers are also tangent to $\partial\Omega$ we have $\mathbf{n}^T\mathbf{a}_n = 0$ and $\mathbf{a}_l^T J_{tot} = 0$; substituting these conditions in (2.9) it follows

$$\mathbf{n}^T D_e D^{-1} D_i \nabla v = 0. \tag{2.10}$$

Disregarding the two additional source terms in (2.8) related to the projections of J_{tot} on the directions across fibers (i.e. $\mathbf{a}_t$ and $\mathbf{a}_n$), it results $\nabla \cdot D_e D^{-1} J_{tot} \approx -\mu_l^e I_{app}^e$. Substituting this approximation in (2.6) and considering the boundary conditions (2.10), we obtain the anisotropic Monodomain model consisting in a single parabolic reaction-diffusion equation for the transmembrane potential v, with the conductivity tensor

$$D_m = D_e D^{-1} D_i \tag{2.11}$$

and applied stimulus

$$I_{app}^m = I_{app}^e\ \sigma_l^i/(\sigma_l^e + \sigma_l^i) \tag{2.12}$$

coupled with the same cellular system:

$$\begin{cases} \partial_t v - \nabla\cdot(D_m\nabla v) + I_{ion}(v,w,c) = I_{app}^m & \text{in } \Omega\times(0,T) \\ \partial_t w - R(v,w) = 0,\ \partial_t c - S(v,w,c) = 0 & \text{in } \Omega\times(0,T) \\ \mathbf{n}^T D_m \nabla v = 0 & \text{in } \partial\Omega\times(0,T) \\ v(\mathbf{x},0) = v_0(\mathbf{x}), w(\mathbf{x},0) = w_0(\mathbf{x}), c(\mathbf{x},0) = c_0(\mathbf{x}) & \text{in } \Omega \end{cases}. \tag{2.13}$$

2.2 Variational formulations

In this section, we briefly describe the variational formulation of both the Monodomain and the Bidomain model, providing some references to their theoretical analysis. We will deal with the following functional spaces: V the Sobolev space $H^1(\Omega)$, $\widetilde{V}$ the quotient space $H^1(\Omega)/\mathbb{R}$ and U their cartesian product $V \times \widetilde{V}$. Let us define

$$\begin{aligned}(\phi, \psi) &= \int_\Omega \phi\psi, \\ a_{i,e}(\phi, \psi) &= \int_\Omega (\nabla\phi)^T D_{i,e} \nabla\psi, \\ a(\phi, \psi) &= \int_\Omega (\nabla\phi)^T D_m \nabla\psi\end{aligned} \tag{2.14}$$

the usual $L^2(\Omega)$ inner product and the elliptic bilinear forms given by the tensors.

The variational formulation of the Monodomain model (2.13) reads as follows. Given v_0, w_0, $c_0 \in L^2(\Omega)$ and $I^m_{app} \in L^2(\Omega\times(0,T))$, find $v \in L^2(0,T;V)$, $w \in L^2(0,T;L^2(\Omega)^M)$ and $c \in L^2(0,T;L^2(\Omega)^P)$ such that $\partial v/\partial t \in L^2(0,T;V)$, $\partial w/\partial t \in L^2(0,T;L^2(\Omega)^M)$, $\partial c/\partial t \in L^2(0,T;L^2(\Omega)^P)$ and $\forall t \in (0,T)$

$$\begin{cases} (\partial_t v(t), \phi) + a(v(t), \phi) + (I_{ion}(v, w, c), \phi) = (I^m_{app}, \phi) & \forall \phi \in V \\ (\partial_t w(t), \psi) = (R(v(t), w(t)), \psi) & \forall \psi \in L^2(\Omega)^M \\ (\partial_t c(t), \psi) = (S(v(t), w(t), c(t)), \psi)) & \forall \psi \in L^2(\Omega)^P \end{cases} \tag{2.15}$$

with appropriate initial conditions on v, w and c and taking into account the compatibility condition (2.3). Analogously, the variational formulation of the Bidomain model (2.2) reads as follows. Given v_0, w_0, $c_0 \in L^2(\Omega)$, $I^e_{app} \in L^2(\Omega\times(0,T))$, find $u_i \in L^2(0,T;V)$, $u_e \in L^2(0,T;\widetilde{V})$, $w \in L^2(0,T;L^2(\Omega)^M)$ and $c \in L^2(0,T;L^2(\Omega)^P)$ such that $\partial v/\partial t \in L^2(0,T;V)$, $\partial w/\partial t \in L^2(0,T;L^2(\Omega)^M)$, $\partial c/\partial t \in L^2(0,T;L^2(\Omega)^P)$ and $\forall t \in (0,T)$

$$\begin{cases} \quad (\partial_t v(t), \hat{u}_i) + a_i(u_i(t), \hat{u}_i) + (I_{ion}(v, w, c), \hat{u}_i) = 0 & \forall \hat{u}_i \in V \\ -(\partial_t v(t), \hat{u}_e) + a_e(u_e(t), \hat{u}_e) - (I_{ion}(v, w, c), \hat{u}_e) = -(I^e_{app}, \hat{u}_e) & \forall \hat{u}_e \in \tilde{V} \\ (w(t), \psi) = (\partial_t R(v(t), w(t)), \psi) & \forall \psi \in L^2(\Omega)^M \\ (c(t), \psi) = (\partial_t S(v(t), w(t), c(t)), \psi) & \forall \phi \in L^2(\Omega)^P \end{cases} \tag{2.16}$$

with initial conditions on v, w and c and taking into account the compatibility condition (2.3).

Many well-known theoretical results available for reaction-diffusion equations (see [12] and [129]) can be applied to the Monodomain model. Less is known on degenerate reaction-diffusion systems such as the Bidomain model. For the Bidomain system with the Fitz-Hugh-Nagumo model, we refer to ([18], [121]) for existence, uniqueness and regularity results, both at the continuous and at the semidiscrete level, and to [121] for a convergence analysis of finite element approximations. A recent mathematical analysis

of the Bidomain model taking into account more general gating systems and intracellular concentrations can be found in [145]. More results are known on the related eikonal approximation describing the propagation of the excitation front; we refer to [16], [17], [61] and [9]. A mathematical analysis of the Bidomain model using Γ-convergence theory can be found in [1].

2.3 Space-Time discretization

Spatial discretization.

The parallelipedal domain Ω is discretized by introducing a structured quasi-uniform grid of hexahedral isoparametric Q_1 elements (see e.g. [113] for a general introduction to the finite element method, FEM) obtained by a uniform subdivision of the intervals $[0, l_x] \times [0, l_y] \times [0, l_z]$, into (n_x, n_y, n_z) subintervals. Using the same symbol for the domain and its FEM approximation, we have $\Omega = \bigcup_{E \in \mathcal{T}_h} E$, where $E = T_E(\hat{E})$, with $\hat{E} = [-1, 1]^3$ and T_E a trilinear map. The associated finite element spaces are given by:

$$V_h = \{\varphi_h \in V : \ \varphi_h \in C^0(\Omega), \ \varphi_{h|E} \circ \mathcal{T}_E \in Q_1(\hat{E}), \ \forall E \in \mathcal{T}_h\}, \tag{2.17}$$

$$\widetilde{V}_h = \{\varphi_h \in V_h : \int_\Omega \varphi_h = 0\}, \tag{2.18}$$

$$U_h = V_h \times \widetilde{V}_h,$$

where $Q_1(\hat{E})$ is the space of the trilinear functions on $\hat{E}$. A semidiscrete problem is first obtained by applying a standard Galerkin procedure and choosing a finite element basis φ_i for V_h. Let $\mathrm{M} = (m_{rs})$, $\mathrm{A} = (a_{rs})$ and $\mathrm{A}^{i,e} = (a^{i,e}_{rs})$ be the symmetric mass and stiffness matrices defined by:

$$m_{rs} = \sum_E \int_E \varphi_r \varphi_s \ \mathrm{dx},$$

$$a_{rs} = \sum_E \int_E \nabla\varphi_r D_m(\mathrm{x}) \nabla\varphi_s \ \mathrm{dx},$$

$$a^{i,e}_{rs} = \sum_E \int_E \nabla\varphi_r D_{i,e}(\mathrm{x}) \nabla\varphi_s \ \mathrm{dx},$$

where the diffusion tensors' appearing in these formulas are from (2.11) and (2.1). Let I^h_{ion}, $I^{m,h}_{app}$ and $I^{e,h}_{app}$ be the finite element interpolants of I_{ion}, I^m_{app} and I^e_{app}, respectively. Denoting by the same letters finite element functions and the vectors of their nodal values, in the Monodomain model, the finite element approximation v_h of the transmembrane potential is the solution of the following nonlinear system of ODEs

$$\mathrm{M}\frac{\partial v_h}{\partial t} + \mathrm{A}v_h + \mathrm{M}I^h_{ion}(v_h, w_h, c_h) = \mathrm{M}I^{m,h}_{app},$$

while in the Bidomain model, the finite element approximations $u_{i,h}$ and $u_{e,h}$ of the intra-ed extracellular potentials are the solutions of the system

$$\begin{cases} \mathrm{M}\dfrac{\partial v_h}{\partial t} + \mathrm{A}_i u_{i,h} + \mathrm{M}I_{ion}^h(v_h, w_h, c_h) = 0 \\ -\mathrm{M}\dfrac{\partial v_h}{\partial t} + \mathrm{A}_e u_{e,h} - \mathrm{M}I_{ion}^h(v_h, w_h, c_h) = -\mathrm{M}I_{app}^{e,h} \end{cases},$$

or in compact form as

$$\mathcal{M}\frac{\partial}{\partial t}\begin{pmatrix} u_{i,h} \\ u_{e,h} \end{pmatrix} + \mathcal{A}\begin{pmatrix} u_{i,h} \\ u_{e,h} \end{pmatrix} + \begin{pmatrix} \mathrm{M}I_{ion}^h(v_h, w_h, c_h) \\ -\mathrm{M}I_{ion}^h(v_h, w_h, c_h) \end{pmatrix} = \begin{pmatrix} 0 \\ -\mathrm{M}I_{app}^{e,h} \end{pmatrix},$$

where $v_h = u_{i,h} - u_{e,h}$ and

$$\mathcal{M} = \begin{bmatrix} \mathrm{M} & -\mathrm{M} \\ -\mathrm{M} & \mathrm{M} \end{bmatrix}, \mathcal{A} = \begin{bmatrix} \mathrm{A}_i & 0 \\ 0 & \mathrm{A}_e \end{bmatrix}.$$

For both models, system's equations are coupled with the semidiscrete approximations of the gating and concentration systems

$$\begin{cases} \dfrac{\partial w_h}{\partial t} = R(v_h, w_h) \\ \dfrac{\partial c_h}{\partial t} = S(v_h, w_h, c_h) \end{cases}.$$

Time discretization.

Time discretization is performed by an IMEX method [3] using for the diffusion term the implicit Euler method, while the nonlinear reaction term is treated explicitly [19]. For a fully implicit approach using the first Luo-Rudy model for cellular reaction see [93]. The implicit treatment of the diffusion terms appearing in the models illustrated before is essential in order to adaptively change the time step according to the stiffness of the various phases of the heart-beat. The ODE system for the gating variables is discretized by the semi-implicit Euler method and the explicit Euler method is applied for solving the ODE system for the ion concentrations. As a consequence, the operator of the full evolution system is splitted by first solving (at time step $n+1$) for gating and ionic concentrations variables given the transmembrane potential at the n-th time-step

$$\begin{cases} \dfrac{w_h^{n+1} - w_h^n}{\delta t} = R(v_h^n, w_h^{n+1}) \\ \dfrac{c_h^{n+1} - c_h^n}{\delta t} = S(v_h^n, w_h^{n+1}, c_h^n) \end{cases}$$

and then solving for v_h^{n+1} in the Monodomain case

$$\left(\frac{1}{\delta t}\mathrm{M} + \mathrm{A}\right) v_h^{n+1} = \frac{1}{\delta t}\mathrm{M}v_h^n - \mathrm{M}I_{ion}^h(v_h^n, w_h^{n+1}, c_h^{n+1}) + \mathrm{M}I_{app}^{m,h} \tag{2.19}$$

and for $u_{i,h}^{n+1}$ and $u_{e,h}^{n+1}$ in the Bidomain case

$$\left(\frac{1}{\delta t}\mathcal{M}+\mathcal{A}\right)\begin{pmatrix}u_{i,h}^{n+1}\\ u_{e,h}^{n+1}\end{pmatrix}=\frac{1}{\delta t}\mathcal{M}\begin{pmatrix}u_{i,h}^{n}\\ u_{e,h}^{n}\end{pmatrix}-\begin{pmatrix}\mathrm{M}I_{ion}^{h}(v_h^n,w_h^{n+1},c_h^{n+1})\\ -\mathrm{M}I_{ion}^{h}(v_h^n,w_h^{n+1},c_h^{n+1})\end{pmatrix}+\begin{pmatrix}0\\ -\mathrm{M}I_{app}^{e,h}\end{pmatrix}. \tag{2.20}$$

The adaptive time-stepping strategy employed is based on controlling the transmembrane potential variation

$$\delta v=\max(v_h^{n+1}-v_h^n)$$

at each time step. In short, the adaptive strategy is the following:

- if $\delta v<\delta v_{min}$ then $\delta t_{new}=\dfrac{\delta v_{max}\delta t_{old}}{\delta v}$
- if $\delta v>\delta v_{min}$ then $\delta t_{new}=\dfrac{\delta v_{min}\delta t_{old}}{\delta v}$

where

$$\delta v_{min}=0.5\,mV,\quad \delta v_{max}=0.5\,mV,\quad \delta t_{min}=0.05\,ms,\quad \delta t_{max}=6\,ms$$

Due to the linearity of the gating equation (1.4) in the Hodgkin-Huxley formalism and in order to also guarantee a control on their variation, gating variables are integrated exactly according to (1.19) yielding a first order approximation provided that the potential variation is bounded (see also [146] and [50]). Higher order approximations of ionic and gating variables should be implemented when considering more advanced Markov Chains for the gating system [137].

A uniform spatial discretization of order h =1E-2 cm is necessary in order to produce simulations free of numerical artifacts and sufficiently accurate, since during the cardiac excitation phase a moving internal layer about $1\ mm$ thick, associated to a fast variation of the transmembrane potential distribution, sweeps the entire tissue. In order to elicit the excitation front, we apply a stimulus of $200\,\mu A/cm^3$ lasting for $1\,ms$ on a small volume of the tissue. Integrals are computed with a 3D trapezoidal quadrature rule, so the mass matrix M is lumped to diagonal form. As in the continuous Bidomain model, v_h^{n+1} is uniquely determined by the given initial and boundary conditions, while $u_{i,h}^{n+1}$ and $u_{e,h}^{n+1}$ are determined only up to the same additive time-dependent constant related to a reference potential. Since we consider bounded domains, we can determine this constant imposing

$$\mathrm{M}u_{e,h}^{n+1}=0,$$

which is the discrete counterpart of (2.4).

Our strategy for building an efficient parallel solver is based on using the parallel library PETSc from Argonne National Laboratory (http://www.mcs.anl.gov/petsc, [6]). In our FORTRAN code, the necessary vectors and matrices are built and subassembled in parallel on each processor and then the solution is advanced in time on each processor in

a synchronous manner. The linear system associated to the Monodomain model given in eq. (2.19) is very well conditioned and it can be solved efficiently with cheap preconditioners: a preconditioning choice for the Monodomain model is to use a block Jacobi preconditioner with ILU(0) solver (BJ) on each block [19]. The blocks are associated with a decomposition of the domain into subdomains and each one is assigned to one processor. Even if one-level preconditioner is not optimal, since the number of iterations of the resulting solver will depend on the number of subdomains, previous numerical results show that for the Monodomain model the number of iterations of the one-level preconditioner BJ is quite satisfactory [19]. The more severe ill-conditioning of the Bidomain matrix seems to be related to its degenerate structure rather than just to the size of doubling the unknowns. In fact, the addition to the stiffness matrices (related to elliptic operators with Neumann boundary conditions) of a zero-order term with the mass matrix stemming from the time stepping scheme, greatly improves the spectrum of the Monodomain iteration matrix but not of the Bidomain iteration matrix (see [19]). More advanced preconditioners, such as multilevel additive Schwarz preconditioners of the overlapping type (see e.g. [123], [104] and also [122]) must be employed in order to efficiently solve the coupled semidefinite Bidomain problem.

2.4 Variational formulations of the stationary problems

In this section we will provide additional results needed for the analysis of non-overlapping preconditioners introduced in the following chapters. Assume that

(H1) the cardiac region Ω is a bounded Lipschitz connected open subset of $\mathbb{R}^3$.

(H2) the tensors $D_{i,e}(\mathbf{x})$ and $D_m(\mathbf{x})$, given in eqs. (2.1) and (2.11) respectively, satisfy the following uniform ellipticity condition:

$$\exists\, \alpha_{i,e,m},\ \beta_{i,e,m} > 0 : \alpha_{i,e,m}|\xi|^2 \leq \xi^T D_{i,e,m}(\mathbf{x})\xi \leq \beta_{i,e,m}|\xi|^2$$

$\forall \xi \in \mathbb{R}^3$ and $\forall \mathbf{x} \in \mathbf{\Omega}$.

The variational formulation of the elliptic stationary Monodomain problem reads as follows: given $f_n \in L^2(\Omega)$ find $v^{n+1} \in V$ such that:

$$a_{mono}(v^{n+1}, \varphi) = f_n(\varphi), \quad \forall \varphi \in V \tag{2.21}$$

with

$$a_{mono}(v, \varphi) = \int_\Omega D_m \nabla v \cdot \nabla \varphi + \gamma \int_\Omega v\varphi, \tag{2.22}$$

$\gamma = 1/\delta t$ and

$$f_n(\varphi) = \int_\Omega (\gamma v^n - I_{ion}(v^n, w^{n+1}, c^{n+1}) + I^m_{app})\varphi, \tag{2.23}$$

where $I_{ion}(v^n, w^{n+1}, c^{n+1})$ is the ionic current and I^m_{app} the applied current per unit volume. For sake of simplicity, we drop the dependence of the tensor from $\mathbf{x}$. The ellipticity

assumption (H2) guaranties the ellipticity of the variational problem (2.21) and thus existence and uniqueness of the solution.

The variational formulation of the elliptic stationary Bidomain problem reads as follows: given $F_n = (f_{n,i}, f_{n,e}) \in L^2(\Omega) \times L^2(\Omega)$ find $u^{n+1} = (u_i^{n+1}, u_e^{n+1}) \in U$ such that:

$$a_{bido}(u^{n+1}, \varphi) = F_n(\varphi), \quad \forall \varphi = (\varphi_i, \varphi_e) \in U \tag{2.24}$$

where

$$f_{n,i}(\varphi_i) = \int_\Omega (\gamma v^n - I_{ion}(v^n, w^{n+1}, c^{n+1}))\varphi_i,$$
$$f_{n,e}(\varphi_e) = -\int_\Omega (\gamma v^n - I_{ion}(v^n, w^{n+1}, c^{n+1}) + I_{app}^e)\varphi_e,$$

v^n the tranmembrane potential at the nth time step and the Bidomain bilinear form defined on $U \times U$ given by

$$a_{bido}(u, \varphi) = \int_\Omega D_i \nabla u_i \cdot \nabla \varphi_i + \int_\Omega D_e \nabla u_e \cdot \nabla \varphi_e + \gamma \int_\Omega (u_i - u_e)(\varphi_i - \varphi_e). \tag{2.25}$$

To prove existence and uniqueness of the variational problem related to the stationary Bidomain model we must first define a norm on U and show the continuity and coercivity of $a_{bido}(\cdot, \cdot)$ with respect to it.

Lemma 2.4.1. *The bilinear form $((\cdot, \cdot)) : U \times U \to \mathbb{R}$ defined as*

$$((u, \varphi)) = \int_\Omega \nabla u_i \cdot \nabla \varphi_i + \int_\Omega \nabla u_e \cdot \nabla \varphi_e + \int_\Omega (u_i - u_e)(\varphi_i - \varphi_e).$$

is an inner product on U

Proof. Clearly $((\cdot, \cdot))$ is symmetric, bilinear and positive semidefinite; if $((u, u)) = 0$ for some $u \in U$, then necessarily $u_i = u_e$ and thus $\int_\Omega |\nabla u_e|^2 = 0$. But since $u_e \in \widetilde{V}$ and (H1) holds, then $u_e = 0$, which in turn implies $u_i = 0$ and thus $((\cdot, \cdot))$ is an inner product on U. □

Denoting with $|||\cdot|||$ the norm on U induced by the inner product $((\cdot, \cdot))$, it is now simple to show the ellipticity of the variational formulation of the stationary Bidomain model on U.

Lemma 2.4.2. *The bilinear form $a_{bido}(\cdot, \cdot)$ is elliptic in U with respect of $|||\cdot|||$.*

Proof. We can easily prove continuity using (H2), usual Cauchy-Schwarz inequalities and definition of $|||\cdot|||$ norm:

$$\begin{aligned} a_{bido}(u, \varphi) &= \int_\Omega D_i \nabla u_i \cdot \nabla \varphi_i + \int_\Omega D_e \nabla u_e \cdot \nabla \varphi_e + \gamma \int_\Omega (u_i - u_e)(\varphi_i - \varphi_e) \\ &\leq \beta_i \int_\Omega \nabla u_i \cdot \nabla \varphi_i + \beta_e \int_\Omega \nabla u_e \cdot \nabla \varphi_e + \gamma \int_\Omega (u_i - u_e)(\varphi_i - \varphi_e) \\ &\leq \max\{\beta_i, \beta_e, \gamma\}((u, \varphi)) \\ &\leq \max\{\beta_i, \beta_e, \gamma\} \, |||u||| \, |||\varphi|||. \end{aligned}$$

Similarly, we can prove the coercivity:

$$\begin{aligned} a_{bido}(u,u) &= \int_\Omega D_i \nabla u_i \cdot \nabla u_i + \int_\Omega D_e \nabla u_e \cdot \nabla u_e + \gamma \int_\Omega (u_i - u_e)(u_i - u_e) \\ &\geq \alpha_i \int_\Omega |\nabla u_i|^2 + \alpha_e \int_\Omega |\nabla u_e|^2 + \gamma \int_\Omega (u_i - u_e)^2 \\ &\geq \min\{\alpha_i, \alpha_e, \gamma\} |||u|||^2. \end{aligned}$$

□

Remark 2.4.3. It can be easily shown that the variational problem of the elliptic stationary Bidomain model given in (2.24) is equivalent to the following one (see [122] for the proof): find $u^{n+1} = (u_i^{n+1}, u_e^{n+1}) \in U$ such that

$$a_{bido}(u^{n+1}, \varphi) = F_n(\varphi) \;\; \forall \varphi \in V \times V.$$

Remark 2.4.4. Regarding assumption (H2), denoting by

$$Q(\mathbf{x}) = \left[\mathbf{a}_l(\mathbf{x}) | \mathbf{a}_t(\mathbf{x}) | \mathbf{a}_n(\mathbf{x})\right]$$

the matrix formed columnwise by the three orthonormal directions at point **x**, from tensors' definition given in (2.1) we will have

$$D_{i,e}(\mathbf{x}) = Q(\mathbf{x}) \Sigma_{i,e} Q(\mathbf{x})^T, \tag{2.26}$$

with

$$\Sigma_{i,e} = \begin{bmatrix} \sigma_l^{i,e} & 0 & 0 \\ 0 & \sigma_t^{i,e} & 0 \\ 0 & 0 & \sigma_n^{i,e} \end{bmatrix}.$$

Since $Q(\mathbf{x})$ is orthonormal at every point **x**, we will have

$$Q(\mathbf{x})^T D_{i,e}(\mathbf{x}) Q(\mathbf{x}) = \Sigma_{i,e},$$

and thus $D_{i,e}(\mathbf{x})$ and $\Sigma_{i,e}$ will have the same eigenvalues, which implies that

$$\alpha_{i,e} = \min_{\bullet = l,t,n} \{\sigma_\bullet^{i,e}\}, \quad \beta_{i,e} = \max_{\bullet = l,t,n} \{\sigma_\bullet^{i,e}\}.$$

For the Monodomain model, recalling that

$$D_m(\mathbf{x}) = D_e(\mathbf{x})(D_i(\mathbf{x}) + D_e(\mathbf{x}))^{-1} D_i(\mathbf{x}),$$

we can use formula (2.26) and the fact that $Q(\mathbf{x})$ is orthonormal at every point **x**, to obtain

$$(D_i(\mathbf{x}) + D_e(\mathbf{x}))^{-1} = \left(Q(\mathbf{x})\Sigma_i Q(\mathbf{x})^T + Q(\mathbf{x})\Sigma_{i,e} Q(\mathbf{x})^T\right)^{-1} = Q(\mathbf{x})(\Sigma_i + \Sigma_e)^{-1} Q(\mathbf{x})^T$$

where

$$(\Sigma_i + \Sigma_e)^{-1} = \begin{bmatrix} \dfrac{1}{\sigma_l^i + \sigma_l^e} & 0 & 0 \\ 0 & \dfrac{1}{\sigma_t^i + \sigma_t^e} & 0 \\ 0 & 0 & \dfrac{1}{\sigma_n^i + \sigma_n^e} \end{bmatrix}.$$

Therefore, we can rewrite the monodomain diffusion tensor as

$$\begin{aligned} D_m(\mathbf{x}) &= D_e(\mathbf{x})(D_i(\mathbf{x}) + D_e(\mathbf{x}))^{-1} D_i(\mathbf{x}) \\ &= Q(\mathbf{x})\Sigma_e Q(\mathbf{x})^T Q(\mathbf{x})(\Sigma_i + \Sigma_e)^{-1} Q(\mathbf{x})^T Q(\mathbf{x})\Sigma_i Q(\mathbf{x})^T \\ &= Q(\mathbf{x})\Sigma_e(\Sigma_i + \Sigma_e)^{-1}\Sigma_i Q(\mathbf{x})^T, \end{aligned}$$

and thus we will have

$$\alpha_m = \min_{\bullet=l,t,n} \{\frac{\sigma_\bullet^i \sigma_\bullet^e}{\sigma_\bullet^i + \sigma_\bullet^e}\}, \quad \beta_m = \max_{\bullet=l,t,n} \{\frac{\sigma_\bullet^i \sigma_\bullet^e}{\sigma_\bullet^i + \sigma_\bullet^e}\}.$$

Chapter 3

Choice of Krylov initial guess and efficient multiple heartbeat simulations

3.1 Introduction

Computational multiscale modeling of the heart (see [132] and [102] for recent reviews) has becoming widely accepted as a tool for future drug design [131] and patient-specific therapies [114]. Thus it is very important to develop efficient solvers at tissue level (see [147] for a review on this subject) and sufficiently detailed models at the cellular level (see Chapter 1 and reference therein). In this chapter, we will analyze two separate approaches in order to reduce the whole computational costs associated with three-dimensional multi-beating simulations using HHRd as cellular model. In the final section of the chapter we will show some numerical results on the influences of transmural cellular heterogeneity on three-dimensional patterns of activation and repolarization wavefronts.

At each time step the main computational costs are associated with updating pointwise the cellular variables and the reaction term, and then solving a sparse linear system

$$\mathrm{M}_{iter}\mathbf{y}^{n+1} = \mathbf{b}^{n+1}, \tag{3.1}$$

where the superscript n indicated the current time step. Since the iteration matrix M_{iter} is symmetric and positive definite for the Monodomain discretization and positive semidefinite for the Bidomain discretization (see Chapter 2), we use the preconditioned conjugate method (PCG) as iterative method to solve (3.1) for which holds the well known formula for the error reduction (see e.g. [113])

$$||\mathbf{y}^{n+1} - \mathbf{y}_m||_{\mathrm{M}_{iter}} \leq 2||\mathbf{y}^{n+1} - \mathbf{y}_0^{n+1}||_{\mathrm{M}_{iter}} \left(\frac{\sqrt{\kappa_2 - 1}}{\sqrt{\kappa_2 + 1}}\right)^m,$$

where $\mathbf{y}_0^{n+1}$ is the PCG initial guess, $\mathbf{y}_m$ the m-th iterate produced by the method and κ_2 is the condition number of the preconditioned system. The choice of the initial guess can thus produce a gain in the iterative solution process, tough it will not be as substantial as using an optimal preconditioner which speed up the iterative solution process. However, the latter can be designed independently from the choice of the initial guess (see chapter 5). In Sections 3.2 to 3.4 we will consider different approaches to the choice of the PCG initial guess using previous computed solution vectors, providing numerical results either for the Monodomain or the Bidomain model. We note that, instead of using the previous solutions, another interesting approach consists in reusing the Krylov vectors generated by the PCG either for the choice of the initial guess, or to augment the preconditioner via a projection (see e.g. [119]).

Another aspect to deal with in multibeating simulations are the initial ionic concentration variables prescribed at the beginning of the simulations. As seen in Chapter 1, cellular models that incorporate ionic concentrations variables requires the simulation of a greater number of beats in reaching a suitable dynamical steady state to study APD and trasnmural dispersion or repolarization (TDR). Drug developing thus requires simulations of several beats, either with the Bidomain or the Monodmain model, in order to accurately analyze the drug effects' at tissue level. In section 3.5 we will consider two different choices of cellular initial conditions simulating for 50 beats the Monodomain model and compare them either from the point of view of the cellular variables, or analyzing the three-dimensional patterns of activation and repolarization wavefronts sweeping the tissue, described in details in the last section.

For the test cases considered in sections 3.2 to 3.4, the slab dimension for the Monodomain model is $1 \times 1 \times 0.5\ cm^3$, discretized with a grid $100 \times 100 \times 50$ and solved with 18 processors, distributed $3 \times 3 \times 2$ across the spatial grid using the Linux cluster Ulisse located at University of Milan. In Bidomain test cases, the slab dimension is $1.92 \times 1.92 \times 0.48\ cm^3$, discretized with a grid $192 \times 192 \times 48$ and solved with 36 processors, distributed $6 \times 4 \times 1$ across the spatial grid using the Linux cluster Topsy located at IMATI-CNR in Pavia. We use HHRd (see Chapter 1) has cellular model. An absolute preconditioned residual norm lesser than 1E-4 has been chosen as stopping criterion for the PCG. For all configurations, transmural cellular heterogeneity is considered as in the 3-slab configuration already introduced in [21]: briefly, the cardiac slab is transmurally subdivided into three equal layers of the same thickness, endocardial, mid-myocardial and epicardial, and the corresponding type of cell (see Chapter 1) is assigned to each layer. Four test cases will be considered:

- TC1: Monodomain model solved with constant time step $\delta_t = 0.05$ ms for 500 ms
- TC2: Monodomain model solved with adaptive time stepping strategy for 2000 ms
- TC3: Bidomain model solved with constant time step $\delta_t = 0.05$ ms for 50 ms
- TC4: Bidomain model solved with adaptive time stepping strategy for 500 ms

3.2 Lagrangian interpolants of previous solutions

In most applications involving the discretization of time dependent PDEs, the initial guess for the linear solver is chosen as the solution at the previous time step. A very simple and computational inexpensive approach to improve this choice is to use lagrangian interpolants in time of previous solutions, i.e. setting

$$\mathbf{y}_0^{n+1} = \sum_{k=0}^{d} \mathbf{y}^{n-d+k} l_k(t^{n+1}), \tag{3.2}$$

where $0 \leq k \leq d$ and

$$l_k(t) = \prod_{j=0, j\neq k}^{d} \frac{t - t^{n-d+j}}{t^{n-d+k} - t^{n-d+j}}$$

are the usual lagrangian polynomials on the time grid $t^{n-d} < t^{n-d+1} < \cdots < t^n$. Note that the choice of the previous computed solution as PCG initial guess can be thought as a zero order polynomial approximation setting $d = 0$ in the above formulas. Figure 3.1 shows the number of iterations and the initial residual

$$||\mathbf{M}_{iter}\mathbf{y}_0^{n+1} - \mathbf{b}^{n+1}||_2;$$

for different choices of interpolation degrees with the Monodomain model solved with constant step size $\delta t = 0.05\, ms$ for 10000 time steps using a Block Jacobi (BJ) preconditioner (TC1). Results are collected in Table 3.1.

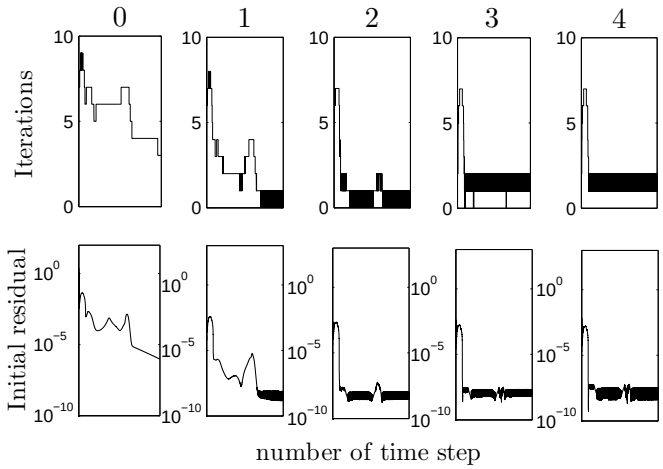

Figure 3.1: PCG iterations (upper panels) and initial residual norm in logarithmic scale (lower panels) at each time step for different degrees of lagrangian interpolation (showed on top) for Monodomain model with constant step size $\delta t = 0.05 ms$. PCG was preconditioned with BJ.

At each time step and for each choice of degree, lagrangian interpolations show to be very effective tools in lowering the initial residual of the Monodomain linear system; moreover, since neglecting the approximation errors introduced by the stopping criterion

Lagrangian initial guesses for TC1

degree	0	1	2	3	4	d_{AD}
Iterations per time step						
phase 0	7.6	6.3	5.5	5.4	5.4	5.4
phase 1-2	6.1	2.5	0.8	1.1	1.1	0.8
phase 3	6.4	2.6	1.0	1.1	1.1	0.8
rest	4.1	0.9	0.8	1.1	1.1	0.5
Admissible Solutions						
phase 0	0	0	0	3	3	3
phase 1-2	0	0	589	9	0	598
phase 3	0	0	334	6	3	339
rest	0	1496	1063	10	6	2100

Table 3.1: PCG-BJ iteration counts for different choices of lagrangian interpolations, from degree 0 to 4; 10000 steps with $\delta t = 0.05\,ms$ with Monodomain model.

of the PCG holds that

$$\mathbf{M}_{iter}\mathbf{y}^k = \mathbf{b}^k,\ \forall k \leq n$$

the initial residual with lagrangian interpolation of degree d can be equivalently expressed as

$$||\sum_{k=0}^{d} \mathbf{b}^{n-d+k} l_k(t^{n+1}) - \mathbf{b}^{n+1}||_2. \tag{3.3}$$

and thus we can directly estimate the initial residual without using matrix vector multiplications and adaptively select the interpolation degree d_{AD} which minimizes (3.3) at each time step. Moreover, equation (3.3) implies that the capabilities of lagrangian interpolants in lowering the initial residual are limited by the dependence of the interpolation error from the smoothness of the rhs. Indeed, it must be noted that some interpolants were able to produce admissible solutions for the linear solver (i.e. initial guesses that automatically fulfill the stopping criterion of the PCG) in the plateau and resting phases of the AP where the reaction term is smoother; on the other hand, the capability in lowering the initial residual saturates with the interpolation degree during the activation phase (see Table 3.1). Quadratic interpolation showed the best performance in terms of total number of iterations (data not shown), reducing them considerably by a factor of 4, and yielding the greatest number of admissible solutions for the solver. Linear interpolation gave the worse results during the first three phases of APs (i.e. when cells are active) and doesn't produce admissible solutions during the plateau phase, but it performed better in the resting phase

regarding to admissible solutions. Results for third and fourth degree interpolation were better in the activation phases but after this phase their approximation properties degraded. For quadratic interpolation, a 20% reduction in the total solving time has been observed: this difference was totally due to a 55% reduction in entire solving time for the linear system, since this interpolation produce a 76% reduction of the whole number of iterations, that is a speed up factor 4. Finally, degree adaptivity was able to select the best initial guess at each time step reducing further the number of iterations and improving the total number of admissible solutions.

The second test case for lagrangian interpolants has been performed using the adaptive time stepping strategy (see Chapter 2) on a time interval of 2000 msec with the Monodomain model (TC2); lagrangian interpolants lowered the initial residual with variable time step size mainly when the cardiac cells in the spatial domain were active rather than in the resting phase of the AP, see Figure 3.2 and Table 3.2. Quadratic interpolation showed the best performance with a speed up factor 2 in terms of total solving time for the linear system, due to a 57% reduction of total number of iterations of the PCG. A 66% reduction in total number of iterations has been achieved using the adaptive selection of the interpolation degree. In all the cases, no admissible solutions were produced.

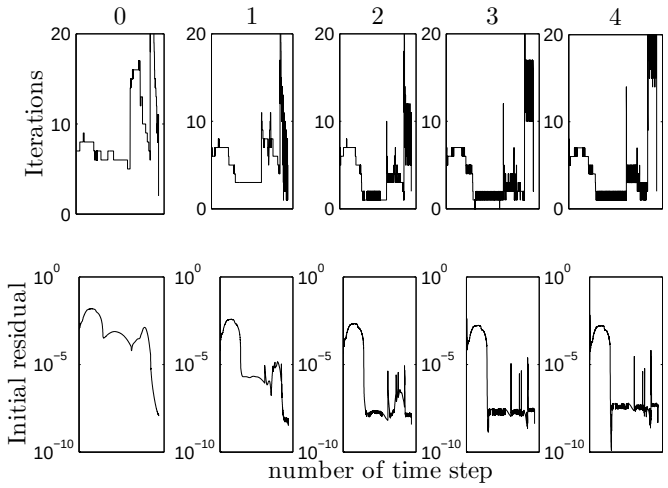

Figure 3.2: PCG iterations (upper panels) and initial residual norm in logarithmic scale (lower panels) at each time step for different degrees of lagrangian interpolation (showed on top) for Monodomain model with adaptive time stepping strategy. PCG was preconditioned with BJ

Until now, we studied lagrangian interpolants for a well conditioned system like the Monodomain model precondioned with BJ. The Bidomain model is an ill-conditioned system due to the singularity of the linear system's matrix, and when preconditioned with BJ it requires a huge number of iterations per time step to achieve convergence. In order to test if an ill-conditioned system can benefit by using lagrangian interpolants, we perform some Bidomain runs with a constant time step size $\delta t = 0.05\, ms$ for 1000 iterations in the activation phase, i.e. the most expensive part of the simulation (TC3). The number of iterations and initial residual norms at each time step are shown in Figure 3.3, the results on

Lagrangian initial guesses for TC2

degree	0	1	2	3	4	d_{AD}
Total number of iterations						
	27913	16001	11927	12235	14425	9926
Total solving time (s) for linear solver						
	1623	1384	875	1031	1230	775

Table 3.2: PCG-BJ iteration counts for different choices of lagrangian interpolations, from degree 0 to 4; 2 seconds of heartbeat for Monodomain model with adaptive time stepping strategy

iteration counts in Table 3.3. Differently from the Monodomain model, linear interpolation in time showed the best results with a speed up factor 2 and other the choices of interpolation degree yielded oscillating results in terms of number of iterations per time step. Using an adaptive interpolation degree doesn't improve further the results in terms of total number of iterations and solving time and, as expected, the convergence remained slow.

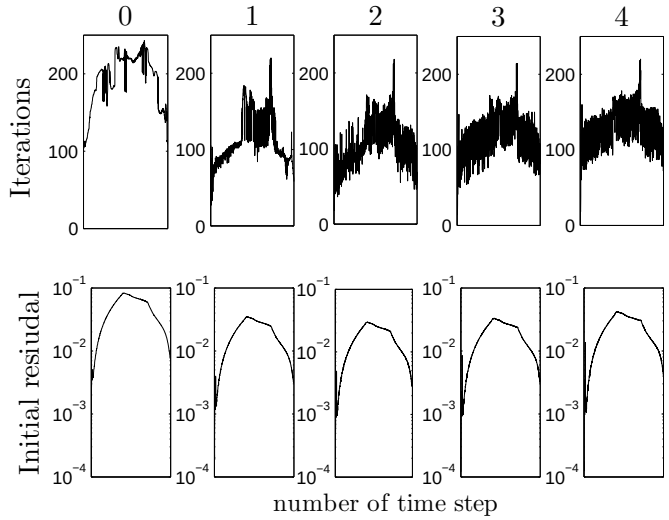

Figure 3.3: PCG iterations (upper panels) and initial residual norms in logarithmic scale (lower panels) at each step for different degrees of lagrangian interpolation (showed on top) with Bidomain model. PCG was preconditioned with BJ

When the Bidomain linear system is preconditioned with a multilevel Schwarz preconditioner, the number of iteration per time step is considerably reduced from hundreds to tens or lower. We then test lagrangian interpolants with the preconditioner MHS(5) published

Lagrangian initial guesses TC3

degree	0	1	2	3	4	d_{AD}
Total number of iterations						
	193278	111234	106357	119555	134685	96195
Total solving time (s) for linear solver						
	54394	28361	35458	39245	44351	27075

Table 3.3: PCG iteration counts for different choices of lagrangian interpolations, from degree 0 to 4; 1000 steps with $\delta t = 0.05\, ms$ with Bidomain model preconditioned with BJ

in [123] in order to analyze the reduction factor with time adaptivity simulating 500 ms (TC4). For additional details on the preconditioner see also [122]. Third order lagrangian interpolants yielded the best results together with the adaptive choice of the interpolation degree, with a speed up factor of more than 2; second and fourth order lagrangian gave almost same results. See Figure 3.4 and Table 3.4.

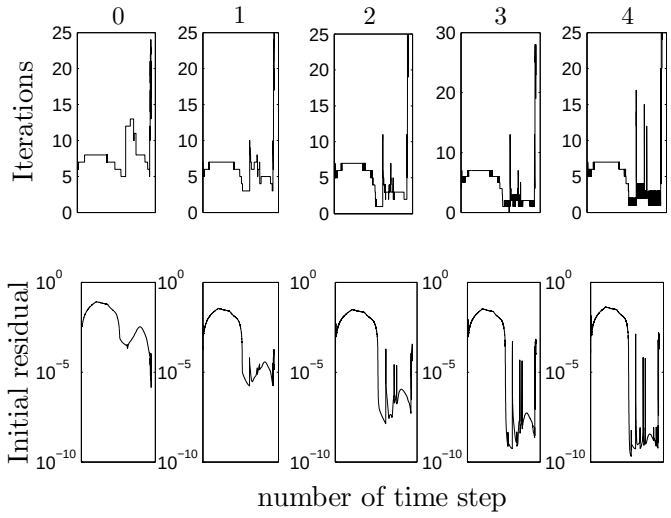

Figure 3.4: PCG iterations (upper panels) and initial residual norms in logarithmic scale (lower panels) at each time step for different degrees of lagrangian interpolation (showed on top) for Bidomain model with adaptive time stepping strategy. PCG was preconditioned with MHS(5)

Despite their simplicity, Lagrangian interpolants in time are effective and computational inexpensive tools for the choice of the initial guess; also, they are very simple to implement. Moreover, the degree adaptation can yield even more gain at a lower additional cost. High order lagrangian interpolants works better with well- rather than ill-conditioned

Lagrangian initial guesses TC4

degree	0	1	2	3	4	d_{AD}
Total number of iterations						
	21002	14212	10227	9579	10263	9173
Total solving time (s) for linear solver						
	48550	38651	27227	27017	27386	26954

Table 3.4: PCG iteration counts for different choices of lagrangian interpolations, from degree 0 to 4; 500 ms of heartbeat for Bidomain model preconditioned with MHS(5) and adaptive time stepping strategy.

linear systems; moreover, the action of suitable preconditioner make them effective also with the Bidomain system. With the adaptive time stepping strategy they run the risk of generating poor initial guesses since they doesn't take into account any information about the underlying system's matrix. In the next section we will thus consider a different approach to the choice of the PCG initial guess.

3.3 Fischer's projection algorithms

Instead of interpolating in time the previous solutions, another possible approach to speed up iterative solution processes is using information generated from previous right-hand sides. In this section we apply two algorithms, first proposed in [37], for extracting information from the previous linear systems to generate initial guesses to the current one. The first approach is equivalent to simply remove any component of the current right hand side $\mathbf{b}^{n+1}$ for which the solution is already known, i.e. by projecting $\mathbf{b}^{n+1}$ onto a set of orthonormal vectors which spans $\{\mathbf{b}^n, \ldots, \mathbf{b}^{n-k}\}$ (having associated solutions $\{\mathbf{y}^n, \ldots, \mathbf{y}^{n-k}\}$), and then solving the linear system with a zero initial guess and the orthogonal component of $\mathbf{b}^{n+1}$ to the finite dimensional set spanned by $\{\mathbf{b}^n, \ldots, \mathbf{b}^{n-k}\}$ as right hand side. Here $1 \leq k \leq K$, and K represents the maximum number of vector to be stored by the algorithm. The second approach is a refinement of the first and exploits the features of the conjugate gradient method that seeks approximations which successively minimize the error in the M_{iter}-norm: the second method looks in fact for the best approximation to $\mathbf{y}^{n+1}$ in the set spanned by $\{\mathbf{y}^n, \ldots, \mathbf{y}^{n-k}\}$ with respect to the M_{iter}-norm when the linear system matrix is symmetric and positive definite, i.e.

$$\mathbf{y}_0^{n+1} = \underset{\mathbf{y} \in \mathrm{span}\{\mathbf{y}^n, \ldots, \mathbf{y}^{n-k}\}}{\operatorname{argmin}} ||\mathbf{y}^{n+1} - \mathbf{y}||_{\mathrm{M}_{iter}}. \tag{3.4}$$

These procedures, summarized below, are in principle superior to those derived from extrapolation techniques based on high-order interpolants in time since such projection techniques yield the best possible approximation within a given basis set. We will test this two approaches only with the Monodomain model, since they implicitly assume the positive definitess of the iteration matrix (see basis updating procedures below) and thus they cannot be directly applied to the Bidomain model; we will overcome this issue using a different technique in the following section.

The choice of the initial guess by the two algorithms described in [37] can be summarized as:

Method 1 : Supposing that we have collected two orthogonal sets $U_k = \{\tilde{\mathbf{y}}_1, \ldots, \tilde{\mathbf{y}}_k\}$ and $B_k = \{\tilde{\mathbf{b}}_1, \ldots, \tilde{\mathbf{b}}_k\}$ and that B_k is orthonormal with respect to an appropriately weighted inner product $< \cdot, \cdot >$, the guess generator at time step $n+1$ is given by:

- evaluate $\beta_i =< \mathbf{b}^{n+1}, \tilde{\mathbf{b}}_i >$, $i = 1, \ldots, k$
- generate the next initial guess as $\mathbf{y}_0^{n+1} = \sum_{i=1}^{k} \beta_i \tilde{\mathbf{y}}_i$
- update the sets B_k and U_k

Method 2 : Supposing that we have collected an orthonormal (with respect to M_{iter}-norm) set $X_k = \{\tilde{\mathbf{y}}_1, \ldots, \tilde{\mathbf{y}}_k\}$, the guess generator at time step $n+1$ is given by:

- evaluate $\beta_i =< \mathbf{b}^{n+1}, \tilde{\mathbf{y}}_i >$, $i = 1, \ldots, k$ (minimization procedure)
- generate the next initial guess as $\mathbf{y}_0^{n+1} = \sum_{i=1}^{k} \beta_i \tilde{\mathbf{y}}_i$
- update the set U_k

The minimization procedure of the residual in the second method is based on the following straightforward calculation: since

$$||\mathbf{y}^{n+1} - \mathbf{y}_0^{n+1}||_{\mathrm{M}_{iter}} = (\mathbf{y}^{n+1})^T \mathbf{M}_{iter} \mathbf{y}^{n+1} - 2 \sum_{i=1}^{k} \beta_i \tilde{\mathbf{y}}_i^T \mathbf{M}_{iter} \mathbf{y}^{n+1} + \sum_{i,j=1}^{k} \beta_i \beta_j \tilde{\mathbf{y}}_i^T \mathbf{M}_{iter} \tilde{\mathbf{y}}_j$$

exploiting the orthonormality of the basis (with respect to the M_{iter}-norm) and requiring a vanishing first variation of the last expression leads to

$$\beta_i =< \mathbf{b}^{n+1}, \tilde{\mathbf{y}}_i > \quad i = 1, \ldots, k.$$

To complete the description of the methods, we summarize algorithmically the basis updating:

Method 1 :

if $k = K$ then
$\tilde{\mathbf{b}}_1 = \mathbf{M}_{iter} \mathbf{y}^{n+1} / ||\mathbf{M}_{iter} \mathbf{y}^{n+1}||$
$\tilde{\mathbf{y}}_1 = \mathbf{y}^{n+1} / ||\mathbf{M}_{iter} \mathbf{y}^{n+1}||$
$k = 1$

else

$\tilde{\mathbf{y}} = \mathbf{y}^{n+1} - \sum_{i=1}^{k} \beta_i \tilde{\mathbf{y}}_i$

$\hat{\mathbf{b}} = \mathbf{M}_{iter}\tilde{\mathbf{y}}$

$\gamma_i =< \hat{\mathbf{b}}, \tilde{\mathbf{b}}_i >,\ i = 1, \ldots, k$

$\tilde{\mathbf{b}}_{k+1} = \left(\hat{\mathbf{b}} - \sum_{i=1}^{k} \gamma_i \tilde{\mathbf{b}_i}\right) / ||\hat{\mathbf{b}} - \sum_{i=1}^{k} \gamma_i \tilde{\mathbf{b}_i}||$

$\tilde{\mathbf{y}}_{k+1} = \left(\tilde{\mathbf{y}} - \sum_{i=1}^{k} \gamma_i \tilde{\mathbf{y}_i}\right) / ||\hat{\mathbf{b}} - \sum_{i=1}^{k} \gamma_i \tilde{\mathbf{b}_i}||$

$k = k + 1$

endif

Method 2 :

if $k = K$ then

$\tilde{\mathbf{y}_1} = \mathbf{y}^{n+1} / ||\mathbf{y}^{n+1}||_{\mathbf{M}_{iter}}$

$k = 1$

else

$\tilde{\mathbf{y}} = \mathbf{y}^{n+1} - \sum_{i=1}^{k} \beta_i \tilde{\mathbf{y}}_i$

$\gamma_i =< \tilde{\mathbf{y}}, \tilde{\mathbf{y}}_i >_{\mathbf{M}_{iter}},\ i = 1, \ldots, k$

$\tilde{\mathbf{y}}_{k+1} = \left(\tilde{\mathbf{y}} - \sum_{i=1}^{k} \gamma_i \tilde{\mathbf{y}_i}\right) / ||\hat{\mathbf{b}} - \sum_{i=1}^{k} \gamma_i \tilde{\mathbf{b}_i}||_{\mathbf{M}_{iter}}$

$k = k + 1$

endif

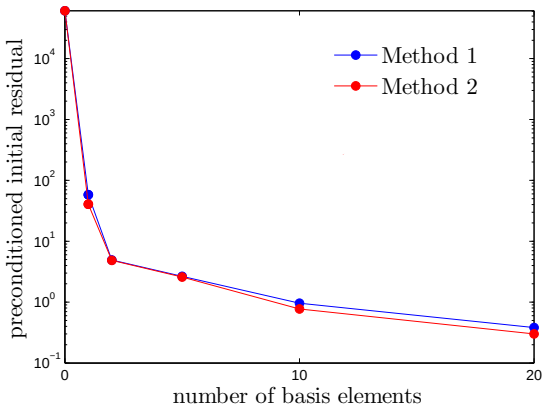

Figure 3.5: Preconditioned initial residual for the two Fischer's methods as a function of stored vector K at the 20-th time step of TC1.

For our numerical experiments we use the implementation of the Fischer's methods provided by the PETSc library. Figure 3.5 shows the preconditioned initial residual as a function of K for both methods applied to TC1 at the 20-th time step with different values K of stored vectors; we choose the 20th time step in order to have a comparison of the methods with the greatest allowed dimension of projection basis for each K (i.e

Fischer's method 2 for TC1

K	0	5	10	20
Iterations per time step				
phase 0	7.6	6.2	5.7	5.4
phase 1-2	6.1	1.5	0.6	0.3
phase 3	6.4	1.5	0.7	0.3
rest	4.1	0.5	0.3	0.3
Admissible Solutions				
phase 0	0	0	2	9
phase 1-2	0	1091	1816	2259
phase 3	0	640	1138	1443
rest	0	2866	3210	3566

Table 3.5: PCG-BJ average number of iterations per time step and number of admissible solutions in different AP phases for different choices of stored vectors K with Fischer's method 2 in TC1 case.

$k = K$ at the 20th time step) since the basis updating procedure suffers from an implicit restart. Numerical results show a saturation in the approximation properties with growing K for both methods thus the performances of projection-based methods suffer from the same saturation problem experienced during the activation phase also by the lagrangian interpolants. Moreover, no significant differences between the two Fischer methods were observed in terms of iterations reduction.

Tables 3.5 and 3.6 collect the results for the second Fischer methods in the TC1 and TC2 case respectively for different choices of K, in order to give a comparison between projection-based methods and lagrangian interpolants (see Table 3.1 and 3.2 respectively). With such projection techniques, a further improvement in reducing the total number of iterations of the TC1 and TC2 simulations is achieved as expected since projection methods produce the best initial guess with respect to a given basis set; on the other hand, such improvement is less pronounced for the total solving time due to expensive Gram-Schmidt orthogonalization procedures inherent in the algorithms.

3.4 Proper Orthogonal Decomposition (POD)

The Proper Orthogonal Decomposition (POD) technique is able to extract, from a given set of snapshots $\{\mathbf{y}_i \,|\, 1 \leq i \leq N\}$ of discrete solutions on a given time grid $t^1 < \cdots < t^N$, a coherent structure which has the largest mean square projection on the observations [128]. Although it is possible to use POD to derive the approximate solution of some classes of

Fischer's method 2 for TC2

K	0	5	10	20
Total number of iterations				
	27913	13833	10365	8341
Total solving time (s) for linear solver				
	1623	1447	778	750

Table 3.6: PCG-BJ iteration counts for different choices of stored vectors K for Fischer's method 2 in TC2.

parabolic problems (see e.g. [71], [40]), due to IMEX approach to the strong nonlinearity of the cardiac models, we are only concerned here in analyzing the performances of a POD based technique in finding suitable PCG initial guesses for the full order linear system (3.1).

Supposing that the solution of the problem of interest is $\mathbf{y} \in X$ where X is a suitable Hilbert space, with the POD approach we seek for its projection $\tilde{\mathbf{y}} \in X_{n_p}$, where X_{n_p} is a finite dimensional subspace of X of dimension n_p. POD aims to construct a suitable basis $\{\boldsymbol{\psi}_k\}_{k=1}^{n_p}$ of X_{n_p} in order to split the solution field as

$$P\mathbf{y} = \sum_{k=1}^{n_p} \alpha_k \boldsymbol{\psi}_k(x), \tag{3.5}$$

where P is the projection operator from X on X_{n_p}. Given a suitable inner product $(\cdot,\cdot)_X$ in X, the key idea of the POD method consists in finding such subspace X_{n_p}, in a way that the basis $\{\boldsymbol{\psi}_k\}_{k=1}^{n_p}$ is orthonormal in X (with respect to the norm induced by the inner product) and captures the highest energy configuration provided by the snapshots. Then, the projection of each snapshot on X_{n_p} can be expressed as

$$P\mathbf{y}_i = \sum_{k=1}^{n_p} (\mathbf{y}_i(x), \boldsymbol{\psi}_k)_X \boldsymbol{\psi}_k. \tag{3.6}$$

From the knowledge of the basis elements, α_k coefficients in (3.5) can be obtained as

$$\alpha_k = (\mathbf{y}_i, \boldsymbol{\psi}_k(x))_X .$$

The idea of POD is based on an optimality argument: given a set of snapshots, it

chooses the first basis element maximizing α_k coefficients in equation (3.5) according to

$$\max_{\boldsymbol{\psi}\in X}\sum_{i=1}^{N}(\mathbf{y}_i,\boldsymbol{\psi})_X^2, \tag{3.7}$$

where the optimization problem is subjected to the constraint $||\boldsymbol{\psi}||_X = 1$ with $||\cdot||_X$ the norm on X induced by the inner product $(\cdot,\cdot)_X$. The second basis element is obtained posing the same maximization problem in the space orthogonal to the first eigenfunction, and by finite induction we can obtain the POD basis of rank $n_p < N$ as the solution of the optimization problem

$$\max_{\boldsymbol{\psi}_1,\ldots,\boldsymbol{\psi}_{n_p}}\sum_{i=1}^{n_p}\sum_{j=1}^{N}(\mathbf{y}_j,\boldsymbol{\psi}_i)_X^2, \tag{3.8}$$

with the constraint $(\boldsymbol{\psi}_i,\boldsymbol{\psi}_j)_X = \delta_{ij}$. Moreover, it can be shown that the latter maximization problem is equivalent to a minimization one

$$\min_{\{\boldsymbol{\psi}_k\}_{k=1}^{n_p}}\sum_{i=1}^{N}||\mathbf{y}_i - \sum_{k=1}^{n_p}(\mathbf{y}_i(x),\boldsymbol{\psi}_k)_X\boldsymbol{\psi}_k||_X^2, \tag{3.9}$$

where again the minimum is constrained to the condition of orthonormality of the basis, i.e.

$$(\boldsymbol{\psi}_i,\boldsymbol{\psi}_j)_X = \delta_{ij}$$

$\forall\ 1 \leq i \leq n_p$, $1 \leq j \leq i$. We note that the POD space describes a typical member of the snapshots' ensemble better than any other finite dimensional subspace of X of dimension n_p, providing the most efficient way of capturing the dominant components of an infinite-dimensional process with only finitely many, and often surprisingly few, modes in the Hilbert space X. This basis is known by different names in the literature: Karhunen-Loeve expansion ([60], [84]), principal components [56], empirical orthogonal eigenvectors [85], factor-analysis [45] and total least squares [43]. Usual choices of the space X in literature are $\mathbb{R}^{N_{\text{dof}}}$ where N_{dof} is the number of degrees of freedom for the FE system, $L^2(\Omega)$ and $H^1(\Omega)$; for sake of simplicity, we will sketch the derivation of the POD basis in the vector space $\mathbb{R}^{N_{\text{dof}}}$; for additional functional details and a more complete treatment of POD see [59], [40] or the monograph [49].

Let us now consider for simplicity the optimization problem (3.8) with $n_p = 1$ and his associated lagrange function

$$\mathcal{L}(\boldsymbol{\psi},\lambda) = \sum_{j=1}^{N}(\mathbf{y}_j,\boldsymbol{\psi})_{\mathbb{R}^{N_{\text{dof}}}}^2 + \lambda(1 - ||\boldsymbol{\psi}||_{\mathbb{R}^{N_{\text{dof}}}}^2).$$

A first order necessary optimality condition can be obtained deriving the latter function

with respect to an arbitrary component ψ_i ($i = 1, \dots, N_{\text{dof}}$) of the vector $\boldsymbol{\psi}$

$$\begin{aligned}
\frac{\partial \mathcal{L}(\boldsymbol{\psi}, \lambda)}{\partial \psi_i} &= \frac{\partial}{\partial \psi_i} \left(\sum_{j=1}^{N} |\sum_{k=1}^{N_{\text{dof}}} Y_{kj}\psi_k|^2 + \lambda(1 - \sum_{k=1}^{N_{\text{dof}}} \psi_k^2) \right) \\
&= 2 \sum_{j=1}^{N} \left(\sum_{k=1}^{N_{\text{dof}}} Y_{kj}\psi_k \right) Y_{ij} - 2\lambda\psi_i \\
&= 2 \left(\sum_{j=1}^{N} \sum_{k=1}^{N_{\text{dof}}} Y_{ij}Y_{kj}\psi_k - \lambda\psi_i \right) \\
&= 2 \left(\sum_{k=1}^{N_{\text{dof}}} (YY^T)_{ik}\psi_k - \lambda\psi_i \right) \\
&= 2((YY^T\boldsymbol{\psi})_i - \lambda(\boldsymbol{\psi})_i),
\end{aligned}$$

where we denoted by Y the matrix formed columnwise by the snapshots, i.e.

$$Y = [\mathbf{y}_1 | \dots | \mathbf{y}_N].$$

Requiring a zero first order variation for each vector component, we obtain the eigenvalue problem

$$YY^T\boldsymbol{\psi} = \lambda\boldsymbol{\psi}, \tag{3.10}$$

where the matrix YY^T is symmetric and positive semi-definite, and therefore all the eigenvalues are real and nonnegative. The first POD basis elements $\boldsymbol{\psi}_1$ is thus the eigenvector which maximizes λ; by finite induction one can prove that the ith POD basis element is the eigenvector of YY^T associated to the ith largest eigenvalue. See [59] for additional details.

Computing the POD basis elements solving the eigenvalue problem (3.10) can be very expensive since the matrix YY^T has dimension $\mathbb{R}_{N_{\text{dof}}} \times \mathbb{R}_{N_{\text{dof}}}$; in order to overcome this issue, the *snapshots method* [128] has been introduced in literature. With this method we can reduce drastically the dimension of the eigenvalue problem for computing the POD basis elements using a Singular Value Decomposition (SVD) argument. First recall the singular value decomposition of a rectangular matrix:

Lemma 3.4.1. *For a matrix $Y \in \mathbb{R}^{m\times k}$ with $k < m$ and rank $r \leq k$ there exist r positive singular values $d_1 \geq d_2 \geq \cdots \geq d_r > 0$ together with orthogonal matrices $U = [\boldsymbol{u}_1 | \dots | \boldsymbol{u}_m] \in \mathbb{R}^{m\times m}$ and $V = [\boldsymbol{v}_1 | \dots | \boldsymbol{v}_k] \in \mathbb{R}^{k\times k}$, which satisfy*

$$Y = UDV^T.$$

The matrix D has nonzero entries only on the diagonal, that is $D_{ii} = d_i$ for $1 \leq i \leq r$. Moreover,

$$\begin{aligned}
Y\boldsymbol{v}_i &= d_i\boldsymbol{u}_i, \\
Y^T\boldsymbol{u}_i &= d_i\boldsymbol{v}_i.
\end{aligned}$$

Corollary 3.4.2. *From SVD Lemma follows directly than the left singular vectors $\mathbf{u}_i$ and the right singular vectors $\mathbf{v}_i$ are eigenvectors of YY^T and Y^TY respectively and their associated eigenvalues satisfies $\lambda_i = d_i^2$.*

Using the SVD we can thus infer that the eigenvalues of the matrix YY^T and Y^TY are the same; moreover the POD basis elements (eigenvectors of YY^T) can be calculated from the eigenvectors of the so called *correlation matrix* Y^TY that are easier to compute since the latter matrix has dimension $N \times N$. The kth POD spatial mode is then reconstructed according to the formula

$$\boldsymbol{\psi}_k = \frac{1}{\sqrt{\lambda_k}} \sum_{j=1}^{N} v_k^j \mathbf{y}_j, \tag{3.11}$$

where v_k^j is the jth element of the kth eigenvector of the correlation matrix $\mathbf{v}_k$, or in matrix form as

$$\Psi = YVD^{-1/2},$$

where

$$D = \text{diag}\,(\lambda_1, \ldots, \lambda_N)$$

is the diagonal matrix of eigenvalues of Y^TY and

$$\Psi = [\boldsymbol{\psi}_1 | \ldots | \boldsymbol{\psi}_N]$$

is the matrix formed columnwise by the finite element approximation of the N spatial modes.

Remark 3.4.3. In order to compute the POD basis elements using a general inner product $(\cdot,\cdot)_X$ the correlation matrix entries will simply be

$$(\mathbf{y}_i, \mathbf{y}_j)_X\,. \tag{3.12}$$

Moreover, the computational costs of building the correlation matrix can be limited noting that at each time step we only need to shift the already computed values and update the last column of the correlation matrix. We choose to assemble and compute eigenvalues and eigenvectors of the correlation matrix on each processor using standard LAPACK subroutines [72] for symmetric eigenvalue problems; then each processor can compute its local part of the POD basis elements using (3.11) without additional communications. For the Bidomain model, we choose to decouple the intra- and the extra-cellular component of the snapshots and construct a correlation matrix separately for each scalar component.

The POD approximation properties with general inner products are guarantied by the following Lemma (for the proof see [128]):

Lemma 3.4.4. *Let $\lambda_1 \geq \cdots \geq \lambda_N \geq 0$ denote the eigenvalues of the correlation matrix given by the N snapshots according to (3.12). We then have the following error formula $\forall n_p \leq N$:*

$$\sum_{i=1}^{N} ||\boldsymbol{y}_i - \sum_{k=1}^{n_p} (\boldsymbol{y}_i, \boldsymbol{\psi}_k)\boldsymbol{\psi}_k||_X^2 = \sum_{k=n_p+1}^{N} \lambda_k.$$

Differently from Fischer's methods illustrated in the previous section, with the POD projection technique we don't necessarily need the iteration matrix to compute the projection basis; moreover we can in principle obtain additional informations on the basis elements using their energies. The eigenvalue of the correlation matrix in fact decay to zero and the faster the decay, the lowest the number of POD basis elements required to accurately approximate the previous solutions. An example of the exponential decay of the eigenvalues at a given time step during the activation phase is plotted in Figure 3.6 for the Monodomain model (black curves) and the Bidomain model (red curves u_e, blue curves u_i) using $N = 10$ snapshots and different discrete inner products (inner product in $L^2(\Omega)$ continuous lines, inner product in $\mathbb{R}^{N_{\text{dof}}}$ dashed lines). Since we are dealing with structured grids with a lumped mass matrix, the choice of the inner product yielded approximatively the same relative decay.

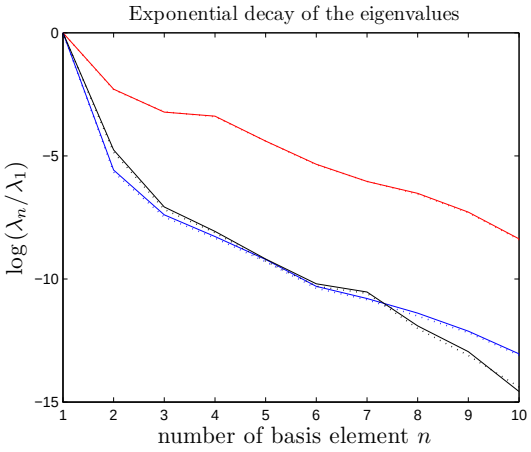

Figure 3.6: Exponential decay of the eigenvalues at a fixed time step during the activation phase. Red curves extracellular potential and blue curves intracellular potential for the Bidomain model; black curves tranmembrane potential for the Monodomain model. Continuos lines $X = L^2(\Omega)$, dashed lines $X = \mathbb{R}^{N_{\text{dof}}}$

Remark 3.4.5. For the application of POD to concrete problems the choice of the number of basis elements is certainly of central importance, as is also the number of snapshots taken. No general a-priori rules are currently available. Rather, the choice of n_p is based on heuristic considerations combined with observing the ratio between the modeled and the total information contained in the snapshot ensemble. A usual procedure in the literature consists in choosing the first n_p eigenvalues that retain a prescribed fraction of the total energy of the system, that is, using Lemma 3.4.4, n_p is the maximum integer lesser than N

for which it holds

$$\frac{\sum_{i=1}^{n_p} \lambda_i}{\sum_{i=1}^{N} \lambda_i} \leq 1 - \varepsilon, \tag{3.13}$$

where ε is a prescribed tolerance, referred to in the sequel as POD *cut-off tolerance*.

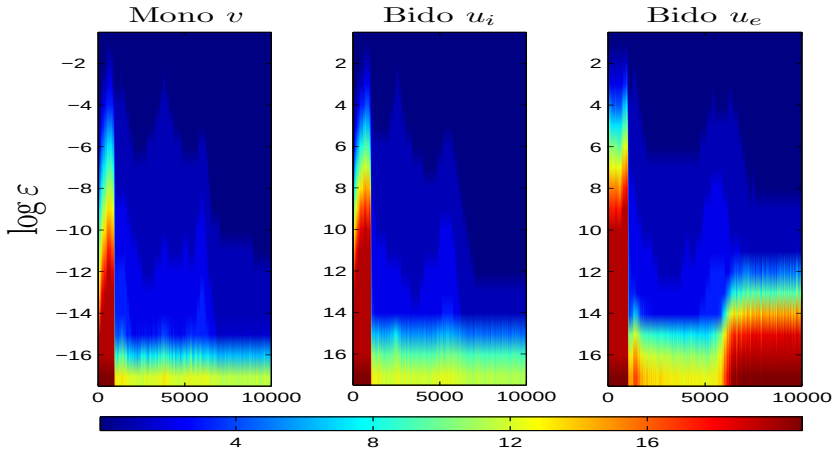

Figure 3.7: Number of POD basis elements (see colorbar) with 20 snapshots for transmembrane potential with Monodomain model, and for intra- and extracellular potentials with the Bidomain model

Figure 3.7 shows the dependence of the number of POD basis elements from the POD cut-off tolerance ε for the cardiac Monodomain (left panel) and Bidomain model (central panel u_i, right panel u_e) both solved with a constant time step $\delta t = 0.05$ ms for 10000 time steps, and considering as snapshots' set the previous 20 computed solutions. As a first observation, the POD technique seems to be able to sense the temporal variation of the AP but also that its approximation properties deteriorates with the presence of localized sharp activation fronts inside the spatial domain: a slower decay of the approximation error is present during the activation phase, which means that a greater number of basis elements is not sufficient to accurately approximate the past dynamics. In the other AP phases, very few POD elements are needed to closely approximate the previous solutions.

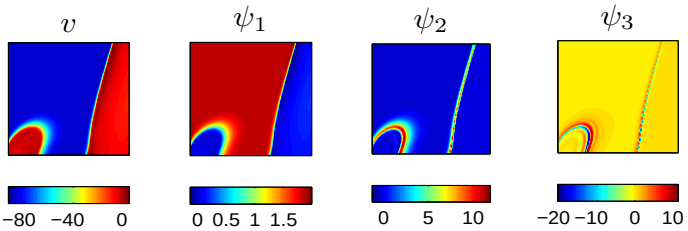

Figure 3.8: Transmembrane potential v and first three most energetic POD basis elements for the Monodomain model during the activation phase

Figures 3.8, 3.9 and 3.10 show layers cut of the three most energetic POD basis elements at different AP phases for the Monodomain model excited in the lower left corner

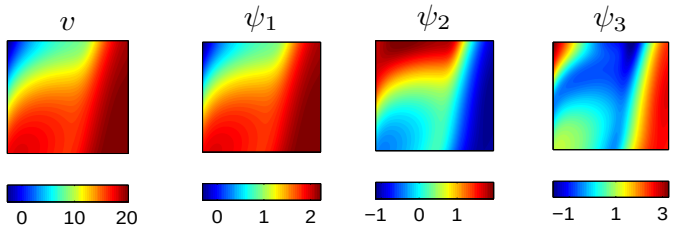

Figure 3.9: Transmembrane potential v and first three most energetic POD basis elements for the Monodomain model during the plateau phase

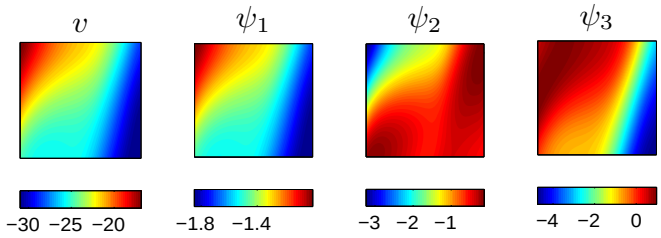

Figure 3.10: Transmembrane potential v and first three most energetic POD basis elements for the Monodomain model during the repolarization phase

and in the right vertical face at different time instances; transmembrane potential distribution is also provided to give a comparison. The activation fronts are evident in Figure 3.8 for the transmembrane potential; POD elements are locally sharp near the fronts, whereas they are almost equal to 0 far away from the fronts. In the other AP phases, the transmembrane potential and the POD elements are smoother.

POD-Galerkin initial guess.

The POD technique can be very efficient used in combination with Galerkin projection schemes in order to obtain lower dimensional systems that, when solved, could produce suitable initial guesses for the PCG [89]; we will refer to this approach as POD-Galerkin scheme. In the general context of Galerkin methods (see e.g [113]), after introducing an approximation space where we seek for the solution, we force the true residual (i.e. the difference between the computed approximated solution and the exact one) to be zero onto the approximation space. Therefore, with a POD-Galerkin scheme, a lower dimensional

system can be derived using as approximation space

$$X_{n_p} = \{\boldsymbol{\varphi} \in X \mid \boldsymbol{\varphi} = \sum_{i=1}^{n_p} \alpha_i \boldsymbol{\psi}_i\}, \tag{3.14}$$

thus using the POD basis elements like test functions in a usual FEM method.

For the Monodomain system's matrix (2.19), the POD-Galerkin scheme at time step $n+1$ can be compactly written in matrix form as:

$$\Psi^T \mathrm{M}_{iter} \Psi \boldsymbol{\alpha}^{n+1} = \Psi^T \mathbf{b}^{n+1}, \tag{3.15}$$

where Ψ is the matrix formed columnwise by the spatial modes computed at the current time step, M_{iter} is the iteration matrix (2.19), $\mathbf{b}^{n+1}$ the right hand side of the full order linear system (3.1) and $\boldsymbol{\alpha}^{n+1}$ the unknowns of the current lower dimensional system.

Analogously, the POD-Galerkin scheme for the Bidomain system's matrix (2.20) can be derived using as approximation space the cartesian product of the two POD spaces for the intra- and extra-cellular components, that is $X^i_{n_p} \times X^e_{n_p}$; therefore the matrix of POD basis elements is

$$\Psi = \begin{bmatrix} \Psi^i & 0 \\ 0 & \Psi^e \end{bmatrix},$$

where

$$\Psi^{i,e} = [\boldsymbol{\psi}^{i,e}_1 | \dots | \boldsymbol{\psi}^{i,e}_{n_p^{i,e}}]$$

are the POD basis element matrices for the intra- and extra-cellular component. Thus the lower dimensional linear system matrix, obtained by projecting the Bidomain iteration matrix (2.20) onto Ψ, is

$$\frac{1}{\delta t} \begin{bmatrix} {\Psi^i}^T \mathrm{M} \Psi^i & {\Psi^i}^T \mathrm{M} \Psi^e \\ {\Psi^e}^T \mathrm{M} \Psi^e & {\Psi^e}^T \mathrm{M} \Psi^e \end{bmatrix} + \begin{bmatrix} {\Psi^i}^T \mathrm{A}_i \Psi_i & 0 \\ 0 & {\Psi^e}^T \mathrm{A}_e \Psi_e \end{bmatrix}, \tag{3.16}$$

where M and $\mathrm{A}_{i,e}$ are respectively the original mass and stiffness matrices. Analogous arguments can be used to construct the right hand side of the lower dimensional system starting from the right hand side of the full-order linear system.

The lower dimensional POD-Galerkin matrices will be symmetric and positive definite either for the Monodomain or the Bidomain model; as for the correlation matrices, we choose to assemble the lower dimensional systems on each processor and then solve them using standard LAPACK subroutines for Cholesky decomposition. Then, each processor compute the local part of the PCG initial guess as

$$\mathbf{y}_0^{n+1} = \Psi \boldsymbol{\alpha}^{n+1}.$$

Remark 3.4.6. The computational limitations of the POD technique mostly resides in the assembling of the lower dimensional matrix, which in principle require at least $n_p(n_p+1)/2$ matrix vector multiplications for symmetric linear systems like the Monodomain

model; in case of unsymmetric systems, the number of matrix vector multiplication becomes n_p^2. This issue can be overcame using suitable inner products in building the correlation matrices. For the Monodomain model, since the iteration matrix is symmetric and positive definite, we can choose it as the discrete inner product. With this choice, the computational costs of assembling the lower dimensional system can be considerably reduced since the lower dimensional system's matrix will become the identity matrix exploiting the orthonormality of the POD basis with respect to the inner product chosen. Moreover, for the recursive nature of the correlation matrix, only one matrix vector multiplication, namely $\mathrm{M}_{iter}\mathbf{y}_n$, must be performed in order to compute the new column

$$(\mathbf{y}_1\mathrm{M}_{iter}\mathbf{y}_n, \ldots, \mathbf{y}_n\mathrm{M}_{iter}\mathbf{y}_n)^T$$

of the correlation matrix at the current time step. In practice, the latter matrix vector multiplication can be avoided noting that its result is equal to the previous right hand side of the full-order system. Note that with this choice of inner product, the POD-Galerkin scheme will strictly resemble the second Fischer method illustrated in Section 3.3. For the Bidomain model, we see that if we use the discrete L^2 inner product (i.e. the lumped mass matrix M) for the calculation of the correlation matrix, the lower dimensional projected matrix can be written as

$$\frac{1}{\delta t}\begin{bmatrix} \mathrm{I} & -\widetilde{\mathrm{M}} \\ -\widetilde{\mathrm{M}}^T & \mathrm{I} \end{bmatrix} + \begin{bmatrix} \tilde{\mathrm{A}}_i & 0 \\ 0 & \tilde{\mathrm{A}}_e \end{bmatrix},$$

where the diagonal blocks of the first matrix are identity matrices of appropriate sizes, the off-diagonal block

$$\widetilde{\mathrm{M}} = {\Psi_i}^T \mathrm{M} \Psi_e$$

is the cross mass matrix between the two POD spaces and

$$\widetilde{\mathrm{A}}_{i,e} = \Psi_{i,e}^T \mathrm{A}_{i,e} \Psi_{i,e}$$

are the projected stiffness matrices. With this inner product additional matrix vector multiplications must be performed to project the stiffness matrices and thus we will not have any computational gain. A suitable choice is to choose as inner products the matrices

$$\frac{1}{\delta t}\mathrm{M} + \mathrm{A}_{i,e}$$

for the intra- and extra-cellular components: in this way, the diagonal blocks of the lower dimensional matrix will become the identity and we need to perform only $n_p^i n_p^e$ additional discrete L^2 dot products to assemble the off diagonal blocks.

Remark 3.4.7. Fischer's methods and POD-Galerkin technique strictly resembles each other, but the latter can also be applied to semidefinite (as in our case) but also indefi-

nite linear systems since the derivation of the lower dimensional system is naturally related to the full dimensional one. Moreover, the former methods possess additional limitations since they suffer from an implicit restart which make the choice of the dimension of the projection subspace untractable without a necessary rebuilding of the basis. Also, with Fischer's algorithms the cost of implementing the Gram-Schmidt orthogonalizations must be taken into account, whereas the computational costs of assemble the lower order system can be drastically reduced with POD-Galerkin method.

Remark 3.4.8. As shown in [71], the choice of inner product does not affect the POD approximation properties, which can be improved by including in the snapshots ensemble the so called *difference quotients*: with the notation introduced at the beginning of the section, the snapshots' ensemble introduced in [71] becomes:

$$\tilde{\mathbf{y}}_i^B = \begin{cases} \mathbf{y}_i & \text{if } 1 \leq i \leq N \\ \dfrac{\mathbf{y}_{i-N+1} - \mathbf{y}_{i-N}}{t^{i+1} - t^i} & \text{if } N+1 \leq i \leq 2N-1 \end{cases}.$$

Note that the difference quotients are usual backward finite difference (and so the B superscript) and that no additional inner products must be performed to assemble the correlation matrix due to the linearity of the inner products involved. With the same idea, we can consider in the snapshots ensemble the centered finite differences

$$\tilde{\mathbf{y}}_i^C = \begin{cases} \mathbf{y}_i & \text{if } 1 \leq i \leq N \\ \dfrac{\mathbf{y}_{i-N+1} - \mathbf{y}_{i-N-1}}{t^{i-N+1} - t^{i-N-1}} & \text{if } N+1 \leq i \leq 2N-1 \end{cases}.$$

In this case, the zero index snapshot must be stored and N additional inner products must be performed. In order to limit the computational costs involved in forming the correlation matrix, we can use the modified snapshots' ensemble with central differences for all time instances but t^1 and t^N:

$$\tilde{\mathbf{y}}_i^{CM} = \begin{cases} \mathbf{y}_i & \text{if } 1 \leq i \leq N \\ \dfrac{\mathbf{y}_{i-N+2} - \mathbf{y}_{i-N}}{t^{i-N+2} - t^{i-N}} & \text{if } N+1 \leq i \leq 2N-2 \end{cases}.$$

In all cases, no additional matrix vector multiplications are needed to assemble the lower dimensional linear system.

Numerical results.

We test the POD-Galerkin schemes for different choices of the snapshots' number N and POD cut-off tolerance ε. The results are summarized in Table 3.4 for TC1, in Table 3.8 for TC2 and in Table 3.4 for TC4 using all spatial modes with positive eigenvalues. We also test the POD-Galerkin method with the Bidomain model BJ preconditioned in TC3

POD-Galerkin method for TC1

N	0	10	20	30
Iterations per time step				
phase 0	7.6	5.3	5.3	5.4
phase 1-2	6.1	0.5	0.7	0.7
phase 3	6.4	0.7	0.9	0.8
rest	4.1	0.5	0.9	1.0
Admissible Solutions				
phase 0	0	0	0	0
phase 1-2	0	1534	879	1021
phase 3	0	550	333	437
rest	0	1866	383	74

Table 3.7: POD initial guess: average iteration count per time step and admissible solutions in different AP phases for TC1. See text for details.

(data not shown): no substantial gain was achieved with respect to the lagrangian choice (see Table 3.3). The very simple derivation of the low-order model and the capability of the POD technique in produce admissible solutions even with few snapshots taken make it the ideal candidate as a tool for the choice of the next initial guess for the cardiac models. Numerical results show that increasing the number of stored snapshots doesn't necessarily produce high dimensional POD spaces suitable in predicting the future, either when sharp fronts are locally moving inside the spatial domain during tissue activation or in the other AP phases. In the activation phase iterations are similar for different values of the number of snapshots and POD cut-off tolerance (see Table 3.9): this can be due to the minimization procedure inherent in the construction of the POD basis which is defined on the whole spatial domain and thus suffering from the strong localization of the fronts. Moreover, a POD space derived from a lower number of snapshots better catch the dynamics, as it can be seen in Table 3.4 taking into account the admissible solutions or in Table 3.8. The best choice with POD-Galerkin method is thus a relatively little number of snapshots and to retain all the spatial modes with positive eigenvalues.

Results including the difference quotients in the snapshots' ensemble for TC1 are shown in table 3.4 for $N = 5$ and $N = 10$ retaining all spatial modes; the inclusion of the difference quotients greatly improve the performances of the POD-Galerkin scheme for the Monodomain model in all AP phases but the activation. Central finite differences show to be the best choice, with a little loss of performance in the modified CM case. Moreover, the inclusion of the difference quotients in the snapshots' ensemble improve

POD-Galerkin method for TC2

N	0	5	10
Total number of iterations			
	27913	8303	7200
Total solving time (s)			
	1623	544	496

Table 3.8: POD initial guess: total number of iterations and total solving time for different numbers of stored snapshots for TC2.

POD-Galerkin method in phase 0 and POD cut-off tolerance

ε	1E-12	1E-13	1E-14	1E-15	1E-16
Iterations per time step					
$N = 10$	5.5	5.5	5.5	5.4	5.4
$N = 20$	5.5	5.4	5.3	5.3	5.3
$N = 30$	5.5	5.4	5.4	5.3	5.3

Table 3.9: Average number of iterations per time step in the activation phase for TC1. Number of snapshots by rows and POD cut-off tolerance ε by columns.

POD-Galerkin method for TC4

N	5	10	15	20
Total number of iterations				
	9852	8338	7933	7914
Admissible solutions				
	65	172	250	257

Table 3.10: Total number of iterations and admissible solutions for the Bidomain model preconditioned with MHS(5) in TC4 for different values of N.

the performances only with lower values of N, confirming the fact that the dimension of the snapshots set can (and must) be small. In Chapter 5 we will provide additional results applying the POD-Galerkin technique to the Schur complement matrix of the Bidomain system.

3.5 Choice of cellular initial conditions

In this section we will concentrate on the cellular initial conditions prescribed at the beginning of the simulations simulating 50 beats with the Monodomain model and adaptive time stepping strategy at different stimulation frequencies. At each time step, the initial guess for the linear solver is chosen using the adaptive lagrangian method descripted in section 3.2 since these results were obtained before studying the POD method. As test case for this section, the dimension of the slab is $1.92 \times 1.92 \times 0.64\ cm^3$ and the grid dimension is $192 \times 192 \times 64$: simulations has been performed with 18 processors, distributed $3 \times 3 \times 2$ across the spatial grid with the Linux cluster Ulisse at University of Milan (www.ulisse.mat.unimi.it). With this solving configuration, each beat requires approximatively 40 minutes to be simulated.

Transmural cellular heterogeneity is considered as in the 3-slab configuration already introduced in [21]: the cardiac slab is subdivided transmurally into three equal layers of the same thickness: endocardial, mid-myocardial and epicardial, composed by the corresponding type of cell provided by the HHRd model developed in Chapter 1. In order to describe the macroscopic features of the excitation and subsequent repolarization process, we extract from the spatiotemporal transmembrane potential the sequence of the propagating excitation and repolarization wave fronts. Since cellular AP waveform is increasingly monotone in the upstroke phase and decreasingly monotone in the repolarization phase (see e.g. Fig-

POD-Galerkin method for TC1 and difference quotients

	nodiff	B	C	CM
Iterations per time step $N = 5$				
phase 0	5.9	5.9	5.4	5.6
phase 1-2	1.0	0.7	0.4	0.5
phase 3	1.2	0.9	0.5	0.6
rest	0.8	0.5	0.4	0.4
Admissible Solutions $N = 5$				
phase 0	0	0	1	2
phase 1-2	838	1026	1699	1381
phase 3	581	657	901	804
rest	2294	2470	2268	2568
Iterations per time step $N = 10$				
phase 0	5.3	5.3	5.3	5.3
phase 1-2	0.5	0.4	0.3	0.4
phase 3	0.7	0.7	0.6	0.6
rest	0.5	0.5	0.7	0.7
Admissible Solutions $N = 10$				
phase 0	0	1	3	1
phase 1-2	1534	1683	1946	1922
phase 3	550	658	767	907
rest	1866	1872	1418	1553

Table 3.11: POD initial guess and difference quotients: average iteration count per time step and admissible solutions in different AP phases for TC1. See text for details.

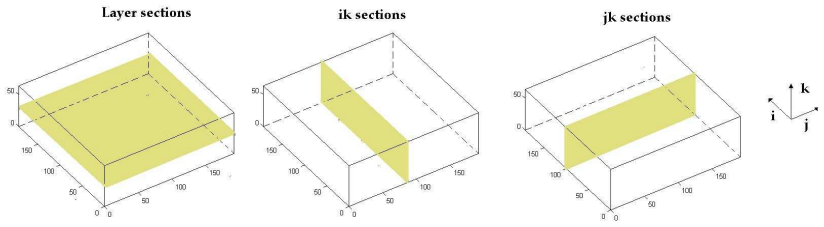

Figure 3.11: Slab sections considered in showing results; numbers in following figures identify the spatial grid

ure 1.2), activation and repolarization times are uniquely determined for fixed threshold values of the transmembrane potential, chosen as $-60\ mV$ for activation (with upward crossing) and $-75\ mV$ for repolarization (with downward crossing). From the knowledge of ACTI and REPO patterns, APD distributions can be obtained as REPO $-$ ACTI. In the following, the level surfaces of activation and repolarization times will be denoted by ACTI and REPO respectively and will be shown as slab sections (see Figure 3.11).

In order to elicit the excitation front, we apply a stimulus of $200\ \mu A/cm^3$ for $1\ ms$ on a small volume (containing 5 mesh points in each x- and y-direction and 3 mesh points in the z-direction) at the center of the endocardial face. The total amount of rotation considered is 120 degrees, starting from 75 degrees at the endocardial face. BCLs considered are 500 ms (in the range of normal canine rates) and 2000 ms (to reproduce bradycardia). We take into account two configurations for the initial conditions (IC) of the cellular system:

IC0D IC from the dynamical steady state of the 0D model

IC1D IC evaluated simulating 500 beats of an heterogeneous monodomain fiber

The transmural fiber has been implemented in MATLAB with a centered finite difference scheme for the spatial discretization and the same IMEX approach (see Chapter 2) for the temporal discretization, using HHRd as cellular model. The grid dimension of the fiber has been chosen equal to the dimension of the z-axis of the three dimensional grid: initial conditions for the cellular model in the slab are then assigned depending on the height (z-value) of the cell in the slab.

Regularities of ACTI and REPO waves through successive waves are summarized in Figure 3.12 for BCL 500 and in Figure 3.13 for BCL 2000: for each beat we collected ACTI and REPO three dimensional patterns and a relative differences between successive waves has been measured by means of the following simple formulas:

$$\frac{||\text{ACTI}_{n+1} - \text{ACTI}_n||_2}{||\text{ACTI}_n||_2}$$
$$\frac{||\text{REPO}_{n+1} - \text{REPO}_n||_2}{||\text{REPO}_n||_2}$$

where $||\cdot||_2$ is the usual euclidean norm.

ACTI patterns result similar among successive beats, whereas REPO patterns depends on different choices of initial conditions and on different stimulation frequencies. At BCL

500 ms, REPO wave alternates starting from endocardial or epicardial sites during the first beats (not shown), until a stable configuration is reached; no substantial differences exist between IC0D and IC1D choices (see Figure 3.12). At BCL 2000 ms, REPO waves are much more stable through multiple beats and IC1D choice perform better than IC0D in terms of relative differences, indicating lesser variation between waves through successive beats, and thus a more stable APD configuration. It must be noted that the two choices of cellular initial conditions yields qualitatively the same three dimensional patterns of activation and repolarizations, either at BCL 500 ms or at BCL 2000 ms, but with different APD mean values as it can be seen in Figure 3.14, where the mean APD on each layer of the slab (for each choice of initial condition) is compared with the dynamical steady state obtained from the 0D model and with its final distribution on the transmural fiber. It was also noted (data not shown) that the total number of iterations per beat decrease in successive beats, for each choice of initial conditions; moreover, IC1D lowers the total number of iterations per beat with respect to IC0D. This can be due to the fact that IC1D introduce a smoother initial distribution of the transmembrane potential that lowers the iterations per time step mainly during the activation phase.

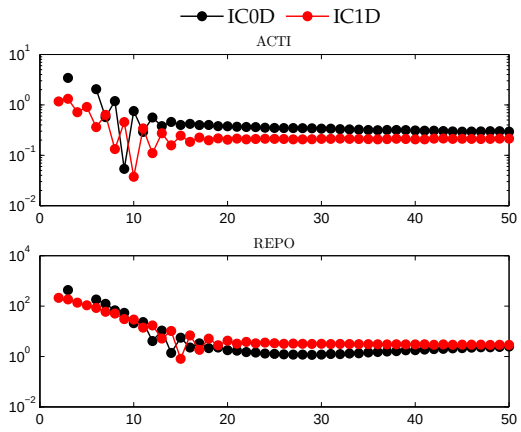

Figure 3.12: Three dimensional relative differences in logarithmic scale of ACTI and REPO patterns for different choice of initial conditions at BCL 500. Red dots curve IC1D, black dots curve IC0D

Next, we analyze the three-dimensional relative differences collected for HHRd cellular variables and the results are shown in Figure 3.15 for BCL 500 and in Figure 3.16 for BCL 2000. Cellular variables that moves slower to their dynamical steady state are, as expected, ionic concentration variables (sodium, potassium and chloride, respectively `nai`, `ki` and `cli` in figures) and subcellular calcium concentrations (denoted by `jsrT` and `nsr` in the figures); for the gating variables (see [54] and [81] for their definitions) the choice of cellular initial conditions doesn't influence the results. Note that the highly oscillatory behaviour of the `irel` variable is a numerical artifact since at the beginning of each beat, its value is almost equal to 0 for each cell of the slab. Relative differences of cellular variables suggest thus that IC1D is closer than IC0D to the three dimensional dynamical steady state, even if it is far from being reachable in three dimensional simulations also with the

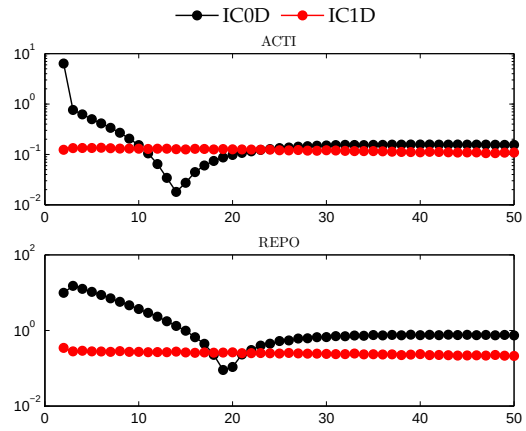

Figure 3.13: Three dimensional relative differences in logarithmic scale of ACTI and REPO patterns for different choice of initial conditions at BCL 2000. Red dots curve IC1D, black dots curve IC0D

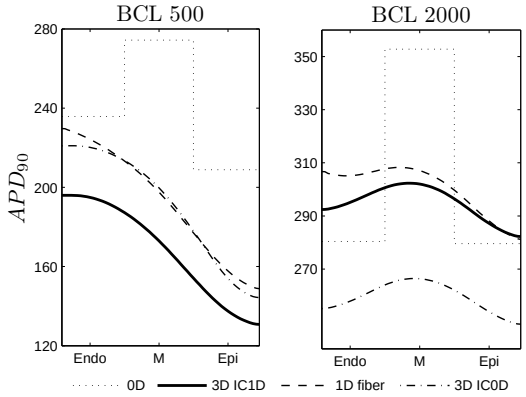

Figure 3.14: APD_{90} distributions at the frequencies considered: cellular model HHRd (dotted lines), one dimensional monodomain fiber (dashed lines), mean on layers of the three-dimensional slab (continuous lines)

Monodomain model. Numerical results suggest also that a lower number of beats simulated with the transmural fiber would give better results in the IC1D case.

3.6 Influence of transmural heterogeneity in three dimensions

In this section we qualitatively describe activation and repolarization patterns at the 50th beats simulated using IC1D as prescribed ionic initial conditions, either at BCL 500 ms or at BCL 2000 ms. Representative three-dimensional ACTI patterns (similar between different BCL considered and initial conditions prescribed) are shown in figures 3.17, 3.18 and 3.19. Their features has been studied extensively with the Monodomain and Bidomain models (see e.g. [20]) and with the approximation of its levels set known as eikonal equations ([16], [17]); here only the main features will be pointed out. Intramural exci-

tation, starting from an endocardial stimulation site, first proceeds toward the epicardium but subsequently, due to fiber rotation, comes back pointing toward the endocardial plane. Due to these intramural return pathways, propagation undergoes an acceleration, in particular in endocardial areas where the excitation moves mainly across fibers. Stimulation at the center of the endocardial face produces approximately elliptical excitation isochrone lines, a clear sign of their anisotropic propagation: the major axes of the oblong excitation isochrones are nearly parallel to the endocardial fiber direction ($5/12\pi$). Also, the excitation isochrones show an inflection corresponding to a dimple-like inflection of the wave front (see also [20] where the slab dimension is greater and these features are more pronounced). These findings, i.e. the accelerating propagation across fibers, the bulging and the dimple-like inflection of the isochrones, are attributed to the influence on the endocardium of the activation processes through the deeper layers (see figure 3.18 where the cut planes are nearly perpendicular to the endocardial fiber direction). Proceeding from endo- to epi-cardium on the intramural planes parallel to the endocardium, the spacing between excitation isochrones increases, the wave front shapes become rounder and we observe a transmural twisting of the isochrones, i.e. the major axis of the oblong isochrones progressively rotates clockwise with increasing depth. However, their rotation lags behind the rotation of the fiber direction at corresponding depths (the fiber direction at the epicardium is $-\pi/4$). On the epicardial plane, the excitation front-boundary collision first occur at the center of the face (BKT, *breakthrough* point) since the model considered does not incorporate the epi- endocardial obliqueness of the fibers ([134]) (see e.g. [17] were this feature was included in the simulations). Subsequent excitation isochrones have a well rounded, elliptical shape centered at the point of epicardial face and the large spacing between successive isochrones indicates a fast excitation.

Following the analysis on relative differences, only REPO and APD patterns for the last beat simulated with IC1D will be shown. Repolarization waves on layers cut are similar for BCL 500 and BCL 2000 ms, and both are faster then the activation ones. At endocardium, REPO waves are faster along than across fibers, yielding almost elliptical shape of the isochrones; through the depth of the slab the front shape rotates clockwise (lesser than the excitation front) from endo- to epicardium maintaining the ellipticity in the central part of the layers. When the repolarization wave approach the boundaries of the slab, the front velocity decreases yielding almost linear isochrones. APD distributions on layers are therefore similar between the two stimulation frequencies considered; with respect to previous simulations, the dispersion od repolarization per layers is higher with HHRd rather than LR1 (see [21]). The only qualitative difference per layers between the two frequencies considered using HHRd ad cellular model has been observed on the endocardial surface in the proximity of the point where we applied the stimulus: at BCL 2000, the repolarization wave start from the stimulus site and proceeds mainly along the fiber direction, whereas at BCL 500 REPO wave starts almost contemporary from two different sites symmetric with respect to the fiber direction as observed experimentally in [101] (see figure 3.20, left panel BCL 500, right panel BCL 2000).

The main differences between REPO waves at the frequencies considered can be enlighted analyzing the vertical sections: at BCL 500 ms, the wave start at the BKT point on the epicardial face and then proceeds almost as a planar wave through the depth of the slab, ending in the slab's angles opposed to the fiber direction and lasting for 80 ms. At BCL 2000 ms, REPO wave starts almost contemporary from the stimulus site at the endocardium and from the the activation BKT at the epicardium; since the front velocity on the boundaries is lower, these two fronts first proceeds faster through the center of the slab and then they come back pointing through the slab's angles opposed at the fiber direction ending in a subendocardial zone after about 40 ms, roughly an half of the duration of the repolarization wave at BCL 500. As a consequence, the APD distribution differs significantly through the depth of the slab, even if it resembles the $0D$ distribution (see figure 1.18); at BCL 500 ms, APD is greater at endocardium rather than at epicardium, with a maximum attained at the stimulus site. At BCL 2000 ms, even if the local maximum is attained at the stimulus site, an island of M-cell can be clearly distinguished in the center of the slab, further supporting the concept of cellular heterogeneity for left ventricular tissue.

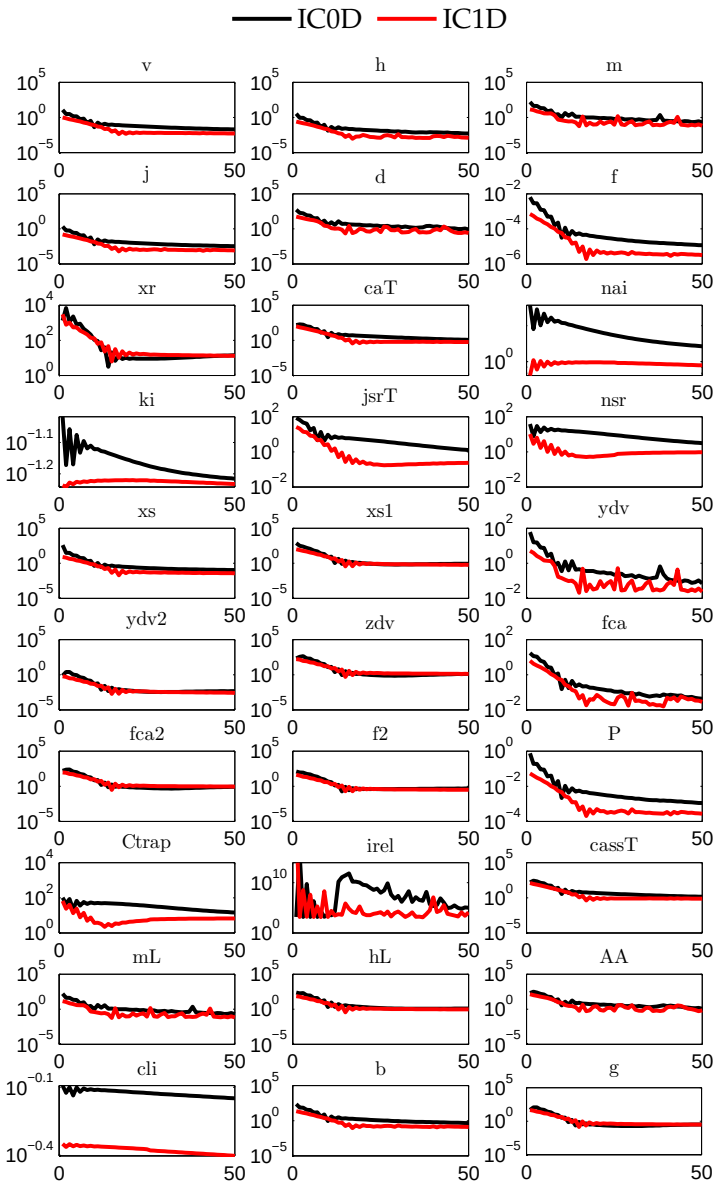

Figure 3.15: Three dimensional relative differences in logarithmic scale for cellular variables for different choice of initial conditions at BCL 500. Red dots curve IC1D, black dots curve IC0D

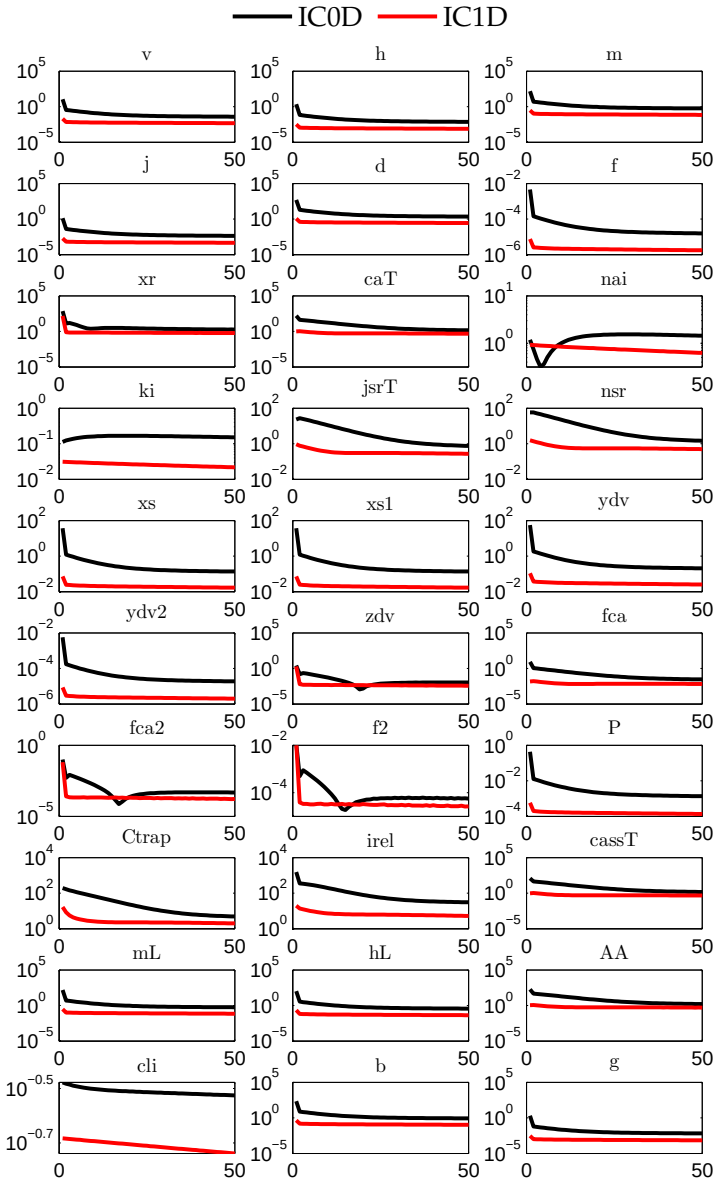

Figure 3.16: Three dimensional relative differences in logarithmic scale for cellular variables for different choice of initial conditions at BCL 2000. Red dots curve IC1D, black dots curve IC0D

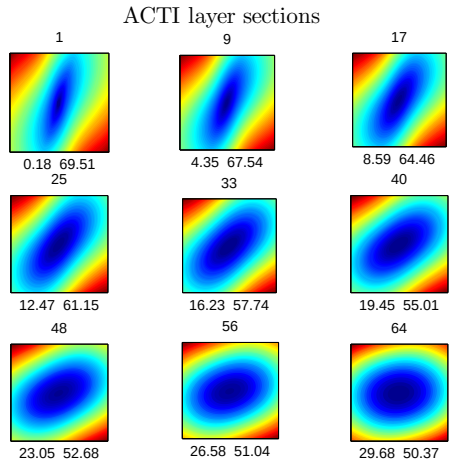

Figure 3.17: Monodomain activation sequence per layers (see figure 3.11) with central endocardial stimulus. For each panel we show the number of layer on top; below minimum and maximum attained.

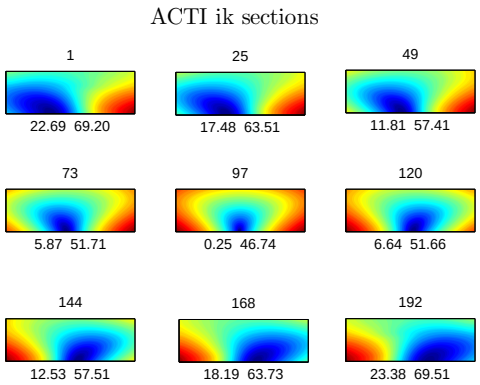

Figure 3.18: Monodomain activation sequence on ik sections (see figure 3.11) with central endocardial stimulus. For each panel we show the number of section on top; below minimum and maximum attained.

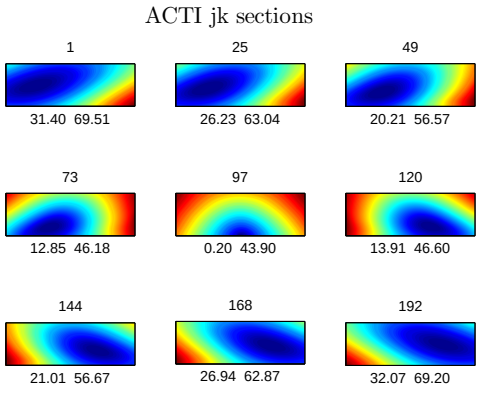

Figure 3.19: Monodomain activation sequence on jk sections (see figure 3.11) with central endocardial stimulus. For each panel we show the number of section on top; below minimum and maximum attained.

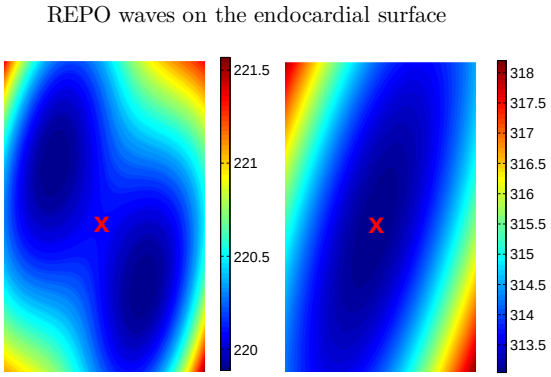

Figure 3.20: Zoom of the repolarization waves at the endocardial face. Left panel: BCL 500. Right panel: BCL 2000. The cross is the stimulus site.

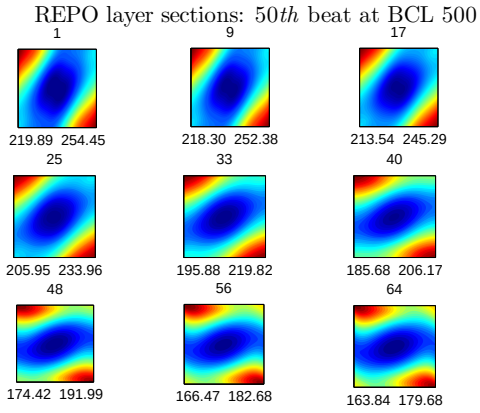

Figure 3.21: Monodomain repolarization sequence per layers (see figure 3.11) with central endocardial stimulus. For each panel we show the number of layer on top; below minimum and maximum attained.

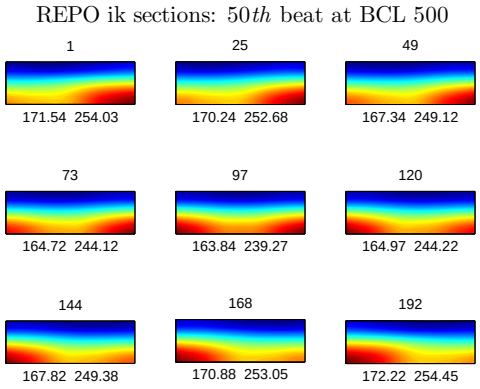

Figure 3.22: Monodomain repolarization sequence on ik sections (see figure 3.11) with central endocardial stimulus. For each panel we show the number of section on top; below minimum and maximum attained.

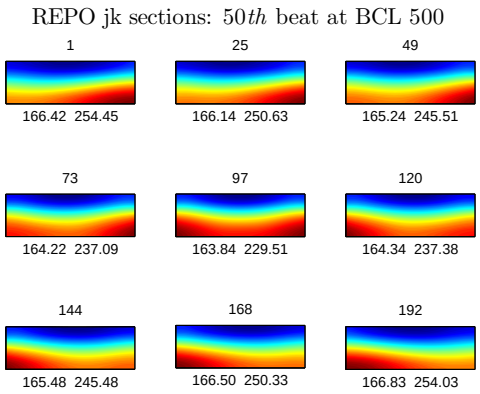

Figure 3.23: Monodomain repolarization sequence on jk sections (see figure 3.11) with central endocardial stimulus. For each panel we show the number of section on top; below minimum and maximum attained.

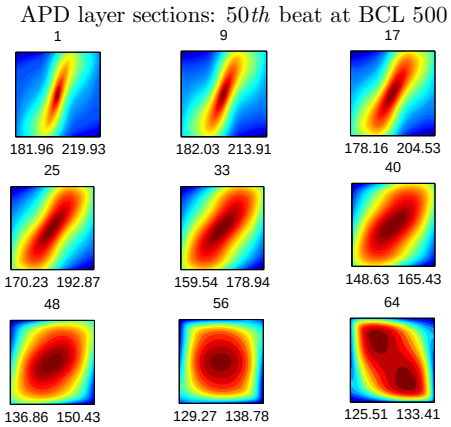

Figure 3.24: Monodomain action potential duration distribution per layers (see figure 3.11) with central endocardial stimulus. For each panel we show the number of layer on top; below minimum and maximum attained.

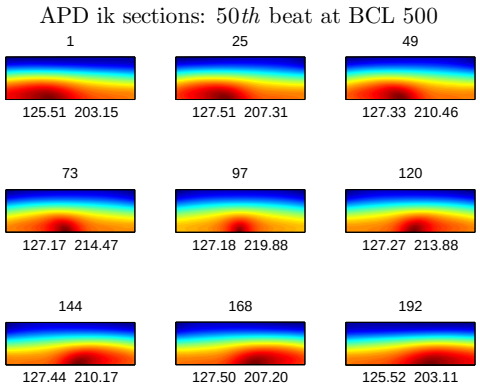

Figure 3.25: Monodomain action potential duration distribution on ik sections (see figure 3.11) with central endocardial stimulus. For each panel we show the number of section on top; below minimum and maximum attained.

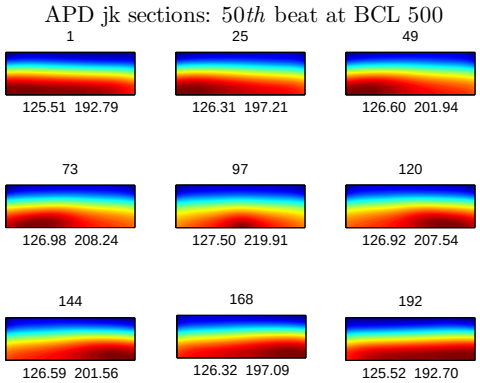

Figure 3.26: Monodomain action potential duration distribution on jk sections (see figure 3.11) with central endocardial stimulus. For each panel we show the number of section on top; below minimum and maximum attained.

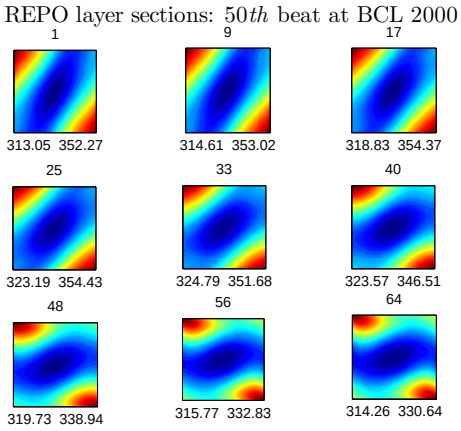

Figure 3.27: Monodomain repolarization sequence per layers (see figure 3.11) with central endocardial stimulus. For each panel we show the number of layer on top; below minimum and maximum attained.

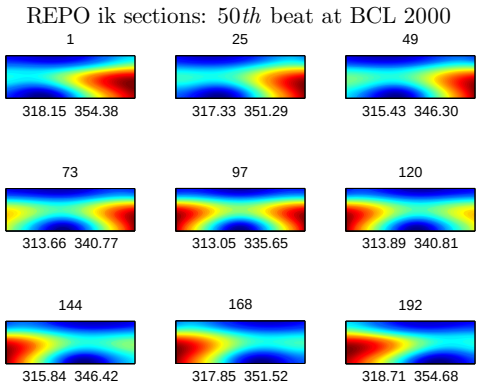

Figure 3.28: Monodomain repolarization sequence on ik sections (see figure 3.11) with central endocardial stimulus. For each panel we show the number of layer on top; below minimum and maximum attained.

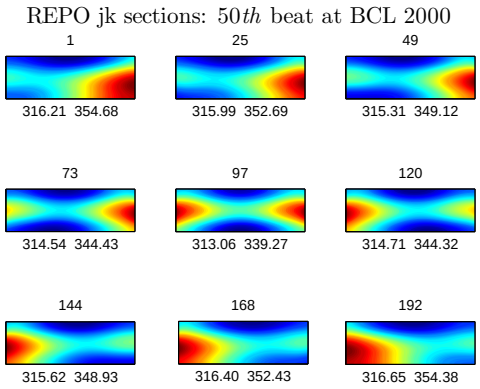

Figure 3.29: Monodomain repolarization sequence on jk section (see figure 3.11) with central endocardial stimulus. For each panel we show the number of layer on top; below minimum and maximum attained.

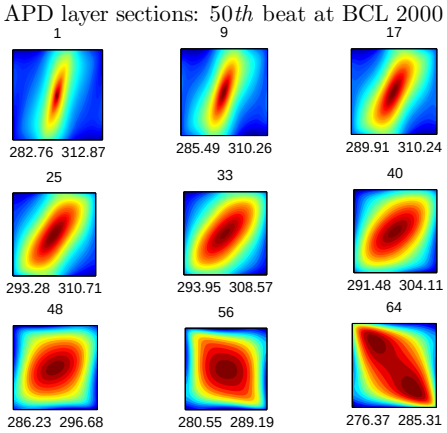

Figure 3.30: Monodomain action potential duration distribution per layers (see figure 3.11) with central endocardial stimulus. For each panel we show the number of layer on top; below minimum and maximum attained.

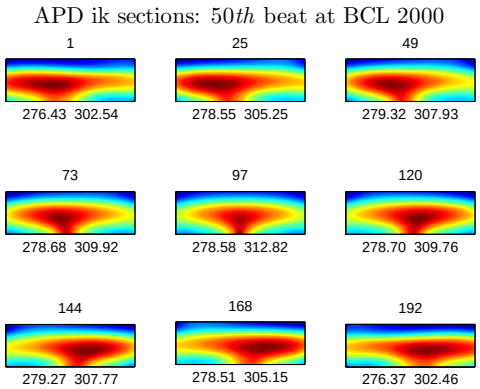

Figure 3.31: Monodomain action potential duration distribution on ik sections (see figure 3.11) with central endocardial stimulus. For each panel we show the number of layer on top; below minimum and maximum attained.

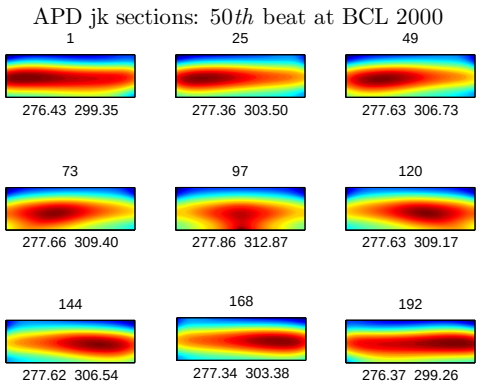

Figure 3.32: Monodomain action potential duration distribution on jk sections (see figure 3.11) with central endocardial stimulus. For each panel we show the number of layer on top; below minimum and maximum attained.

Chapter 4

Neumann-Neumann preconditioners for cardiac models

4.1 Introduction

In this chapter we will introduce and analyze non-overlapping domain decomposition preconditioners of Neumann-Neumann type for the cardiac Monodomain and Bidomain model. For a general introduction to these methods, the interested reader is referred to the monographs [140], [88] and [130]. In this section we will provide a brief introduction to the iterative substructuring approach. We decompose a polyhedral domain Ω into N *non-overlapping* open subdomains Ω_i of the same diameter H (often referred to as *substructures*) such that the union of their closures is the closure of Ω, i.e.

$$\overline{\Omega} = \bigcup_{i=1}^{N} \overline{\Omega}_i$$

and each of which is the union of shape-regular elements with the finite element nodes on the boundaries of neighboring subdomains matching across the interface.

Definition 4.1.1. Following [140] we define the *interface*:

$$\Gamma = \bigcup_{i \neq j} \partial\Omega_i \cap \partial\Omega_j$$

as the union of

- the subdomain *faces*, regarded as open sets, that are shared by two subregions,
- the subdomain *edges*, also regarded as open, that are shared by more than two subregions,

- the subdomain *vertices*, which are endpoints of edges.

Each local interface will be denoted by

$$\Gamma^{(i)} = \partial\Omega_i \cap \Gamma.$$

Remark 4.1.2. If a subdomain edge is a part of $\partial\Omega$ and is common to the boundaries of only two subdomains, we will regard that edge as a part of the face common to this pair of subdomains. Similarly, we will regard a subdomain vertex on $\partial\Omega$ part of an interior edge. The subdomain faces which belong to $\partial\Omega$ are not part of the interface Γ; the nodal values on $\partial\Omega$ which belong to only one subdomain will effectively belong to the subdomain interior.

Following the usual notation of substructuring algorithms, we will denote with $\mathbf{W}^{(i)}$ the finite element space defined on Ω_i: in particular $\mathbf{W}^{(i)} = V_h(\Omega_i)$ for the Monodomain discretization and $\mathbf{W}^{(i)} = V_h(\Omega_i) \times V_h(\Omega_i)$ for the Bidomain discretization (see definitions given in eqs. (2.17) and (2.18)). Each $\mathbf{W}^{(i)}$ is then decomposed into a subdomain interior part $\mathbf{W}_I^{(i)}$ and a subdomain interface part $\mathbf{W}_\Gamma^{(i)}$ such that

$$\mathbf{W}^{(i)} = \mathbf{W}_I^{(i)} \bigoplus \mathbf{W}_\Gamma^{(i)}.$$

We will denote the associated product spaces by

$$\mathbf{W} = \prod_{i=1}^{N} \mathbf{W}^{(i)}, \quad \mathbf{W}_I = \prod_{i=1}^{N} \mathbf{W}_I^{(i)}, \quad \mathbf{W}_\Gamma = \prod_{i=1}^{N} \mathbf{W}_\Gamma^{(i)}$$

and thus we will have

$$\mathbf{W} = \mathbf{W}_I \bigoplus \mathbf{W}_\Gamma.$$

Note that the functions belonging to $\mathbf{W}$ will not be in general continuous across the interface; we will denote the space of functions defined on Ω and continuous across Γ with $\widehat{\mathbf{W}}$, i.e.

$$\widehat{\mathbf{W}} = \mathbf{W}_I \bigoplus \widehat{\mathbf{W}}_\Gamma,$$

where we denoted the subspace of $\mathbf{W}_\Gamma$ of continuous functions on Γ by $\widehat{\mathbf{W}}_\Gamma$. With abuse of notation, we will make no distinction between the space of finite element functions and the space of degrees of freedoms (dofs) of the finite element functions.

Denoting the faces of Ω_i by $\mathcal{F}^{ij}$, its edges by $\mathcal{E}^{ik}$ and its vertices by $\mathcal{V}^{il}$, and introducing the set

$$\mathcal{N}_x = \{\, j \,|\, x \in \mathbf{W}^{(j)}\,,\ j = 1, \ldots, N\}$$

we can now describe the sets of nodes on $\mathcal{F}^{ij}$, $\mathcal{E}^{ik}$ and $\mathcal{V}^{il}$ for our case of structured grid

by equivalence classes:

$$x \in \mathcal{F}^{ij} \iff |\mathcal{N}_x| = 2$$
$$x \in \mathcal{E}^{ik} \iff |\mathcal{N}_x| = 4$$
$$x \in \mathcal{V}^{il} \iff |\mathcal{N}_x| = 8$$

where $|\mathcal{N}_x|$ denotes the cardinality of the set $\mathcal{N}_x$; clearly

$$x \in \mathbf{W}_I^{(i)} \iff |\mathcal{N}_x| = 1.$$

Figure 4.1 shows the union of the wirebaskets, i.e. the union of edges and vertices for a global cubic grid $9 \times 9 \times 9$ decomposed with a $2 \times 2 \times 2$ subdomain grid with $H/h = 5$.

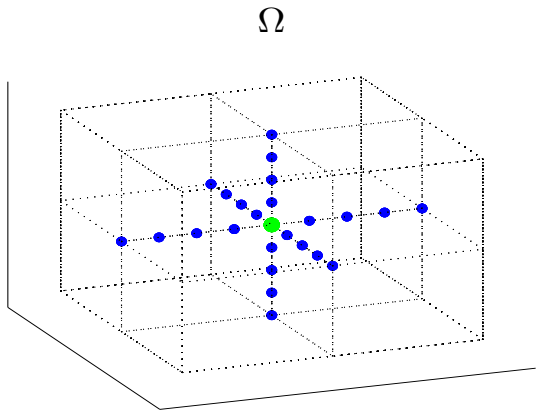

Figure 4.1: Edges nodes (blue circles) and vertices (green circles) for a 2x2x2 decopomposition of Ω.

In order to describe the iterative substructuring algorithms, we need to introduce several restriction, extension, and scaling operators between different spaces. The restriction operator $R^{(i)}$ maps a vector of the space $\widehat{\mathbf{W}}$ to its restriction to the subdomain subspace $\mathbf{W}^{(i)}$, whereas the restriction operator $R_\Gamma^{(i)}$ maps a vector of the space $\widehat{\mathbf{W}}_\Gamma$ to its restriction to the subdomain subspace $\mathbf{W}_\Gamma^{(i)}$. The extension operators $R^{(i)^T}$ and $R_\Gamma^{(i)^T}$ perform the inverted transformations. Furthermore, we introduce the restriction operator R, which maps functions defined on $\widehat{\mathbf{W}}$ to $\mathbf{W}$, as the direct sum of the $R^{(i)}$, and R_Γ, which maps functions defined on $\widehat{\mathbf{W}}_\Gamma$ to $\mathbf{W}_\Gamma$, as the direct sum of the $R_\Gamma^{(i)}$, together with their inverted transformations R^T and R_Γ^T. Restriction and extension operators are rectangular matrices with boolean values; for a formal definition of such entries see [88].

Another important tool of substructuring algorithms is the so called *partition of unity* operator, defined by the quantities

$$\delta_i(x) = \frac{\sum_{j \in \mathcal{N}_x} a_j^\gamma(x)}{a_i^\gamma(x)} \tag{4.1}$$

for some $\gamma \in [1/2, \infty)$, where $a_j(x)$ is a representative value for subdomain j at the node

x. Coefficients given in (4.1) provide a partition of unity in the sense that

$$\sum_{i=1}^{N} {R_\Gamma^{(i)}}^T \delta_i^\dagger(x) = 1, \ \forall x \in \Gamma. \tag{4.2}$$

where $\delta_i^\dagger(x)$ is the pseudo-inverse of $\delta_i(x)$. Clearly, for the Bidomain discretization, we will have two subdomain representative values associated to the two components of the finite element space. Denoting with $D^{(i)}$ the diagonal matrix with $\delta_i^\dagger(x)$ along the diagonal, we obtain the operator $R_{D,\Gamma}^{(i)}$ multiplying each $R_\Gamma^{(i)}$ by $D^{(i)}$, and the operator $R_{D,\Gamma}$ as the direct sum of the $R_{D,\Gamma}^{(i)}$. We than introduce the *average operator*

$$E_D : \mathbf{W}_\Gamma \to \widehat{\mathbf{W}}_\Gamma$$

whose action on $u \in \mathbf{W}_\Gamma$ is given by

$$E_D u = \sum_{i=1}^{N} {R_\Gamma^{(i)}}^T I^h(\delta_i^\dagger u_i) \tag{4.3}$$

where I^h is the usual Lagrangian interpolation operator. Note that E_D is equal to the identity when restricted on $\widehat{\mathbf{W}}_\Gamma$ thanks to formula (4.2).

Ordering the nodes interior to the subdomains first, followed by those on the interface Γ we can then write each symmetric linear system assembled on $\widehat{\mathbf{W}}$

$$\widehat{A}u = \widehat{f}$$

as

$$\begin{pmatrix} A_{II} & A_{I\Gamma} \\ A_{I\Gamma}^T & A_{\Gamma\Gamma} \end{pmatrix} \begin{pmatrix} u_I \\ u_\Gamma \end{pmatrix} = \begin{pmatrix} f_I \\ f_\Gamma \end{pmatrix}. \tag{4.4}$$

From now on, the hat symbol will denote an assembled matrix.

Within the substructuring approach, each bilinear form and load vector defined on Ω are written in terms of contributions from individual subregions, simply restricting their integration set to each Ω_i: denoting with $a(\cdot,\cdot)$ and $a_i(\cdot,\cdot)$ the discrete bilinear forms on $\widehat{\mathbf{W}}$ and $\mathbf{W}^{(i)}$ respectively, we can state the subassembly relation for the these forms as:

$$a(u,v) = \sum_{i=1}^{N} a_i(R^{(i)}u, R^{(i)}v), \quad \forall u, v \in \widehat{\mathbf{W}}$$

where clearly each subdomain contribution is zero outside the substructure. The global finite element system can then be expressed by subassembling, i.e.

$$\widehat{A} = R^T A R = \sum_{i=1}^{N} {R^{(i)}}^T A^{(i)} R^{(i)}, \ \ \widehat{f} = \sum_{i=1}^{N} {R^{(i)}}^T f^{(i)}$$

where the local system matrices $A^{(i)}$, the global unassembled matrix A, and the local load vectors $f^{(i)}$ are given by

$$A^{(i)} = \begin{pmatrix} A_{II}^{(i)} & A_{I\Gamma}^{(i)} \\ A_{I\Gamma}^{(i)^T} & A_{\Gamma\Gamma}^{(i)} \end{pmatrix}, \tag{4.5}$$

$$A = \begin{pmatrix} A^{(1)} & 0 & 0 \\ 0 & \ddots & 0 \\ 0 & 0 & A^{(N)} \end{pmatrix}$$

and

$$f^{(i)} = \begin{pmatrix} f_I^{(i)} \\ f_\Gamma^{(i)} \end{pmatrix}.$$

Thus, in order to perform a matrix-vector multiplication with $\widehat{A}$, we first restrict properly the vectors u_I and u_Γ to each $\mathbf{W}^{(i)}$, then multiply them by the individual substructure matrices and, finally, obtain the product $\widehat{A}u$ by extending by zeros and adding the resulting vectors.

4.2 Schur Complement and discrete harmonic extensions

Let us now consider how to represent the inverse of the symmetric, positive (semi)definite block matrix given in eq. (4.4). Provided the invertibility of the A_{II} block, we can use block Cholesky elimination (see [79]) and split the matrix as

$$\begin{pmatrix} I_{II} & 0 \\ A_{I\Gamma}^T A_{II}^{-1} & I_{\Gamma\Gamma} \end{pmatrix} \begin{pmatrix} A_{II} & 0 \\ 0 & A_{\Gamma\Gamma} - A_{I\Gamma}^T A_{II}^{-1} A_{I\Gamma} \end{pmatrix} \begin{pmatrix} I_{II} & A_{II}^{-1} A_{I\Gamma} \\ 0 & I_{\Gamma\Gamma} \end{pmatrix} \tag{4.6}$$

where I_{II} and $I_{\Gamma\Gamma}$ are identity matrices of appropriate sizes. The symmetric matrix

$$\widehat{S}_\Gamma = A_{\Gamma\Gamma} - A_{I\Gamma}^T A_{II}^{-1} A_{I\Gamma}$$

is the *Schur complement* of the matrix (4.4) assembled at the interface nodes.

Differently to the *direct substructuring*, in the *iterative substructuring* approach the matrix $\widehat{S}_\Gamma$ is not formed explicitly, since this is a potentially expensive operation. Indeed, the Schur complement matrix $\widehat{S}_\Gamma$ will have a block dense structure depending on the ordering of nodes in Γ. If two nodes x_i and x_j lie on some common subdomain boundary, then entry $\widehat{S}_{ij}$ will typically be nonzero, otherwise, the entry $\widehat{S}_{ij}$ will be zero. The magnitude of a nonzero entry $\widehat{S}_{ij}$ typically decreases with increasing distance between the nodes x_i and x_j. Instead of explicitly assemble $\widehat{S}_\Gamma$, in the iterative substructuring approach a sparse representation of $A_{I\Gamma}$, whose action can be evaluated by subassembly, and the sparse, triangular factors of the A_{II} are stored, and the action of $\widehat{S}_\Gamma$ on an interface vector is obtained by subassembly, i.e.

$$\widehat{S}_\Gamma = R_\Gamma^T S R_\Gamma = \sum_{i=1}^{N} R_\Gamma^{(i)^T} S^{(i)} R_\Gamma^{(i)}$$

where

$$S = \begin{pmatrix} S^{(1)} & 0 & 0 \\ 0 & \ddots & 0 \\ 0 & 0 & S^{(N)} \end{pmatrix} \tag{4.7}$$

is the unassembled Schur complement defined on $\mathbf{W}_\Gamma$ and

$$S^{(i)} = A_{\Gamma\Gamma}^{(i)} - A_{I\Gamma}^{(i)T} {A_{II}^{(i)}}^{-1} A_{I\Gamma}^{(i)} \tag{4.8}$$

are the local Schur complement operators acting on the spaces $\mathbf{W}_\Gamma^{(i)}$.

Remark 4.2.1. Note that the action of A_{II}^{-1} is evaluated subdomain per subdomain in parallel since it is a block diagonal matrix, with subdomain blocks ${A_{II}^{(i)}}^{-1}$, due to the fact that

$$\mathbf{W}_I^{(i)} \cap \mathbf{W}_I^{(j)} = \emptyset, \quad i \neq j.$$

Its application to a vector corresponds to the parallel solution of problems with Dirichlet boundary conditions on $\Gamma^{(i)}$ and, eventually, homogeneous Neumann data on $\partial\Omega_i \cap \partial\Omega$. For both configurations, the presence of a Dirichlet boundary make these local problems always solvable, either for the Monodomain or the Bidomain model.

We can thus formally invert the three factors of (4.6), finding:

$$\begin{aligned} \begin{pmatrix} A_{II} & A_{I\Gamma} \\ A_{I\Gamma}^T & A_{\Gamma\Gamma} \end{pmatrix}^{-1} &= \begin{pmatrix} I_{II} & -A_{II}^{-1}A_{I\Gamma} \\ 0 & I_{\Gamma\Gamma} \end{pmatrix} \begin{pmatrix} A_{II}^{-1} & 0 \\ 0 & \widehat{S}_\Gamma^{-1} \end{pmatrix} \begin{pmatrix} I_{II} & 0 \\ -A_{I\Gamma}^T A_{II}^{-1} & I_{\Gamma\Gamma} \end{pmatrix} \\ &= \begin{pmatrix} A_{II}^{-1} & 0 \\ 0 & 0 \end{pmatrix} + \Phi \widehat{S}_\Gamma^{-1} \Phi^T \end{aligned} \tag{4.9}$$

where

$$\Phi = \begin{pmatrix} -A_{II}^{-1}A_{I\Gamma} \\ I_{\Gamma\Gamma} \end{pmatrix}.$$

Therefore, in order to solve a symmetric positive (semi)definite linear system with matrix (4.4), we first solve on $\widehat{\mathbf{W}}_\Gamma$, through conjugate gradient iterations, the Schur complement system defined on the interface

$$\widehat{S}_\Gamma u_\Gamma = \widehat{g}_\Gamma \tag{4.10}$$

with right hand side given by

$$\widehat{g}_\Gamma = \Phi^T f = f_\Gamma - A_{I\Gamma}^T A_{II}^{-1} f_I = \sum_{i=1}^{N} R_\Gamma^{(i)^T} \left(f_\Gamma^{(i)} - A_{I\Gamma}^{(i)^T} {A_{II}^{(i)}}^{-1} f_I^{(i)} \right) \tag{4.11}$$

then we extend the solution on $\widehat{\mathbf{W}}$ by solving for u_I the block diagonal system:

$$A_{II}u_I = f_I - A_{I\Gamma}u_\Gamma.$$

Due to this fact, we will sometime refer to the Schur system as the *reduced* system, in contrast to the *global* system represented by $\widehat{A}$.

It can be easily seen that the reduced Schur complement system inherits the positive (semi)definitess from the global system, together with the system solvability, through the concept of *discrete harmonic functions*:

Definition 4.2.2. *A function $u^{(i)}$ defined on Ω_i is said to be discrete harmonic on Ω_i if*

$$A_{II}^{(i)}u_I^{(i)} + A_{I\Gamma}^{(i)}u_\Gamma^{(i)} = 0.$$

From this definition and the assumption of invertibility of local problems represented by A_{II}, we can see that $u^{(i)}$ is fully determined by $u_\Gamma^{(i)}$, i.e. the value of $u^{(i)}$ on $\Gamma^{(i)}$. We will use the notation $u^{(i)} = \mathcal{H}_i u_\Gamma^{(i)}$ and call $\mathcal{H}_i$ the discrete harmonic extension operator on Ω_i defining

$$\mathcal{H}_i u_\Gamma^{(i)} = \begin{cases} -{A_{II}^{(i)}}^{-1} A_{I\Gamma}^{(i)} u_\Gamma^{(i)} & \text{on} \mathbf{W}_I^{(i)} \\ u_\Gamma^{(i)} & \text{on} \mathbf{W}_\Gamma^{(i)} \end{cases}$$

A direct consequence of Definition 4.2.2 is that

$${v^{(i)}}^T A^{(i)} \mathcal{H}_i u_\Gamma^{(i)} = 0$$

$\forall\, v^{(i)}$ that vanishes on $\Gamma^{(i)}$. We then have the following properties of the discrete harmonic extension and discrete harmonic functions (see [140]) that can be obtained with elementary matrix algebra arguments using the 2x2 block decomposition of each $A^{(i)}$ given in eq. (4.5).

Lemma 4.2.3. *Let $u_\Gamma^{(i)}$ be the restriction of a finite element function $u^{(i)}$ to $\Gamma^{(i)}$. Then, we can equivalently define the action of the local Schur complements matrices as*

$$\begin{pmatrix} A_{II}^{(i)} & A_{I\Gamma}^{(i)} \\ {A_{I\Gamma}^{(i)}}^T & A_{\Gamma\Gamma}^{(i)} \end{pmatrix} \begin{pmatrix} -{A_{II}^{(i)}}^{-1} A_{I\Gamma}^{(i)} u_\Gamma^{(i)} \\ u_\Gamma^{(i)} \end{pmatrix} = \begin{pmatrix} 0 \\ S^{(i)} u_\Gamma^{(i)} \end{pmatrix}$$

and thus the discrete harmonic extension satisfies the following matrix equivalence

$${u_\Gamma^{(i)}}^T S^{(i)} u_\Gamma^{(i)} = (\mathcal{H}_i u_\Gamma^{(i)})^T A^{(i)} \mathcal{H}_i u_\Gamma^{(i)}.$$

We can thus empirically define the local Schur bilinear forms as

$$s_i(u_\Gamma^{(i)}, v_\Gamma^{(i)}) = a_i(\mathcal{H}_i u_\Gamma^{(i)}, \mathcal{H}_i v_\Gamma^{(i)}) \tag{4.12}$$

and state the following Lemma (see also [140])

Lemma 4.2.4. *The local Schur bilinear forms satisfies the energy minimization property*

$$s_i(u_\Gamma^{(i)}, u_\Gamma^{(i)}) \leq a_i(u^{(i)}, u^{(i)})$$

where $u_\Gamma^{(i)}$ *is the restriction to* $\Gamma^{(i)}$ *of a finite element function* $u^{(i)} \in \boldsymbol{W}^{(i)}$.

Remark 4.2.5. We can also define the *piecewise discrete harmonic extension operator* $\mathcal{H}$ as direct sum of $\mathcal{H}_i$ operators: defining the Schur bilinear form from the following sub-assembly relation

$$\mathcal{S}(u_\Gamma, v_\Gamma) = \sum_{i=1}^{N} s_i(R_\Gamma^{(i)} u_\Gamma, R_\Gamma^{(i)} v_\Gamma) \tag{4.13}$$

then, if u_Γ is the restriction of a finite element function u to Γ, the piecewise discrete harmonic extension of u_Γ into the interior of the subdomains satisfies

$$\mathcal{S}(u_\Gamma, v_\Gamma) = a(\mathcal{H}u_\Gamma, \mathcal{H}v_\Gamma).$$

Remark 4.2.6. Clearly, the Schur bilinear form $\mathcal{S}(\cdot,\cdot)$ inherits all the properties of the elliptic bilinear form $a(\cdot,\cdot)$ since it is the restriction of the latter on the subspace of piecewise discrete harmonic extension. Therefore, $\mathcal{S}(\cdot,\cdot)$ will be positive definite for the Monodomain model and (at least) positive semidefinite for the Bidomain model. The same will hold for the local bilinear forms.

Remark 4.2.7. Regarding to the Bidomain model, it is easy to show that $\mathbf{1}_\Gamma^{(i)}$ spans the null space of all the local Schur system, i.e.

$$\mathbf{1}_{\Omega_i} = \mathcal{H}_i(\mathbf{1}_{\Gamma^{(i)}}).$$

where $\mathbf{1}_{\Omega_i}$ and $\mathbf{1}_{\Gamma^{(i)}}$ are the identity vectors of appropriate sizes and thus that

$$\mathbf{1}_\Omega = \mathcal{H}(\mathbf{1}_\Gamma).$$

In fact, since $\mathbf{1}_{\Omega_i}$ spans the null space of $a_i(\cdot,\cdot)$, from the positive semidefinitess of $s_i(\cdot,\cdot)$ and the energy minimization property follows

$$0 \leq \mathbf{1}_{\Gamma^{(i)}}^T S^{(i)} \mathbf{1}_{\Gamma^{(i)}} \leq \mathbf{1}_{\Omega_i}^T A^{(i)} \mathbf{1}_{\Omega_i} = 0$$

and thus $\mathbf{1}_{\Gamma^{(i)}}$ belongs to the null space of $S^{(i)}$. Otherwise, let $u_\Gamma^{(i)}$ belongs to the null space of $S^{(i)}$. Then for the definition of the local Schur bilinear forms it will hold that

$$0 = {u_\Gamma^{(i)}}^T S^{(i)} u_\Gamma^{(i)} = (\mathcal{H}_i u_\Gamma^{(i)})^T A^{(i)} \mathcal{H}_i u_\Gamma^{(i)}.$$

Therefore $\mathcal{H}_i u_\Gamma^{(i)}$, and thus $u_\Gamma^{(i)}$, must be constant vectors.

Table 4.1 shows some preliminary results on conjugate gradient iterations applied to

	Monodomain				Bidomain			
	iter	$\|\|r\|\|_2$	$\|\|e\|\|_2$	$\|\|e\|\|_\infty$	iter	$\|\|r\|\|_2$	$\|\|e\|\|_2$	$\|\|e\|\|_\infty$
$\widehat{A}$	29	6.5E-9	5.2E-4	9.6E-5	164	9.9E-9	7.5E-3	3.5E-4
$\widehat{S}_\Gamma$	22	8.9E-9	3.1E-4	2.4E-5	73	9.5E-9	1.1E-3	5.1E-5

Table 4.1: Conjugate gradient iterations of the Monodomain and Bidomain system, using the global assembled system $\widehat{A}$ or the Schur system $\widehat{S}_\Gamma$. Test case considered is h =1E-2, global grid 17x17x17, random right-hand side, null initial guess and absolute residual tolerance 1E-8. Substrucutres subdivision in the three dimensions is 2x2x2. For each solve, number of iteration, euclidean residual norm $||r||_2$, euclidean and infinity norm of the exact error are shown.

the solution of the Monodomain and Bidomain systems and to their assembled Schur complements. Test cases considered are descripted in the caption.

4.3 Technical tools

In this section, we will present some technical tools routinely employed in the analysis of domain decomposition algorithms and that will be used throughout this and the next chapter; unless otherwise stated, these results can be found in [140] and references therein. Assume we have a bounded open Lipschitz set $\Omega \subset \mathbb{R}^n$ with Lipschitz continuous boundary according to the next definition:

Definition 4.3.1. *The boundary $\partial\Omega$ is Lipschitz continuous if there exist a finite number of open sets $\mathcal{O}_i$, $i = 1, \ldots, m$, that cover $\partial\Omega$ such that, for every i, the intersection $\partial\Omega \cap \mathcal{O}_i$ is the graph of a Lipschitz continuous function and $\Omega \cap \mathcal{O}_i$ lies on one side of this graph*

We will deal with the usual functional Sobolev spaces defined on Ω:

$$L^2(\Omega) = \{u : \Omega \to \mathbb{R} \quad | \quad \int_\Omega |u|^2 < \infty\}$$

and

$$H^1(\Omega) = \{u : \Omega \to \mathbb{R} \quad | \quad \int_\Omega |\nabla u|^2 + \int_\Omega |u|^2 < \infty\}.$$

These spaces are equipped with the norms

$$||u||^2_{L^2(\Omega)} = \int_\Omega |u|^2, \quad ||u||^2_{H^1(\Omega)} = |u|^2_{H^1(\Omega)} + ||u||^2_{L^2(\Omega)}$$

with the seminorm on $H^1(\Omega)$ defined by

$$|u|^2_{H^1(\Omega)} = \int_\Omega |\nabla u|^2.$$

Given a proper subset $\Gamma \subseteq \partial\Omega$ with non vanishing $(n-1)$-dimensional measure and

relatively open with respect to $\partial\Omega$, we can define the space $H^s(\Gamma)$, $s \geq 0$, consisting of functions on Γ such that:

$$||u||^2_{H^s(\Gamma)} = ||u||^2_{H^{[s]}(\Gamma)} + |u|^2_{H^s(\Gamma)} < \infty$$

where $[s]$ denotes the greater natural number lesser than s and the seminorm is defined as:

$$|u|^2_{H^s(\Gamma)} = \sum_{[\alpha]=[s]} \int_\Gamma \int_\Gamma \frac{|D^\alpha u(x) - D^\alpha u(y)|^2}{|x-y|^{2\sigma+n-1}} dxdy$$

with $\sigma = s - [s]$, $\alpha = (\alpha_1, \ldots, \alpha_N)$ is a multi-index with $|\alpha| = \sum_{i=1}^n \alpha_i$, $\alpha_i > 0$ and

$$D^\alpha u = \frac{\partial^{|\alpha| u}}{\partial^{\alpha_1} x_1 \ldots \partial^{\alpha_n} x_n}$$

If $|\alpha| = (0 \ldots, 0)$, than $D^\alpha u = u$. The following two lemmas hold:

Lemma 4.3.2. *Let Ω be a Lipschitz region and $s > 1/2$. Then, the operator*

$$\gamma : C^\infty(\overline{\Omega}) \to C^\infty(\Gamma)$$

mapping a function into its restriction on Γ, can be extended continuously to an operator

$$\gamma_0 : H^s(\Omega) \to H^{s-1/2}(\Gamma).$$

Lemma 4.3.3. *With the same assumptions of the previous lemma, there exist a continuous lifting operator*

$$\mathcal{R}_0 : H^{s-1/2}(\Gamma) \to H^s(\Omega)$$

such that $\gamma_0(\mathcal{R}_0 u) = u$ with $u \in H^{s-1/2}(\Gamma)$.

Even if Γ is a proper subset of $\partial\Omega$, $H^s_0(\Gamma)$ (the space defined by the kernel of γ_0) coincides with $H^s(\Gamma)$ for $s \leq 1/2$; on the other hand, the extension by zero of functions in $H^{1/2}_0(\Gamma)$ do not, in general, belong to $H^{1/2}(\partial\Omega)$. We thus define the space

$$H^{1/2}_{00}(\Gamma) = \{u \in H^{1/2}(\Gamma) \mid \mathcal{E}u \in H^{1/2}(\partial\Omega)\}$$

where $\mathcal{E}u$ is the extension by zero of u to $\partial\Omega$. The latter space coincides with the interpolation space $[H^1_0(\Gamma), L^2(\Gamma)]_{1/2}$ defined by

$$[H^1_0(\Gamma), L^2(\Gamma)]_{1/2} = \{u \in L^2(\Gamma)]_{1/2} \mid t^{-1} K(t, u; H^1_0(\Gamma), L^2(\Gamma)) \in L^2(0, \infty)\}$$

where

$$K(t, u; L^2(\Gamma), H^1_0(\Gamma))^2 = \inf_{u_0 + u_1 = u} \{||u_0||^2_{L^2(\Gamma)} + t^2 ||u_1||^2_{H^1_0(\Gamma)}\}.$$

The interpolation space can be equipped with the norm

$$||u||_{H_{00}^{1/2}(\Gamma)} = ||u||^2_{L^2(\Gamma)} + \int_0^\infty t^{-2} K(t, u; L^2(\Gamma), H_0^1(\Gamma))^2 dt.$$

Remark 4.3.4. If $u \in H^{1/2}(\partial\Omega)$ vanishes almost everywhere on $\partial\Omega \setminus \Gamma$, then it can be shown that the two norms $||u||_{H^{1/2}(\partial\Omega)}$ and $||u||_{H_{00}^{1/2}(\Gamma)}$ are equivalent norms.

The following lemma relates the H^1 seminorm of a finite element function in $u \in H^1(\Omega)$ with the seminorm of its trace on Γ.

Lemma 4.3.5. *There exist two constant C_1 and C_2, depending only on the shape of Ω and not on its size, such that*

$$C_1 |u_\Gamma|_{H^{1/2}(\Gamma)} \leq |u|_{H^1(\Omega)} \leq C_2 |u_\Gamma|_{H^{1/2}(\Gamma)}$$

for every $u_\Gamma \in H^{1/2}(\Gamma)$ which is the trace on Γ of a finite element function $u \in H^1(\Omega)$.

We note that the proof of the following lemma relates for the first inequality on the trace theorem given in lemma 4.3.2 and some scaling arguments; for the second inequality, some regularity results for the Laplace problem with appropriate boundary conditions must be employed. In particular, an $H^{3/2}(\Omega)$ regularity for the Laplace problem with non homogenous Dirichlet boundary conditions is needed when Γ coincides with $\partial\Omega$; otherwise, if Γ is a proper subset of $\partial\Omega$, an $H^{3/2}(\Omega)$ regularity result for the Laplace problem with mixed Dirichlet (on Γ) and Neumann (on $\partial\Omega \setminus \Gamma$) boundary conditions is needed. A suitable result for the mixed problem for three-dimensional polyhedral domains can be found in [24] or in [25]. For the proof of the latter lemma, see Lemma 4.6 in [140] and references therein.

The following lemma is known in literature as Poincarè-Friedrichs inequality. For simplicity, we will only present the results for three-dimensional domains.

Lemma 4.3.6. *Let $\Omega \subset \mathbb{R}^3$ be Lipschitz continuous with diameter H and $u \in H^1(\Omega)$. Then, there exist a constant C that depend only on the shape of Ω but not on its size such that:*

$$||u||^2_{L^2(\Omega)} \leq C H^2 |u|^2_{H^1(\Omega)}$$

if u has vanishing mean value on Ω or vanishes on a two dimensional subset Γ of $\partial\Omega$ with non-vanishing measure.

Finally, in order to give estimates for the condition number of the preconditioned Schur system, we must employ some results which relates the norm of a conforming finite element solution of an elliptic second order problem on the faces and edges of the subdomains plus estimates for the dofs on the vertices. Unless otherwise stated, their proofs can be found in [140]. We first proceed with face terms. The following Lemma can be found in [13].

Lemma 4.3.7. *For any face $\mathcal{F}$ of a parallelepipedal domain Ω, there exist a finite element function $\vartheta_{\mathcal{F}} \in V^h(\Omega)$ that equals 1 at the nodal points of $\mathcal{F}$, vanishes on $\partial\Omega \setminus \mathcal{F}$ and*

satisfies for any $u \in V^h(\Omega)$

$$||I^h(\vartheta_{\mathcal{F}} u)||^2_{H^{1/2}_{00}(\mathcal{F})} \leq C(1+\log(H/h))^2 \left(|u|^2_{H^1(\Omega)} + H^{-2}||u||^2_{L^2(\Omega)}\right)$$

and

$$||I^h(\vartheta_{\mathcal{F}}(u-\overline{u}_{\mathcal{F}}))||^2_{H^{1/2}_{00}(\mathcal{F})} \leq C(1+\log(H/h))^2 |u|^2_{H^1(\Omega)}$$

where $\overline{u}_{\mathcal{F}}$ *is the average value of* u *on* $\mathcal{F}$.

Lemma 4.3.8. *Let* $\mathcal{E}$ *be an edge of* Ω*; then there exist a constant* C*, independent of* h *and* H*, such that for any* $u \in V^h(\Omega)$

$$||u||^2_{L^2(\mathcal{E})} \leq C(1+\log(H/h)) \left(|u|^2_{H^1(\Omega)} + H^{-2}||u||^2_{L^2(\Omega)}\right)$$

and

$$||u-\overline{u}_{\mathcal{E}}||^2_{L^2(\mathcal{E})} \leq C(1+\log(H/h))|u|^2_{H^1(\Omega)}$$

where $\overline{u}_{\mathcal{E}}$ *is the average value of* u *on* $\mathcal{E}$.

Given an edge $\mathcal{E}$ of Ω, let $\vartheta_{\mathcal{E}} \in V^h(\Omega)$ be the finite element function that vanishes at all nodes of $\overline{\Omega}$ except on the nodes of $\mathcal{E}$ where it takes the value 1. Then the following will hold:

Lemma 4.3.9. *Let* $\mathcal{E}$ *be an edge of* Ω *and* u *any finite element function in* $V^h(\Omega)$*. Then there exist a constant* C*, independent of* h *and* H*, such that*

$$|I^h(\vartheta_{\mathcal{E}} u)|^2_{H^{1/2}(\Gamma)} \leq C||u||^2_{L^2(\mathcal{E})}$$

Finally, we need a result for a vertex $\mathcal{V}$ of Ω. As for the edges, we introduce a finite element cut-off function $\vartheta_{\mathcal{V}} \in V^h(\Omega)$ which vanishes at all nodes of $\overline{\Omega}$ except on the vertex $\mathcal{V}$ where it takes the value 1. Then the following result will hold:

Lemma 4.3.10. *Let* $\mathcal{V}$ *be a vertex of* Ω *and let* $u \in V^h(\Omega)$*. Then there exist a constant* C *independent of* h *and* H *such that*

$$|u(\mathcal{V})\vartheta_{\mathcal{V}}|^2_{H^{1/2}(\Gamma)} \leq C\left(|u|^2_{H^1(\Omega)} + H^{-2}||u||^2_{L^2(\Omega)}\right)$$

4.4 A Neumann-Neumann preconditioner for the Monodomain model

In this Section we will introduce the basic ingredients of a Neumann-Neumann preconditioner for the Monodomain problem. Recall (see Section 2.4) that the local bilinear forms $a_i(\cdot,\cdot)$ are given in this case by

$$a_i(u,v) = \int_{\Omega_i} D_m \nabla u \cdot \nabla v + \gamma \int_{\Omega_i} uv$$

where $\gamma = 1/\delta_t$. By subassembly, they define the assembled elliptic form $a_{mono}(\cdot,\cdot)$ given in formula (2.22): the resulting Schur symmetric elliptic bilinear form on $\widehat{\mathbf{W}}_\Gamma$ is obtained restricting the bilinear form $a_{mono}(\cdot,\cdot)$ on the subspace of piecewise discrete harmonic functions as in eq. (4.13).

Neumann-Neumann (NN) domain decomposition methods are a widely used family of preconditioners for Schur complement matrices in two and three dimensions. From a computational viewpoint, these preconditioners solve a Neumann problem on each subdomain (see section 4.8), and hence the name; in addition a Dirichlet problem must be solved on each subdomain in the application of the Schur matrix. From the viewpoint of Schwarz subspace methods (see e.g. [130]), a Neumann-Neumann preconditioner has the structure of an additive Schwarz preconditioner for $\widehat{S}_\Gamma$. An abstract *additive Schwarz* preconditioner is specified by a decomposition of the space $\widehat{\mathbf{W}}_\Gamma$ into the subspaces $\mathbf{W}_\Gamma^{(i)}$ and by symmetric elliptic bilinear forms $\tilde{s}_i(\cdot,\cdot)$ defined on $\mathbf{W}_\Gamma^{(i)}$ as

$$\tilde{s}_i(u_\Gamma^{(i)}, v_\Gamma^{(i)}) = s_i(\delta_i u_\Gamma^{(i)}, \delta_i v_\Gamma^{(i)}); \tag{4.14}$$

in an abstract Schwarz framework we are using inexact local solvers on each subdomain. Clearly, from definition (4.13)

$$\mathcal{S}(u_\Gamma, v_\Gamma) = \sum_{i=1}^{N} \tilde{s}_i(R_{D,\Gamma}^{(i)} u_\Gamma, R_{D,\Gamma}^{(i)} v_\Gamma).$$

For the Monodomain discretization, each subdomain bilinear form $\tilde{s}_i(\cdot,\cdot)$ is continuous and positive definite: therefore each local variational problem defined by $\tilde{s}_i(\cdot,\cdot)$ will be well defined and it will have a unique solution due to the Lax-Milgram Lemma. The Schwarz framework then introduces a projection-like operator on each subdomain

$$P_i = {R_\Gamma^{(i)}}^T \widetilde{P}_i$$

given by the local problem

$$\tilde{s}_i(\widetilde{P}_i u_\Gamma, v_\Gamma^{(i)}) = \mathcal{S}(u_\Gamma, {R_\Gamma^{(i)}}^T v_\Gamma^{(i)}), \quad \forall\, v_\Gamma^{(i)} \in \mathbf{W}_\Gamma^{(i)}. \tag{4.15}$$

It can be easily proved (see [140]) that each P_i can be written in matrix form as

$$P_i = R_{D,\Gamma^{(i)}}^T {S^{(i)}}^{-1} R_{D,\Gamma^{(i)}} \widehat{S}_\Gamma \tag{4.16}$$

and then the partition of unity Neumann-Neumann abstract Schwarz operator can be defined by:

$$P_{NN} = \sum_{i=1}^{N} P_i. \tag{4.17}$$

Moreover, each P_i will be selfadjoint with respect to the scalar product induced by $\mathcal{S}(\cdot,\cdot)$. Taking into account the Schur complement operator defined on the product space $\mathbf{W}_\Gamma$ as

subd	PCG-BJ			PCG-AS			PCG-NN Schur		
	it	$\|\|r\|\|_2$	$\|\|e\|\|_2$	it	$\|\|r\|\|_2$	$\|\|e\|\|_2$	it	$\|\|r\|\|_2$	$\|\|e\|\|_2$
2x2x2	15	1.4E-13	3.7E-9	9	3.1E-13	8.7E-9	4	4.8E-14	2.7E-11
8x1x1							4	3.7E-15	3.1E-12
1x8x1							4	3.3E-15	2.6E-12
1x1x8							2	2.6E-15	1.5E-12

Table 4.2: Comparison between different solvers for the Monodomain model. Test case considered: h =1E-2, global grid 17x17x17, random right-hand side, null initial guess and absolute residual tolerance 1E-8. Subdomains subdivision in the three dimensions is showed on the left. For each solver, number of iteration, euclidean residual $||r||_2$ and exact error $||e||_2$ norms are shown.

in equation (4.8), the action of the standard one-level Neumann-Neumann preconditioner M_{NN} on the residual can be represented by:

$$M_{NN}^{-1} = R_{D,\Gamma}^T S^{-1} R_{D,\Gamma} = \sum_{i=1}^{N} R_{D,\Gamma^{(i)}}^T {S^{(i)}}^{-1} R_{D,\Gamma^{(i)}}, \tag{4.18}$$

and thus

$$P_{NN} = M_{NN}^{-1} \widehat{S}_\Gamma.$$

The use of the scaling means that we partition the residual on the interface and then, after solving the local problems, we restore the continuity across the interface averaging the resulting values.

Remark 4.4.1. Test results for the one-level Neumann-Neumann preconditioner applied to the conjugate gradient solution of the Schur complement of the Monodomain model are shown in Table 4.2, together with the results of other one-level preconditioners such as Block Jacobi (BJ) and the Additive Schwarz (AS) applied to the global system, in order to give a comparison among widely used one-level preconditioners. NN preconditioner performs better than the other two preconditioners considered, either in terms of number of iterations or of accuracy. Moreover, since the conductivity coefficients are constants on all the slab and the principal axes of conduction are constant on plane parallel to the $(x, y)-$axis, the *strip-like* decomposition performs better than the other type of decompositions as expected, due to the layer structure of the modeled conduction system (see [88] Section 3.8.6).

4.5 Monodomain theoretical estimates

In the Schwarz framework, bounds for the condition number of the additive operator P_{NN} given in eq. (4.17) are derived by considering the linear system

$$P_{NN}u_\Gamma = M_{NN}^{-1}\hat{g}_\Gamma$$

which is equivalent to system (4.10), and estimating the minimum λ_m and maximum λ_M eigenvalue for the Rayleigh quotient associated to P_{NN} in the inner product generated by the Schur complement, i.e.

$$\lambda_m\mathcal{S}(u_\Gamma, u_\Gamma) \leq \mathcal{S}(P_{NN}u_\Gamma, u_\Gamma) \leq \lambda_M\mathcal{S}(u_\Gamma, u_\Gamma), \quad \forall u_\Gamma \in \widehat{\mathbf{W}}_\Gamma, u_\Gamma \neq 0 \tag{4.19}$$

since P_{NN} is self-adjoint with respect to $\mathcal{S}(\cdot,\cdot)$. We will adopt the abstract Schwarz results only for the minimum eigenvalue. The maximum eigenvalue will be estimated directly as in [140]. The next Lemma states a property known in the Schwarz framework as *stable decomposition* which gives a lower bound for the minimum eigenvalue λ_m.

Lemma 4.5.1. *Assume that there exist a constant C_0 such that every $u_\Gamma \in \widehat{\boldsymbol{W}}_\Gamma$ admits a decomposition*

$$u_\Gamma = \sum_{i=1}^{N} R_\Gamma^{(i)^T} v_\Gamma^{(i)}$$

that satisfies

$$\sum_{i=1}^{N} \tilde{s}_i(v_\Gamma^{(i)}, v_\Gamma^{(i)}) \leq C_0^2\mathcal{S}(u_\Gamma, u_\Gamma) \tag{4.20}$$

with $v_\Gamma^{(i)} \in \boldsymbol{W}_\Gamma^{(i)}$. Then

$$\mathcal{S}(P_{NN}u_\Gamma, u_\Gamma) \geq C_0^{-1}\mathcal{S}(u_\Gamma, u_\Gamma)$$

that is $\lambda_m \geq C_0^{-1}$.

Proof. See Lemma 2.5 in [140]. □

Recalling that

$$P_{NN}u_\Gamma = M_{NN}^{-1}\widehat{S}_\Gamma u_\Gamma = R_{D,\Gamma}^T S^{-1} R_{D,\Gamma}\widehat{S}_\Gamma u_\Gamma$$

we can define $w \in \mathbf{W}_\Gamma$ locally as

$$w_i = {S^{(i)}}^{-1} D^{(i)} R_\Gamma^{(i)} \widehat{S}_\Gamma u_\Gamma. \tag{4.21}$$

Then, it follows easily that

$$E_D w = P_{NN}u_\Gamma \tag{4.22}$$

where E_D is the average operator introduced in eq (4.3). Define also the Schur seminorm

on $\mathbf{W}_\Gamma$ as

$$|w|_S^2 = \sum_{i=1}^{N} |w_i|_{S^{(i)}}^2, \quad \forall w \in \mathbf{W}_\Gamma$$

where

$$|w_i|_{S^{(i)}}^2 = s_i(w_i, w_i).$$

Note that, if $w \in \widehat{\mathbf{W}}_\Gamma$, than by subassembly we will have $|w|_S^2 = \mathcal{S}(w, w)$.

An auxiliary result for the upper bound of P_{NN} is given by the following Lemma. We will write $u \lesssim w$ whenever $u \leq Cw$ with C independent of h, H, δ_t, the conductivity coefficients and the number N of subtructures. In order to simplify the notations and the discussion, we will assume that the conductivity coefficients have no jumps across substructures. The jumping coefficients case will be analyzed later in Remark 4.5.4.

Lemma 4.5.2. *Let $w \in \boldsymbol{W}_\Gamma$ be defined as in formula (4.21). Then for the Monodomain model*

$$|E_D w|_S^2 \lesssim \frac{\sigma_M \delta_t + H^2}{\min\{H^2, \sigma_m \delta_t\}} (1 + \log(H/h))^2 |w|_S^2$$

where σ_M and σ_m are the maximum and minimum eigenvalue of the diffusion tensor given in eq. (2.11) and δ_t is the time step.

Proof. As in [140], we will give bounds for each substructure contribution to $E_D w$: more precisely we will estimate each contribution $|v_i|_{S^{(i)}}^2$ where

$$v_i(x) = (E_D w(x))_i = \sum_{j \in \mathcal{N}_x} I^h(\delta_j(x)^\dagger w_j(x))$$

Using the cut-off functions $\vartheta_\bullet$ ($\bullet = \mathcal{F}, \mathcal{E}, \mathcal{V}$) introduced in Section 4.3, we can split the boundary vector v_i in a sum of face, edge and vertex components:

$$v_i = \sum_{\mathcal{F} \subset \Gamma^{(i)}} I^h(\vartheta_\mathcal{F} v_i) + \sum_{\mathcal{E} \subset \Gamma^{(i)}} I^h(\vartheta_\mathcal{E} v_i) + \sum_{\mathcal{V} \subset \Gamma^{(i)}} I^h(\vartheta_\mathcal{V} v_i).$$

Since each $s_i(\cdot, \cdot)$ is positive definite, it follows that

$$|v_i|_{S^{(i)}}^2 \lesssim \sum_{\mathcal{F} \subset \Gamma^{(i)}} |I^h(\vartheta_\mathcal{F} v_i)|_{S^{(i)}}^2 + \sum_{\mathcal{E} \subset \Gamma^{(i)}} |I^h(\vartheta_\mathcal{E} v_i)|_{S^{(i)}}^2 + \sum_{\mathcal{V} \subset \Gamma^{(i)}} |I^h(\vartheta_\mathcal{V} v_i)|_{S^{(i)}}^2.$$

We will estimate the contribution of faces, edges and vertices separately. The coercivity and continuity for the local Schur bilinear forms of the Monodomain model yields (see Remark 2.4.4):

$$\begin{aligned} s_i(u_\Gamma^{(i)}, u_\Gamma^{(i)}) &\geq \sigma_m |\mathcal{H}_i u_\Gamma^{(i)}|_{H^1(\Omega_i)}^2 + \gamma ||\mathcal{H}_i u_\Gamma^{(i)}||_{L^2(\Omega_i)}^2 \\ s_i(u_\Gamma^{(i)}, u_\Gamma^{(i)}) &\leq \sigma_M |\mathcal{H}_i u_\Gamma^{(i)}|_{H^1(\Omega_i)}^2 + \gamma ||\mathcal{H}_i u_\Gamma^{(i)}||_{L^2(\Omega_i)}^2 \end{aligned} \tag{4.23}$$

where σ_m and σ_M are the minimum and maximum eigenvalue for the diffusion tensor and $\gamma = 1/\delta_t$. For each of the functions $I^h(\vartheta_\bullet v_i)$ the Poincarè-Friedrichs inequality (see

Lemma 4.3.6) holds since these functions vanish on a subset of $\partial\Omega$:

$$||\mathcal{H}_i I^h(\vartheta_\bullet v_i)||^2_{L^2(\Omega_i)} \lesssim H^2 |\mathcal{H}_i I^h(\vartheta_\bullet v_i)|^2_{H^1(\Omega_i)}$$

and thus, for Lemma 4.3.5

$$|I^h(\vartheta_\bullet v_i)|^2_{S^{(i)}} \lesssim (\sigma_M + H^2\gamma)|I^h(\vartheta_\bullet v_i)|^2_{H^{1/2}(\Gamma^{(i)})}. \tag{4.24}$$

Face terms. For the face terms, noting that $\forall x \in \Gamma^{(i)}$

$$\delta_i^\dagger(x) \leq 1 \quad \forall i \in \{1, \dots, N\}$$

we can use Remark 4.3.4 and Lemma 4.3.7 and obtain

$$\begin{aligned}
|I^h(\vartheta_\mathcal{F} v_i)|^2_{H^{1/2}(\Gamma^{(i)})} &\lesssim ||I^h(\vartheta_\mathcal{F} v_i)||^2_{H^{1/2}_{00}(\mathcal{F})} \\
&\lesssim ||I^h(\vartheta_\mathcal{F} w_i)||^2_{H^{1/2}_{00}(\mathcal{F})} + ||I^h(\vartheta_\mathcal{F} w_j)||^2_{H^{1/2}_{00}(\mathcal{F})} \\
&\lesssim (1+\log(H/h))^2 \left(|\mathcal{H}_i w_i|^2_{H^1(\Omega_i)} + H^{-2}||\mathcal{H}_i w_i||^2_{L^2(\Omega_i)} \right) \\
&+ (1+\log(H/h))^2 \left(|\mathcal{H}_j w_j|^2_{H^1(\Omega_j)} + H^{-2}||\mathcal{H}_j w_j||^2_{L^2(\Omega_j)} \right).
\end{aligned}$$

Therefore, if $H^2\gamma \leq \sigma_m$

$$\begin{aligned}
&(1+\log(H/h))^{-2}|I^h(\vartheta_\mathcal{F} v_i)|^2_{S^{(i)}} \\
&\lesssim \frac{\sigma_M + H^2\gamma}{H^2\gamma} \left(H^2\gamma |\mathcal{H}_i w_i|^2_{H^1(\Omega_i)} + \gamma ||\mathcal{H}_i w_i||^2_{L^2(\Omega_i)} \right) \\
&+ \frac{\sigma_M + H^2\gamma}{H^2\gamma} \left(H^2\gamma |\mathcal{H}_j w_j|^2_{H^1(\Omega_j)} + \gamma ||\mathcal{H}_j w_j||^2_{L^2(\Omega_j)} \right)
\end{aligned}$$

and thus

$$|I^h(\vartheta_\mathcal{F} v_i)|^2_{S^{(i)}} \lesssim \frac{\sigma_M + H^2\gamma}{H^2\gamma}(1+\log(H/h))^2 \left(|w_i|^2_{S^{(i)}} + |w_j|^2_{S^{(j)}} \right).$$

Otherwise, if $H^2\gamma \geq \sigma_m$

$$\begin{aligned}
&(1+\log(H/h))^{-2}|I^h(\vartheta_\mathcal{F} v_i)|^2_{S^{(i)}} \\
&\lesssim \frac{\sigma_M + H^2\gamma}{\sigma_m} \left(\sigma_m |\mathcal{H}_i w_i|^2_{H^1(\Omega_i)} + H^{-2}\sigma_m ||\mathcal{H}_i w_i||^2_{L^2(\Omega_i)} \right) \\
&+ \frac{\sigma_M + H^2\gamma}{\sigma_m} \left(\sigma_m |\mathcal{H}_j w_j|^2_{H^1(\Omega_j)} + H^{-2}\sigma_m ||\mathcal{H}_j w_j||^2_{L^2(\Omega_j)} \right)
\end{aligned}$$

and thus

$$|I^h(\vartheta_\mathcal{F} v_i)|^2_{S^{(i)}} \lesssim \frac{\sigma_M + H^2\gamma}{\sigma_m}(1+\log(H/h))^2 \left(|w_i|^2_{S^{(i)}} + |w_j|^2_{S^{(j)}} \right)$$

Therefore, for the face terms, we will have

$$|I^h(\vartheta_{\mathcal{F}} v_i)|^2_{S^{(i)}} \lesssim \frac{\sigma_M + H^2\gamma}{\min\{H^2\gamma, \sigma_m\}}(1+\log(H/h))^2 \left(|w_i|^2_{S^{(i)}} + |w_j|^2_{S^{(j)}}\right) \tag{4.25}$$

Edge terms. For the edges, we can proceed as in [140] using Lemmas 4.3.9 and a triangle inequality to bound

$$|I^h(\vartheta_{\mathcal{E}} v_i)|^2_{H^{1/2}(\Gamma^{(i)})} \lesssim \sum_{k\in\mathcal{K}_{\mathcal{E}}} ||w_k||^2_{L^2(\mathcal{E})}$$

where $\mathcal{K}_{\mathcal{E}}$ is the set of subdomain indices sharing edge $\mathcal{E}$. Now, using eq. (4.24), Lemma 4.3.8 and the same arguments on the interaction between $H^2\gamma$ and σ_m as before we find

$$|I^h(\vartheta_{\mathcal{E}} v_i)|^2_{S^{(i)}} \lesssim \frac{\sigma_M + H^2\gamma}{\min\{H^2\gamma, \sigma_m\}}(1+\log(H/h)) \sum_{k\in\mathcal{K}_{\mathcal{E}}} |w_k|^2_{S^{(i)}} \tag{4.26}$$

Vertex terms. Similarly, using Lemma 4.3.10 we bound also the vertex components as

$$|I^h(\vartheta_{\mathcal{V}} v_i)|^2_{S^{(i)}} \lesssim \frac{\sigma_M + H^2\gamma}{\min\{H^2\gamma, \sigma_m\}} \sum_{k\in\mathcal{K}_{\mathcal{V}}} |w_k|^2_{S^{(i)}} \tag{4.27}$$

where $\mathcal{K}_{\mathcal{V}}$ is the set of subdomain indices sharing vertex $\mathcal{V}$.

Therefore the thesis follows using estimates (4.25), (4.26) and (4.27) and summing over faces, edges and vertices of Ω_i and then over the substructures noting that

$$\frac{\sigma_M + H^2\gamma}{H^2\gamma} = \frac{\sigma_M\delta_t + H^2}{H^2}$$

and

$$\frac{\sigma_M + H^2\gamma}{\sigma_m} = \frac{\sigma_M\delta_t + H^2}{\sigma_m\delta_t}$$

□

We are then ready to prove the main theorem for the one-level Neumann-Neumann preconditioner applied to the Schur complement of the Monodomain model.

Theorem 4.5.3. *The condition number of the preconditioned Schur complement system of the Monodomain model satisfies:*

$$\kappa_2(M^{-1}_{NN}\widehat{S}_\Gamma) \lesssim \frac{\sigma_M\delta_t + H^2}{\min\{H^2, \sigma_m\delta_t\}}(1+\log(H/h))^2 \tag{4.28}$$

Proof. **Lower Bound.** A partition of unity NN preconditioner has the advantage that a stable decomposition is immediately available with $C_0 = 1$. In fact, choosing

$$v^{(i)}_\Gamma = \delta^\dagger_i R^{(i)}_\Gamma u_\Gamma$$

in Lemma 4.5.1, we will have

$$u_\Gamma = \sum_{i=1}^N {R^{(i)}_\Gamma}^T v^{(i)}_\Gamma$$

and by subassembly

$$\sum_{i=1}^{N} \tilde{s}_i(v_\Gamma^{(i)}, v_\Gamma^{(i)}) = \sum_{i=1}^{N} s_i(R_\Gamma^{(i)} u_\Gamma, R_\Gamma^{(i)} u_\Gamma) = \mathcal{S}(u_\Gamma, u_\Gamma).$$

This implies that λ_m in (4.19) is exactly one.

Upper Bound. Using the definitions of w given in eq. (4.21) and of the operators $\widetilde{P}_i$ given in eq. (4.15) we have

$$\begin{aligned} |w|_S^2 &= \sum_{i=1}^{N} s_i(w_i, w_i) = \sum_{i=1}^{N} s_i(D^{(i)^{-1}} \widetilde{P}_i w_i, D^{(i)^{-1}} \widetilde{P}_i w_i) \\ &= \sum_{i=1}^{N} \mathcal{S}(u_\Gamma, R_\Gamma^{(i)^T} \widetilde{P}_i u_\Gamma) = \mathcal{S}(P_{NN} u_\Gamma, u_\Gamma). \end{aligned} \tag{4.29}$$

Therefore using the latter result, eq. (4.22) and Lemma 4.5.2 we have

$$\begin{aligned} \mathcal{S}(P_{NN} u_\Gamma, P_{NN} u_\Gamma) = |P_{NN} u_\Gamma|_S^2 &= |E_D w|_S^2 \\ &\lesssim \frac{\sigma_M \delta_t + H^2}{\min\{H^2, \sigma_m \delta_t\}} (1 + \log(H/h))^2 |w|_S^2 \\ &= \frac{\sigma_M \delta_t + H^2}{\min\{H^2, \sigma_m \delta_t\}} (1 + \log(H/h))^2 \mathcal{S}(P_{NN} u_\Gamma, u_\Gamma) \end{aligned}$$

and thus, since for the Cauchy-Schwarz inequality holds that

$$\mathcal{S}(P_{NN} u_\Gamma, u_\Gamma) \leq \mathcal{S}(P_{NN} u_\Gamma, P_{NN} u_\Gamma)^{1/2} \mathcal{S}(u_\Gamma, u_\Gamma)^{1/2}$$

we will have, canceling a common term and squaring,

$$\mathcal{S}(P_{NN} u_\Gamma, u_\Gamma) \lesssim \frac{\sigma_M \delta_t + H^2}{\min\{H^2, \sigma_m \delta_t\}} (1 + \log(H/h))^2 \mathcal{S}(u_\Gamma, u_\Gamma)$$

and thus the maximum eigenvalue of the Rayleigh quotient (4.19) can be bounded by

$$\lambda_M \lesssim \frac{\sigma_M \delta_t + H^2}{\min\{H^2, \sigma_m \delta_t\}} (1 + \log(H/h))^2.$$

□

Remark 4.5.4. In Lemma 4.5.2, we assumed that the conductivity coefficients were constants among the substructures to simplify the notations. Now, we will analyze the case of discontinuous conductivity coefficients with jumps aligned with the interface. Before we didn't use any particular choice of the partition of unity coefficients but we only used the coefficients were all less than one; now we will use as partition of unity

$$\delta_i^\dagger(x) = \frac{\sigma_M^{(i)}}{\sum_{j \in \mathcal{N}_x} \sigma_M^{(j)}}$$

where $\sigma_M^{(i)}$ is the maximum eigenvalue of the diffusion tensor of the i-th substructure. We did not explore the possibility of using representative values which includes terms with δ_t since the time step is the same for all substructures. For the choice made for partition of unity, the following property holds (see [140])

$$\sigma_M^{(i)}\delta_j^{\dagger^2} \leq \min\{\sigma_M^{(i)}, \sigma_M^{(j)}\} \quad \forall i,j \in \{1,\dots,N\}. \tag{4.30}$$

The coercivity and continuity for the local Schur bilinear forms now reads

$$\begin{aligned} s_i(u_\Gamma^{(i)}, u_\Gamma^{(i)}) &\geq \sigma_m^{(i)}|\mathcal{H}_i u_\Gamma^{(i)}|^2_{H^1(\Omega_i)} + \gamma||\mathcal{H}_i u_\Gamma^{(i)}||^2_{L^2(\Omega_i)} \\ s_i(u_\Gamma^{(i)}, u_\Gamma^{(i)}) &\leq \sigma_M^{(i)}|\mathcal{H}_i u_\Gamma^{(i)}|^2_{H^1(\Omega_i)} + \gamma||\mathcal{H}_i u_\Gamma^{(i)}||^2_{L^2(\Omega_i)} \end{aligned}$$

where $\sigma_m^{(i)}$ is the minimum eigenvalue for the diffusion tensor of the i-th substructure and $\gamma = 1/\delta_t$. We proceed similarly to Lemma 4.5.2 using the Poincarè-Friedrichs inequality and the trace theorem 4.3.5 bounding from above the local Schur seminorm

$$|I^h(\vartheta_\bullet v_i)|^2_{S^{(i)}} \lesssim (\sigma_M^{(i)} + H^2\gamma)|I^h(\vartheta_\bullet v_i)|^2_{H^{1/2}(\Gamma^{(i)})} = \sigma_M^{(i)}(1 + \frac{H^2\gamma}{\sigma_M^{(i)}})|I^h(\vartheta_\bullet v_i)|^2_{H^{1/2}(\Gamma^{(i)})}.$$

We will only present the algebra related to the face terms: edges and vertices can be treated similarly. For the face terms we proceed as before and use in addition eq. (4.30)

$$\begin{aligned} \sigma_M^{(i)}|I^h(\vartheta_\mathcal{F} v_i)|^2_{H^{1/2}(\Gamma^{(i)})} &\lesssim \sigma_M^{(i)}||I^h(\vartheta_\mathcal{F} v_i)||^2_{H^{1/2}_{00}(\mathcal{F})} \\ &\lesssim \sigma_M^{(i)}\delta_i^{\dagger^2}||I^h(\vartheta_\mathcal{F} w_i)||^2_{H^{1/2}_{00}(\mathcal{F})} + \sigma_M^{(i)}\delta_j^{\dagger^2}||I^h(\vartheta_\mathcal{F} w_j)||^2_{H^{1/2}_{00}(\mathcal{F})} \\ &\lesssim \sigma_M^{(i)}(1+\log(H/h))^2\left(|\mathcal{H}_i w_i|^2_{H^1(\Omega_i)} + H^{-2}||\mathcal{H}_i w_i||^2_{L^2(\Omega_i)}\right) \\ &+ \sigma_M^{(j)}(1+\log(H/h))^2\left(|\mathcal{H}_j w_j|^2_{H^1(\Omega_j)} + H^{-2}||\mathcal{H}_j w_j||^2_{L^2(\Omega_j)}\right). \end{aligned}$$

Now consider only the i-th term of the previous summation disregarding the $(1+\log(H/h))^2$ factor. If $H^2\gamma \leq \sigma_m^{(i)}$

$$\begin{aligned} &\sigma_M^{(i)}\left(|\mathcal{H}_i w_i|^2_{H^1(\Omega_i)} + H^{-2}||\mathcal{H}_i w_i||^2_{L^2(\Omega_i)}\right) \\ &\lesssim \frac{\sigma_M^{(i)}}{H^2\gamma}\left(H^2\gamma|\mathcal{H}_i w_i|^2_{H^1(\Omega_i)} + \gamma||\mathcal{H}_i w_i||^2_{L^2(\Omega_i)}\right) \\ &\lesssim \frac{\sigma_M^{(i)}}{H^2\gamma}\left(\sigma_m^{(i)}|\mathcal{H}_i w_i|^2_{H^1(\Omega_i)} + \gamma||\mathcal{H}_i w_i||^2_{L^2(\Omega_i)}\right) \\ &= \frac{\sigma_M^{(i)}}{H^2\gamma}|w_i|^2_{S^{(i)}} \end{aligned}$$

Otherwise, if $H^2\gamma \geq \sigma_m^{(i)}$

$$\begin{aligned}
&\sigma_M^{(i)} \left(|\mathcal{H}_i w_i|^2_{H^1(\Omega_i)} + H^{-2}||\mathcal{H}_i w_i||^2_{L^2(\Omega_i)} \right) \\
&\lesssim \frac{\sigma_M^{(i)}}{\sigma_m^{(i)}} \left(\sigma_m^{(i)} |\mathcal{H}_i w_i|^2_{H^1(\Omega_i)} + H^{-2}\sigma_m^{(i)}||\mathcal{H}_i w_i||^2_{L^2(\Omega_i)} \right) \\
&\lesssim \frac{\sigma_M^{(i)}}{\sigma_m^{(i)}} \left(\sigma_m^{(i)} |\mathcal{H}_i w_i|^2_{H^1(\Omega_i)} + \gamma||\mathcal{H}_i w_i||^2_{L^2(\Omega_i)} \right) \\
&= \frac{\sigma_M^{(i)}}{\sigma_m^{(i)}} |w_i|^2_{S^{(i)}}
\end{aligned}$$

For the j-th term we can do the same and, supposing that $\sigma_m^{(i)} \leq \sigma_m^{(j)}$, and denoting by

$$\begin{aligned}
M_1 &= \max_{\bullet=i,j} \{ \frac{\sigma_M^{(\bullet)}}{\sigma_m^{(\bullet)}} + \frac{H^2\gamma}{\sigma_m^{(\bullet)}} \} \\
M_2 &= \frac{\max_{\bullet=i,j}\{\sigma_M^{(\bullet)}\}}{H^2\gamma} \\
M_3 &= \max\{M_1, M_2\}
\end{aligned}$$

we obtain

$$|I^h(\vartheta_{\mathcal{F}} v_i)|^2_{S^{(i)}} \lesssim \begin{cases} CM_1 \left(|w_i|^2_{S^{(i)}} + |w_j|^2_{S^{(j)}} \right) & \text{if } \sigma_m^{(j)} \leq H^2\gamma \\ CM_3 \left(|w_i|^2_{S^{(i)}} + |w_j|^2_{S^{(j)}} \right) & \text{if } \sigma_m^{(i)} \leq H^2\gamma \leq \sigma_m^{(j)} \\ CM_2 \left(|w_i|^2_{S^{(i)}} + |w_j|^2_{S^{(j)}} \right) & \text{if } \sigma_m^{(i)} \geq H^2\gamma \end{cases}$$

where $C = (1+\log(H/h))^2$. Since for edges and vertices we will obtain the same qualitative estimates, we conclude that for the Monodomain model with discontinuous coefficients it will hold

$$|E_D w|^2_S \lesssim \max\{M_1, M_2\}(1+\log(H/h))^2 |w|^2_S.$$

Remark 4.5.5. We note that, for very small δ_t, the Monodomain operator is dominated by the L^2 term, and thus no preconditioning is needed at all. The estimates developed in this Section have a leading term of $H^2/(\sigma_m \delta_t)$, which can get very large for small δ_t, coming from the inequality (4.24) which is needed to work with trace seminorms.

4.6 A Balancing Neumann-Neumann preconditioner for the Bidomain model

In this section we will construct Balancing Neumann-Neumann preconditioners for the Bidomain model. Recall (see Section 2.4) that the local bilinear forms $a_j(\cdot,\cdot)$ are given by

$$a_j(u,v) = \int_{\Omega_j} D_i^{(j)} \nabla u_i \cdot \nabla v_i + \int_{\Omega_j} D_e^{(j)} \nabla u_e \cdot \nabla v_e + \gamma \int_{\Omega_j} (u_i - u_e)(v_i - v_e).$$

where $\gamma = 1/\delta_t$ and $D_{i,e}^{(j)}$ are the anisotropic diffusion tensors (see eq. (2.1)) of the jth substructure with associated conductivity coefficients $\sigma_l^{i,e^{(j)}}, \sigma_t^{i,e^{(j)}}, \sigma_n^{i,e^{(j)}}$. In case of constant conductivity coefficients, the local bilinear forms define by subassembly the assembled elliptic form $a_{bido}(\cdot,\cdot)$ given in formula (2.25): since the resulting Schur symmetric elliptic bilinear form on $\widehat{\mathbf{W}}_\Gamma$ is obtained restricting the bilinear form $a_{bido}(\cdot,\cdot)$ on the subspace of piecewise discrete harmonic functions as in eq. (4.13), from the definition of piecewise discrete harmonic extensions and Remark 4.2.7, we must choose the finite element space as

$$\widehat{\mathbf{W}} = V_h(\Omega) \times V_h(\Omega)/\mathbb{R}.$$

in order to make $\mathcal{S}(\cdot,\cdot)$ an inner product on $\widehat{\mathbf{W}}_\Gamma$. While the one-level Neumann-Neumann preconditioner P_{NN} has the structure of an additive Schwarz preconditioner, a Balancing Neumann-Neumann (BNN) preconditioner can be viewed as an hybrid Schwarz preconditioner for $\widehat{S}_\Gamma$. It is specified by the same additive decomposition of the space $\widehat{\mathbf{W}}_\Gamma$ into the subspaces defined for the Neumann-Neumann preconditioner combined, in a multiplicative way, to a *coarse space* $\mathbf{W}_\Gamma^{(0)}$ (see e.g. [130]). The latter plays a special role, providing a mechanism of global transport of information between the subdomains and assuring the well posedness of Neumann-Neumann additive Schwarz operator P_{NN}, providing compatible right hand sides in the case of singular local problems; moreover, a suitable choice of coarse space will provide quasi-optimal bounds for the condition number of the preconditioned Bidomain operator as a function of the subtructures' diameter H.

For the Bidomain model each local projection-like operator $\widetilde{P}_j u_\Gamma$ as in eq. (4.15) can be defined only for those $u_\Gamma \in \widehat{\mathbf{W}}_\Gamma$ for which

$$\mathcal{S}(u_\Gamma, R_{D,\Gamma}^{(j)^T} \mathbf{1}_{\Gamma^{(j)}}) = 0$$

since the local Schur systems are singular with a null space spanned by the constant vectors (see Remark 4.2.7). A right hand side for the local problems (4.15) satisfying these compatibility conditions is said to be *balanced*. Then a solution will exist for each local problem, though it will not be unique, as any scalar multiple of the null space may be added to. The non-uniqueness of the local solutions can be formalized using the pseudo-inverses $S^{(j)^\dagger}$ of $S^{(j)}$ (see e.g. [43]) and the action of the local operators can be written as

$$P_j = R_{D,\Gamma^{(j)}}^T S^{(j)^\dagger} R_{D,\Gamma^{(j)}} \widehat{S}_\Gamma.$$

As pointed out in [140], the choice of this local solution will not affect the algorithm at all; it will be only required for the analysis. See Lemmas 4.7.3 and 4.7.4 for additional details.

In order to assure balancing, we must include in the coarse space the local constant vectors scaled with the partition of unity; thus a minimal coarse space for the Bidomain model is

$$\mathbf{W}_{\Gamma,n}^{(0)} = \text{span}\{R_{D,\Gamma}^{(j)^T} \mathbf{1}_{\Gamma^{(j)}} \mid j = 1, \ldots, N\}. \tag{4.31}$$

In the following, we will refer to the space $\mathbf{W}_{\Gamma,n}^{(0)}$ as *natural* coarse space. A natural coarse

function $u^{(0)} \in \mathbf{W}^{(0)}_{\Gamma,n}$ will thus be identified by a vector $\alpha = (\alpha_1, \ldots, \alpha_N)$ having one component for each substructure and we will write

$$u^{(0)} = \sum_{j=1}^{N} \alpha_j R^{(j)^T}_{D,\Gamma} \mathbf{1}_{\Gamma^{(j)}} = \sum_{j=1}^{N} R^{(j)^T}_{D,\Gamma} \alpha_j \mathbf{1}_{\Gamma^{(j)}}.$$

In order to obtain quasi-optimal bounds for the condition number as a function of the substructures diameter H (see Lemma 4.7.4 for details) we will also consider an *enriched* coarse space given by

$$\mathbf{W}^{(0)}_{\Gamma,e} = \text{span}\{R^{(j)^T}_{D,\Gamma} \mathbf{1}_{\Gamma^{(j)}}, R^{(j)^T}_{D,\Gamma} \mathbf{1}^*_{\Gamma^{(j)}} \mid j = 1, \ldots, N\}, \tag{4.32}$$

where $\mathbf{1}^*_{\Gamma^{(j)}} \in \mathbf{W}^{(j)}_{\Gamma}$ is the vector which equals one for the intracellular component and minus one for the extracellular component. An enriched coarse function $u^{(0)} \in \mathbf{W}^{(0)}_{\Gamma,e}$ will be identified by a vector $\alpha = (\alpha_{1,1}, \alpha_{1,2}, \ldots, \alpha_{N,1}, \alpha_{N,2})$ with two components for each substructure (one for each vector defining the coarse basis functions) and we will write

$$u^{(0)} = \sum_{j=1}^{N} R^{(j)^T}_{D,\Gamma} \left(\alpha_{j,1} \mathbf{1}_{\Gamma^{(j)}} + \alpha_{j,2} \mathbf{1}^*_{\Gamma^{(j)}}\right).$$

Given a coarse space, either the natural $\mathbf{W}^{(0)}_{\Gamma,n}$ or the enriched $\mathbf{W}^{(0)}_{\Gamma,e}$ coarse space, the Schwarz framework than construct the coarse bilinear form by projecting the Schur bilinear form on the coarse basis functions

$$s_0(\alpha, \beta) = \mathcal{S}(R^{(0)^T}_{\Gamma} \alpha, R^{(0)^T}_{\Gamma} \beta)$$

where α and β are coarse vectors, or in matrix form as

$$S^{(0)} = R^{(0)}_{\Gamma} \widehat{S}_{\Gamma} R^{(0)^T}_{\Gamma} \tag{4.33}$$

where $R^{(0)^T}_{\Gamma}$ is the matrix formed columnwise by the coarse basis functions. Note that we must employ an exact solver for matrix (4.33) in order to assure balancing and make the resulting coarse operator a projection.

Remark 4.6.1. Using the fundamental property of the partition of unity given in eq. (4.2), we can easily show that the Bidomain coarse problem will be singular. Consider for simplicity the natural coarse space (4.31) and the coarse constant vector $\mathbf{1}$, it will hold

$$S^{(0)} \mathbf{1} = R^{(0)}_{\Gamma} \widehat{S}_{\Gamma} R^{(0)^T}_{\Gamma} \mathbf{1} = R^{(0)}_{\Gamma} \widehat{S}_{\Gamma} \mathbf{1}_{\Gamma} = R^{(0)}_{\Gamma} \mathbf{0}_{\Gamma} = 0.$$

The same will hold also for the enriched coarse space (4.32), which will have a null space spanned by the coarse vector

$$(1, 0, \ldots, 1, 0)^T.$$

Remark 4.6.2. The choice of the partition of unity can enlarge the null space of the resulting coarse problem. Take for example the usual counting function as partition of unity for both the intra- and extracellular components, i.e. formula (4.1) with $a_j^{i,e}(x) = 1 \; \forall \, j = 1, \ldots, N$ and $\forall x \in \Gamma^{(j)}$ and, for simplicity, the natural coarse space (4.31). Then the coarse vector with a checkerboard pattern of +1 and -1 values will generate the null interface vector, and thus it will span the null space of the coarse problem. In order to guarantee that the null space of the coarse problem will be generated only by the null space of the Schur system and, therefore, that the coarse problem will be solvable, we must choose a representative value for node x which will yield a different coefficient of partition of unity at least on the vertices of the substructures. A possible choice for the representative values of the intra- and extra-cellular components is

$$\begin{aligned} a_j^i(x) &= \int_{\Omega_j} D_i^{(j)} \nabla \phi_x \cdot \nabla \phi_x \\ a_j^e(x) &= \int_{\Omega_j} D_e^{(j)} \nabla \phi_x \cdot \nabla \phi_x \end{aligned} \tag{4.34}$$

where ϕ_x is the finite element function which is zero elsewhere unless at x where it takes on the value 1.

Remark 4.6.3. For the definition of the representative values $a_j^{i,e}(x)$ given in eq. (4.34), it follows easily that

$$\sigma_M^{i,e^{(j)}} \, \delta_k^{i,e^\dagger}(x)^2 \lesssim \min\{\sigma_M^{i,e^{(j)}}, \sigma_M^{i,e^{(k)}}\} \; \forall x \in \Gamma^{(j)}, \tag{4.35}$$

where $\sigma_M^{i,e^{(j)}}$ are the maximum eigenvalues of the tensors $D_{i,e}^{(j)}$. In fact, it is possible to show that the representative values given in formula (4.34) can be estimated for linear finite elements as

$$c\sigma_M^{i,e^{(j)}} \, h \leq a_j^{i,e}(x) \leq C\sigma_M^{i,e^{(j)}} \, h \tag{4.36}$$

with positive constants c and C independent from the discretization step h and the conductivity coefficients of the tensors. In details, since $\forall \, x \in \Omega_j$ we can split the gradient

$$\nabla \phi_x = \beta_l \mathbf{a}_l(x) + \beta_t \mathbf{a}_t(x) + \beta_n \mathbf{a}_n(x)$$

using the orthonormal triplet of the fibers $\{\mathbf{a}_l(x), \mathbf{a}_t(x), \mathbf{a}_n(x)\}$ (see Sections 2.1.1 and 2.4 for additional details), due to the definition of the conductivity tensors given in eq. (2.1), we will have

$$D_{i,e}^{(j)} \nabla \phi_x \cdot \nabla \phi_x = \sigma_l^{i,e^{(j)}} \beta_l^2 + \sigma_t^{i,e^{(j)}} \beta_t^2 + \sigma_n^{i,e^{(j)}} \beta_n^2.$$

Thus estimate (4.36) follows, since

$$\sigma_M^{i,e^{(j)}} = \max_{\bullet = l,t,n} \sigma_\bullet^{i,e^{(j)}}$$

and there exist positive constants c and C independent from h such that

$$ch^{-2} \leq \beta_{l,t,n}^2 \leq Ch^{-2}.$$

Then, using (4.36) we obtain

$$\sigma_M^{i,e^{(j)}} \delta_k^{i,e^\dagger}(x)^2 \leq \sigma_M^{i,e^{(j)}} \left(\frac{C\sigma_M^{i,e^{(k)}} h}{\sum_{l \in \mathcal{N}_x} c\sigma_M^{i,e^{(l)}} h} \right)^2 \lesssim \sigma_M^{i,e^{(j)}} \left(\frac{\sigma_M^{i,e^{(k)}}}{\sum_{l \in \mathcal{N}_x} \sigma_M^{i,e^{(l)}}} \right)^2$$

and thus eq. (4.35) follows using formula (4.30) for each component.

The projection operator P_0 can be written as

$$P_0 = {R_\Gamma^{(0)}}^T {S^{(0)}}^\dagger R_\Gamma^{(0)} \widehat{S}_\Gamma \tag{4.37}$$

where we employed a pseudo-inverse to take into account the singularity of the coarse problem. The following properties will hold for P_0, either with natural or enriched coarse space. We provide their proofs since in domain decomposition literature (see e.g. [140]) they have been proved for nonsingular coarse matrices.

Lemma 4.6.4. *The operator P_0 is the $\widehat{S}_\Gamma$-orthogonal projection on the space $\mathbf{W}_\Gamma^{(0)}$ and it holds:*

$$P_0^2 = P_0$$
$$\mathcal{S}(P_0 u_\Gamma, v_\Gamma) = \mathcal{S}(u_\Gamma, P_0 v_\Gamma)$$
$$\mathcal{S}(P_0 u_\Gamma, v_\Gamma) = \mathcal{S}(P_0 u_\Gamma, P_0 v_\Gamma)$$

Proof. For the first equality, a fundamental property of pseudoinverses (see e.g. [43]) states

$${S^{(0)}}^\dagger S^{(0)} {S^{(0)}}^\dagger = {S^{(0)}}^\dagger$$

thus for the definition of $S^{(0)}$ given in eq. (4.33)

$$P_0^2 = {R_\Gamma^{(0)}}^T {S^{(0)}}^\dagger R_\Gamma^{(0)} \widehat{S}_\Gamma {R_\Gamma^{(0)}}^T {S^{(0)}}^\dagger R_\Gamma^{(0)} \widehat{S}_\Gamma = {R_\Gamma^{(0)}}^T {S^{(0)}}^\dagger S^{(0)} {S^{(0)}}^\dagger R_\Gamma^{(0)} \widehat{S}_\Gamma = P_0.$$

For the second equality

$$\mathcal{S}(P_0 u_\Gamma, v_\Gamma) = u_\Gamma^T P_0^T \widehat{S}_\Gamma v_\Gamma = u_\Gamma^T \widehat{S}_\Gamma^T {R_\Gamma^{(0)}}^T {S^{(0)^\dagger}}^T R_\Gamma^{(0)} \widehat{S}_\Gamma v_\Gamma.$$

Since pseudoinversion commutes with the transposition (see e.g. [133]) and the matrix $\widehat{S}_\Gamma$ is symmetric, we deduce that

$${S^{(0)}}^\dagger = {S^{(0)^\dagger}}^T$$

and thus

$$\mathcal{S}(P_0 u_\Gamma, v_\Gamma) = u_\Gamma^T \widehat{S}_\Gamma {R_\Gamma^{(0)}}^T {S^{(0)}}^\dagger R_\Gamma^{(0)} \widehat{S}_\Gamma v_\Gamma = \mathcal{S}(u_\Gamma, P_0 v_\Gamma).$$

Regarding to the third equality, using the definition of $S^{(0)}$ and the fundamental property of the pseudoinverses we obtain

$$\begin{aligned}\mathcal{S}(P_0 u_\Gamma, P_0 v_\Gamma) &= u_\Gamma^T P_0^T \widehat{S}_\Gamma P_0 v_\Gamma \\ &= u_\Gamma^T \widehat{S}_\Gamma^T R_\Gamma^{(0)^T} S^{(0)^\dagger} R_\Gamma^{(0)} \widehat{S}_\Gamma R_\Gamma^{(0)^T} S^{(0)^\dagger} R_\Gamma^{(0)} \widehat{S}_\Gamma v_\Gamma \\ &= u_\Gamma^T \widehat{S}_\Gamma^T R_\Gamma^{(0)^T} S^{(0)^\dagger} S^{(0)} S^{(0)^\dagger} R_\Gamma^{(0)} \widehat{S}_\Gamma v_\Gamma \\ &= u_\Gamma^T \widehat{S}_\Gamma^T R_\Gamma^{(0)^T} S^{(0)^\dagger} R_\Gamma^{(0)} \widehat{S}_\Gamma v_\Gamma \\ &= \mathcal{S}(P_0 u_\Gamma, v_\Gamma).\end{aligned}$$

□

The *Balancing Neumann-Neumann* abstract hybrid Schwarz operator P_{BNN} can then be stated as (see [140] and [88])

$$P_{BNN} = P_0 + (I - P_0) P_{NN} (I - P_0). \tag{4.38}$$

or equivalently

$$P_{BNN} = M_{BNN}^{-1} \widehat{S}_\Gamma.$$

where M_{BNN}^{-1} is the preconditioner.

Remark 4.6.5. Because of the definition of the projection operator P_0 given in eq. (4.37), at each application of the BNN preconditioner the right hand side of the coarse problem will result compatible to the singular coarse matrix since for any vector $v_\Gamma \in \text{range}(\widehat{S}_\Gamma)$ it will hold

$$\mathbf{1}_\Gamma^T v_\Gamma = 0.$$

Remark 4.6.6. Due to the second application of $(I - P_0)$ in eq. (4.38), we can add any linear combination of the coarse basis functions to the output of the additive operator P_{NN} without affecting the Balancing Neumann-Neumann operator P_{BNN}, which can thus be equivalently expressed with the enriched coarse space as

$$P_{BNN}^* = P_0 + (I - P_0) P_{NN}^* (I - P_0), \tag{4.39}$$

with

$$P_{NN}^* v_\Gamma = P_{NN} v_\Gamma + \sum_{j=1}^{N} R_{D,\Gamma}^{(j)^T} \left(\alpha_{j,1} \mathbf{1}_{\Gamma^{(j)}} + \alpha_{j,2} \mathbf{1}_{\Gamma^{(j)}}^* \right).$$

For the theoretical analysis of the next Section, we will need only $\alpha_{j,2} \neq 0$ and we will thus write

$$P_{NN}^* v_\Gamma = P_{NN} v_\Gamma + \sum_{j=1}^{N} R_{D,\Gamma}^{(j)^T} \alpha_j \mathbf{1}_{\Gamma^{(j)}}^*. \tag{4.40}$$

subd	CG Schur				PCG-BNN Schur			
	it	$\|\|r\|\|_2$	$\|\|e\|\|_2$	$\|\|e\|\|_\infty$	it	$\|\|r\|\|_2$	$\|\|e\|\|_2$	$\|\|e\|\|_\infty$
2x2x2	73	9.5E-9	1.1E-3	5.1E-5	19	6.9E-14	4.2E-9	3.5E-10
8x1x1	111	8.1E-9	1.7E-3	8.7E-5	34	7.7E-14	4.3E-9	1.7E-10
1x8x1	112	9.8E-9	2.1E-3	7.5E-5	36	4.1E-14	4.5E-9	2.1E-10
1x1x8	101	8.8E-9	2.7E-3	1.1E-4	7	1.7E-14	1.2E-9	3.9E-11

Table 4.3: Comparison between different solvers for the Schur complement of the Bidomain model. Test case considered: h =1E-2, global grid 17x17x17, random right-hand side, null initial guess and absolute residual tolerance 1E-8. Subdomains subdivision in the three dimensions is showed on the left. For each solver, number of iteration, euclidean residual $||r||_2$ and exact error $||e||_2$ norms, infinity norm of the exact error $||e||_\infty$ are shown.

Remark 4.6.7. First test results for the BNN preconditioner with the natural coarse space applied to the Schur complement of the Bidomain model are shown in Table 4.3, together with the results of the unpreconditioned Schur complement. As for the NN preconditioner, the *strip-like* decomposition performs better than the other type of decompositions as expected, due to the layer structure of the modeled conduction system (see [88] Section 3.8.6).

4.7 Bidomain theoretical estimates

As for the additive P_{NN} operator introduced for the Monodomain model we will consider the solution of the equivalent preconditioned systems

$$P_{BNN} u_\Gamma = M_{BNN}^{-1} \widehat{g}_\Gamma$$

for the natural coarse space (4.31) and

$$P_{BNN}^* u_\Gamma = M_{BNN}^{*^{-1}} \widehat{g}_\Gamma$$

for the enriched coarse space (4.32); since both P_{BNN} and P_{BNN}^* are self-adjoint in the inner product $\mathcal{S}(\cdot,\cdot)$ generated by $\widehat{S}_\Gamma$ on $\widehat{\mathbf{W}}_\Gamma$, their condition numbers κ_2 and κ_2^* can be estimated as previously as the ratio of the largest and smallest eigenvalues of their generalized Rayleigh quotient, i.e. for the natural coarse space

$$\lambda_m \mathcal{S}(u_\Gamma, u_\Gamma) \leq \mathcal{S}(P_{BNN} u_\Gamma, u_\Gamma) \leq \lambda_M \mathcal{S}(u_\Gamma, u_\Gamma), \quad \forall u_\Gamma \in \widehat{\mathbf{W}}_\Gamma, u_\Gamma \neq 0_{\widehat{\mathbf{W}}_\Gamma}, \qquad (4.41)$$

and for the enriched coarse space

$$\lambda_m^* \mathcal{S}(u_\Gamma, u_\Gamma) \leq \mathcal{S}(P_{BNN}^* u_\Gamma, u_\Gamma) \leq \lambda_M^* \mathcal{S}(u_\Gamma, u_\Gamma), \quad \forall u_\Gamma \in \widehat{\mathbf{W}}_\Gamma, u_\Gamma \neq 0_{\widehat{\mathbf{W}}_\Gamma}. \tag{4.42}$$

We will need some auxiliary results; the next Lemma (borrowed from [88]) states that we can estimate the lower and upper bounds of the operator P_{NN} (4.17) on the subspace range$(I - P_0)$ in order to give bounds for the operator P_{BNN}.

Lemma 4.7.1. *Suppose that exists positive real numbers c_m and c_M such that*

$$c_m \leq \frac{\mathcal{S}(P_{NN}(I - P_0)u_\Gamma, (I - P_0)u_\Gamma)}{\mathcal{S}((I - P_0)u_\Gamma, (I - P_0)u_\Gamma)} \leq c_M$$

$\forall\, u_\Gamma \in \widehat{\boldsymbol{W}}_\Gamma$. *Then $\lambda_m \geq \min\{c_m, 1\}$ and $\lambda_M \leq \max\{c_M, 1\}$.*

Proof. Using the definition of P_{BNN} given in eq (4.38) and the properties of P_0 given in Lemma 4.6.4, we have

$$\begin{aligned}
\mathcal{S}(P_{BNN}u_\Gamma, u_\Gamma) &= \mathcal{S}(P_0 + (I - P_0)P_{NN}(I - P_0)u_\Gamma, u_\Gamma) \\
&= \mathcal{S}(P_0 u_\Gamma, u_\Gamma) + \mathcal{S}((I - P_0)P_{NN}(I - P_0)u_\Gamma, u_\Gamma) \\
&= \mathcal{S}(P_0 u_\Gamma, P_0 u_\Gamma) + \mathcal{S}(P_{NN}(I - P_0)u_\Gamma, (I - P_0)u_\Gamma)
\end{aligned}$$

and

$$\mathcal{S}(u_\Gamma, u_\Gamma) = \mathcal{S}(P_0 u_\Gamma, P_0 u_\Gamma) + \mathcal{S}((I - P_0)u_\Gamma, (I - P_0)u_\Gamma).$$

Thus from the hypothesis it follows

$$\min\{c_m, 1\} \leq \frac{\mathcal{S}(P_0 u_\Gamma, P_0 u_\Gamma) + \mathcal{S}(P_{NN}(I - P_0)u_\Gamma, (I - P_0)u_\Gamma)}{\mathcal{S}(P_0 u_\Gamma, P_0 u_\Gamma) + \mathcal{S}((I - P_0)u_\Gamma, (I - P_0)u_\Gamma)} \leq \max\{c_M, 1\}$$

and thus the thesis follows. □

Remark 4.7.2. Due to Remark 4.6.6, in order to perform the theoretical analysis of the BNN preconditioner with the enriched coarse space we will consider the operator P_{NN}^* given in eq. (4.40). The results of Lemma 4.7.1 still hold; moreover

$$\begin{aligned}
P_{NN}^*(I - P_0)u_\Gamma &= P_{NN}(I + P_0)u_\Gamma + \sum_{j=1}^{N} R_{D,\Gamma}^{(j)^T} \alpha_j \mathbf{1}_{\Gamma^{(j)}}^* \\
&= E_D w + E_D \alpha \mathbf{1}^* \\
&= E_D(w + \alpha \mathbf{1}^*),
\end{aligned} \tag{4.43}$$

where

$$\alpha = (\alpha_1, \ldots, \alpha_N), \quad \alpha_j \in \mathbb{R},$$

and $\mathbf{1}^* \in \mathbf{W}_\Gamma$ is the vector with local components $\mathbf{1}_{\Gamma^{(j)}}^*$.

As previously done for the Monodomain model, we can define $w \in \mathbf{W}_\Gamma$ locally as

$$w_j = S^{(j)\,\dagger} D^{(j)} R_\Gamma^{(j)} \widehat{S}_\Gamma (I - P_0) u_\Gamma. \tag{4.44}$$

An equality similar to eq. (4.22) holds by using the fundamental properties of the pseudoinverses (see [88] for further details), and thus we can write

$$E_D w = P_{NN}(I - P_0) u_\Gamma. \tag{4.45}$$

We then proceed estimating the upper bound of the average operator. In order to simplify the notations, we will first assume that the conductivity coefficients have no jumps across substructures. We note that with the natural coarse space (4.31) we cannot obtain a general bound in case of jumping coefficients with jumps aligned with the interface due to more complicated nature of the Bidomain problem. However, we will derive such bounds using the enriched coarse space (4.32).

Lemma 4.7.3. *Let $w \in \boldsymbol{W}_\Gamma$ be defined as in formula (4.44). Then for the Bidomain model with natural coarse space (4.31) it will hold*

$$|E_D w|_S^2 \lesssim \frac{\sigma_M \delta_t + H^2}{\min\{H^2, \sigma_m \delta_t\}} (1 + \log(H/h))^2 |w|_S^2$$

where $\sigma_M = \max\{\sigma_M^i, \sigma_M^e\}$ and $\sigma_m = \min\{\sigma_m^i, \sigma_m^e\}$ with $\sigma_M^{i,e}$ and $\sigma_m^{i,e}$ the maximum and minimum eigenvalues of the intra- and extracellular diffusion tensors given in eq. (2.1), and δ_t is the time step.

Proof. As already done in Lemma 4.5.2, we will estimate each contribution $|v_j|^2_{S^{(j)}}$ where

$$v_j(x) = (E_D w)_j(x) = \left(\sum_{k \in \mathcal{N}_x} I^h(\delta_k^{i\,\dagger}(x) w_k^i(x)), \sum_{k \in \mathcal{N}_x} I^h(\delta_k^{e\,\dagger}(x) w_k^e(x)) \right)$$

where δ_k^i and δ_k^e are the partition of unity coefficients and w_k^i and w_k^e are the the intra- and extra-cellular components of w_j. Using splitting functions for each component of the solution given by

$$\Theta_\bullet v_j = (\vartheta_\bullet v_j^i, \vartheta_\bullet v_j^e),$$

where the cut-off functions $\vartheta_\bullet$ are given in Section 4.3, we can split (with an abuse of notation on the lagrangian interpolator) the boundary vector v_j in a sum of faces, edges and vertices components, for both the intra and extracellular components:

$$v_j = \sum_{\mathcal{F} \subset \Gamma^{(j)}} I^h(\Theta_\mathcal{F} v_j) + \sum_{\mathcal{E} \subset \Gamma^{(j)}} I^h(\Theta_\mathcal{E} v_j) + \sum_{\mathcal{V} \subset \Gamma^{(j)}} I^h(\Theta_\mathcal{V} v_j)$$

Noting that each $s_j(\cdot,\cdot)$ defines a seminorm, it follows that

$$s_j(u_\Gamma^{(j)}, v_\Gamma^{(j)}) \lesssim s_j(u_\Gamma^{(j)}, u_\Gamma^{(j)}) + s_j(v_\Gamma^{(j)}, v_\Gamma^{(j)}) \;\; \forall u_\Gamma^{(j)}, v_\Gamma^{(j)} \in \mathbf{W}_\Gamma^{(j)}$$

therefore

$$|v_j|^2_{S^{(j)}} \lesssim \sum_{\mathcal{F}\subset\Gamma^{(j)}} |I^h(\Theta_{\mathcal{F}} v_j)|^2_{S^{(j)}} + \sum_{\mathcal{E}\subset\Gamma^{(j)}} |I^h(\Theta_{\mathcal{E}} v_j)|^2_{S^{(j)}} + \sum_{\mathcal{V}\subset\Gamma^{(j)}} |I^h(\Theta_{\mathcal{V}} v_j)|^2_{S^{(j)}}$$

The coercivity and continuity for the local Schur bilinear forms yields (see Remark 2.4.4):

$$s_j(u_\Gamma^{(j)}, u_\Gamma^{(j)}) \geq \sigma_m^i |(\mathcal{H}_j u_\Gamma^{(j)})^i|^2_{H^1(\Omega_j)} + \sigma_m^e |(\mathcal{H}_j u_\Gamma^{(j)})^e|^2_{H^1(\Omega_j)} + \gamma ||(\mathcal{H}_j u_\Gamma^{(j)})^i - (\mathcal{H}_j u_\Gamma^{(j)})^e||^2_{L^2(\Omega_j)}$$
$$s_j(u_\Gamma^{(j)}, u_\Gamma^{(j)}) \leq \sigma_M^i |(\mathcal{H}_j u_\Gamma^{(j)})^i|^2_{H^1(\Omega_j)} + \sigma_M^e |(\mathcal{H}_j u_\Gamma^{(j)})^e|^2_{H^1(\Omega_j)} + \gamma ||(\mathcal{H}_j u_\Gamma^{(j)})^i - (\mathcal{H}_j u_\Gamma^{(j)})^e||^2_{L^2(\Omega_j)}$$

where σ_m^i, σ_M^i (respectively σ_m^e, σ_M^e) are the minimum and maximum eigenvalues for the intracellular (extracellular) diffusion tensors and $\gamma = 1/\delta_t$. Noting that the function

$$(\mathcal{H}_j(I^h(\Theta_\bullet v_j)))^i - (\mathcal{H}_j(I^h(\Theta_\bullet v_j)))^e$$

vanishes on a two-dimensional subset of $\Gamma^{(j)}$, we can use a Poincarè-Friedrichs inequality (see Lemma 4.3.6) and obtain:

$$\begin{aligned} &||(\mathcal{H}_j(I^h(\Theta_\bullet v_j)))^i - (\mathcal{H}_j(I^h(\Theta_\bullet v_j)))^e||^2_{L^2(\Omega_j)} \lesssim \\ &H^2 |(\mathcal{H}_j(I^h(\Theta_\bullet v_j)))^i|^2_{H^1(\Omega_j)} + H^2 |(\mathcal{H}_j(I^h(\Theta_\bullet v_j)))^e|^2_{H^1(\Omega_j)} \end{aligned}$$

and thus we can work with the $H^{1/2}(\Gamma^{(j)})$ seminorm using Lemma 4.3.5:

$$\begin{aligned} |I^h(\Theta_\bullet v_j)|^2_{S^{(j)}} &\lesssim (\sigma_M^i + H^2\gamma)|I^h(\vartheta_\bullet v_j^i)|^2_{H^{1/2}(\Gamma^{(j)})} + (\sigma_M^e + H^2\gamma)|I^h(\vartheta_\bullet v_j^e)|^2_{H^{1/2}(\Gamma^{(j)})} \\ &\lesssim (\sigma_M + H^2\gamma)\left(|I^h(\vartheta_\bullet v_j^i)|^2_{H^{1/2}(\Gamma^{(j)})} + |I^h(\vartheta_\bullet v_j^e)|^2_{H^{1/2}(\Gamma^{(j)})}\right) \end{aligned}$$

where $\sigma_M = \max\{\sigma_M^i, \sigma_M^e\}$. As done previously in Lemma 4.5.2, we can estimate the contribution of faces, edges and vertices separately.

Face terms. For the face terms we obtain as previously done for the Monodomain model in Lemma 4.5.2 using Remark 4.3.4 and Lemma 4.3.7:

$$\begin{aligned} |I^h(\vartheta_{\mathcal{F}} v_j^i)|^2_{H^{1/2}(\Gamma^{(j)})} \lesssim &(1+\log(H/h))^2 \left(|(\mathcal{H}_j w_j)^i|^2_{H^1(\Omega_j)} + H^{-2}||(\mathcal{H}_j w_j)^i||^2_{L^2(\Omega_j)}\right) + \\ &(1+\log(H/h))^2 \left(|(\mathcal{H}_k w_k)^i|^2_{H^1(\Omega_k)} + H^{-2}||(\mathcal{H}_k w_k)^i||^2_{L^2(\Omega_k)}\right) \\ |I^h(\vartheta_{\mathcal{F}} v_j^e)|^2_{H^{1/2}(\Gamma^{(j)})} \lesssim &(1+\log(H/h))^2 \left(|(\mathcal{H}_j w_j)^e|^2_{H^1(\Omega_j)} + H^{-2}||(\mathcal{H}_j w_j)^e||^2_{L^2(\Omega_j)}\right) + \\ &(1+\log(H/h))^2 \left(|(\mathcal{H}_k w_k)^e|^2_{H^1(\Omega_k)} + H^{-2}||(\mathcal{H}_k w_k)^e||^2_{L^2(\Omega_k)}\right) \end{aligned}$$

and summing over the two cellular components

$$\begin{aligned} &(1+\log(H/h))^{-2}\left[|I^h(\vartheta_{\mathcal{F}} v_j^i)|^2_{H^{1/2}(\Gamma^{(j)})} + |I^h(\vartheta_{\mathcal{F}} v_j^e)|^2_{H^{1/2}(\Gamma^{(j)})}\right] \lesssim \\ &|(\mathcal{H}_j w_j)^i|^2_{H^1(\Omega_j)} + |(\mathcal{H}_j w_j)^e|^2_{H^1(\Omega_j)} + H^{-2}\left(||(\mathcal{H}_j w_j)^i||^2_{L^2(\Omega_j)} + ||(\mathcal{H}_j w_j)^e||^2_{L^2(\Omega_j)}\right) + \\ &|(\mathcal{H}_k w_k)^i|^2_{H^1(\Omega_k)} + |(\mathcal{H}_k w_k)^e|^2_{H^1(\Omega_k)} + H^{-2}\left(||(\mathcal{H}_k w_k)^i||^2_{L^2(\Omega_k)} + ||(\mathcal{H}_k w_k)^e||^2_{L^2(\Omega_k)}\right). \end{aligned} \tag{4.46}$$

Edge terms. For edge terms we can proceed as in [140] using Lemma 4.3.9, a triangle inequality and then Lemma 4.3.8, to obtain a bound for each local component

$$|I^h(\vartheta_{\mathcal{E}} v_j^i)|^2_{H^{1/2}(\Gamma^{(j)})} \lesssim (1+\log(H/h))^2 \sum_{k\in\mathcal{K}_{\mathcal{E}}} \left(|(\mathcal{H}_k w_k)^i|^2_{H^1(\Omega_k)} + H^{-2}||(\mathcal{H}_k w_k)^i||^2_{L^2(\Omega_k)} \right)$$
$$|I^h(\vartheta_{\mathcal{E}} v_j^e)|^2_{H^{1/2}(\Gamma^{(j)})} \lesssim (1+\log(H/h))^2 \sum_{k\in\mathcal{K}_{\mathcal{E}}} \left(|(\mathcal{H}_k w_k)^e|^2_{H^1(\Omega_k)} + H^{-2}||(\mathcal{H}_k w_k)^e||^2_{L^2(\Omega_k)} \right)$$

where $\mathcal{K}_{\mathcal{E}}$ is the set of subdomain indices sharing edge $\mathcal{E}$. Summing over the two cellular components we will find a bound similar to that given in formula (4.46).

Vertex terms. Similarly, using Lemma 4.3.10 we bound also the vertex components as

$$|I^h(\vartheta_{\mathcal{V}} v_j^i)|^2_{H^{1/2}(\Gamma^{(j)})} \lesssim (1+\log(H/h))^2 \sum_{k\in\mathcal{K}_{\mathcal{V}}} \left(|(\mathcal{H}_k w_k)^i|^2_{H^1(\Omega_k)} + H^{-2}||(\mathcal{H}_k w_k)^i||^2_{L^2(\Omega_k)} \right)$$
$$|I^h(\vartheta_{\mathcal{V}} v_j^e)|^2_{H^{1/2}(\Gamma^{(j)})} \lesssim (1+\log(H/h))^2 \sum_{k\in\mathcal{K}_{\mathcal{V}}} \left(|(\mathcal{H}_k w_k)^e|^2_{H^1(\Omega_k)} + H^{-2}||(\mathcal{H}_k w_k)^e||^2_{L^2(\Omega_k)} \right)$$

where $\mathcal{K}_{\mathcal{V}}$ is the set of subdomain indices sharing vertex $\mathcal{V}$ obtaining a bound similar to (4.46) summing up the two cellular components.

Now consider only the L^2 contribution from one substructure to formula (4.46) (the contributions from other substructures can be treated similarly): since the intra- and the extra-cellular components of the local Schur complements solutions are unique modulo a constant and the discrete harmonic function of a constant is a constant function itself (see Remark 4.2.7), we can choose w_j such that

$$\int_{\Omega_j} (\mathcal{H}_j w_j)^i + (\mathcal{H}_j w_j)^e = 0; \tag{4.47}$$

In fact, let $w_j = \widetilde{w}_j + \beta_j$ with $\beta_j \in \mathbb{R}$ and

$$\int_{\Omega_j} (\mathcal{H}_j \widetilde{w}_j)^e = 0$$

a solution of the local discrete harmonic Bidomain problem; denoting with $|\Omega_j|$ the volume of Ω_j we can write

$$\int_{\Omega_j} (\mathcal{H}_j w_j)^i + (\mathcal{H}_j w_j)^e = 2\beta_j|\Omega_j| + \int_{\Omega_j} (\mathcal{H}_j \widetilde{w}_j)^i + (\mathcal{H}_j \widetilde{w}_j)^e$$

which is equal to zero by choosing

$$\beta_j = -\frac{1}{2|\Omega_j|} \int_{\Omega_j} (\mathcal{H}_j \widetilde{w}_j)^i.$$

Thus for the parallelogram identity of Hilbert spaces and Lemma 4.3.6, it follows that

$$\begin{aligned}
&H^{-2}\left(||(\mathcal{H}_j w_j)^i||^2_{L^2(\Omega_j)} + ||(\mathcal{H}_j w_j)^e||^2_{L^2(\Omega_j)}\right)\\
\lesssim &H^{-2}\left(||(\mathcal{H}_j w_j)^i - (\mathcal{H}_j w_j)^e||^2_{L^2(\Omega_j)} + ||(\mathcal{H}_j w_j)^i + (\mathcal{H}_j w_j)^e||^2_{L^2(\Omega_j)}\right)\\
\lesssim &H^{-2}\left(||(\mathcal{H}_j w_j)^i - (\mathcal{H}_j w_j)^e||^2_{L^2(\Omega_j)} + H^2|(\mathcal{H}_j w_j)^i + (\mathcal{H}_j w_j)^e|^2_{H^1(\Omega_j)}\right)\\
\lesssim &H^{-2}||(\mathcal{H}_j w_j)^i - (\mathcal{H}_j w_j)^e||^2_{L^2(\Omega_j)} + |(\mathcal{H}_j w_j)^i|^2_{H^1(\Omega_j)} + |(\mathcal{H}_j w_j)^e|^2_{H^1(\Omega_j)}.
\end{aligned}$$

We thus obtain for the face terms

$$\begin{aligned}
&(1+\log(H/h))^{-2}\left[|I^h(\vartheta_{\mathcal{F}} v_j^i)|^2_{H^{1/2}(\Gamma^{(j)})} + |I^h(\vartheta_{\mathcal{F}} v_j^e)|^2_{H^{1/2}(\Gamma^{(j)})}\right]\\
\lesssim &|(\mathcal{H}_j w_j)^i|^2_{H^1(\Omega_j)} + |(\mathcal{H}_j w_j)^e|^2_{H^1(\Omega_j)} + H^{-2}||(\mathcal{H}_j w_j)^i - (\mathcal{H}_j w_j)^e||^2_{L^2(\Omega_j)}\\
+&|(\mathcal{H}_k w_k)^i|^2_{H^1(\Omega_k)} + |(\mathcal{H}_k w_k)^e|^2_{H^1(\Omega_k)} + H^{-2}||(\mathcal{H}_k w_k)^i - (\mathcal{H}_k w_k)^e||^2_{L^2(\Omega_k)}
\end{aligned}$$

Therefore, if $H^2\gamma \leq \sigma_m$, with $\sigma_m = \min\{\sigma_m^i, \sigma_m^e\}$

$$\begin{aligned}
&\frac{H^2\gamma}{\sigma_M + H^2\gamma}(1+\log(H/h))^{-2}|I^h(\Theta_{\mathcal{F}} v_j)|^2_{S^{(j)}}\\
\lesssim &H^2\gamma|(\mathcal{H}_j w_j)^i|^2_{H^1(\Omega_j)} + H^2\gamma|(\mathcal{H}_j w_j)^e|^2_{H^1(\Omega_j)} + \gamma||(\mathcal{H}_j w_j)^i - (\mathcal{H}_j w_j)^e||^2_{L^2(\Omega_j)}\\
+&H^2\gamma|(\mathcal{H}_k w_k)^i|^2_{H^1(\Omega_k)} + H^2\gamma|(\mathcal{H}_k w_k)^e|^2_{H^1(\Omega_k)} + \gamma||(\mathcal{H}_k w_k)^i - (\mathcal{H}_k w_k)^e||^2_{L^2(\Omega_k)}
\end{aligned}$$

and thus

$$|I^h(\Theta_{\mathcal{F}} v_j)|^2_{S^{(j)}} \lesssim (1+\log(H/h))^2\frac{\sigma_M + H^2\gamma}{H^2\gamma}\left(|w_j|^2_{S^{(j)}} + |w_k|^2_{S^{(k)}}\right)$$

Otherwise, if $H^2\gamma \geq \sigma_m$

$$\begin{aligned}
&\frac{\sigma_m}{\sigma_M + H^2\gamma}(1+\log(H/h))^{-2}|I^h(\Theta_{\mathcal{F}} v_j)|^2_{S^{(j)}}\\
\lesssim &\sigma_m|(\mathcal{H}_j w_j)^i|^2_{H^1(\Omega_j)} + \sigma_m|(\mathcal{H}_j w_j)^e|^2_{H^1(\Omega_j)} + \sigma_m H^{-2}||(\mathcal{H}_j w_j)^i - (\mathcal{H}_j w_j)^e||^2_{L^2(\Omega_j)}\\
+&\sigma_m|(H_k w_k)^i|^2_{H^1(\Omega_k)} + \sigma_m|(\mathcal{H}_k w_k)^e|^2_{H^1(\Omega_k)} + \sigma_m H^{-2}||(\mathcal{H}_k w_k)^i - (\mathcal{H}_k w_k)^e||^2_{L^2(\Omega_k)}
\end{aligned}$$

and thus

$$|I^h(\Theta_{\mathcal{F}} v_j)|^2_{S^{(j)}} \lesssim (1+\log(H/h))^2\frac{\sigma_M + H^2\gamma}{\sigma_m}\left(|w_j|^2_{S^{(j)}} + |w_k|^2_{S^{(k)}}\right)$$

Therefore, for the face terms we will have

$$|I^h(\Theta_{\mathcal{F}} v_j)|^2_{S^{(j)}} \lesssim (1+\log(H/h))^2\frac{\sigma_M + H^2\gamma}{\min\{H^2\gamma, \sigma_m\}}\left(|w_j|^2_{S^{(j)}} + |w_k|^2_{S^{(k)}}\right)$$

We can proceed similarly for edge and vertex terms bounding L^2 contributions from each subtructure using the same $w_j = \widetilde{w}_j + \beta_j$; the thesis then follows by summing over faces, edges and vertices of Ω_j and then over the substructures. □

Lemma 4.7.4. *Let $w \in \boldsymbol{W}_\Gamma$ be defined as in formula (4.44). Then for the Bidomain model with enriched coarse space (4.32) exists $\alpha = (\alpha_1, \ldots, \alpha_N)$ such that*

$$|E_D(w + \alpha \mathbf{1}^*)|_S^2 \lesssim \max_{\bullet=i,e} \left(\max_{j=1,\ldots,N} \frac{\sigma_M^{\bullet^{(j)}} \delta_t + H^2}{\sigma_m^{\bullet^{(j)}} \delta_t} \right) (1 + \log(H/h))^2 |w|_S^2$$

where $\sigma_M^{i,e^{(j)}}$ and $\sigma_m^{i,e^{(j)}}$ are the maximum and minimum eigenvalues of the intra- and extracellular diffusion tensors for the jth substructure and δ_t is the time step.

Proof. We can proceed as before in Lemma 4.7.3 and obtain

$$|I^h(\Theta_\bullet v_j)|_{S^{(j)}}^2 \lesssim (\sigma_M^{i^{(j)}} + H^2\gamma)|I^h(\vartheta_\bullet v_j^i)|_{H^{1/2}(\Gamma^{(j)})}^2 + (\sigma_M^{e^{(j)}} + H^2\gamma)|I^h(\vartheta_\bullet v_j^e)|_{H^{1/2}(\Gamma^{(j)})}^2, \tag{4.48}$$

where now

$$\begin{aligned} v_j(x) &= (E_D(w + \alpha \mathbf{1}^*))_j(x) \\ &= \left(\sum_{k \in \mathcal{N}_x} I^h(\delta_k^{i\,\dagger}(x) w_k^i(x) + \delta_k^{i\,\dagger}(x)\alpha_k), \sum_{k \in \mathcal{N}_x} I^h(\delta_k^{e\,\dagger}(x) w_k^e(x) - \delta_k^{e\,\dagger}(x)\alpha_k) \right). \end{aligned}$$

As before, we can estimate the face, edge and vertex contributions separately. We explicitly develop the algebra related to the face terms; edge and vertex terms can be treated similarly as already done in Lemma 4.7.3 using in addition the same arguments developed in the following. For the face terms we first obtain using Remark 4.3.4

$$\begin{aligned} |I^h(\vartheta_{\mathcal{F}} v_j^i)|_{H^{1/2}(\Gamma^{(j)})}^2 &\lesssim ||I^h(\vartheta_{\mathcal{F}} v_j^i)||_{H_{00}^{1/2}(\mathcal{F})}^2 \\ &\lesssim \overline{\delta}_j^{i^{\dagger^2}} ||I^h(\vartheta_{\mathcal{F}}(w_j^i + \alpha_j))||_{H_{00}^{1/2}(\mathcal{F})}^2 + \overline{\delta}_k^{i^{\dagger^2}} ||I^h(\vartheta_{\mathcal{F}}(w_k^i + \alpha_k))||_{H_{00}^{1/2}(\mathcal{F})}^2 \\ |I^h(\vartheta_{\mathcal{F}} v_j^e)|_{H^{1/2}(\Gamma^{(j)})}^2 &\lesssim ||I^h(\vartheta_{\mathcal{F}} v_j^e)||_{H_{00}^{1/2}(\mathcal{F})}^2 \\ &\lesssim \overline{\delta}_j^{e^{\dagger^2}} ||I^h(\vartheta_{\mathcal{F}}(w_j^e - \alpha_j))||_{H_{00}^{1/2}(\mathcal{F})}^2 + \overline{\delta}_k^{e^{\dagger^2}} ||I^h(\vartheta_{\mathcal{F}}(w_k^e - \alpha_k))||_{H_{00}^{1/2}(\mathcal{F})}^2, \end{aligned}$$

where

$$\overline{\delta}_k^{i,e^\dagger} = \max_{x \in \Gamma^{(j)}} \delta_k^{i,e^\dagger}(x).$$

Using Lemma 4.3.7 we can bound from above each of the $H_{00}^{1/2}(\mathcal{F})$ norms by

$$\begin{aligned} &(1 + \log(H/h))^2 \left(|(\mathcal{H}_{j,k}(w_{j,k} + \alpha_{j,k}))^i|_{H^1(\Omega_{j,k})}^2 + H^{-2} ||(\mathcal{H}_{j,k}(w_{j,k} + \alpha_{j,k}))^i||_{L^2(\Omega_{j,k})}^2 \right) \\ &(1 + \log(H/h))^2 \left(|(\mathcal{H}_{j,k}(w_{j,k} - \alpha_{j,k}))^e|_{H^1(\Omega_{j,k})}^2 + H^{-2} ||(\mathcal{H}_{j,k}(w_{j,k} - \alpha_{j,k}))^e||_{L^2(\Omega_{j,k})}^2 \right) \end{aligned}$$

Since the discrete Bidomain harmonic extension of a constant function is a constant itself, we can replace the arguments of the H^1 seminorm in the latter expressions by

$$\begin{aligned} |(\mathcal{H}_{j,k}(w_{j,k} + \alpha_{j,k}))^i|_{H^1(\Omega_{j,k})}^2 &= |(\mathcal{H}_{j,k}(w_{j,k}))^i|_{H^1(\Omega_{j,k})}^2 \\ |(\mathcal{H}_{j,k}(w_{j,k} - \alpha_{j,k}))^e|_{H^1(\Omega_{j,k})}^2 &= |(\mathcal{H}_{j,k}(w_{j,k}))^e|_{H^1(\Omega_{j,k})}^2. \end{aligned}$$

We then sum over the two cellular components as previously done in Lemma 4.7.3; as before, we thus need only to analyze the $L^2(\Omega_{j,k})$ contributions, i.e.

$$H^{-2}(||(\mathcal{H}_j(w_j+\alpha_j))^i||^2_{L^2(\Omega_j)}+||(\mathcal{H}_j(w_j-\alpha_j))^e||^2_{L^2(\Omega_j)}),$$
$$H^{-2}(||(\mathcal{H}_k(w_k+\alpha_k))^i||^2_{L^2(\Omega_k)}+||(\mathcal{H}_k(w_k-\alpha_k))^e||^2_{L^2(\Omega_k)})$$

We then use the parallelogram identity in Hilbert spaces and the fact that the Bidomain discrete harmonic function of a constant is a constant function itself (see Remark 4.2.7) to bound from above the $L^2(\Omega_j)$ contribution by

$$\begin{aligned}&||(\mathcal{H}_j(w_j+\alpha_j))^i+(\mathcal{H}_j(w_j-\alpha_j))^e||^2_{L^2(\Omega_j)}+||(\mathcal{H}_j(w_j+\alpha_j))^i-(\mathcal{H}_j(w_j-\alpha_j))^e||^2_{L^2(\Omega_j)}\\&=||(\mathcal{H}_jw_j)^i+(\mathcal{H}_jw_j)^e||^2_{L^2(\Omega_j)}+||(\mathcal{H}_jw_j)^i-(\mathcal{H}_jw_j)^e+2\alpha_j||^2_{L^2(\Omega_j)}.\end{aligned}\tag{4.49}$$

As done before in Lemma 4.7.3, the first term on the right hand side of eq. (4.49) can be bounded from above by the sum of the H^1 seminorms using a Poincarè inequality and a triangle inequality, since we can add a suitable constant function to w_j, i.e. we can choose $w_j=\widetilde{w}_j+\beta_j$ with

$$\int_{\Omega_j}(\mathcal{H}_j\widetilde{w}_j)^e=0$$

and

$$\beta_j=-\frac{1}{2|\Omega_j|}\int_{\Omega_j}(\mathcal{H}_j\widetilde{w}_j)^i.$$

For the second term on the right hand side of eq. (4.49), we can proceed similarly choosing α_j such that

$$\begin{aligned}0&=\int_{\Omega_j}(\mathcal{H}_jw_j)^i-(\mathcal{H}_jw_j)^e+2\alpha_j=\int_{\Omega_j}(\mathcal{H}_j\widetilde{w}_j+\beta_j)^i-(\mathcal{H}_j\widetilde{w}_j+\beta_j)^e+2\alpha_j\\&=2\alpha_j|\Omega_j|+\int_{\Omega_j}(\mathcal{H}_j\widetilde{w}_j)^i-(\mathcal{H}_j\widetilde{w}_j)^e\end{aligned}$$

i.e.

$$\alpha_j=-\frac{1}{2|\Omega_j|}\int_{\Omega_j}(\mathcal{H}_j\widetilde{w}_j)^i.$$

We thus end up with the estimate for the face terms

$$\begin{aligned}&(1+\log(H/h))^{-2}|I^h(\Theta_{\mathcal{F}}v_j)|^2_{S^{(j)}}\\\lesssim&\overline{\delta}_j^{i^{\dagger^2}}(\sigma_M^{i^{(j)}}+H^2\gamma)|(\mathcal{H}_jw_j)^i|^2_{H^1(\Omega_j)}+\overline{\delta}_j^{e^{\dagger^2}}(\sigma_M^{e^{(j)}}+H^2\gamma)|(\mathcal{H}_jw_j)^e|^2_{H^1(\Omega_j)}\\+&\overline{\delta}_k^{i^{\dagger^2}}(\sigma_M^{i^{(j)}}+H^2\gamma)|(\mathcal{H}_kw_k)^i|^2_{H^1(\Omega_k)}+\overline{\delta}_k^{e^{\dagger^2}}(\sigma_M^{e^{(j)}}+H^2\gamma)|(\mathcal{H}_kw_k)^e|^2_{H^1(\Omega_k)}\\\lesssim&(\sigma_M^{i^{(j)}}+H^2\gamma)|(\mathcal{H}_jw_j)^i|^2_{H^1(\Omega_j)}+(\sigma_M^{e^{(j)}}+H^2\gamma)|(\mathcal{H}_jw_j)^e|^2_{H^1(\Omega_j)}\\+&(\sigma_M^{i^{(k)}}+H^2\gamma)|(\mathcal{H}_kw_k)^i|^2_{H^1(\Omega_k)}+(\sigma_M^{e^{(k)}}+H^2\gamma)|(\mathcal{H}_kw_k)^e|^2_{H^1(\Omega_k)}\end{aligned}$$

where we have used formula (4.35) to obtain the last inequality. Thus, we can finally bound

the face terms

$$|I^h(\Theta_{\mathcal{F}} v_j)|^2_{S^{(j)}} \lesssim \max_{\bullet=i,e} \left(\max_{l=j,k} \frac{\sigma_M^{\bullet^{(l)}} \delta_t + H^2}{\sigma_m^{\bullet^{(l)}} \delta_t} \right) (1+\log(H/h))^2 (|w|^2_{S^{(j)}} + |w|^2_{S^{(k)}}).$$

The thesis then follows proceeding similarly for edge and vertex terms using the same w_j, and then summing over faces, edges and vertices and finally over the subtructures.

□

We are then ready to prove the main theorems for the condition number of the preconditioned Bidomain model.

Theorem 4.7.5. *The condition number of the preconditioned Schur complement system of the Bidomain model with natural coarse space (4.31) satisfies:*

$$\kappa_2(M^{-1}_{BNN} \widehat{S}_\Gamma) \lesssim \frac{\sigma_M \delta_t + H^2}{\min\{H^2, \sigma_m \delta_t\}} (1+\log(H/h))^2. \tag{4.50}$$

Proof. **Lower Bound.** A lower bound of one for the Rayleigh quotient of the additive operator P_{NN}, and thus for Rayleigh quotient of P_{BNN} (4.41) using Lemma 4.7.1, can be deduced by the existence of a stable decomposition of the bilinear form $\mathcal{S}(\cdot,\cdot)$ in terms of $\tilde{s}_j(\cdot,\cdot)$ with a constant C_0 equal to one.

Upper Bound. The equality stated in formula (4.29) still holds (see e.g. [140]) with a slight modification, that is

$$|w|^2_S = \mathcal{S}(P_{NN}(I-P_0)u_\Gamma, (I-P_0)u_\Gamma) \tag{4.51}$$

where w is given as in eq. (4.44). Proceeding as before in Theorem 4.5.3 using eq. (4.45) and the estimate given in Lemma 4.7.3, we obtain

$$\frac{\mathcal{S}(P_{NN}(I-P_0)u_\Gamma, (I-P_0)u_\Gamma)}{\mathcal{S}((I-P_0)u_\Gamma, (I-P_0)u_\Gamma)} \lesssim \frac{\sigma_M \delta_t + H^2}{\min\{H^2, \sigma_m \delta_t\}} (1+\log(H/h))^2$$

and thus the thesis follows using Lemma 4.7.1. □

As for the one-level Neumann-Neumann preconditioner for the Monodomain model analyzed in Section 4.5, the estimates for the Bidomain model with a balancing preconditioner possess a leading term proportional to H^{-2} for very large values of δ_t using the natural coarse space. We next show that augmenting the coarse space of the Balancing preconditioner considering the enriched coarse space (4.32) will give us quasi-optimal bounds.

Theorem 4.7.6. *The condition number of the preconditioned Schur complement system of the Bidomain model with enriched coarse space (4.32) satisfies:*

$$\kappa_2(M^{*^{-1}}_{BNN} \widehat{S}_\Gamma) \lesssim \max_{\bullet=i,e} \left(\max_{j=1,\ldots,N} \frac{\sigma_M^{\bullet^{(j)}} \delta_t + H^2}{\sigma_m^{\bullet^{(j)}} \delta_t} \right) (1+\log(H/h))^2.$$

Proof. We first estabilish the same equality of (4.51) for the operator P^*_{NN} using the fact that P_0 is an orthogonal projection (see Lemma 4.6.4):

$$\begin{aligned}
&\mathcal{S}(P^*_{NN}(I-P_0)u_\Gamma,(I-P_0)u_\Gamma) = \\
&= \mathcal{S}(P_{NN}(I-P_0)u_\Gamma,(I-P_0)u_\Gamma) + \mathcal{S}(\sum_{j=1}^{N}\alpha_j R_{D,\Gamma}^{(j)^T}\mathbf{1}^*_{\Gamma^{(j)}},(I-P_0)u_\Gamma) \\
&= \mathcal{S}(P_{NN}(I-P_0)u_\Gamma,(I-P_0)u_\Gamma) + \sum_{j=1}^{N}\alpha_j \mathcal{S}(R_{D,\Gamma}^{(j)^T}\mathbf{1}^*_{\Gamma^{(j)}},(I-P_0)u_\Gamma) \\
&= \mathcal{S}(P_{NN}(I-P_0)u_\Gamma,(I-P_0)u_\Gamma) + \sum_{j=1}^{N}\alpha_j \mathcal{S}(R_{D,\Gamma}^{(j)^T}\mathbf{1}^*_{\Gamma^{(j)}},P_0(I-P_0)u_\Gamma) \\
&= \mathcal{S}(P_{NN}(I-P_0)u_\Gamma,(I-P_0)u_\Gamma)
\end{aligned}$$

for all possible values of the constants α_j. Thus, using eq. (4.51) we have

$$\mathcal{S}(P^*_{NN}(I-P_0)u_\Gamma,(I-P_0)u_\Gamma) = \mathcal{S}(P_{NN}(I-P_0)u_\Gamma,(I-P_0)u_\Gamma) = |w|^2_S. \quad (4.52)$$

Lower Bound. A lower bound for the additive operator P^*_{NN} on the subspace range $(I-P_0)$, and therefore for P^*_{BNN} using Lemma 4.7.1, can be obtained using the lower bound of the operator P_{NN} on the subspace range $(I-P_0)$ and eq. (4.52):

$$\begin{aligned}
&\mathcal{S}((I-P_0)u_\Gamma,(I-P_0)u_\Gamma) \\
&\leq \mathcal{S}(P_{NN}(I-P_0)u_\Gamma,(I-P_0)u_\Gamma) \\
&= \mathcal{S}(P^*_{NN}(I-P_0)u_\Gamma,(I-P_0)u_\Gamma)
\end{aligned}$$

and thus the minimum eigenvalue of the Rayleigh quotient (4.42) for the enriched coarse space is equal to one.

Upper Bound. For the upper bound, we can proceed as in Theorem 4.5.3 using eq. (4.43), Lemma 4.7.4 and eq. (4.52) to obtain

$$\begin{aligned}
&\mathcal{S}(P^*_{NN}(I-P_0)u_\Gamma,P^*_{NN}(I-P_0)u_\Gamma) \\
&= |P^*_{NN}(I-P_0)u_\Gamma|^2_S \\
&= |E_D(w+\alpha\mathbf{1}^*)|^2_S \\
&\lesssim \max_{\bullet=i,e}\left(\max_{j=1,\dots,N}\frac{\sigma_M^{\bullet^{(j)}}\delta_t+H^2}{\sigma_m^{\bullet^{(j)}}\delta_t}\right)(1+\log(H/h))^2|w|^2_S \\
&= \max_{\bullet=i,e}\left(\max_{j=1,\dots,N}\frac{\sigma_M^{\bullet^{(j)}}\delta_t+H^2}{\sigma_m^{\bullet^{(j)}}\delta_t}\right)(1+\log(H/h))^2\mathcal{S}(P^*_{NN}(I-P_0)u_\Gamma,(I-P_0)u_\Gamma)
\end{aligned}$$

and thus, using a Cauchy-Schwarz inequality, canceling a common term and squaring as in

Theorem 4.5.3, we obtain

$$\begin{aligned}&\mathcal{S}(P_{NN}^{*}(I-P_0)u_\Gamma,(I-P_0)u_\Gamma)\\&\lesssim \max_{\bullet=i,e}\left(\max_{j=1,\dots,N}\frac{\sigma_M^{\bullet(j)}\delta_t+H^2}{\sigma_m^{\bullet(j)}\delta_t}\right)(1+\log(H/h))^2\mathcal{S}((I-P_0)u_\Gamma,(I-P_0)u_\Gamma),\end{aligned}$$

and thus, using Lemma 4.7.1, the maximum eigenvalue of the Rayleigh quotient (4.42) for the enriched coarse space can be bounded by

$$\lambda_M^{*}\lesssim \max_{\bullet=i,e}\left(\max_{j=1,\dots,N}\frac{\sigma_M^{\bullet(j)}\delta_t+H^2}{\sigma_m^{\bullet(j)}\delta_t}\right)(1+\log(H/h))^2.$$

□

4.8 Implementational details and numerical results

The code has been written in Fortran 90 and the MPI library has been used for parallelization, assigning one subdomain to one MPI process. The PETSc library has been used to manage local data structures such as sparse matrices and vectors in order to assure portability of the code. The actions of the assembled matrices on given vectors are evaluated exploiting the subassembling relations and an exchanging subroutine with non-blocking MPI sends and receives using derived MPI datatypes to avoid additional copies and fully exploit the local cache.

Each local Dirichlet problem involved in the computation of the Schur matrix vector product is factorized in a preprocessing step using LU factorization provided by the serial library UMFPACK [142]; forward and backward substitutions are then used whenever local Schur matrices must be applied on some vectors. The Neumann problems involved in the application of the additive part of the NN preconditioners, i.e. M_{NN}^{-1} given in eq. (4.18), are solved using the LU factorizations of the local stiffness matrices $A^{(j)}$ since the vector

$$u_\Gamma^{(j)}=S^{(j)^{-1}}r_\Gamma^{(j)}$$

can be found by solving the local system

$$A^{(j)}\begin{pmatrix}u_I^{(j)}\\u_\Gamma^{(j)}\end{pmatrix}=\begin{pmatrix}0\\r_\Gamma^{(j)}\end{pmatrix}.$$

In order to minimize the bandwidth of the local stiffness matrices and reduce the amount of fill-in of the local LU factorizations, we have reordered the unknowns and have written for every node the intra- and extra-cellular components consecutively.

For the application of the Balancing preconditioner to the Bidomain model, we use the algorithm 3.7.2 given in Section 3.7 of [88]. The coarse problem of the Balancing operator is evaluated in the preprocessing step; it is assigned to one MPI process and it is solved

using serial factorization for sparse matrices provided by UMFPACK [142]. Usual MPI scatter and gather operations are then used for the communications involved in assembling the coarse right hand side and distributing the coarse solution.

Numerical tests were performed on Linux clusters Ulisse (84 cores) and Nemo (48 cores) located at the University of Milan (see ulisse.mat.unimi.it) and IBM clusters BCX (power5) and SP6 (power6) located at CINECA (see hpc.cineca.it).

Monodomain H/h dependence.

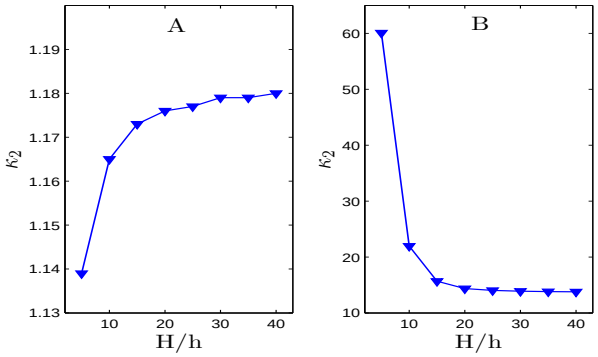

Figure 4.2: Condition number of PCG-NN solver for the Schur complement of the Monodomain model as a function of H/h with different sets of conductivity coefficients. Test case with $3 \times 3 \times 3$ subdomains, h =1E-2, δ_t =1E-2, random right-hand side and null initial guess; PCG iteration is stopped when the absolute preconditioned residual is lower then 1E-8. Details for the values of the conductivity coefficients are given in the text.

Numerical results on the estimated condition number, evaluated using the usual Lanczos' method, of the Monodomain system preconditioned with M_{NN}^{-1} are shown in Table 4.4 and Figure 4.2. Figure 4.2 shows the condition number as a function of H/h considering a cubic 3x3x3 decomposition of the spatial domain Ω; we note that, since we kept constant the domain decomposition, in the test case considered the dimension of Ω increases as the ratio H/h increases. We considered two different sets of conductivity coefficients: the first set of conductivity coefficients, whose results are shown in Panel A of Figure 4.2, is that normally used in our cardiac simulations (see Table 2.1.1 and Remark 2.4.4); the second set of conductivity coefficients (panel B) is given by σ_M =1, σ_m=1E-2 with the intermediate eigenvalue equal to 1E-1. With the former set, the condition number increases as the number of subdomain elements (i.e. H/h) increases and the dependence of the condition number from $\min\{H^2, \sigma_m \delta_t\}$ is masked by the small values of the conductivity coefficients. The dependence from H^{-2} is indeed evident in Panel B, where the condition number decreases as the number of subdomain elements increases and it grows rapidly as the number of elements decreases under ten. We note that we can drop the H^{-2} dependence of the Monodomain condition number using a natural balancing operator for the Monodomain model.

NN preconditioner Scaled Speedup, Monodomain model.

Scalability PCG-NN Schur Monodomain

subd	$\widehat{\mathbf{W}}$ dofs	$\widehat{\mathbf{W}}_\Gamma$ dofs	iter	λ_{min}	λ_{max}	κ_2
2x2x1	30'420	1'540	4	1.000	1.165	1.165
4x4x1	118'580	9'060	4	1.000	1.170	1.170
6x6x1	264'500	22'500	4	1.000	1.172	1.172
8x8x1	468'180	41'860	4	1.000	1.173	1.173
10x10x1	729'620	67'140	4	1.000	1.173	1.173
12x12x1	1'048'820	98'340	4	1.000	1.174	1.174
14x14x1	1'425'780	135'460	4	1.000	1.174	1.174
16x16x1	1'860'500	178'500	4	1.000	1.174	1.174

Table 4.4: Monodomain Schur complement scaled speedup test for PCG-NN solver. Test case with h =1E-2, $H/h = 20$, δ_t =1E-2, random right-hand side and null initial guess; PCG iteration is stopped when the initial preconditioned residual is reduced by a factor 1E-6. For each run, subdomain subdivision in the three dimensions, number of global grid and interface dofs, number of iterations, extreme eigenvalues and condition number are shown.

Table 4.4 shows the scalability (scaled speedup) of the NN preconditioner for the conductivity coefficients usually used for cardiac simulations. In this type of test, we fix the local sizes of the substructures and progressively increase the number of substructures, thus let growing the dimension of Ω keeping fixed h and H. As predicted by the theory, the minimum eigenvalue of the preconditioned system is exactly one, whereas the maximum eigenvalue, and thus the condition number, remains almost constant as the number of the substructures increases. We note that, instead of increasing the number substructures only in two directions, we could also increase it uniformly in all three directions but this strategy would have quickly exceeded our computational resources.

Monodomain with jumping coefficients.

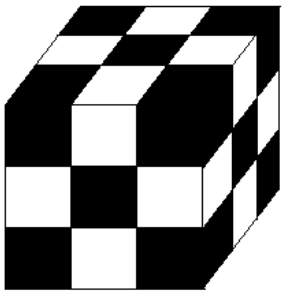

Figure 4.3: CheckerBoard pattern for discontinuous coefficients test case. See text for details.

PCG-NN Schur Monodomain
Jumping Coefficients

p	1	1E1	1E2	1E3	1E4
κ_2	7.41	21.93	105.76	976.24	9686.64

Table 4.5: Monodomain Schur complement dependence from jumps in the conductivity coefficient. Test case with 3x3x3 subdomains, $h = 0.01$, $H/h = 15$, δ_t =1E-2, random right-hand side and null initial guess; PCG iteration is stopped when the initial residual is reduced by a factor of 1E-6. For each run, jumping factor p (see text for details) and condition number for the preconditioned $P_{NN}^{-1}\widehat{S}_\Gamma$ Monodomain operator are shown.

To validate the results in Remark 4.5.4, we will consider a 3x3x3 decomposition of the whole domain and a checkerboard pattern (see Figure 4.3) of discontinuities in the conductivity coefficients such that the ratio

$$\left(\max_{j=1,\ldots,N}\frac{\sigma_M^{(j)}}{\sigma_m^{(j)}}\right).$$

will remain constant. We initially set the eigenvalues of the diffusion tensor as σ_M =1, σ_m =1E-2 with the intermediate eigenvalue equal to 1E-1; then we fix a factor p and multiply each eigenvalue by p in the black subdomains and by $1/p$ in the others. Since the term $H^2\gamma$ and the ratio between the extreme eigenvalues remain constants varying the factor p, the condition number should depend only on the maximum among the local maximum eigenvalues (see Remark 4.5.4). Numerical results confirm the theoretical estimates, showing an asymptotical linear dependence of the condition number of the Monodomain operator $P_{NN}^{-1}\widehat{S}_\Gamma$ on the factor p (see Table 4.5).

BNN preconditioner H/h dependence, Bidomain model.

PCG-BNN Schur Bidomain
H/h dependence

H/h	5	10	15	20	25
κ_2	5.93E4 (453)	1.81E4 (408)	8.96E3 (406)	5.43E3 (374)	3.67E3 (350)
κ_2^*	18.91 (37)	28.83 (47)	34.91 (55)	39.39 (58)	42.93 (63)

Table 4.6: Condition number (number of iterations in parenthesis) of PCG-BNN solver for the Schur complement of the Bidomain discretization as a function of H/h. Coarse space as natural coarse space (4.31) and enriched coarse space (4.32). Test case with $3 \times 3 \times 3$ subdomains, h =1E-2, δ_t =1E1, random right-hand side and null initial guess; PCG iteration is stopped when the preconditioned residual is lower then 1E-4. For the values of the conductivity coefficients see text.

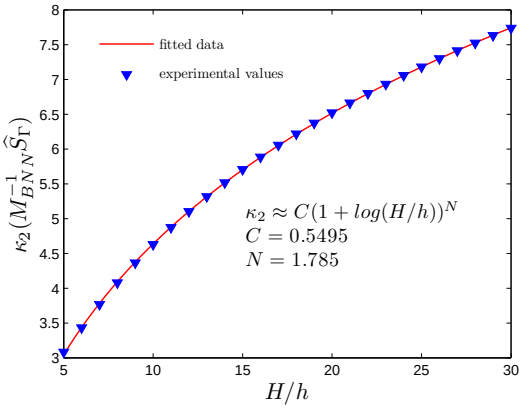

Figure 4.4: Condition number of PCG-BNN solver for the Schur complement of the Bidomain discretization as a function of H/h. Coarse space as natural coarse space (4.31). Test case with $3 \times 3 \times 3$ subdomains, h =1E-2, δ_t =1E-2, conductivity coefficients as in Table 2.1.1, random right-hand side and null initial guess; PCG iteration is stopped when the preconditioned residual is lower then 1E-8.

Numerical results on the H/h the dependence of the BNN preconditioner for the Bidomain model with natural coarse space are shown in Figure 4.4; as already noted for the same test on the additive NN preconditioner for the Monodomain model, the dimension of Ω increases as the ratio H/h increases. A typical $(1 + \log(H/h))^2$ behavior of the condition number has been observed for conductivity values usually used for our cardiac simulations and a time step of the order 1E-2 (see figure 4.4); we don't show the computational results using the enriched coarse space since it doesn't improve the results with this set of parameters. On the other hand, the robustness of the enriched coarse space with respect to the substructure diameter H is indeed evident in Table 4.6, where a different set of parameters has been used; δ_t =1E1 and conductivity coefficients such that $\sigma_M^{i,e}$ =1E1, $\sigma_m^{i,e}$ =1E-1 with the intermediate eigenvalues equal to 1.

Bidomain Scaled speedup.

Table 4.7 shows the scalability (scaled speedup) of the BNN preconditioner for the conductivity coefficients usually used for cardiac simulations and natural coarse space. As predicted by the theory, the minimum eigenvalue of the preconditioned system is exactly one, whereas the maximum eigenvalue, and thus the condition number, initially grows and finally remains almost constant as the number of the substructures increases, being thus independent from the number of substructures. We obtained the same results using the enriched coarse space (data not shown).

Bidomain δ_t dependence.

Finally, we compare the performance of natural and enriched coarse spaces testing the dependence of the condition number of BNN preconditioner from the time step δ_t, using

Scalability PCG-BNN Schur Bidomain

subd	$\widehat{\mathbf{W}}$ dofs	$\widehat{\mathbf{W}}_\Gamma$ dofs	iter	λ_{min}	λ_{max}	κ_2
2x2x1	120'050	4'850	11	1.00	3.63	3.63
4x4x1	470'450	28'650	14	1.00	5.08	5.08
6x6x1	1'051'250	71'250	15	1.00	5.53	5.53
8x8x1	1'862'450	132'650	15	1.00	5.75	5.75
10x10x1	2'904'050	212'850	16	1.00	5.86	5.86
12x12x1	4'176'050	311'850	16	1.00	5.91	5.91
14x14x1	5'678'450	429'650	16	1.00	5.78	5.78
16x16x1	7'411'250	566'250	16	1.00	5.84	5.84
18x18x1	9'374'450	721'650	16	1.00	5.89	5.89
20x20x1	11'568'050	895'850	16	1.00	5.93	5.93
22x22x1	13'992'050	1'088'850	16	1.00	5.97	5.97
24x24x1	16'646'450	1'300'650	16	1.00	5.99	5.99

Table 4.7: Bidomain Schur complement scalability test for PCG-BNN solver with natural coarse space. Test case with $h = 0.01$, $H/h = 25$, random right-hand side and null initial guess; PCG iteration is stopped when the initial preconditioned residual is reduced by a factor of 1E-6. For each run, subdomain subdivision in the three dimensions, global grid and interface dofs, number of iterations, extreme eigenvalues and condition number are shown.

physiological conductivity coefficients (see Table 2.1.1) and keeping fixed the local size. The estimated dependence of the condition number from δ_t is in agreement (see Theorems 4.7.5 and 4.7.6) with the numerical results listed in Table 4.8, since for the natural coarse space we will have

$$\frac{\sigma_M \delta_t + H^2}{\min\{H^2, \sigma_m \delta_t\}} \approx \begin{cases} O(\delta_t) & \delta_t \to \infty \\ O\left(\delta_t^{-1}\right) & \delta_t \to 0 \end{cases}$$

PCG-BNN Schur Bidomain δ_t dependence

δ_t	1E-5	1E-4	1E-3	1E-2	1E-1	1E0	1E1	1E2	1E3	1E4
κ_2	2.71E2	29.17	5.26	3.79	3.82	4.81	9.34	19.45	1.27E2	1.23E3
κ_2^*	2.71E2	29.17	5.26	3.79	3.81	4.78	8.35	12.50	14.20	14.44

Table 4.8: Bidomain Schur complement δ_t dependence test for PCG-BNN solver with natural (κ_2) and enriched (κ_2^*) coarse space. Test case with 2x2x2 subdomains, $h = 0.01$, $H/h = 15$, conductivity coefficients as in Table 2.1.1, random right-hand side and null initial guess; PCG iteration is stopped when the initial preconditioned residual is reduced by a factor of 1E-6. For each run, time step δ_t and condition numbers are shown.

whereas for the enriched coarse space we will have

$$\max_{\bullet=i,e}\left(\frac{\sigma_M^{\bullet}\delta_t+H^2}{\sigma_m^{\bullet}\delta_t}\right)\begin{cases}O\left(1\right) & \delta_t\to\infty\\ \\ O\left(\delta_t^{-1}\right) & \delta_t\to 0\end{cases}.$$

Bidomain with jumping coefficients.

PCG-BNN Schur Bidomain
Jumping Coefficients

	A			**B**		
p	$\kappa_2(P_{BNN})$	$\kappa_2(P_{BNN}^*)$	$\kappa_2(\widehat{S}_\Gamma)$	$\kappa_2(P_{BNN})$	$\kappa_2(P_{BNN}^*)$	$\kappa_2(\widehat{S}_\Gamma)$
1	34.89	34.89	1.04E5	34.89	34.89	1.04E5
1E1	58.98	27.50	2.64E5	29.67	29.05	2.16E5
1E2	491.79	27.11	1.78E6	29.32	28.67	2.91E6
1E3	4840.13	27.11	div.	29.30	28.65	div.
1E4	48317.41	27.11	div.	29.30	28.65	div.

Table 4.9: Bidomain Schur complement dependence from jumps in the conductivity coefficient for PCG-BNN solver with natural and enriched coarse spaces. Test case with 3x3x3 subdomains, $h=0.01$, $H/h=15$, δ_t =1E-2, random right-hand side and null initial guess; PCG iteration is stopped when the initial residual is reduced by a factor of 1E-6. For each run, jumping factor p (see text for details) and condition number for the preconditioned P_{BNN}^{-1}, P_{BNN}^{*-1} and unpreconditioned $\widehat{S}_\Gamma$ operators are shown.

To analyze the jumping coefficients case, we will consider a 3x3x3 decomposition of the whole domain and a checkerboard pattern (see Figure 4.3) of discontinuities in the conductivity coefficients, with two different sets of discontinuities, but such that the ratio

$$\max_{\bullet=i,e}\left(\max_{j=1,\ldots,N}\frac{\sigma_M^{\bullet(j)}}{\sigma_m^{\bullet(j)}}\right).$$

will remain constant. We initially set the conductivity coefficients as $\sigma_l^{i,e}$ =1E1, $\sigma_t^{i,e}$ =1 and $\sigma_n^{i,e}$ =1E-1, then we consider a first test case, fixing a factor p and then multiplying each conductivity coefficient, either intra- or extracellular, by p in the black subdomains and by $1/p$ in the others. In the second test case, we multiply differently the intracellular and extracellular coefficients in the two coloured regions: in the black subdomains we multiply the intracellular conductivity coefficients by p and the extracellular ones by $1/p$. In the white subdomains we will do the viceversa. Numerical results are summarized in Table 4.9 using the natural and enriched coarse spaces: columns labelled by **A** refer to the

first type of discontinuity, whereas columns **B** refer to the second one. Results for the unpreconditioned Schur complement operator $\widehat{S}_\Gamma$ are also shown to give a comparison. For the natural coarse space, in case **A** the condition number depends linearly on the factor p and the preconditioned system diverges for large values of p. On the other hand, in case **B** the condition number with natural coarse space remains almost constant while varying largely p. As predicted by the theory, the enriched coarse space is robust for the jumping coefficients case and gives optimal results with respect to both cases considered.

Chapter 5

Balancing by Constraints (BDDC) preconditioner for the Bidomain model

5.1 Introduction

In this chapter we will introduce and analyze the Balancing Domain Decomposition by Constraints (BDDC) preconditioner for the Bidomain problem. BDDC methods can be regarded as an evolution of BNN methods where all local and coarse problems are treated additively and a proper set of primal continuity constraints across the interface of the subdomains is selected. These primal constraints can be point (vertex) constraints and averages over edges and/or faces of the subdomains. We will show that appropriate sets of primal constraints can be associated with the subdomain vertices, edges, and faces, so that the resulting BDDC methods have a fast convergence rate and we will prove that the condition number of the BDDC preconditioned operator of the cardiac Bidomain model depends only on the ratio H/h of subdomain to element diameters, while being independent of the number of subdomains. Parallel numerical results will confirm the theoretical estimates and illustrate the effects of the choice of the primal constraints. Numerical results will also show the independence of the condition number of the preconditioned Bidomain problem from large jumps in the conductivity coefficients aligned with the interface. We remark that the results obtained in this chapter will also apply to the related FETI-DP algorithms (see e.g. [36]) defined by the same set of primal constraints, since it is known that the BDDC and FETI-DP operators have the same eigenvalues with the exception of at most two ([79], [87], [11]). The BDDC algorithm has been extended to a variety of cases, including Gauss-Lobatto-Legendre (GLL) spectral elements in the scalar elliptic case ([103], [69]), mortar discretizations ([65], [66]), discontinuous Galerkin methods [32], advection-diffusion [141], indefinite problems [80], Reissner-Mindlin plates [8] and incompressible

Stokes [77]. We also developed a BDDC method for the three dimensional linear elasticity system in the almost incompressible case and discretized with GLL spectral elements [105]. For BDDC application to biomechanics problems see [70].

5.2 Dual and primal finite element spaces

An interface is defined similarly to Section 4.1 with a different treatment of the nodal values on the Neumann boundary of the global problem; in details, the nodal values defining the interface will remain the same but we will treat as edges the subdomain edges on the Neumann boundary and then define the vertices as endpoints of edges; figure 5.1 shows edges and vertices for this configuration (compare it with Figure 4.1).

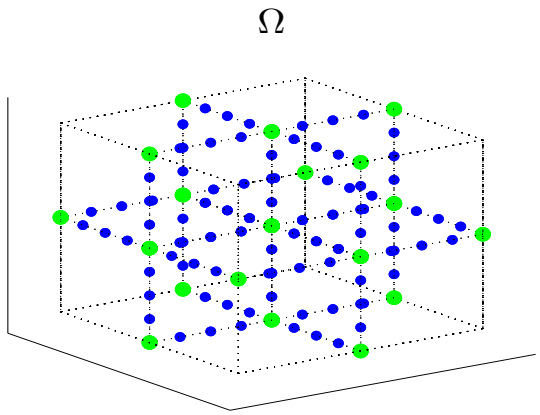

Figure 5.1: Edges nodes (blue circles) and vertices (green circles) for a 2x2x2 decopomposition of Ω and $H/h = 5$

A finite element space $\widetilde{\mathbf{W}}_\Gamma$, intermediate between $\widehat{\mathbf{W}}_\Gamma$ and $\mathbf{W}_\Gamma$, and constituted by partially continuous variables, can be defined by

$$\widetilde{\mathbf{W}}_\Gamma = \mathbf{W}_\Delta \bigoplus \widehat{\mathbf{W}}_\Pi$$

where $\widehat{\mathbf{W}}_\Pi$ is the continuous *primal* variable space, typically spanned by the discrete harmonic extensions with respect to a certain Schur complement $S_{\Pi\Pi}$ acting on subdomain corner nodal basis functions and/or selected edge and face averages. For details see Section 5.4. $\mathbf{W}_\Delta$ is the product space of the subdomain *dual* variable spaces

$$\mathbf{W}_\Delta = \prod_{j=1}^{N} \mathbf{W}_\Delta^{(j)}$$

which consist of functions with zero values at the primal degrees of freedom. The functions in the space $\widetilde{\mathbf{W}}_\Gamma$ will be continuous at the coarse primal level and discontinuous elsewhere across the subdomain interface.

Additional restriction and extension operators between the interface spaces need to be

defined. $R_{\Delta}^{(j)}$ is the restriction operator that extracts the subdomain part $\mathbf{W}_{\Delta}^{(j)}$ from the dual space $\mathbf{W}_{\Delta}$ and R_{Δ} is the direct sum of the $R_{\Delta}^{(j)}$ operators. Similarly, $R_{\Pi}^{(j)}$ extracts the subdomain component $\mathbf{W}_{\Pi}^{(j)}$ from the assembled primal space $\widehat{\mathbf{W}}_{\Pi}$, with R_{Π} the direct sum of the $R_{\Pi}^{(j)}$ operators. Furthermore, $R_{\Gamma\Delta}$ is the restriction operator from the space $\mathbf{W}_{\Gamma}$ onto the subspace $\mathbf{W}_{\Delta}$. For the analysis of the BDDC preconditioner, we will also need a jump operator P_D, complementary of the average operator already introduced in equation (4.3), defined as (see Lemma 6.10 in [140])

$$P_D = I - E_D. \tag{5.1}$$

Since

$$\sum_{k \in \mathcal{N}_x} \delta_k^{i,e\,\dagger}(x) = 1, \quad x \in \Gamma^{(i)}$$

for both the intra- and the extra-cellular components of the partition of unity, the local action of the jump operator an a given vector $w \in \mathbf{W}_{\Gamma}$ can be written as

$$(P_D w(x))_j = \left(\sum_{k \in \mathcal{N}_x} \delta_k^{i\,\dagger}(w_j^i(x) - w_k^i(x)) \, , \sum_{k \in \mathcal{N}_x} \delta_k^{e\,\dagger}(w_j^e(x) - w_k^e(x)) \right) \tag{5.2}$$

$\forall x \in \Gamma^{(j)}$.

5.3 Original formulation of the BDDC preconditioner

In this section we will briefly introduce the BDDC preconditioner as originally formulated in [30]. It is a two-level preconditioner such as the BNN preconditioner, but with BDDC the coarse (often referred to also as *primal*) and local problems are treated additively; the balancing procedure is performed by imposing a set of constraints on each substructure in order to guarantee existence and uniqueness of the local problems involved in the application of the preconditioner. The coarse-level problem is assembled from a special set of coarse basis functions, which are the minimum energy extension on the subdomains subject to sets of primal constraints: they usually represent continuity at the substructures corners plus common edge or face averages across the interface.

The action of the BDDC preconditioner can be written in the form:

$$M_{BDDC}^{-1} = R_{D,\Gamma}^T \left[P_{local} + P_{coarse} \right] R_{D,\Gamma}. \tag{5.3}$$

The coarse correction operator P_{coarse} is defined by

$$P_{coarse} = \Psi \left(\Psi^T S \Psi \right)^{-1} \Psi^T$$

where the coarse basis function matrix

$$\Psi = \begin{pmatrix} \Psi^{(1)} \\ \vdots \\ \Psi^{(N)} \end{pmatrix}$$

is determined by solving individual subdomain problems

$$\Psi = \underset{Cw=\mathcal{I}, w\in\mathbf{W}_\Gamma}{\operatorname{argmin}} \; w^T S w \tag{5.4}$$

where S is the unassembled Schur complement acting on the space $\mathbf{W}_\Gamma$ introduced in eq. (4.7) and $\mathcal{I}$ is a boolean matrix whose number of rows is the sum of the number of local constraints and whose number of columns is the global number of constraints. The non-zero values of a fixed column of $\mathcal{I}$ locally represents the constraint, since one global constraint corresponds to a set of constraints applied on different substructures. Therefore, the number of columns of the coarse basis function matrix Ψ equals the number of global constraints imposed. The local constraints are imposed through the matrix

$$C = \begin{pmatrix} C^{(1)} & & \\ & \ddots & \\ & & C^{(N)} \end{pmatrix}$$

with $C^{(j)}$ a rectangular matrix representing the primal constraints imposed on $\Gamma^{(j)}$; the number of rows of $C^{(j)}$ equals the number of local constraints and the number of columns equals the number of nodes on $\Gamma^{(j)}$.

Remark 5.3.1. Here we will construct the local constraint matrices $C^{(j)}$. Only a few values of a row of $C^{(j)}$ will be non-zero, namely those associated with the local constraint. For simplicity, we will consider only a single scalar component of the PDE: a generalization to vector valued PDEs is straightforward. We first reorder the local interface variables with faces first, then edges and last the vertex variables, i.e.

$$u_\Gamma^{(j)} = \left(u_{\mathcal{F}^1}, \ldots, u_{\mathcal{F}^{\mathcal{N}_\mathcal{F}}}, u_{\mathcal{E}^1}, \ldots, u_{\mathcal{E}^{\mathcal{N}_\mathcal{E}}}, u_{\mathcal{V}^1}, \ldots, u_{\mathcal{V}^{\mathcal{N}_\mathcal{V}}}\right)^T$$

where $\mathcal{N}_\mathcal{F}$, $\mathcal{N}_\mathcal{E}$ and $\mathcal{N}_\mathcal{V}$ are the number of local faces, edges and vertices respectively. If we require vertex constraints only, we will choose the matrix $C^{(j)}$ as

$$C^{(j)} = \begin{pmatrix} 0 & I_{\mathcal{N}_\mathcal{V}} \end{pmatrix}$$

with $I_{\mathcal{N}_\mathcal{V}}$ the identity matrix of size $\mathcal{N}_\mathcal{V}$. If we also require edge average constraints, then

$$C^{(j)} = \begin{pmatrix} 0 & C_{\mathcal{N}_\mathcal{E}} & 0 \\ 0 & 0 & I_{\mathcal{N}_\mathcal{V}} \end{pmatrix}$$

where $C_{\mathcal{N}_\mathcal{E}}$ is a rectangular matrix with $\mathcal{N}_\mathcal{E}$ rows and $\sum_k n_{\mathcal{E}^k}$ columns, with $n_{\mathcal{E}^k}$ the number of edge nodes for the k-th edge. Let α_i^k be the quadrature weights defined by the discretization of the one dimensional edge integral by the following nodal quadrature rule

$$\int_{\mathcal{E}^k} f \approx \sum_{i=1}^{n_{\mathcal{E}^k}} \alpha_i^k f(x_i^k)$$

where x_i^k are the nodes of the k-th edge. Each row of matrix $C_{\mathcal{N}_\mathcal{E}}$ impose the average constraints if we set it as

$$\left(0, \ldots, 0, \alpha_1^k, \ldots, \alpha_{n_{\mathcal{E}^k}}^k, 0, \ldots, 0\right).$$

Analogous arguments can be used to build the rows of matrix $C^{(j)}$ associated to the face averages.

The minimization problem (5.4) can be solved using the method of Lagrange multipliers introducing an equivalent saddle point formulation; the latter can be solved in parallel by solving individual subdomain problems with multiple right hand sides of type

$$\begin{pmatrix} S^{(j)} & C^{(j)^T} \\ C^{(j)} & 0 \end{pmatrix} \begin{pmatrix} \Psi^{(j)} \\ \Lambda^{(j)} \end{pmatrix} = \begin{pmatrix} 0 \\ \mathcal{I}^{(j)} \end{pmatrix} \tag{5.5}$$

where $\Lambda^{(j)}$ is a local matrix with columns made by the Lagrange multipliers and $\mathcal{I}^{(j)}$ the submatrix of $\mathcal{I}$ which has as many rows as the number of local constraints and as many columns as the number of global constraints.

The subdomain correction operator is defined by

$$P_{local} = \sum_{j=1}^{N} (R_\Gamma^{(j)^T} \quad 0) \begin{pmatrix} S^{(j)} & C^{(j)^T} \\ C^{(j)} & 0 \end{pmatrix}^{-1} \begin{pmatrix} R_\Gamma^{(j)^T} \\ 0 \end{pmatrix} \tag{5.6}$$

and it gives subdomain corrections for which all primal constraints vanish. Additional details on the solution of the saddle point problems appearing in formulas (5.5) and (5.6) will be given in the next chapter. Here we will adopt a different strategy, proposed in [79] to impose the primal constraints on the subdomains.

Remark 5.3.2. It must be noted that the choice of the primal constraints must guarantee the solvability of local saddle point problems given in (5.5). For the Bidomain system, vertex constraints are enough to guarantee existence and uniqueness of their solutions; the set of primal constraints must be enriched with additional averages on edges and faces in order to obtain a good bound on the condition number as a function of the substructures diameter.

5.4 BDDC with a change of basis

In this section we will introduce a reformulation of the BDDC preconditioner adopting the strategy proposed in [67]: we will perform a change of basis so that each primal constraint will correspond to an explicit degree of freedom; in this way we can work in the coarse primal space without enforcing any saddle point problem for the Lagrange multipliers as in eq. (5.5). We will briefly present how such a reformulation can be performed, and then we will reformulate the main ingredients of the BDDC preconditioner.

Consider the unknowns $u_{\mathcal{E}}$ on an edge $\mathcal{E}$ of a single scalar component of the PDE, and define a transformation matrix $T_{\mathcal{E}}$ that performs the change of basis from the coefficients in the new basis $\hat{u}_{\mathcal{E}}$ to the coefficients in the original nodal basis $u_{\mathcal{E}}$

$$T_{\mathcal{E}}\hat{u}_{\mathcal{E}} = u_{\mathcal{E}}.$$

To make explicit the edge average, we can choose matrix $T_{\mathcal{E}}$ as

$$T_{\mathcal{E}} = \begin{pmatrix} 1 & 0 & \dots & 0 & 1 \\ & \ddots & & & \vdots \\ & & 1 & & 1 \\ & & & \ddots & \vdots \\ -\frac{\alpha_1}{\alpha_n} & \dots & \dots & -\frac{\alpha_{n-1}}{\alpha_n} & 1 \end{pmatrix}$$

where n is the number of edge nodes and α_i the quadrature weights of the one dimensional nodal quadrature rule of the edge integral. We will thus have

$$u_{\mathcal{E}} = \hat{u}_n \begin{pmatrix} 1 \\ \vdots \\ 1 \end{pmatrix} + \begin{pmatrix} \hat{u}_1 \\ \vdots \\ \hat{u}_{n-1} \\ -\sum_{i=1}^{n-1} \frac{\alpha_i}{\alpha_n}\hat{u}_i \end{pmatrix}$$

splitting the dofs of the original basis in a sum of a constant function (represented by the last coefficient of the edge $\hat{u}_n$ in the new basis) and another function with vanishing average. For structured equispaced grids like that generated by using $Q1$ elements, the quadrature weights are the same, that is

$$\frac{\alpha_i}{\alpha_n} = 1 \;\; \forall i = 1, \dots, n-1.$$

Analogous transformation matrices $T_{\mathcal{F}}$ can be defined for the implementation of the face constraints. As for the edges, the last element of the dual part of each scalar component on a face can be chosen as primal, and face averages can be obtained with a transformation matrix structurally similar to $T_{\mathcal{E}}$: the elements on the main diagonal and in the last column are equal to one, while the other values are all zero except for the last row, associated

with the new primal degrees of freedom, which are given by the ratios α_i/α_n with α_i the quadrature weights of the two-dimensional quadrature rule employed and n the number of nodes of $\mathcal{F}$.

All the transformations introduced can be constructed separately for each component of the solution on each face and edge of the substructure interface $\Gamma^{(j)}$: since this is a local procedure it can be carried out face by face and edge by edge, as long as the sets of variables being transformed do not contain any common degrees of freedom, a condition satisfied by definition of the interface points. Denoting with $T^{(j)}$ the resulting transformation of basis, a local linear system for the j-th substructure

$$A^{(j)}u^{(j)} = f^{(j)}$$

can be equivalently written as

$$\overline{A}^{(j)}\hat{u}^{(j)} = {T^{(j)}}^T A^{(j)} T^{(j)}\hat{u}^{(j)} = {T^{(j)}}^T f^{(j)}$$

with

$$\overline{A}^{(j)} = \begin{pmatrix} A_{II}^{(j)} & \overline{A}_{I\Delta}^{(j)} & \overline{A}_{I\Pi}^{(j)} \\ {\overline{A}_{I\Delta}^{(j)}}^T & \overline{A}_{\Delta\Delta}^{(j)} & \overline{A}_{\Delta\Pi}^{(j)} \\ {\overline{A}_{I\Pi}^{(j)}}^T & {\overline{A}_{\Delta\Pi}^{(j)}}^T & \overline{A}_{\Pi\Pi}^{(j)} \end{pmatrix}.$$

Here the superscript Π defines the new explicit dofs representing vertex constraints, edge and faces averages. The resulting matrix $\overline{A}^{(j)}$ will be denser than the original stiffness matrix $A^{(j)}$ but only the blocks related to the interface degrees of freedom will be affected by the transformation, while the block corresponding to the subdomain interior degrees of freedom will not. From now on, in this chapter we will assume that the subdomain variables have been changed when primal vertices, edges or faces are used and we will drop the bar superscript in the following formulas. For additional details see [67].

Once we have changed the local variables, the Lagrange multipliers are no longer needed to enforce the primal continuity constraints and no saddle point problems must be solved in practice (see also [79]). Equation (5.5) is thus replaced by a Schur complement argument on the local primal nodes

$$\begin{pmatrix} A_{II}^{(j)} & A_{I\Delta}^{(j)} & A_{I\Pi}^{(j)} \\ {A_{I\Delta}^{(j)}}^T & A_{\Delta\Delta}^{(j)} & A_{\Delta\Pi}^{(j)} \\ {A_{I\Pi}^{(j)}}^T & {A_{\Delta\Pi}^{(j)}}^T & A_{\Pi\Pi}^{(j)} \end{pmatrix} \begin{pmatrix} w_I^{(j)} \\ \Psi_\Delta^{(j)} \\ R_\Pi^{(j)} \end{pmatrix} = \begin{pmatrix} 0 \\ 0 \\ S_{\Pi\Pi}^{(j)} R_\Pi^{(j)} \end{pmatrix} \tag{5.7}$$

where the coarse basis functions spanning $\widehat{\mathbf{W}}_\Pi$ are the columns of the matrix

$$\Psi = \begin{pmatrix} \Psi^{(1)} \\ \vdots \\ \Psi^{(N)} \end{pmatrix}$$

which are given subdomainwise by

$$\Psi^{(j)} = \begin{pmatrix} \Psi_{\Delta}^{(j)} \\ R_{\Pi}^{(j)} \end{pmatrix}.$$

The number of columns of each $\Psi^{(j)}$ is the same as the number of global coarse-level degrees of freedom. Only a few columns of each $\Psi^{(j)}$ are non-zero namely those supported in $\Gamma^{(j)}$. To compute a non-zero column of $\Psi^{(j)}$, a subdomain Neumann problem is solved subject to the given primal constraint, which corresponds to a non-zero column of the matrix $R_{\Pi}^{(j)}$. We can see from equation (5.7), that each non-zero column of $\Psi^{(j)}$ is the minimum energy extension to the substructure Ω_j setting one of the primal constraints equal to 1 and all others equal to 0. The dual part of the local matrices $\Psi^{(j)}$ can thus be compactly written as the following problem with multiple right hand sides

$$\Psi_{\Delta}^{(j)} = \begin{pmatrix} 0 & -I_{\Delta}^{(j)} \end{pmatrix} \begin{pmatrix} A_{II}^{(j)} & A_{I\Delta}^{(j)} \\ A_{I\Delta}^{(j)^T} & A_{\Delta\Delta}^{(j)} \end{pmatrix}^{-1} \begin{pmatrix} A_{I\Pi}^{(j)} \\ A_{\Delta\Pi}^{(j)} \end{pmatrix} R_{\Pi}^{(j)}.$$

The subdomain contribution $S_{\Pi\Pi}^{(j)}$ to the operator $S_{\Pi\Pi}$, the Schur complement assembled at the primal nodes, can be written

$$S_{\Pi\Pi}^{(j)} = A_{\Pi\Pi}^{(j)} - \begin{pmatrix} A_{I\Pi}^T & A_{\Delta\Pi}^T \end{pmatrix} \begin{pmatrix} A_{II}^{(j)} & A_{I\Delta}^{(j)} \\ A_{I\Delta}^{(j)^T} & A_{\Delta\Delta}^{(j)} \end{pmatrix}^{-1} \begin{pmatrix} A_{I\Pi}^{(j)} \\ A_{\Delta\Pi}^{(j)} \end{pmatrix}.$$

Moreover, since from eq. (5.7) and the definition of the local Schur complement $S^{(j)}$ given in Lemma 4.2.3 follows that

$$S^{(j)}\Psi^{(j)} = \begin{pmatrix} 0 \\ S_{\Pi\Pi}^{(j)} R_{\Pi}^{(j)} \end{pmatrix},$$

it can be shown that

$$\Psi^T S \Psi = \sum_{j=1}^{N} \Psi^{(j)^T} S^{(j)} \Psi^{(j)} = \sum_{j=1}^{N} R_{\Pi}^{(j)^T} S_{\Pi\Pi}^{(j)} R_{\Pi}^{(j)} = S_{\Pi\Pi}. \tag{5.8}$$

Since, changing variables, we can enforce zero primal constraints by simply restricting the operators to the dual interface space $\mathbf{W}_{\Delta}$, the subdomain correction operator given in eq. (5.6) can be equivalently expressed as

$$P_{local} = R_{\Gamma\Delta}^T S_{\Delta}^{-1} R_{\Gamma\Delta} \tag{5.9}$$

where the action of the Schur complement S_Δ on the product space $\mathbf{W}_\Delta$

$$S_\Delta = \begin{pmatrix} S_\Delta^{(1)} & & \\ & \ddots & \\ & & S_\Delta^{(N)} \end{pmatrix}$$

is defined by

$$\begin{pmatrix} A_{II}^{(1)} & A_{I\Delta}^{(1)} & & & \\ {A_{I\Delta}^{(1)}}^T & A_{\Delta\Delta}^{(1)} & & & \\ & & \ddots & & \\ & & & A_{II}^{(N)} & A_{I\Delta}^{(N)} \\ & & & {A_{I\Delta}^{(N)}}^T & A_{\Delta\Delta}^{(N)} \end{pmatrix} \begin{pmatrix} w_I^{(1)} \\ w_\Delta^{(1)} \\ \vdots \\ w_I^{(N)} \\ w_\Delta^{(N)} \end{pmatrix} = \begin{pmatrix} 0 \\ S_\Delta^{(1)} w_\Delta^{(1)} \\ \vdots \\ 0 \\ S_\Delta^{(N)} w_\Delta^{(N)} \end{pmatrix}. \tag{5.10}$$

Remark 5.4.1. The primal problem of the BDDC operator will be singular for the Bidomain model using vertex and/or edge averages and/or face averages primal constraints. In fact, let $\mathbf{1}_{\Pi^{(j)}}$ be the vector of local primal constraints equal to one and suppose to use only vertex constraints for both the components of the solution. Then $\Psi^{(j)}\mathbf{1}_{\Pi^{(j)}}$ will be a vector of $\mathbf{W}_\Gamma^{(j)}$ with all ones at the vertices. Therefore, since each local contribution $S_{\Pi\Pi}^{(j)}$ to the primal problem is the Schur complement of $S^{(j)}$ at the local primal nodes we will have

$$\mathbf{1}_{\Pi^{(j)}}^T S_{\Pi\Pi}^{(j)} \mathbf{1}_{\Pi^{(j)}} = \mathbf{1}_{\Pi^{(j)}}^T {\Psi^{(j)}}^T S^{(j)} \Psi^{(j)} \mathbf{1}_{\Pi^{(j)}} \leq \mathbf{1}_{\Gamma^{(j)}}^T S^{(j)} \mathbf{1}_{\Gamma^{(j)}} = 0$$

and thus $S_{\Pi\Pi}^{(j)}$ will be singular with a null space spanned by the constant vectors. Analogous arguments will be valid if we use the same set of edge and/or face averages, even without vertex constraints, noting that a function with constant average on an edge (or a face) and zero values at the dual nodes will represent the constant function on that edge (or face) in the original dof basis. It must be noted that the singularity of the primal problem is not harmful for the BDDC operator as long as the primal system is consistent, that is, the primal right-hand side does not have any component onto the null space of $S_{\Pi\Pi}$.

Using eqs. (5.9) and (5.8), the action of the BDDC preconditioner given in eq. (5.3) can than be reformulated as

$$M_{BDDC}^{-1} = R_{D,\Gamma}^T \left[R_{\Gamma\Delta}^T S_\Delta^{-1} R_{\Gamma\Delta} + \Psi S_{\Pi\Pi}^\dagger \Psi^T \right] R_{D,\Gamma} \tag{5.11}$$

where we employ the pseudoinverse of $S_{\Pi\Pi}$ taking into account its singularity.

5.5 Bidomain theoretical estimates

In this section we will give estimates for the preconditioned operator $M_{BDDC}^{-1}\widehat{S}_\Gamma$. As for the Neumann-Neumann preconditioners, we will estimate its condition number κ_2 as the

ratio of the largest and smallest eigenvalues of the generalized Rayleigh quotient

$$\lambda_m \mathcal{S}(u_\Gamma, u_\Gamma) \leq \mathcal{S}(M_{BDDC}^{-1}\widehat{S}_\Gamma u_\Gamma, u_\Gamma) \leq \lambda_M \mathcal{S}(u_\Gamma, u_\Gamma), \quad \forall u_\Gamma \in \widehat{\mathbf{W}}_\Gamma, u_\Gamma \neq 0_{\widehat{\mathbf{W}}_\Gamma}.$$

We will follow the approach of [87]: the following Lemmas can be found in the latter reference.

Lemma 5.5.1. *The local partially continuous space $\widetilde{\boldsymbol{W}}_\Gamma^{(j)} = \boldsymbol{W}_\Delta^{(j)} \bigoplus \boldsymbol{W}_\Pi^{(j)}$ is s_j-orthogonal, that is*

$$s_j(w_\Delta^{(j)}, w_\Pi^{(j)}) = 0$$

with $w = w_\Delta^{(j)} + w_\Pi^{(j)}$, where $w_\Pi^{(j)} = \Psi^{(j)} w_c$ with w_c a vector of primal dofs, or equivalently

$$s_j(w, w) = s_j(w_\Delta^{(j)}, w_\Delta^{(j)}) + s_j(w_\Pi^{(j)}, w_\Pi^{(j)}).$$

Proof. Using eq. (5.7), we obtain

$$\begin{aligned} s_j(w_\Delta^{(j)}, \Psi^{(j)} w_c) &= \begin{pmatrix} 0 & w_\Delta^{(j)^T} & 0 \end{pmatrix} \begin{pmatrix} A_{II}^{(j)} & A_{I\Delta}^{(j)} & A_{I\Pi}^{(j)} \\ A_{I\Delta}^{(j)^T} & A_{\Delta\Delta}^{(j)} & A_{\Delta\Pi}^{(j)} \\ A_{I\Pi}^{(j)^T} & A_{\Delta\Pi}^{(j)^T} & A_{\Pi\Pi}^{(j)} \end{pmatrix} \begin{pmatrix} w_I^{(j)} \\ \Psi_\Delta^{(j)} \\ R_\Pi^{(j)} \end{pmatrix} w_c \\ &= \begin{pmatrix} 0 & w_\Delta^{(j)^T} & 0 \end{pmatrix} \begin{pmatrix} 0 \\ 0 \\ S_{\Pi\Pi}^{(j)} R_\Pi^{(j)} \end{pmatrix} w_c = 0. \end{aligned}$$

□

Lemma 5.5.2. *The preconditioned operator $M_{BDDC}^{-1}\widehat{S}_\Gamma$ satisfies $\forall u_\Gamma \in \widehat{\boldsymbol{W}}_\Gamma$*

$$M_{BDDC}^{-1}\widehat{S}_\Gamma u_\Gamma = R_{D,\Gamma}^T w$$

with $w \in \widetilde{\boldsymbol{W}}_\Gamma$ defined by

$$v^T S w = v^T R_{D,\Gamma} \widehat{S}_\Gamma u_\Gamma = \mathcal{S}(u_\Gamma, R_{D,\Gamma}^T v)$$

$\forall v \in \widetilde{\boldsymbol{W}}_\Gamma$.

Proof. Using eq. (5.11), we can see that the action of the BDDC preconditioner on a given residual vector r can be obtained as

$$M_{BDDC}^{-1} r = R_{D,\Gamma}^T (R_{\Gamma\Delta}^T w_\Delta + w_\Pi)$$

where $w_\Pi = \Psi w_c$ with

$$\begin{aligned} \Psi^T S \Psi w_c &= \Psi^T R_{D,\Gamma} r \\ S_\Delta w_\Delta &= R_{\Gamma\Delta} R_{D,\Gamma} r. \end{aligned} \tag{5.12}$$

Let $v \in \widetilde{\mathbf{W}}_\Gamma$, $v = R_{\Gamma\Delta}^T v_\Delta + v_\Pi$ with $v_\Pi = \Psi v_c$; using the s_j-orthogonality of local subspaces $\mathbf{W}_\Delta^{(j)}$ and $\mathbf{W}_\Pi^{(j)}$ given in Lemma 5.5.1 it follows that

$$\begin{aligned} v^T S w &= \sum_{j=1}^N s_j(v_\Delta^{(j)} + \Psi^{(j)} v_c, w_\Delta^{(j)} + \Psi^{(j)} w_c) \\ &= \sum_{j=1}^N \Big(s_j(v_\Delta^{(j)}, w_\Delta^{(j)}) + s_j(\Psi^{(j)} v_c, \Psi^{(j)} w_c) \Big) \\ &= v_\Delta^T R_{\Gamma\Delta} S R_{\Gamma\Delta}^T w_\Delta + v_\Pi^T S w_\Pi. \end{aligned}$$

Letting $r = \widehat{S} u_\Gamma$, from the first equation in (5.12) it follows

$$v_\Pi^T S w_\Pi = v_\Pi^T R_{D,\Gamma} \widehat{S}_\Gamma u_\Gamma. \tag{5.13}$$

For the second equation we can deal with the subdomain component of w_Δ and, recalling the definition of $S_\Delta^{(j)}$ given in eq (5.10) we obtain:

$$\begin{aligned} (v_\Delta^{(j)^T} \quad 0) S^{(j)} \begin{pmatrix} w_\Delta^{(j)} \\ 0 \end{pmatrix} &= (0 \quad v_\Delta^{(j)^T} \quad 0) \begin{pmatrix} A_{II}^{(j)} & A_{I\Delta}^{(j)} & A_{I\Pi}^{(j)} \\ A_{I\Delta}^{(j)^T} & A_{\Delta\Delta}^{(j)} & A_{\Delta\Pi}^{(j)} \\ A_{I\Pi}^{(j)^T} & A_{\Delta\Pi}^{(j)^T} & A_{\Pi\Pi}^{(j)} \end{pmatrix} \begin{pmatrix} w_I^{(j)} \\ w_\Delta^{(j)} \\ 0 \end{pmatrix} \\ &= (0 \quad v_\Delta^{(j)^T} \quad 0) \begin{pmatrix} 0 \\ S_\Delta^{(j)} w_\Delta^{(j)} \\ A_{I\Pi}^{(j)^T} w_I^{(j)} + A_{\Delta\Pi}^{(j)^T} w_\Delta^{(j)} \end{pmatrix} = v_\Delta^{(j)^T} S_\Delta^{(j)} w_\Delta^{(j)} \end{aligned}$$

and thus from the second equation of (5.12) and the fact that $S_\Delta = R_{\Gamma\Delta} S R_{\Gamma\Delta}^T$ we obtain

$$v_\Delta^T R_{\Gamma\Delta} S R_{\Gamma\Delta}^T w_\Delta = v_\Delta^T S_\Delta w_\Delta = v_\Delta^T R_{\Gamma\Delta} R_{D,\Gamma} \widehat{S}_\Gamma u_\Gamma. \tag{5.14}$$

The thesis then follows by summing the contributions (5.13) and (5.14). □

Remark 5.5.3. Since

$$E_D u_\Gamma = R_\Gamma^T R_{D,\Gamma} u_\Gamma = u_\Gamma \quad \forall u_\Gamma \in \widehat{\mathbf{W}}_\Gamma,$$

we can assert that the average operator is a projector on $\widetilde{\mathbf{W}}_\Gamma$, i.e.

$$E_D^2 = E_D.$$

As in [87], we will use an additional result between complementary projectors which can be found in [57], which assures that

$$|E_D w|_S^2 = |(I - E_D) w|_S^2 \tag{5.15}$$

$\forall w \in \widetilde{\mathbf{W}}_\Gamma$, noting that the Bidomain seminorm $|\cdot|_S^2$ is actually and inner product on $\widetilde{\mathbf{W}}_\Gamma$,

since the latter space doesn't contain any local constant function. For additional properties of average and jump operators, see [140] and [87].

Remark 5.5.4. For BDDC estimates we will consider discontinuous conductivity coefficients for both the intra- and extracellular diffusion tensors, with jumps aligned with the substructures interface. As partition of unity, we will use

$$\delta_j^{i\,\dagger}(x) = \frac{\sigma_M^{i^{(j)}}}{\sum_{k\in\mathcal{N}_x}\sigma_M^{i^{(k)}}}\,, \quad \delta_j^{e\,\dagger}(x) = \frac{\sigma_M^{e^{(j)}}}{\sum_{k\in\mathcal{N}_x}\sigma_M^{e^{(k)}}}$$

where $\sigma_M^{i^{(j)}}$ is the maximum eigenvalue of the intracellular diffusion tensor for the j-th substructure; clearly the same notation will hold for the extracellular part of the partition of unity. We will use an elementary result proved in [140], that is

$$\sigma_M^{i,e^{(j)}}\,{\delta_k^{i,e}}^{\dagger\,2} \leq \min\{\sigma_M^{i,e^{(j)}}, \sigma_M^{i,e^{(k)}}\}. \tag{5.16}$$

Finally, we will need an estimate of the norm of the jump operator P_D defined in (5.2) on the subspace $\widetilde{\mathbf{W}}_\Gamma$.

Lemma 5.5.5. *If edge and face averages are included in the primal space $\widehat{\boldsymbol{W}}_\Pi$ for both the intra- and extracellular components together with vertex constraints, the jump operator P_D satisfies:*

$$|P_D w|_S^2 \lesssim \max_{\bullet=i,e}\left(\max_{j=1,\dots,N}\frac{\sigma_M^{\bullet^{(j)}}\delta_t + H^2}{\sigma_m^{\bullet^{(j)}}\delta_t}\right)(1+\log(H/h))^2|w|_S^2$$

$\forall w \in \widetilde{\boldsymbol{W}}_\Gamma$.

Proof. As already done in the previous chapter, we will estimate the contribution of each substructure, namely

$$\begin{aligned} v(x)_j &:= (P_D w(x))_j \\ &= \left(\sum_{k\in\mathcal{N}_x} I^h({\delta_k^i}^\dagger(x)(w_j^i(x) - w_k^i(x))), \sum_{k\in\mathcal{N}_x} I^h(\delta_k^{e\,\dagger}(x)(w_j^e(x) - w_k^e(x)))\right) \\ &= \sum_{\mathcal{F}\subset\Gamma^{(j)}} I^h(\Theta_{\mathcal{F}} v_j) + \sum_{\mathcal{E}\subset\Gamma^{(j)}} I^h(\Theta_{\mathcal{E}} v_j). \end{aligned}$$

where $\Theta_\bullet v_j = (\vartheta_\bullet v_j^i, \vartheta_\bullet v_j^e)$, with the definitions of the cutoff functions $\vartheta_\bullet$ provided in Section 4.3. Note that the vertex component of the previous summation vanishes; in fact, since we consider vertex constraints in the primal space, it will hold that $w_j^i(x) = w_k^i(x)$ and $w_j^e(x) = w_k^e(x)\ \forall x \in \mathcal{V}$ and $j,k \in \mathcal{N}_x$. Therefore, we need to bound only the face and edge components.

Face terms. Using the same arguments used in Lemmas 4.5.2 and 4.7.3 we can bound

$$\begin{aligned}
|I^h(\Theta_{\mathcal{F}}v_j)|^2_{S^{(j)}} \lesssim\ & \sigma_M^{i^{(j)}}|I^h(\vartheta_{\mathcal{F}}v_j^i)|^2_{H^{1/2}(\Gamma^{(j)})} + H^2\gamma|I^h(\vartheta_{\mathcal{F}}v_j^i)|^2_{H^{1/2}(\Gamma^{(j)})} \\
& + \sigma_M^{e^{(j)}}|I^h(\vartheta_{\mathcal{F}}v_j^e)|^2_{H^{1/2}(\Gamma^{(j)})} + H^2\gamma|I^h(\vartheta_{\mathcal{F}}v_j^i)|^2_{H^{1/2}(\Gamma^{(j)})} \\
\lesssim\ & \sigma_M^{i^{(j)}}||I^h(\vartheta_{\mathcal{F}}v_j^i)||^2_{H^{1/2}_{00}(\mathcal{F})} + H^2\gamma||I^h(\vartheta_{\mathcal{F}}v_j^i)||^2_{H^{1/2}_{00}(\mathcal{F})} \\
& + \sigma_M^{e^{(j)}}||I^h(\vartheta_{\mathcal{F}}v_j^e)||^2_{H^{1/2}_{00}(\mathcal{F})} + H^2\gamma||I^h(\vartheta_{\mathcal{F}}v_j^e)||^2_{H^{1/2}_{00}(\mathcal{F})} \\
\lesssim\ & \sigma_M^{i^{(j)}}{\delta_k^i}^{\dagger^2}||I^h(\vartheta_{\mathcal{F}}(w_j^i - w_k^i))||^2_{H^{1/2}_{00}(\mathcal{F})} \\
& + H^2\gamma{\delta_k^i}^{\dagger^2}||I^h(\vartheta_{\mathcal{F}}(w_j^i - w_k^i))||^2_{H^{1/2}_{00}(\mathcal{F})} \\
& + \sigma_M^{e^{(j)}}{\delta_k^e}^{\dagger^2}||I^h(\vartheta_{\mathcal{F}}(w_j^e - w_k^e))||^2_{H^{1/2}_{00}(\mathcal{F})} \\
& + H^2\gamma{\delta_k^e}^{\dagger^2}||I^h(\vartheta_{\mathcal{F}}(w_j^e - w_k^e))||^2_{H^{1/2}_{00}(\mathcal{F})}
\end{aligned}$$

Let $\overline{w}_{\mathcal{F}}^{i,e}$ be the face average values common between the j-th and k-th substructure of the intra- and the extracellular component. From the hypothesis, the faces averages are included in the primal space, thus for the triangle inequality

$$\begin{aligned}
||I^h(\vartheta_{\mathcal{F}}(w_j^{i,e} - w_k^{i,e}))||^2_{H^{1/2}_{00}(\mathcal{F})} &= ||I^h(\vartheta_{\mathcal{F}}(w_j^{i,e} - \overline{w}_{\mathcal{F}}^{i,e} - w_k^{i,e} + \overline{w}_{\mathcal{F}}^{i,e}))||^2_{H^{1/2}_{00}(\mathcal{F})} \\
&\lesssim ||I^h(\vartheta_{\mathcal{F}}(w_j^{i,e} - \overline{w}_{\mathcal{F}}^{i,e}))||^2_{H^{1/2}_{00}(\mathcal{F})} \\
&\quad + ||I^h(\vartheta_{\mathcal{F}}(w_k^{i,e} - \overline{w}_{\mathcal{F}}^{i,e}))||^2_{H^{1/2}_{00}(\mathcal{F})}
\end{aligned}$$

We will thus have for the face terms using the second equation of Lemma 4.3.7 and eq. (5.16)

$$\begin{aligned}
(1+\log(H/h))^{-2}|I^h(\Theta_{\mathcal{F}}v_j)|^2_{S^{(j)}} \lesssim\ & (\sigma_M^{i^{(j)}} + H^2\gamma)|(\mathcal{H}_j w_j)^i|_{H^1(\Omega_j)} \\
& + (\sigma_M^{e^{(j)}} + H^2\gamma)|(\mathcal{H}_j w_j)^e|_{H^1(\Omega_j)} \\
& + (\sigma_M^{i^{(k)}} + H^2\gamma)|(\mathcal{H}_k w_k)^i|_{H^1(\Omega_k)} \\
& + (\sigma_M^{e^{(k)}} + H^2\gamma)|(\mathcal{H}_k w_k)^e|_{H^1(\Omega_k)}.
\end{aligned}$$

Therefore, for the face terms, we obtain

$$|I^h(\Theta_{\mathcal{F}}v_j)|^2_{S^{(j)}} \lesssim \max_{\bullet=i,e}\left(\max_{l=j,k}\frac{\sigma_M^{\bullet^{(l)}}\delta_t + H^2}{\sigma_m^{\bullet^{(l)}}\delta_t}\right)(1+\log(H/h))^2\left(|w|^2_{S^{(j)}} + |w|^2_{S^{(k)}}\right). \tag{5.17}$$

Edge terms. We can prooced as in Lemma 4.5.2, and, since the edge averages are included in the primal space, we can exploit the same arguments used before for the face terms.

Therefore, from the second equation of Lemma 4.3.8 we conclude that

$$|I^h(\Theta_{\mathcal{F}} v_j)|^2_{S^{(j)}} \lesssim \max_{\bullet=i,e} \left(\max_{k \in \mathcal{K}_{\mathcal{E}}} \frac{\sigma_M^{\bullet^{(k)}} \delta_t + H^2}{\sigma_m^{\bullet^{(k)}} \delta_t} \right) (1 + \log(H/h)) \sum_{k \in \mathcal{K}_{\mathcal{E}}} |w|^2_{S^{(k)}} \tag{5.18}$$

where $\mathcal{K}_{\mathcal{E}}$ is the set of subdomain indices sharing edge $\mathcal{E}$.

The thesis then follows by summing over faces and edges of Ω_j and then over the substructures. □

We are then ready to prove the following:

Theorem 5.5.6. *If edge and face averages are included in the primal space $\widehat{\mathbf{W}}_\Pi$ for both the intra- and extracellular components together with vertex constraints, the condition number of the preconditioned operator $M^{-1}_{BDDC}\widehat{S}_\Gamma$ for the Bidomain model satisfies:*

$$\kappa_2(M^{-1}_{BDDC}\widehat{S}_\Gamma) \lesssim \max_{\bullet=i,e} \left(\max_{j=1,\dots,N} \frac{\sigma_M^{\bullet^{(j)}} \delta_t + H^2}{\sigma_m^{\bullet^{(j)}} \delta_t} \right) (1 + \log(H/h))^2. \tag{5.19}$$

Proof. **Lower bound.** Since

$$R_\Gamma^T R_{D,\Gamma} u_\Gamma = R_{D,\Gamma}^T R_\Gamma u_\Gamma = u_\Gamma \quad \forall u_\Gamma \in \widehat{\mathbf{W}}_\Gamma,$$

we have by using Lemma 5.5.2, with w defined in Lemma 5.5.2 and $v = R_\Gamma u_\Gamma \in \widetilde{\mathbf{W}}_\Gamma$,

$$\begin{aligned} \mathcal{S}(u_\Gamma, u_\Gamma) &= \mathcal{S}(u_\Gamma, R_{D,\Gamma}^T R_\Gamma u_\Gamma) \\ &= u_\Gamma^T R_\Gamma^T S w \\ &\leq (w^T S w)^{1/2} (u_\Gamma^T R_\Gamma^T S R_\Gamma u_\Gamma)^{1/2} \\ &= |w|_S \ |R_\Gamma u_\Gamma|_S \end{aligned} \tag{5.20}$$

where we have used the Cauchy-Schwarz inequality applied to the inner product generated by the Schur complement S acting on the product space $\mathbf{W}_\Gamma$. Setting $v = w \in \widetilde{\mathbf{W}}_\Gamma$ and using again Lemma 5.5.2 we can rewrite

$$|w|_S^2 = \mathcal{S}(u_\Gamma, R_{D,\Gamma}^T w) = \mathcal{S}(u_\Gamma, M^{-1}_{BDDC}\widehat{S}_\Gamma u_\Gamma). \tag{5.21}$$

By subassembly, we also get

$$|R_\Gamma u_\Gamma|_S^2 = \mathcal{S}(u_\Gamma, u_\Gamma). \tag{5.22}$$

Substituting (5.21) and (5.22) into (5.20), canceling the common terms and squaring we obtain

$$\mathcal{S}(u_\Gamma, u_\Gamma) \leq \mathcal{S}(u_\Gamma, M^{-1}_{BDDC}\widehat{S}_\Gamma u_\Gamma)$$

and thus $\lambda_{min} \geq 1$.

Upper bound. For the upper bound, since by subassembly it holds

$$\mathcal{S}(M_{BDDC}^{-1}\widehat{S}_\Gamma u_\Gamma, M_{BDDC}^{-1}\widehat{S}_\Gamma u_\Gamma) = |R_\Gamma M_{BDDC}^{-1}\widehat{S}_\Gamma u_\Gamma|_S^2$$

using the definition of $|\cdot|_S$, w and eq. (5.21) we get

$$\begin{aligned}|R_\Gamma M_{BDDC}^{-1}\widehat{S}_\Gamma u_\Gamma|_S^2 = |R_\Gamma R_{D,\Gamma}^T w|_S^2 = |E_D w|_S^2 \leq |w|_S^2 \sup_{w\in\widetilde{\mathbf{W}}_\Gamma} \frac{|E_D w|_S^2}{|w|_S^2} \\ \lesssim \sup_{w\in\widetilde{\mathbf{W}}_\Gamma} \frac{|E_D w|_S^2}{|w|_S^2}\, \mathcal{S}(u_\Gamma, M_{BDDC}^{-1}\widehat{S}_\Gamma u_\Gamma).\end{aligned}$$

Now, using eq. (5.15), the definition of the jump operator (5.1) and Lemmma 5.5.5 we obtain

$$|R_\Gamma M_{BDDC}^{-1}\widehat{S}_\Gamma u_\Gamma|_S^2 \lesssim \max_{\bullet=i,e}\left(\max_{j=1,\dots,N} \frac{\sigma_M^{\bullet(j)}\delta_t + H^2}{\sigma_m^{\bullet(j)}\delta_t}\right)(1+\log(H/h))^2\, \mathcal{S}(u_\Gamma, M_{BDDC}^{-1}\widehat{S}_\Gamma u_\Gamma).$$

Since for the Cauchy-Schwarz inequality it holds that

$$\mathcal{S}(u_\Gamma, M_{BDDC}^{-1}\widehat{S}_\Gamma u_\Gamma) \leq \mathcal{S}(u_\Gamma, u_\Gamma)^{1/2}\mathcal{S}(M_{BDDC}^{-1}\widehat{S}_\Gamma u_\Gamma, M_{BDDC}^{-1}\widehat{S}_\Gamma u_\Gamma)^{1/2}$$

using subassebly relations and a little algebra (see [87] for additional details) we can prove

$$\mathcal{S}(u_\Gamma, M_{BDDC}^{-1}\widehat{S}_\Gamma u_\Gamma) \lesssim \max_{\bullet=i,e}\left(\max_{j=1,\dots,N} \frac{\sigma_M^{\bullet(j)}\delta_t + H^2}{\sigma_m^{\bullet(j)}\delta_t}\right)(1+\log(H/h))^2\mathcal{S}(u_\Gamma, u_\Gamma)$$

and thus

$$\lambda_{max} \lesssim \max_{\bullet=i,e}\left(\max_{j=1,\dots,N} \frac{\sigma_M^{\bullet(j)}\delta_t + H^2}{\sigma_m^{\bullet(j)}\delta_t}\right)(1+\log(H/h))^2.$$

□

5.6 Numerical results

In this section we will give additional details on the implementation of the BDDC preconditioner and some numerical results to confirm our theoretical estimates. Regarding to the implementational aspects, many details have been already given in Section 4.8; here we will only treat the implementational aspects related to the primal elements of the BDDC preconditioner. The coarse basis functions are first assembled locally, then the local part of the coarse matrix is evaluated using eq. (5.8) and a parallel matrix is assembled summing properly the local contributions. Local-to-global and global-to-local operations associated to the parallel coarse vectors are performed using the VecScatter objects provided by PETSc; we then use the parallel LU factorization provided by the MUMPS library [92] in order to solve exactly the primal problem at each application of the preconditioner. We note that we can also use a different solving approach to the coarse problem, replicating

the coarse matrix and then solving the coarse problem on each processor without using the parallel LU factorization; collective MPI communications will be needed. See Section 6.4 for the computational comparison of this two primal approaches.

BDDC dependence from H/h.

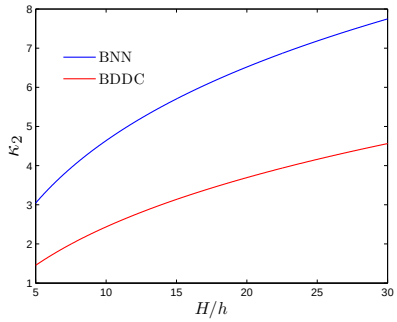

Figure 5.2: Comparison of the condition number of PCG-BDDC (with vertex and edge averages constraints) and PCG-BNN solver for the Schur complement of the Bidomain discretization as a function of H/h. Test case with $3 \times 3 \times 3$ processors, h =1E-2, δ_t =1E-2, conductivity coefficients as in Table 2.1.1, random right-hand side and null initial guess; PCG iteration is stopped when the preconditioned residual is lower then 1E-8.

Figure 5.2 shows the H/h dependence of the condition number of the BDDC preconditioner with only vertex and edges averages constraints, a set of constraints poorer than that required for the analysis. Results for vertex constraints plus edge and faces averages does not improve substantially these results. It must be noted that, also with this set of primal constraints, BDDC outperforms the BNN preconditioner with the Bidomain model on the same test case. A least squares fitting of the data shows that the power of the factor $(1 + \log(H/h))$ is approximatively 2 for both the preconditioners; their fittings differ only for a constant coefficient which multiplies the latter factor. Table 5.1 shows the results with only vertex constraints, which suggest an additional linear dependence of the condition number from H/h as expected by the theory (see e.g. [140])

We then reproduce the numerical test performed to enlight the dependence of the condition number of BNN preconditioned Bidomain problem with natural coarse space from H^{-2} (see Section 4.8) in order to compare with the performances of the BDDC method. Results (compare them with the results listed in Table 4.6) for the BDDC preconditioner are shown in Table 5.2 using δ_t =1E1 and conductivity coefficients $\sigma_M^{i,e}$ =1E1, $\sigma_m^{i,e}$ =1E-1 with the intermediate eigenvalues equal to 1. With this set of parameters, BDDC outperforms BNN preconditioner with enriched coarse space.

BDDC scaled speedup.

In Table 5.3 we show the scalability of the BDDC preconditioner with vertices and edge averages as primal constraints. If we add faces averages to the primal space we will obtain slightly better results but without a substantial improvement (data not shown).

PCG-BDDC Schur Bidomain H/h dependence
Vertex constraints only

H/h	5	10	15	20	25
κ_2	6.93	22.68	42.97	66.15	91.24

Table 5.1: Bidomain Schur complement H/h dependence test for PCG-BDDC solver with only vertex constraints as primal variables. Test case with 3x3x3 processors, h =1E-2, δ_t =1E-2, conductivity coefficients as in Table 2.1.1, random right-hand side and null initial guess; PCG iteration is stopped when the preconditioned residual is lower then 1E-8.

H/h	5	10	15	20
κ_2	2.61	4.91	7.07	9.02

Table 5.2: Bidomain Schur complement H/h dependence test for PCG-BDDC solver with vertex and edges averages constraints as primal variables. Test case with 3x3x3 processors, h =1E-2, δ_t =1E1, random right-hand side and null initial guess; PCG iteration is stopped when the preconditioned residual is lower then 1E-8. For the conductivity coefficients, see text.

BDDC dependence from δ_t.

Next, we tested the estimated dependence of the condition number by the time step δ_t and we collected the results in Table 5.4 using vertex and edge averages as primal space: differently from the BNN preconditioner (see Section 4.8) the experimental condition numbers show a sigmoidal dependence from δ_t of the form

$$c_1 \frac{\delta_t^m + 1}{\delta_t^m + c_2}$$

with $m > 0$. The same qualitative behavior was observed adding also the faces averages. The theoretical estimates thus overestimate the dependence of the condition number form δ_t when it approaches zero. Figure 5.3 shows the comparison between the values of the condition number provided in Table 5.4 and their least square fitting with a sigmoidal curve with $c_1 = 6.372 \pm 0.28$, $c_2 = 2.425 \pm 0.18$ and $m = 0.8574 \pm 0.41$ with 95% confidence to validate the experimental findings.

BDDC with jumping coefficients.

From Theorem 5.5.6 we infer that the condition number of the Bidomain operator $M_{BDDC}^{-1}\widehat{S}_\Gamma$ will be independent of jumps in the conductivity coefficients aligned with the

PCG-BDDC Schur Bidomain Scalability
Vertex and edge averages constraints

subd	$\widehat{\mathbf{W}}$ dofs	$\widehat{\mathbf{W}}_\Gamma$ dofs	$\widehat{\mathbf{W}}_\Pi$ dofs	iter	λ_{min}	λ_{max}	κ_2
2x2x1	120'050	4'850	46	10	1.00	3.09	3.09
4x4x1	470'450	28'650	222	12	1.00	3.33	3.33
6x6x1	1'051'250	71'250	509	12	1.00	3.46	3.46
8x8x1	1'862'450	132'650	910	13	1.00	3.51	3.51
10x10x1	2'904'050	212'850	1'422	13	1.00	3.55	3.55
12x12x1	4'176'050	311'850	2'046	14	1.00	3.56	3.56
14x14x1	5'678'450	429'650	2'782	14	1.00	3.58	3.58
16x16x1	7'411'250	566'250	3'630	14	1.00	3.59	3.59
18x18x1	9'374'450	721'650	4'589	14	1.00	3.59	3.59
20x20x1	11'568'050	895'850	5'662	14	1.00	3.59	3.59
22x22x1	13'992'050	1'088'850	6'846	14	1.00	3.60	3.60
24x24x1	16'646'450	1'300'650	8'141	14	1.00	3.60	3.60

Table 5.3: Bidomain Schur complement scalability test for PCG-BDDC solver with vertices and edge average constraints as primal variables. Test case with $h = 0.01$, $H/h = 25$, $\delta_t = 1e-2$, conductivity coefficients as in Table 2.1.1, random right-hand side and null initial guess; PCG iteration is stopped when the initial preconditioned residual is reduced by a factor of 1E-6. For each run, subdomain subdivision in the three dimensions, number of global, interface and primal dofs, number of iterations, extreme eigenvalues and condition number are shown.

interface; it will depend on the conductivity coefficients at most through the factor

$$\max_{\bullet=i,e} \left(\max_{j=1,\ldots,N} \frac{\sigma_M^{\bullet(j)} \delta_t + H^2}{\sigma_m^{\bullet(j)} \delta_t} \right). \tag{5.23}$$

To validate this finding, as for the Neumann-Neumann preconditioners in the previous chapter, we will consider a 3x3x3 decomposition of the whole domain and a checkerboard pattern (see Figure 4.3) of discontinuities in the conductivity coefficients, with two different sets of discontinuities. We initially set the conductivity coefficients as $\sigma_l^{i,e}$ =1E1, $\sigma_t^{i,e}$ =1 and $\sigma_n^{i,e}$ =1E-1, then we consider a first test case, fixing a factor p and then multiplying

PCG-BDDC Schur Bidomain δ_t dependence

δ_t	1E-4	1E-3	1E-2	1E-1	1E0	1E1	1E2	1E3	1E4
κ_2	2.73	2.74	2.75	2.88	3.78	5.45	6.19	6.35	6.37
iter	10	10	10	10	12	14	16	16	16

Table 5.4: Bidomain Schur complement δ_t dependence test for PCG-BDDC solver with vertices and edge average constraints as primal variables. Test case with 2x2x2 subdomains, $h = 0.01$, $H/h = 15$, conductivity coefficients as in Table 2.1.1, random right-hand side and null initial guess; PCG iteration is stopped when the initial preconditioned residual is reduced by a factor of 1E-6. For each run, time step δ_t, condition number and number of iterations are shown.

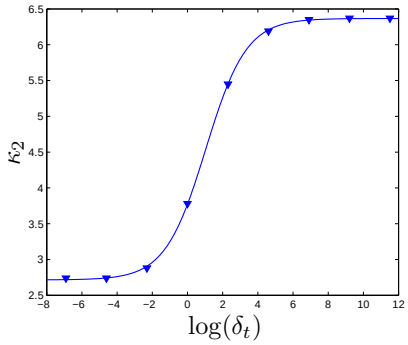

Figure 5.3: Bidomain Schur complement δ_t dependence test for PCG-BDDC solver with vertices and edge average constraints as primal variables. Condition number as a function of $\log(\delta_t)$: the triangles are the experimental values and the continuous curve represents their fitting. Test case with 2x2x2 subdomains, $h = 0.01$, $H/h = 15$, conductivity coefficients as in Table 2.1.1, random right-hand side and null initial guess; PCG iteration is stopped when the initial preconditioned residual is reduced by a factor of 1E-6.

each conductivity coefficient, either intra- or extracellular, by p in the black subdomains and by $1/p$ in the others. In the second test case, we multiply differently the intracellular and extracellular coefficients in the two coloured regions: in the black subdomains we multiply the intracellular conductivity coefficients by p and the extracellular ones by $1/p$. In the white regions we will do the viceversa. Numerical results are summarized in Table 5.5: column labelled by **A** refers to the first type of discontinuity, whereas column **B** refers to the second one. In either case, the condition number and the number of iterations remains almost constants varying largely the factor p: note that the theoretical results are not sharp in the case of jumping coefficients due to the presence of the H^2 addendum in (5.23) introduced by the Poincarè-Friedrichs inequalities for the L^2 norms. In fact, without the H^2 addendum, the factor (5.23) will be independent of jumps in the conductivity coefficients.

PCG-BDDC Schur Bidomain
Jumping Coefficients

	A		**B**	
p	it	κ_2	it	κ_2
1	18	7.16	18	7.16
1E1	19	8.51	18	8.11
1E2	19	8.61	18	8.52
1E3	20	8.71	18	8.52
1E4	20	9.05	18	8.52

Table 5.5: Bidomain Schur complement dependence from jumps in the conductivity coefficient. PCG-BDDC solver with vertices and edge average constraints as primal variables. Test case with 3x3x3 subdomains, $h = 0.01$, $H/h = 15$, δ_t =1E-2, random right-hand side and null initial guess; PCG iteration is stopped when the initial residual is reduced by a factor of 1E-6. For each run, jumping factor p (see text for details), number of iteration and condition number for the preconditioned $M^{-1}_{BDDC}\widehat{S}_\Gamma$ operator are shown.

BDDC and lagrangian initial guesses

degree	0	1	2	3	4
Iterations per time step					
phase 0	5.73	4.17	3.73	3.73	3.91
phase 1-2	4.04	1.79	1.36	1.99	2.55
phase 3	5.52	2.22	1.47	2.11	4.35
Admissible Solutions					
phase 0	0	0	0	0	0
phase 1-2	0	17	9	0	0
phase 3	0	0	10	0	0

Table 5.6: An heartbeat with BDDC preconditioner and different choice of the polynomial order for Lagrangian initial guesses. For each Lagrangian degree, average number of iterations per time step and number of admissible solutions for the linear solver are shown for different AP phases. See text for further details.

An heartbeat with BDDC preconditioner and different initial guesses.

We then test the BDDC preconditioner in a heartbeat simulation. We consider a global grid $43 \times 43 \times 43$ decomposed with $3 \times 3 \times 3$ subdomains ($H/h = 15$) and we simulate an heartbeat with the Bidomain model for 350 ms stimulating the lower left (endocardial) corner of the slab using HHRd as ionic cellular model (see Chapter 1) and the adaptive time stepping strategy (see Chapter 2). We note that with this configuration, the repolarization wave ends after 335 ms from the stimulus injection. Results for the Lagrangian choice of the PCG initial guess are shown in Table 5.6 whereas for the POD-Galerkin technique in Table 5.7 using the notation adopted in Chapter 3. Note that the case with PCG initial guess as the solution at the previous time step is contained in the Lagrangian case as a zero order polynomial approximation.

For POD-Galerkin, the choice of inner products to build the correlation matrices needs some discussion since we don't assemble the Schur matrix. At each time step, we need to solve the full order Schur symmetric linear system, which can be reordered as

$$\widehat{S}_\Gamma = \begin{pmatrix} S_\Gamma^{ii} & S_\Gamma^{ie} \\ S_\Gamma^{ie^T} & S_\Gamma^{ee} \end{pmatrix}$$

splitting the Schur degrees of freedom in intra- end extra-cellular dofs, and thus the lower

BDDC and POD initial guesses

N	2	3	4	5	10
		Iterations per time step			
phase 0	4.35	3.77	3.54	3.47	3.56
phase 1-2	1.54	1.18	1.02	0.89	0.68
phase 3	1.52	1.21	0.97	0.80	0.60
		Admissible Solutions			
phase 0	0	1	3	6	13
phase 1-2	7	55	109	139	210
phase 3	42	51	90	151	215

Table 5.7: An heartbeat with BDDC preconditioner and POD initial guess for different number of snapshots n_p. For each n_p, average number of iterations per time step and number of admissible solutions for the linear solver are shown for different AP phases. See text for further details.

order POD-Galerkin system becomes (see Section 3.4)

$$\begin{pmatrix} {\Psi^i}^T S_\Gamma^{ii} \Psi^i & {\Psi^i}^T S_\Gamma^{ie} \Psi^e \\ {\Psi^e}^T {S_\Gamma^{ie}}^T \Psi^i & {\Psi^e}^T S_\Gamma^{ee} \Psi^e \end{pmatrix}$$

where the matrix of POD basis elements is

$$\Psi = \begin{pmatrix} \Psi^i & 0 \\ 0 & \Psi^e \end{pmatrix}.$$

Next, in order to reduce the computational costs of assembling the lower order POD system (see Remark 3.4.6), we can choose as inner products S_Γ^{ii} and S_Γ^{ee} for the intra- and extracellular components respectively and thus obtain a lower dimensional matrix which has the diagonal blocks equal to identity matrices of appropriate sizes. Splitting the jth snapshot vector in intra- and extracellular component, i.e.

$$\mathbf{y}_j = \begin{pmatrix} \mathbf{y}_j^i \\ \mathbf{y}_j^e \end{pmatrix}$$

it holds

$$\begin{pmatrix} S_\Gamma^{ii} & S_\Gamma^{ie} \\ {S_\Gamma^{ie}}^T & S_\Gamma^{ee} \end{pmatrix} \begin{pmatrix} \mathbf{y}_j^i \\ 0 \end{pmatrix} = \begin{pmatrix} S_\Gamma^{ii} \mathbf{y}_j^i \\ {S_\Gamma^{ie}}^T \mathbf{y}_j^i \end{pmatrix}$$
$$\begin{pmatrix} S_\Gamma^{ii} & S_\Gamma^{ie} \\ {S_\Gamma^{ie}}^T & S_\Gamma^{ee} \end{pmatrix} \begin{pmatrix} 0 \\ \mathbf{y}_j^e \end{pmatrix} = \begin{pmatrix} S_\Gamma^{ie} \mathbf{y}_j^e \\ S_\Gamma^{ee} \mathbf{y}_j^e \end{pmatrix};$$

therefore, the action of S_Γ^{ii} (resp. S_Γ^{ee}) on a given intracellular (extracellular) interface snapshot vector can be obtained extending by zero the vector in the extracellular (intracellular) part, multiplying the resulting vector by the Schur matrix and then restrict the result on the intracellular (extracellular) part. Therefore, we need to perform only two Schur matrix-vector multiplications in order to assemble the correlation matrix at each time step. In addition, for the lower dimensional system we don't need to perform any additional matrix vector multiplication involving the off diagonal block S_Γ^{ie}; in fact, consider to compute the general entry of the lower dimensional off-diagonal block

$$(\Psi^{i\,T} S_\Gamma^{ie} \Psi^e)_{km} = \boldsymbol{\psi}_k^{i\,T} S_\Gamma^{ie} \boldsymbol{\psi}_m^e.$$

Using eq. (3.11) and denoting by superscripts i, e the eigenvalues and eigenvectors of the intra- and extra-cellular correlation matrices, we obtain

$$\begin{aligned}\boldsymbol{\psi}_k^{i\,T} S_\Gamma^{ie} \boldsymbol{\psi}_m^e &= \frac{1}{\sqrt{\lambda_k^i \lambda_m^e}} (\sum_{j=1}^N v_k^{j,i} \mathbf{y}_j^i)^T S_\Gamma^{ie} (\sum_{j=1}^N v_k^{j,e} \mathbf{y}_j^e) \\ &= \frac{1}{\sqrt{\lambda_k^i \lambda_m^e}} \sum_{j,l=1}^N v_k^{j,i} v_m^{l,e} \mathbf{y}_j^{i\,T} S_\Gamma^{ie} \mathbf{y}_l^e.\end{aligned}$$

Thus, if we store the vectors $S_\Gamma^{ie} \mathbf{y}_j^e$ for all $j = 1, \ldots, N$ already computed during the correlation matrices assembling, we need to perform only some additional dot products to assemble the lower order POD-Galerkin system with the result that additional expensive Schur matrix-vector products can be avoided.

Results show efficiency for both approaches in all AP phases but the activation phase, in which the reduction of the number of iterations saturates increasing either the interpolation degree, or the dimension of the POD snapshot ensemble N. In other AP phases, POD shows the best results, either in terms of average number of iteration per time step, or taking into account the admissible solutions; moreover, the approximation properties of POD are better than the lagrangian approach when considering the same number of stored snapshots (compare the columns for whose the lagrangian degree is equal to $N - 1$ POD snapshots). As noted in Chapter 5, the dimension of the snapshot ensemble for POD need not to be large, and for this test case 5 snapshots are enough to obtain a satisfactory reduction of the number of iterations per time step.

Chapter 6

Approximate BDDC for the Bidomain model

6.1 Introduction

The local problems of the BDDC preconditioner can be computational bottlenecks if the subdomains' sizes are large. In fact, one of the shortcomings of BDDC is that the direct solutions for the local Dirichlet and Neumann problems used by the method may require too much time and memory if the number of degrees of freedom N_{dof} in any substructure is too large. For example, in three dimensions the floating point operations needed to factor and solve, through backward and forward substitutions, either of the local problems for the discrete Laplacian and an optimal Nested Dissection ordering are indeed asymptotical to $O(N_{\text{dof}}^2)$ and $0(N_{\text{dof}}^{4/3})$ respectively (see [33]). One technique for removing these difficulties consists in using multigrid preconditioners as inexact solvers for these problems, since multigrid computational costs are asymptotical to $O(N_{\text{dof}})$, still maintaining the scalability of the preconditioner and a good rate of convergence with respect to the spatial discretization. An inexact approach to the FETI-DP methods can be found in [68]

The Dirichlet solver is used to obtain the action of the Schur complement matrix on the interface unknowns: we will thus end up solving a different system if we just replace it by an inexact solver in the Schur matrix application. In order to overcome this issue, we must iterate on the assembled matrix $\widehat{A}$ given in formula (4.6) instead of $\widehat{S}_\Gamma$ and construct a BDDC preconditioner for the operator $\widehat{A}$. The Neumann solver is involved in the computation of the coarse basis functions and thus in the resulting coarse problem during the preprocessing step; moreover, we need it also in the application of the BDDC preconditioner during the conjugate gradient iterations. Inexact Neumann solvers should thus be chosen to guarantee the positive semidefiniteness of the Bidomain coarse matrix and preserve the null space during the conjugate gradient iterations.

Here we will follow the algebraic approach proposed by Dohrmann [31]. We will deal with the original formulation of the BDDC preconditioner (see Section 5.3 for the

details) without imposing the change of variables since it would guaranties that multigrid preconditioners, used as black-boxes for the inexact solvers, will be spectrally equivalent to the exact problems (see the next section for details). A different inexact approach to BDDC with change of basis can be found in [78]. To explain the construction of such an approximate BDDC, we first need some additional restriction operators: let

$$R_I : \widehat{\mathbf{W}} \to \mathbf{W}_I$$

the operator which extracts the interior dofs from $\widehat{\mathbf{W}}$ and let R_D the scaled restriction operator from $\widehat{\mathbf{W}}$ to $\mathbf{W}$ using a suitable partition of unity. We can then define an equivalent BDDC preconditioner for matrix $\widehat{A}$ as:

$$M^{-1} = M_I^{-1} + (I - M_I^{-1}\widehat{A})M_{BDDC}^{-1}(I - \widehat{A}M_I^{-1}) \tag{6.1}$$

where

$$M_I^{-1} = R_I^T A_{II}^{-1} R_I$$

and M_{BDDC}^{-1} is, with a little abuse of notation, given similarly to its formulation given in eq. (5.3)

$$M_{BDDC}^{-1} = R_D^T \left[P_{coarse} + P_{local}\right] R_D$$

assuming that now the BDDC operators P_{coarse} and P_{local} act on $\mathbf{W}$. The coarse parts of the preconditioner can be defined by

$$P_{coarse} = \Psi A_c^{-1} \Psi^T, \quad A_c = \Psi^T A \Psi$$

with the coarse basis function matrix given by the solution of the following minimization problem posed on $\mathbf{W}$

$$\Psi = \underset{Cw=\mathcal{I}, w\in\mathbf{W}}{\operatorname{argmin}} \; w^T A w. \tag{6.2}$$

where A is the unassembled stiffness matrix and C is the block matrix imposing the local constraints. The action of the additive part of the preconditioner is then given by

$$\begin{pmatrix} A & C^T \\ C & 0 \end{pmatrix} \begin{pmatrix} P_{local}\, g \\ \mu \end{pmatrix} = \begin{pmatrix} g \\ 0 \end{pmatrix}.$$

See eq. (5.6) for a comparison.

Remark 6.1.1. Due to the Schur complement definition given in Lemma 4.2.3, problem (5.4) is equivalent to problem (6.2). The matrix C is similar to the matrix built in Remark 5.3.1 except that now the number of columns of each $C^{(j)}$ equals the number of nodes on $\mathbf{W}^{(j)}$, and thus the number of rows of Ψ (i.e. the support of the coarse basis functions) equals the number of dofs of $\mathbf{W}$. The same arguments hold true also for the matrix $\mathcal{I}$. See Remark 5.3.1 for the construction of such matrices.

Remark 6.1.2. As it can be seen, the same block saddle point problem needed for the

additive part of the preconditioner and also involved in the computation of the coarse basis function and the resulting coarse problem can be generalized as

$$\begin{pmatrix} A & C^T \\ C & 0 \end{pmatrix} \begin{pmatrix} w \\ \mu \end{pmatrix} = \begin{pmatrix} g \\ h \end{pmatrix}. \tag{6.3}$$

Here we will illustrate how problem (6.3) can be solved directly as descripted in [31]. Suppose to have an ordering of **W** with the vertex nodes (denoted with a subscript v) ordered last, i.e.

$$A = \begin{pmatrix} A_{rr} & A_{rv} \\ A_{rv} & A_{vv} \end{pmatrix}$$

with

$$A_{rr} = \begin{pmatrix} A_{rr}^{(1)} & & \\ & \ddots & \\ & & A_{rr}^{(N)} \end{pmatrix}, \quad A_{rv} = \begin{pmatrix} A_{rv}^{(1)} & & \\ & \ddots & \\ & & A_{rv}^{(N)} \end{pmatrix}$$

and

$$A_{vv} = \begin{pmatrix} A_{vv}^{(1)} & & \\ & \ddots & \\ & & A_{vv}^{(N)} \end{pmatrix}.$$

In turn, nodes reordering induces a reordering of the constraints matrix

$$C = \begin{pmatrix} C_r & 0 \\ 0 & I \end{pmatrix}.$$

The number of rows of C_r is the sum of averages imposed on each substructure and the size of the identity matrix is the number of unassembled vertex constraints; using the latter splitting of the dofs, the solution of the saddle point system (6.3) is given by

$$\begin{aligned} \mu_r &= \left(C_r A_{rr} C_r^T\right)^{-1} \left[C_r A_{rr}^{-1}(g_r - A_{rv} h_v) - h_r\right] \\ w_r &= A_{rr}^{-1}\left(g_r - A_{rv} h_v - C_r^T \mu_r\right) \\ w_v &= h_v \\ \mu_v &= g_v - A_{rv}^T w_r - A_{vv} h_v. \end{aligned} \tag{6.4}$$

The action of operator P_{local} is thus calculated by setting $h = 0$. Denoting with n_c the global number of constraints imposed, the matrix of coarse basis function Ψ can be obtained solving n_c problems of the type (6.3) with $g = 0$ and μ a vector of all zeros except for the indices which represent one global constraints where it takes on the value 1. The w solution of the latter problem will thus represent the columns of the coarse matrix. Once the coarse basis function matrix has been calculated, the coarse problem A_c can be efficiently obtained as

$$A_c = \Psi^T A \Psi = -\Psi^T C^T \Lambda$$

where Λ is the matrix formed columnwise by the μ solutions obtained by calculating the coarse basis function matrix: expensive matrix-vector products involving matrix A are thus not needed. Additional details can be found in [30] and [31].

Remark 6.1.3. Solving problem (6.3) requires the solution of two local problems, one sparse and given by A_{rr}^{-1}, and a second small and dense problem given by $(C_r A_{rr} C_r^T)^{-1}$. Therefore, in order to solve problem (6.3) we will need only the action of A_{rr}^{-1}. With the inexact approach proposed in [31], we substitute matrix A_{rr}^{-1} with the action of multigrid preconditioners.

The following theorem holds:

Theorem 6.1.4. *The BDDC operator M^{-1} given in eq. (6.1) satisfies*

$$M^{-1}\widehat{A} = \begin{pmatrix} I & A_{II}^{-1}A_{I\Gamma}(I - M_{BDDC}^{-1})\widehat{S}_\Gamma \\ 0 & M_{BDDC}^{-1}\widehat{S}_\Gamma \end{pmatrix}$$

and thus the preconditioned operator $M^{-1}\widehat{A}$ has the same eigenvalues of $M_{BDDC}^{-1}\widehat{S}_\Gamma$ plus some additional eigenvalues, whose number equals the number of interior dofs, equal to 1.

Proof. See [31]. □

6.2 Approximate BDDC

In this section we will expose in details the construction of the approximate BDDC preconditioner using inexact solvers for problems A_{II} and A_{rr}. Let $A^\flat$ be the assembled matrix which is equal to the assembled matrix $\widehat{A}$ except for the coupling of the interior dofs, i.e.

$$A^\flat = \begin{pmatrix} A_{II}^\flat & A_{I\Gamma} \\ A_{I\Gamma}^T & A_{\Gamma\Gamma} \end{pmatrix},$$

and let $A^\sharp$ be the unassembled matrix which is similar to A except for the block related to the Neumann problem of the BDDC preconditioner (see Remark 6.1.3), i.e.

$$A^\sharp = \begin{pmatrix} A_{rr}^\sharp & A_{rv} \\ A_{rv}^T & A_{vv} \end{pmatrix}.$$

Matrices $A_{II}^\flat$ and $A_{rr}^\sharp$ must be suitable chosen to construct the approximate BDDC preconditioner; they are not known explicitly and represents an approximation of the exact matrices corresponding to using inexact Dirichlet and Neumann solvers respectively. The inexact approach proposed in [31] requires two basic assumptions on such inexact matrices:

- **Null space property:** The null space of matrices $A^\flat$ and $A^\sharp$ must be the same of $\widehat{A}$ and A respectively.
- **Spectral equivalence:** Matrices $A^\flat$ and $A^\sharp$ must be spectrally equivalent to $\widehat{A}$ and A respectively; we thus need the existence of positive real numbers $0 < \gamma_1 \leq \gamma_2$ and

$0 < \alpha_1 \leq \alpha_2$, independent of the characteristic sizes of the spatial discretizations h and H, such that

$$\begin{aligned} \gamma_1 g^T \widehat{A} g \leq g^T A^\flat g \leq \gamma_2 g^T \widehat{A} g \quad \forall g \in \widehat{\mathbf{W}} \\ \alpha_1 g^T A g \leq g^T A^\sharp g \leq \alpha_2 g^T A g \quad \forall g \in \mathbf{W} \end{aligned} \tag{6.5}$$

Null space property

The null space property for the Dirichlet solver of the Bidomain model requires that

$$\begin{pmatrix} A_{II}^\flat & A_{I\Gamma} \\ A_{I\Gamma}^T & A_{\Gamma\Gamma} \end{pmatrix} \begin{pmatrix} \mathbf{1}_I \\ \mathbf{1}_\Gamma \end{pmatrix} = \begin{pmatrix} A_{II} & A_{I\Gamma} \\ A_{I\Gamma}^T & A_{\Gamma\Gamma} \end{pmatrix} \begin{pmatrix} \mathbf{1}_I \\ \mathbf{1}_\Gamma \end{pmatrix} = \begin{pmatrix} 0 \\ 0 \end{pmatrix}$$

where $\mathbf{1}_I$, and $\mathbf{1}_\Gamma$ are identity vectors of appropriate sizes. A simple calculation reveals that

$$A_{II}^{\flat^{-1}} A_{II} \mathbf{1}_I = \mathbf{1}_I$$

must be satisfied. Now let P_{II}^{-1} be a candidate preconditioner for $A_{II}^{\flat^{-1}}$. The following correction of P_{II}^{-1} was proposed in [31] to obtain a preconditioner $A_{II}^{\flat^{-1}}$ for the Dirichlet problem that satisfies the null space property:

$$A_{II}^{\flat^{-1}} = \mathbf{1}_I (\mathbf{1}_I^T A_{II} \mathbf{1}_I)^{-1} \mathbf{1}_I^T + E_I^T P_{II}^{-1} E_I \tag{6.6}$$

where

$$E_I = I - A_{II} \mathbf{1}_I (\mathbf{1}_I^T A_{II} \mathbf{1}_I)^{-1} \mathbf{1}_I^T$$

with I the identity matrix of appropriate size. The same arguments will hold true for the Neumann problem, and thus we will use

$$A_{rr}^{\sharp^{-1}} = \mathbf{1}_r (\mathbf{1}_r^T A_{rr} \mathbf{1}_r)^{-1} \mathbf{1}_r^T + E_r^T P_{rr}^{-1} E_r \tag{6.7}$$

where

$$E_r = I - A_{rr} \mathbf{1}_r (\mathbf{1}_r^T A_{rr} \mathbf{1}_r)^{-1} \mathbf{1}_r^T$$

where P_{rr}^{-1} is a candidate preconditioner for $A_{rr}^{\sharp^{-1}}$.

Spectral equivalence

A priori estimates for the constants appearing in eqs. (6.5) are difficult to obtain directly. As noted in [31], the spectral equivalent constants can be estimated by conjugate gradient

iterations (even if they are not required by the implementation) as

$$\gamma_1 = 1/\lambda_{max}(A^{\flat^{-1}}\widehat{A}), \quad \gamma_2 = 1/\lambda_{min}(A^{\flat^{-1}}\widehat{A}),$$
$$\alpha_1 = 1/\lambda_{max}(A^{\sharp^{-1}}\widehat{A}), \quad \alpha_2 = 1/\lambda_{min}(A^{\sharp^{-1}}\widehat{A}).$$

where the action of the inverses appearing in the above formulas can be obtained with a Schur complement argument (see eq. (4.6)) as

$$A^{\flat^{-1}} g = \begin{pmatrix} A_{II}^{\flat^{-1}}(g_I - A_{I\Gamma} g_\Gamma) \\ S_\Gamma^{\flat^{-1}}(g_\Gamma - A_{I\Gamma}^T A_{II}^{\flat^{-1}} g_I) \end{pmatrix},$$
$$A^{\sharp^{-1}} g = \begin{pmatrix} A_{rr}^{\sharp^{-1}}(g_r - A_{rv} g_v) \\ S_v^{\sharp^{-1}}(g_r - A_{rv}^T A_{rr}^{\sharp^{-1}} g_r) \end{pmatrix},$$

with

$$S_\Gamma^{\flat^{-1}} = A_{\Gamma\Gamma} - A_{I\Gamma}^T A_{II}^{\flat^{-1}} A_{I\Gamma},$$
$$S_v^{\sharp^{-1}} = A_{vv} - A_{rv}^T A_{rr}^{\sharp^{-1}} A_{rv}.$$

In [31] three inexact preconditioner were proposed: the first inexact preconditioner uses only inexact Neumann solvers, whereas the second generalizes the first using both inexact Dirichlet and Neumann solvers. For both preconditioners, the inexact local solvers must satisfy the null space and spectral equivalence properties. The third preconditioner proposed uses both inexact problems but the null space property for the Dirichlet problem can be relaxed. Since the second and third preconditioners gave nearly the same results in [31], here we will deal with the second preconditioner because we can bound its condition number in terms of the exact BDDC preconditioner. The action of the second approximate BDDC preconditioner proposed in [31], here denoted by $\widetilde{M}^{-1}$, can be defined as:

$$\widetilde{M}^{-1} = M_I^{\flat^{-1}} + (I - M_I^{\flat^{-1}} A^\flat) M_{BDDC}^{\sharp^{-1}} (I - A^\flat M_I^{\flat^{-1}}) \tag{6.8}$$

where the superscript $\flat$ (resp. $\sharp$) denote quantities obtained by replacing matrix $\widehat{A}$ (resp. A) by $A^\flat$ (resp. $A^\sharp$) in all equations where they appear. Thus

$$M_I^{\flat^{-1}} = R_I^T A_{II}^{\flat^{-1}} R_I$$

and

$$M_{BDDC}^{\sharp^{-1}} = R_D^T \left[P_{coarse}^\sharp + P_{local}^\sharp \right] R_D$$

with

$$P_{coarse}^\sharp = \Psi^\sharp A_c^{\sharp^{-1}} \Psi^{\sharp^T}, \quad A_c^\sharp = \Psi^{\sharp^T} A^\sharp \Psi^\sharp$$

and the block saddle point problem (6.3) replaced by

$$\begin{pmatrix} A^\sharp & C^T \\ C & 0 \end{pmatrix} \begin{pmatrix} w^\sharp \\ \mu^\sharp \end{pmatrix} = \begin{pmatrix} g \\ h \end{pmatrix}.$$

Note that we must take into account the null space property and thus we use equations (6.6) and (6.7) in order to solve the Dirichlet and Neumann problems respectively.

Then the following theorem will hold (see [31] for the proof) for the condition number of the approximate BDDC.

Theorem 6.2.1. *Let*

$$\omega = \sup_{w \in \widetilde{\boldsymbol{W}}_\Gamma} \frac{|P_D w|_S^2}{|w|_S^2}$$

the supremum of the jump operator (5.1) on the partially continuous space $\widetilde{\boldsymbol{W}}_\Gamma$ with respect to the Schur complement seminorm. Then, the condition number of the approximate BDDC preconditioner (6.8) satisfies

$$\kappa_2(\widetilde{M}^{-1}\widehat{A}) \leq \omega \frac{\alpha_2 \gamma_2^3}{\alpha_1 \gamma_1^3}$$

where γ_1 and γ_2 are the spectral equivalence constants for the Dirichlet problem and α_1 and α_2 the spectral equivalence constants for the Neumann problem given in (6.5). In other words (see Theorem 5.5.6)

$$\frac{\kappa_2(\widetilde{M}^{-1}\widehat{A})}{\kappa_2(M^{-1}\widehat{A})} \lesssim \frac{\alpha_2 \gamma_2^3}{\alpha_1 \gamma_1^3}.$$

Corollary 6.2.2. *If we solve inexactly the inexact coarse problem $A_c^\sharp$ by the action of a preconditioner $A_c^{\sharp\sharp^{-1}}$ which satisfies*

$$\beta_1 g^T A_c^{\sharp^{-1}} g \leq g^T A_c^{\sharp\sharp^{-1}} g \leq \beta_2 g^T A_c^{\sharp^{-1}} g$$

for all primal vectors g with $0 < \beta_1 \leq \beta_2$, we then have

$$\kappa_2(\widetilde{M}^{-1}\widehat{A}) \leq \omega \frac{\max\{1, \beta_2\}}{\min\{1, \beta_1\}} \frac{\alpha_2 \gamma_2^3}{\alpha_1 \gamma_1^3}.$$

Remark 6.2.3. The constants β_1 and β_2 associated to the inexact coarse problem can be estimated directly by conjugate gradient iterations on the preconditioned system $A_c^{\sharp\sharp^{-1}} A_c^\sharp$. In fact, calculating the extreme eigenvalues of the resulting tridiagonal Lanczos matrix, we will have

$$\lambda_{min} g^T g \leq g^T A_c^{\sharp\sharp^{-1}} A_c^\sharp g \leq \lambda_{max} g^T g$$

for all primal vectors g. Denoting with $\rho(A_c^{\sharp\sharp^{-1}})$ the spectrum of the $A_c^{\sharp\sharp^{-1}}$ operator, it will hold

$$\rho(A_c^{\sharp\sharp^{-1}}) = \rho(A_c^{\sharp\sharp^{-1}} A_c^{\sharp} A_c^{\sharp^{-1}}) = \rho(A_c^{\sharp^{-1/2}} A_c^{\sharp\sharp^{-1}} A_c^{\sharp} A_c^{\sharp^{-1/2}})$$

and thus we will have

$$\beta_1 g^T A_c^{\sharp^{-1}} g \leq g^T A_c^{\sharp\sharp^{-1}} g \leq \beta_2 g^T A_c^{\sharp^{-1}} g$$

where

$$\beta_1 = \lambda_{min}(A_c^{\sharp\sharp^{-1}} A_c^{\sharp}), \quad \beta_2 = \lambda_{max}(A_c^{\sharp\sharp^{-1}} A_c^{\sharp}).$$

6.3 Algebraic multigrid preconditioners

Multigrid methods are efficient numerical algorithms either for solving partial differential equations or instead used as preconditioners for the discretized problem using a hierarchy of discretizations. The main idea of multigrid is to accelerate the convergence of a basic iterative method by the recursive smoothing and correction of the residual error through the hierarchy of operators associated to the hierarchy of discretizations. An extension of multigrid methods include techniques where no partial differential equation nor geometrical problem background is used to construct the multilevel hierarchy. In contrast to other methods, Algebraic MultiGrid methods (AMG) (see e.g. [118]) are general in that they can treat arbitrary regions and boundary conditions, moreover they do not depend on the separability of the equations or other special properties of underlying PDE. Such AMG methods construct their hierarchy of operators directly from the linear system matrix, and the levels of the hierarchy are simply subsets of unknowns without any geometric interpretation, thus becoming true black-box solvers for sparse matrices.

To simplify the discussion we will briefly explain how a two-level AMG method works. With AMG, fine (F) and coarse (C) grid points (which represent the next level of hierarchy) are selected in such a way that the degrees of freedoms at coarse points maximally influence the dofs at fine points using a suitable interpolation

$$P : C \rightarrow F$$

between coarse and fine grid. Either the grid point subdivision or the interpolation operators are constructed using solely the knowledge of the matrix entries. The two main components of an AMG method are then the smoothing and the coarse-grid correction operators. The smoother is generally a simple pointwise iterative method which eliminates all but the *smooth errors* which are then transferred to the coarse-grid correction. It must be noted that in order to use AMG as a preconditioner for the PCG, we must use a symmetric smoother such as Gauss-Seidel to preserve the symmetric nature of the preconditioned linear system.

The most common approach for the coarse-grid correction is to use the Galerkin projection of the original matrix (denoted with A) onto the coarse mesh through the interpolation operator, namely,

$$A_c = P^T A P$$

which guaranties (for symmetric positive definite matrices A) that the maximum eigenvalue of the preconditioned operator will be less or equal 1 (see e.g. [100]). The action on a given residual vector r of a one-level AMG method used as a preconditioner can then be stated as:

Do ν_1 smoothing steps on $Au = r$

Compute the fine grid residual $r_F = r - Au$

Solve at the coarse grid $A_c e_c = P^T r_F$

Correct $u = u + P e_c$

Do ν_2 smoothing steps on $Au = r$

The latter method is often referred to in literature as a two-level V_{ν_1,ν_2}-cycle. The generalization to more levels can be obtained replacing the solve step on the coarse grid with the action of nested two-level V_{ν_1,ν_2}-cycles using prolongation and coarse grid operators builded starting from the matrix at the previous level of hierarchy. For the Bidomain local matrices (see eq. (2.20)), the presence of negative off diagonal elements, due to the matrix $-1/\delta_t M$, and the larger weight of the diagonal entries, due to the matrix $1/\delta_t M$, makes the coarsening procedure very effective and results in a very efficient preconditioner. See also the numerical results provided in [147] and [108] where AMG preconditioner has been applied respectively to the parallel and serial solution of the Bidomain linear system.

Remark 6.3.1. If we apply the inexact approach to BDDC with change of basis, we will have the same Dirichlet problem since the block diagonal matrix A_{II} will not change with changing the basis (see Section 5.4); the Neumann problem will be affected by the transformation and we must solve the block diagonal system with matrix

$$A_{\mathcal{NN}} = \begin{pmatrix} A_{\mathcal{NN}}^{(1)} & & \\ & \ddots & \\ & & A_{\mathcal{NN}}^{(N)} \end{pmatrix}$$

where

$$A_{\mathcal{NN}}^{(j)} = \begin{pmatrix} A_{II}^{(j)} & A_{I\Delta}^{(j)} \\ A_{I\Delta}^{(j)^T} & A_{\Delta\Delta}^{(j)} \end{pmatrix}.$$

Table 6.1 shows the extreme eigenvalues of block diagonal problems A_{II}, A_{rr} and $A_{\mathcal{NN}}$ preconditioned with AMG methods (whose actions are denoted by P_{II}^{-1}, P_{rr}^{-1} and $P_{\mathcal{NN}}^{-1}$ respectively) using *boomerAMG* preconditioner provided by the HYPRE library [55] developed at the Lawrence Livermore National Laboratory; in details, each local linear system is solved until machine precision with a random right hand side and null initial guess,

	$P_{II}^{-1}A_{II}$		$P_{rr}^{-1}A_{rr}$		$P_{\mathcal{NN}}^{-1}A_{\mathcal{NN}}$	
H/h	λ_{min}	λ_{max}	λ_{min}	λ_{max}	λ_{min}	λ_{max}
5	8.5E-1	1.00	8.3E-1	1.00	6.3E-1	1.00
10	8.3E-1	1.00	7.3E-1	1.00	1.6E-1	1.00
15	7.8E-1	1.00	6.6E-1	1.00	5.6E-2	1.00
20	7.6E-1	1.00	6.4E-1	1.00	2.5E-2	1.00
25	7.6E-1	1.00	6.7E-1	1.00	1.3E-2	1.00
30	7.2E-1	1.00	6.0E-1	1.00	6.2E-3	1.00
35	7.5E-1	1.00	7.0E-1	1.00	2.8E-3	1.00
40	6.6E-1	1.00	6.0E-1	1.00	1.1E-3	1.00

Table 6.1: Bidomain local AMG based solvers as a function of H/h. Vertices and edge averages as primal constraints. Test case with $3\times3\times3$ subdomains, $h = 0.01$, random right-hand side and null initial guess; iterative solver is stopped when the preconditioned residual is lower than 1E-12. For each run extreme eigenvalues of the local problems are shown.

and then the global minimum of local minimum eigenvalues and the global maximum of local maximum eigenvalues are collected. Results show the effectiveness of the AMG preconditioner for the local Dirichlet and Neumann problems with the original formulation of the BDDC preconditioner; on the other hand, AMG preconditioner did not results in a spectrally equivalent preconditioner for the Neumann problem after performing the change of basis. Numerical results were obtained using one multilevel $V_{1,1}$-cycle with Gauss-Seidel smoothing and without any other explicit settings of the other parameters offered to the user by the HYPRE library.

Remark 6.3.2. Note that, if we want to use AMG preconditioner as a local inexact solver for a more difficult problem than the Bidomain model, we must assure independence of the minimum eigenvalue of the preconditioned operators of the local problems as in Table 6.1 from h and H and any other parameters of the underlying PDE, otherwise the rate of convergence of the inexact BDDC can deteriorate. A different inexact strategy could be to construct local and robust BDDC preconditioners for Dirichlet and Neumann problems; from the computational viewpoint using such a *recursive* BDDC can be easier to implement than develop and implement an ad-hoc multigrid preconditioner, since in the former case we can use an already existing code. We are planning to apply these ideas to an inexact formulation of the BDDC preconditioner of the system of linear elasticity in the almost incompressible case in three dimensions where black boxes AMG preconditioners does not give satisfactory results. Results of scalability and robustness of exact BDDC methods for the latter system have been already obtained in [105] in collaboration with Prof Olof B. Widlund (Courant Institute, NYU) and Prof Luca F. Pavarino (University of Milan).

	$M^{-1}\widehat{A}$				$\widetilde{M}^{-1}\widehat{A}$			
H/h	λ_{min}	λ_{max}	κ_2	it	λ_{min}	λ_{max}	κ_2	it
5	1.00	1.45	1.45	6	0.88	1.42	1.61	7
10	1.00	2.28	2.28	9	0.87	2.14	2.45	10
15	1.00	2.98	2.98	11	0.87	2.66	3.06	11
20	1.00	3.49	3.49	11	0.85	3.17	3.71	13
25	1.00	4.02	4.02	13	0.85	3.56	4.18	14
30	*out of memory*				0.76	3.91	5.14	15
35	*out of memory*				0.75	4.23	5.60	16
40	*out of memory*				0.70	4.43	6.27	16

Table 6.2: Inexact BDDC H/h dependence. Exact BDDC preconditioner versus inexact BDDC with local AMG based preconditioners. Vertices and edge averages as primal constraints. Test case with 3x3x3 subdomains, $h = 0.01$, random right-hand side and null initial guess; iterative solver is stopped when the initial preconditioned residual is reduced by a factor of 1E-6. For each run, extreme eigenvalues, condition number and number of iterations are shown. Coarse problem is solved exactly.

6.4 Implementational details and numerical results

The action of the BDDC preconditioner has been descripted in details in the previous sections. In order to complete the description of the action of $\widetilde{M}^{-1}$ on a given residual vector r, we must calculate the action of the variational corrections $(I-A^\flat M^{\flat^{-1}})$ and $(I-M^{\flat^{-1}}A^\flat)$, needed respectively before and after the application of $M^{\sharp^{-1}}_{BDDC}$, and given by

$$(I - A^\flat M^{\flat^{-1}})r = \begin{pmatrix} 0 & 0 \\ -A_{I\Gamma}^T A_{II}^{\flat^{-1}} & I \end{pmatrix} \begin{pmatrix} r_I \\ r_\Gamma \end{pmatrix}$$

and

$$(I - M^{\flat^{-1}} A^\flat)s = \begin{pmatrix} 0 & -A_{II}^{\flat^{-1}} A_{I\Gamma} \\ 0 & I \end{pmatrix} \begin{pmatrix} s_I \\ s_\Gamma \end{pmatrix}$$

where s is the output of $M^{\sharp^{-1}}_{BDDC}$.Finally, in the following we will refer to the ratio

$$\frac{\kappa_2(\widetilde{M}^{-1}\widehat{A})}{\kappa_2(M^{-1}\widehat{A})}$$

as experimental inexact factor.

Approximate BDDC H/h dependence.

First, we study the H/h dependence (fixing the time step) using inexact local solvers given by eqs. (6.6) and (6.7) and compare it with the exact approach. One $V_{1,1}$-cycle with Gauss-Seidel smoothing is used for the AMG methods. Results are listed in Table 6.2: for the inexact approach, the inexact coarse problem is solved exactly with a parallel factoriza-

PCG-BDDC Inexact Bidomain Scalability
Vertex and edge averages constraints

subd	exact κ_2 (it)	inexact κ_2 (it)	β_1	β_2	inex. fact.
2x2x1	3.09 (10)	3.51 (12)	0.87	1.00	1.14
4x4x1	3.33 (12)	3.71 (13)	0.80	1.00	1.15
6x6x1	3.46 (12)	3.72 (13)	0.80	1.00	1.07
8x8x1	3.51 (13)	3.79 (14)	0.80	1.00	1.08
10x10x1	3.55 (13)	3.76 (13)	0.80	1.00	1.06
12x12x1	3.56 (14)	3.87 (14)	0.79	1.00	1.08
14x14x1	3.58 (14)	3.84 (14)	0.75	1.00	1.07

Table 6.3: Inexact BDDC Scaled Speedup. PCG-BDDC inexact solver with vertices and edge average constraints as primal variables; local and coarse problems solved with boomerAMG. Test case with $h = 0.01$, $H/h = 25$, random right-hand side and null initial guess; PCG iteration is stopped when the initial preconditioned residual is reduced by a factor of 1E-6. For each run, subdomain subdivision in the three dimensions, condition number (number of iterations in parenthesis) are shown for both exact and inexact formulations. For a comparison with the exact BDDC, extreme eigenvalues of the inexact coarse problem and inexact experimental factor (inex. fact.) are also shown (see text for details).

tion. As it can be seen, using inexact local solvers spectrally equivalent to the original ones does not deteriorate the properties of the BDDC preconditioner with respect to h and H and it permits to manage larger local problems, since the memory requirements for a multigrid preconditioner are linear in the local size. Moreover, the minimum eigenvalue of the inexact preconditioned operator is worse than the exact one, but the maximum eigenvalue is better.

Approximate BDDC scaled speedup.

Next, we reproduce the scaled speed up test performed on the exact BDDC preconditioner (see Table 5.3) and compare the results in Table 6.3 with the inexact approach using eqs. (6.6) and (6.7) with one AMG $V_{1,1}$-cycle for the local problems. Moreover we solved inexactly the coarse problem with one AMG $V_{1,1}$-cycle. The condition number of the inexact approach remains bounded as the number of subdomains increases as for the exact one.

Approximate BDDC δ_t dependence.

From our numerical experiments we deduce that the condition number of the inexact operator will be independent of the spatial constants of discretizations h and H; however, the performances of the AMG methods can depend on the time step taken. We therefore reproduce the test case for the δ_t dependence of the exact BDDC operator (see Table 5.4) and list the inexact results in Table 6.4. The sigmoidal dependence from δ_t remains un-

PCG-BDDC Inexact Bidomain δ_t dependence

δ_t	1E-3	1E-2	1E-1	1E0	1E1	1E2	1E3
κ_2	2.76	2.86	3.60	5.98	10.43	12.97	13.40
iter	10	10	11	14	17	20	20

Table 6.4: Inexact BDDC dependence from δ_t. PCG-BDDC solver with vertices and edge average constraints as primal variables. Test case with 2x2x2 subdomains, $h = 0.01$, $H/h = 15$, conductivity coefficients as in Table 2.1.1, random right-hand side and null initial guess; PCG iteration is stopped when the initial preconditioned residual is reduced by a factor of 1E-6. For each run, time step δ_t, condition number and number of iterations are shown.

altered using two $V_{2,2}$-cycles for the application of the AMG preconditioner in equations (6.6) and (6.7).

Approximate BDDC with jumping coefficients.

PCG-BDDC Inexact
Jumping Coefficients

	A			**B**		
p	it	κ_2	inex. fact.	it	κ_2	inex. fact.
1	20	10.47	1.47	20	10.47	1.47
1E1	22	12.41	1.46	21	12.12	1.49
1E2	22	12.54	1.46	24	13.70	1.60
1E3	23	13.75	1.57	24	15.13	1.78

Table 6.5: Inexact BDDC dependence from jumps in the conductivity coefficient. PCG-BDDC solver with vertices and edge average constraints as primal variables. Test case with 3x3x3 subdomains, $h = 0.01$, $H/h = 15$, random right-hand side and null initial guess; PCG iteration is stopped when the initial preconditioned residual is reduced by a factor of 1E-6. For each run, jumping factor p (see text for details), number of iteration and condition number for inexact BDDC are shown. Inexact experimental factor (inex. fact.) is also shown (see text for details).

We test the independence of the inexact approach from jumps in the conductivity coefficients reproducing the test case described in the previous chapter for the exact BDDC and using one $V_{1,1}$-cycle. The inexact coarse problem has been solved exactly with a parallel LU factorization. The condition number of the inexact BDDC remains constant varying largely the factor p and the experimental ratio between the condition number of inexact and exact BBDC preconditioners remains bounded. Note that the condition number of the exact BDDC is not shown in table.

Approximate BDDC computational times.

Approximate BDDC Scalability

CPUs	2x2x2	4x4x4	6x6x6	8x8x8
κ_2	5.63	4.08	3.59	3.07
λ_M	4.02	3.50	3.12	2.69
λ_m	0.71	0.85	0.86	0.87
iter	15	13	12	11
T_{PP}(s)	37.69	3.55	3.46	6.42
T_{CS}(s)	37.92	3.24	0.75	0.61

Table 6.6: PCG scalability with approximate BDDC preconditioner with vertices and edge average constraints as primal variables. Test case with $h = 0.01$, global grid 80x80x80, random right-hand side and null initial guess; PCG iteration is stopped when the initial preconditioned residual is reduced by a factor of 1E-6. For each run, number of subdomains (one per cpu) per dimension, condition number, extreme eigenvalues and number of iterations are shown. Computational times in seconds are reported for both primal approaches descripted in text.

Tables 6.6 and 6.7 collect some computational times of the inexact BDDC code developed; results have been obtained using the Linux cluster Matrix of CASPUR (for cluster's details see http://hpc.caspur.it) located in Rome. We considered two different approaches for dealing with the primal problem. Approach denoted by PP (Point-to-point Parallel) consists in assemble and solve a parallel problem distributed across the processors, using for the solving step the parallel LU factorization for sparse matrices provided by MUMPS [92] and the VecScatter objects provided by PETSc [6] to perform the point-to-point communications related to assemble the primal right hand side and distribute the primal solution at each application of the preconditioner. With approach denoted by CS (Collective Serial) we assemble the primal problem on each processor using collective MPI gathering operations and then solve them with the serial package UMFPACK [142] for sparse matrices; note that with this approach, we need only one collective MPI operation to gather the primal right hand side to all processors at each application of the BDDC preconditioner.

Table 6.6 reports on the parallel scalability of the PCG method with approximate BDDC: we first fix the dimension of the global grid (80x80x80 corresponding to one million dofs approximatively) and then subdivide it along each spatial dimension, assigning one subdomain to one cpu. One $V_{1,1}$ cycle has been used as AMG method for solving both the Dirichlet (6.6) and Neumann (6.7) local problems. In both cases, the BDDC code scales superlinearly until 64 processors since the communication costs are limited and the substructure diameter decreases together with the number of iterations; the CS approach continues scaling until 512 processors even if the scaling is not linear; on the other hand, the PP approach suffers over 64 processors since the communication costs of the parallel LU solving step dominate the overall computational costs (data not shown).

Table 6.7 contains the computational times of the scaled speed-up of the PCG with approximate BDDC for the PP and CS approaches described previously. We used physiological conductivity coefficients (see Table 2.1.1) and a fixed local grid 40x40x40 for all substructures ($H/h = 40$); one $V_{1,1}$ cycle has been used as AMG method for solving both

Approximate BDDC Scaled speed up

CPUs	8	32	72	128	200	288	392	512
κ_2	5.16	4.95	4.96	4.95	5.08	5.05	5.23	5.21
λ_M	3.99	4.15	4.18	4.19	4.18	4.18	4.18	4.17
λ_m	0.77	0.73	0.84	0.84	0.82	0.82	0.80	0.80
iter	15	15	15	15	16	16	17	17
T_{PP} (s)	40.55	50.60	52.03	52.85	57.44	65.85	64.13	65.88
T_{CS} (s)	36.26	39.88	41.97	44.14	47.69	48.07	50.65	50.33
$\widehat{\mathbf{W}}$ dofs	1.0M	3.9M	8.7M	15.5M	24.2M	34.8M	47.3M	61.7M

Table 6.7: Scaled speed up of PCG method and approximate BDDC preconditioner with vertices and edge average constraints as primal variables. Test case with $h = 0.01$, local grid 40x40x40, random right-hand side and null initial guess; PCG iteration is stopped when the initial preconditioned residual is reduced by a factor of 1E-6. For each run, number of subdomains (one per cpu), condition number, extreme eigenvalues, umber of iterations and global number of dofs are shown. Computational times in seconds are reported for both primal approaches descripted in text.

the Dirichlet (6.6) and Neumann (6.7) local problems. CS approach perform better than the PP approach also in this case; for both approaches the overall computational costs initially increase with increasing the number of subdomains and then remains almost constants until 512 processors and more than 60 million dofs.

Conclusions

In this thesis we have considered different aspects related to the mathematical modeling of cardiac electrophysiology, either from the cellular or from the tissue perspective, and we have developed novel numerical methods for the parallel iterative solution of the resulting reaction-diffusion models.

In Chapter one, starting from a recently published ionic model for epicardial cells, we have developed and validated the HHRd model, which accounts for transmural cellular heterogeneities of the canine left ventricle. The HHRd model has been developed using available published experimental data on epicardial, midmyocardial and endocardial cells, reproducing numerically the same experimental conditions described in the experimental papers; numerical simulations of cellular action potentials have shown a good agreement with experimental data on steady state action potential duration, intracellular diastolic ionic concentrations and force frequency relationship for each type of cell considered by the HHRd model. Future studies should investigate the effects of specified drugs on the different type of cells modeled by HHRd.

Next, we have introduced the reaction-diffusion models describing the spread of excitation in cardiac tissue, namely the anisotropic Bidomain and Monodomain models. For their discretization, we have considered trilinear isoparametric finite elements in space and a semi-implicit IMEX method in time. In order to reduce the computational costs of parallel three-dimensional cardiac simulations, in Chapter three we have considered different strategies to accelerate convergence of the Preconditioned Conjugate Gradient method used for the solution of the large and sparse linear systems coming from the finite element discretization of both cardiac models. We have considered novel choices for the Krylov initial guess in order to reduce the number of iterations per time step, namely lagrangian interpolants in time of the previous computed solutions, or the projected solution, using a usual Galerkin technique, on the lower order subspace generated by using the Proper Orthogonal Decomposition technique applied to a subset of previous computed solutions. Both approaches were found to be very efficient only if combined with a suitable preconditioner, which optimizes the rate of convergence of the preconditioned conjugate gradient method. POD-Galerkin approach has shown the best results in terms of reduction of total number of iterations in heartbeat simulations using only few solution vectors to generate the POD basis either for the Bidomain or the Monodomain model. Moreover, in Chapter five we have applied both strategies to the preconditioned Schur complement system of the car-

diac Bidomain model, providing in addition a technique to reduce the computational costs associated to the POD-Galerkin technique. Our results suggest that future works should investigate strategies to simulate all but the activation phase in cardiac tissue by using lower order POD basis without solving for the full order finite element basis.

In the last three chapters we have constructed and analyzed non-overlapping domain decomposition methods for both cardiac reaction-diffusion models. In Chapter four we have dealt with preconditioners of the Neumann-Neumann type, in particular we have considered the additive Neumann-Neumann method for the Monodomain model and the Balancing Neumann-Neumann method for the Bidomain model. In Chapter five we have constructed and analyzed a Balancing Domain Decomposition by Constraint method for the Bidomain model, whereas in Chapter six we have investigated the use of an approximate BDDC method for the Bidomain model, in order to reduce the memory and computational requirements of the exact BDDC approach. For all preconditioners considered, we have developed novel theoretical estimates for the condition number of the preconditioned systems with respect to the spatial discretization, to the subdomains' diameter and to the time step, also in case of discontinuity in the conductivity coefficients of the cardiac tissue, with jumps aligned with the interface among subdomains. In particular, we were able to prove scalability and quasi-optimality for the two balancing methods considered for the Bidomain model using suitable coarse (or primal) spaces. Using the same theoretical framework, proofs of quasi-optimality can be easily developed for balancing methods for the Monodomain model. Parallel numerical results have confirmed the theoretical estimates; numerical results on the parallel scalability of the inexact BDDC preconditioner were also provided.

The code developed for the BDDC method was also applied to the spectral element discretization of Almost Incompressible Elasticity in three dimensions; a robust inexact BDDC method for this problem is under study.

Bibliography

[1] L. Ambrosio, P. Colli Franzone and G. Savarè (2000). *On the asymptotic behaviour of anisotropic energies arising in the cardiac bidomain model*. Interfaces Free Bound. 2(3): 213-266.

[2] C. Antzelevitch, J. Fish (2001). *Electrical heterogeneity within the ventricular wall*, Basic Res. Cardiol. 96: 517-527.

[3] O. M. Ascher, S. J. Ruuth and B. T. R. Wetton (1995). *Implicit-explicit methods for time-dependent partial differential equations*. SIAM J. Numer. Anal. 32 (3): 797-823.

[4] D. D. Bainov, P. S. Simeonov (1995). *Impulsive differential equations: Asymptotic properties of the solutions*, Singapore World Scientific.

[5] B. Balati, A. Varro, J. G. Papp (1998). *Comparison of the cellular electrophysiological characteristics of canine left ventricular epicardium, M cells, endocardium and Purkinje fibres*, Acta Physiol. Scand. 164: 181-90.

[6] S. Balay, K. Buschelman, W. D. Gropp, D. Kaushik, M. Knepley, L. Curfman McInnes, B. F. Smith and H. Zhang (2002). *PETSc Users Manual*. Tech. Rep. ANL-95/11 - Revision 2.1.5, Argonne National Laboratory.

[7] T. Banyasz, L. Fulop, J. Magyar, N. Szentandrassya, A. Varro, P. P. Nanasia (2003). *Endocardial versus epicardial differences in L-type calcium current in canine ventricular myocytes studied by action potential voltage clamp*, Cardiovascular Research 58: 66-75

[8] L. Beirao da Veiga, C. Chinosi, C. Lovadina, and L. F. Pavarino (2010). *Robust BDDC preconditioners for Reissner-Mindlin plate bending problems and MITC elements*, SIAM J. Numer. Anal., 47 , pp. 4214-4238.

[9] G. Bellettini, P. Colli Franzone and M. Paolini (1997). *Convergence of front propagation for anisotropic bistable reaction-diffusion equations*. Asymp. Anal., 15, 325-358.

[10] A. P. Benson, O. V. Aslanidi, H. Zhang, A. V. Holden (2008). *The canine virtual ventricular wall: A platform for dissecting pharmacological effects on propagation and arrhythmogenesis*, Prog. Biophys. Mol. Biol. 96: 187-208.

[11] S. C. Brenner and L. Y. Sung (2007). *BDDC and FETI-DP without matrices or vectors*, Comput. Methods Appl. Mech. Engrg., 196, pp. 1429-1435

[12] N. F. Britton (1986). *Reaction-diffusion equations and their applications to biology*, Academic Press, London.

[13] M. A. Casarin (1996). *Schwarz preconditioners for spectral and mortar finite element methods with applications to incompressible fluids*, Ph.D. Thesis, Courant Institute of Mathematical Sciences, TR-717 Department of Computer Science.

[14] A. W. Cates and A. E. Pollard (1998). *A model study of intramural dispersion of action potential duration in the canine pulmonary conus.* Ann. Biomed. Eng. 26: 567-576.

[15] J.C. Clements, J. Nenonen, P.K.J. Li, B.M. Horacek (2004), *Activation dynamics in anisotropic cardiac tissue via decoupling*, Ann. Biomed. Eng. 26: 567.

[16] P. Colli Franzone, L. Guerri (1993). *Spread of excitation in 3-D models of the anisotropic cardiac tissue. I:Validation of the eikonal approach*. Math. Biosci. 113:145-209.

[17] P. Colli Franzone, L. Guerri, M. Pennacchio, and B. Taccardi (1993). *Spread of excitation in 3-D models of the anisotropic cardiac tissue. II: Effects of fber architecture and ventricular geometry*. Math. Biosci. 147: 131-171.

[18] P. Colli Franzone and G. Savarè (2002). *Degenerate evolution systems modeling the cardiac electric field at micro and macroscopic level*. In Evolution equations, Semigroups and Functional Analysis, A. Lorenzi and B. Ruf, Editors, 49-78, Birkhauser.

[19] P. Colli Franzone and L. F. Pavarino(2004). *A Parallel solver for reaction diffusion systems in computational electrocardiology*, M3AS 14: 883-911.

[20] P. Colli Franzone, L. F. Pavarino, B. Taccardi (2005) *Simulating patterns of excitation, repolarization and action potential duration with cardiac Bidomain and Monodomain models* Math. Biosci. 197: 35-66

[21] P. Colli Franzone, L. F. Pavarino, B. Taccardi (2006). *Effects of transmural electrical heterogeneities and electrotonic interactions on the dispersion of cardiac repolarization and action potential duration: A simulation study*, Math. Biosci. 204: 132-165.

[22] D. Colquhoun, A. G. Hawkes (1995). *A Q-matrix cookbook: how to write only one program to calculate the single-channel and macroscopic predictions for any kinetic mechanism*, In Single Channel Recording, 2nd Ed. B. Sakmann and E. Neher, editors. Plenum Press, New York. 589-636

[23] J. M. Cordeiro, L. Greene, C. Heilmann, D. Antzelevitch, C. Antzelevitch (2003). *Transmural heterogeneity of calcium activity and mechanical function in the canine left ventricle*, Am. J. Physiol. Heart Circ. Physiol. 286: H1471-H1479.

[24] M. Dauge (1988). *Elliptic boundary value problems on corner domains*, Springer-Verlag New York.

[25] M. Dauge (1992). *Neumann and mixed problems on curvilinear polyhedra*, Integral Equations Operator Theory, 15(2), 227-261.

[26] J. W. Demmel, M. T. Heath and H. A. van der Vorst (1993). *Parallel numerical linear algebra*, Acta Numerica 111-197.

[27] A. Destexhe, J. R. Huguenard (2000). *Nonlinear Thermodynamic Models of Voltage-Dependent Currents*, J. Comp. Neurosci. 9: 259-270.

[28] D. DiFrancesco, D. Noble (1985). *A model of cardiac electrical activity incorporating ionic pumps and concentration changes*, Phil. Trans. R. Soc. Lond. B 307: 353-398

[29] K. W. Dilly, C. F. Rossow, V. Scott Votaw, J. S. Meabon, J. L. Cabarrus, L. F. Santana (2006). *Mechanisms underlying variations in excitation-contraction coupling across the mouse left ventricular free wall*, J. Physiol. 572: 227-241.

[30] C. R. Dohrmann (2003). *A preconditioner for substructuring based on constrained energy minimization*, SIAM J. Sci. Comput., 25 246-258

[31] C. R. Dohrmann (2007). *An approximate BDDC preconditioner*, Numerical Linear Algebra with Applications 14 (2), 149-168.

[32] M. Dryja, J. Galvis, and M. Sarkis (2007), *BDDC methods for discontinuous Galerkin discretization of elliptic problems*, J. Complexity, 23: 715-739.

[33] S. C. Eisenstat, M. H. Schultz, and A. H. Sherman (1975). *Applications of an element model for Gaussian elimination*. In Sparse matrix computations (Proc. Sympos.,Argonne Nat. Lab., Lemont, Ill., 1975), pages 85-96. Academic Press, New York, 1976.

[34] G. M. Faber, Y. Rudy (2000). *Action potential and contractility changes in* $[Na]_i$ *overloaded cardiac myocytes: a simulation study*, Biophys. J. 78: 2392-2404.

[35] G. M. Faber, Y. Rudy (2007). *Calsequestrin mutation and catecholaminergic polymorphic ventricular tachycardia: A simulation study of cellular mechanism*, Cardiovascular Research 75: 79-88

[36] C. Farhat, M. Lesoinne, P. LeTallec, K. Pierson, and D. Rixen (2001). *FETI-DP: a dual-primal unified FETI method - part I. A faster alternative to the two-level FETI method*, Internat. J. Numer. Meth. Engrg., 50: 1523-1544.

[37] P. F. Fischer (1993). *Projection techniques for iterative solution of* $Ax = b$ *with successive right-hand sides*, ICASE Report No. 93-90.

[38] S. N. Flaim, W. R. Giles, A. D. McCulloch (2006). *Contributions of sustained I_{Na} and I_{Kv43} to transmural heterogeneity of early repolarization and arrhythmogenesis in canine left ventricular myocytes*, Am. J. Physiol. Heart Circ. Physiol. 291: H2617-H2629.

[39] Gaborit N., Le Bouter S., Szuts V., Varro A., Escande D., Nattel S., Demolombe S. (2007). *Regional and tissue specific transcript signatures of ion channel genes in the non-diseased human heart*, J. Physiol., 582: 675-693.

[40] P. Galan del Sastre, R. Bermejo (2008). *Error estimates of proper orthogonal decomposition eigenvectors and Galerkin projection for a general dynamical system arising in fluid models*, Numer. Math. 110:49-81

[41] J. Gao, W. Wang, I. S. Cohen, R. T. Mathias (2005). *Transmural Gradients in Na/K Pump Activity and $[Na]_i$ in Canine Ventricle*, Biophys. J. 89: 1700-1709.

[42] A. Garfinkel, Y-H. Kim, O. Voroshilovsky, Z. Qu, J. R. Kil, M-H. Lee, H. S. Karagueuzian, J. N. Weiss and P-S. Chen (2000). *Preventing ventricular fibrillation by attening cardiac restitution*. Proc. Nat. Acad. Sci. USA 97 (11): 6061-6066.

[43] G.H. Golub and C.F. van Loan (1996). *Matrix Computations*, 3rd Ed. Johns Hopkins University Press, Baltimore.

[44] J. L. Greenstein, R. Hinch, R. L. Winslow (2006). *Mechanisms of Excitation-Contraction Coupling in an Integrative Model of the Cardiac Ventricular Myocyte*, Biophys. J. 90: 77-91

[45] H. Harman (1960). *Modern Factor Analysis*. University of Chicago Press, Chicago.

[46] C. S. Henriquez, A. L. Muzikant and C. K. Smoak (1996). *Anisotropy, fiber curvature, and bath loading effects on activation in thin and thick cardiac tissue preparations: Simulations in a three-dimensional bidomain model*. J. Cardiovasc. Electrophysiol. 7 (5): 424-444.

[47] B. Hille (1992). *Ionic channels of excitable membranes*, Sinauer (2nd ed).

[48] A.L. Hodgkin nad A.F. Huxley (1952). *A quantitative description of membrane currents and its application to conduction and excitation in nerve.* J. Physiol. (Lond), 117: 500-544.

[49] P. Holmes, J. Lumley and G. Berkooz (1996). *Turbulence, Coherent Structures, Dynamical Systems and Symmetry*, Cambridge University Press.

[50] N. Hooke (1992). *Efficient simulation of action potential propagation in a bidomain*. Ph. D. Thesis, Duke Univ., Dept. of Comput. Sci.

[51] N. Hooke, C. S. Henriquez, P. Lanzkrom, and D. Rose (1994). *Linear algebraic transformations of the bidomain equations: implications for numerical methods*. Math. Biosc. 120:127-145.

[52] D. A. Hooks, M. L. Trew, B. J. Caldwell, G. B. Sands, I. J. LeGrice, B. H. Smaill (2007) *Laminar Arrangement of Ventricular Myocytes Influences Electrical Behavior of the Heart*, Circ Res. 101: e103-e112.

[53] T. J. Hund, J. P. Kucera, N. F. Otani, Y. Rudy (2001). *Ionic charge conservation and long-term steady state in the Luo-Rudy dynamic cell model*, Biophys. J. 81: 3324-3331.

[54] T. J. Hund, Y. Rudy (2004). *Rate dependence and regulation of action potential and calcium transient in a canine cardiac ventricular cell model*, Circulation 110: 3168-3174.

[55] HYPRE home page: http://acts.nersc.gov/hypre/

[56] S.R. Idelson and A. Cardona (1985). *A reduction method for nonlinear structural dynamic analysis*, Computer Methods in Applied Mechanics and Engineering 49: 253-279.

[57] I. C. F. Ipsen, C. D. Meyer (1995). *The angle between complementary subspaces*, NCSU Tech Report NA-019501.

[58] F. H. Johnson, H. Eyring, B. J. Stover (1974). *The Theory of Rate Processes in Biology and Medicine*, J. Wiley, New York.

[59] M. Kahlbacher (2006), *POD for parameter estimation of bilinear elliptic problems*, Master Thesis, University of Graz, Institute for mathematics and scientific computing.

[60] K. Karhunen (1946). *Zur Spektraltheorie stochastischer Prozesse*. Annales Academiae Scientarum Fennicae, 37.

[61] J. P. Keener (1991). *An eikonal-curvature equation for the action potential propagation in myocardium*, J. Math Biol. 29: 629-651

[62] J.P. Keener (1996), *Direct activation and defibrillation of cardiac tissue* J. Theor. Biol 178: 313.

[63] J. P. Keener and K. Bogar (1998). *A numerical method for the solution of the bidomain equations in cardiac tissue*. Chaos 8 (1): 234-241.

[64] J. P. Keener, J. Sneyd, L. Sirovich, S. Wiggins, L. P. Kadanoff, J. E. Marsden (1998). *Mathematical Physiology* Springer.

[65] H. H. Kim (2008). *A BDDC algorithm for mortar discretization of elasticity problems*, SIAM J. Numer. Anal., 46: 2090-2111.

[66] H. H. Kim and X. Tu (2009). *A three-level BDDC algorithm for mortar discretizations*, SIAM J. Numer. Anal., 47: 1576-1600.

[67] A. Klawonn and O. B. Widlund (2006). *Dual-Primal FETI methods for linear elasticty*, Comm. Pure and Appled Math. 59: 1523-1572.

[68] A. Klawonn and O. Rheinbach (2007). *Inexact FETI-DP methods*, Int. J. Numer. Meth. Eng. 69 (2): 284-307.

[69] A. Klawonn, L. F. Pavarino, and O. Rheinbach (2008). *Spectral element FETI-DP and BDDC preconditioners with multi-element subdomains*, Comput. Meth. Appl. Mech. Engrg., 198, pp. 511-523.

[70] A. Klawonn and O. Rheinbach (2010). *Highly scalable parallel domain decomposition methods with an application to biomechanics*, ZAMM-Zeitschrift fur angewandte mathematik und mechanik 90(1): 5-32.

[71] K. Kunisch, S. Volkwein (2001). *Galerkin proper orthogonal decomposition methods for parabolic problems*, Numer. Math. 90: 117-148.

[72] LAPACK home page: http://www.netlib.org/lapack

[73] K. R. Laurita, R. Katra, B. Wible, X. Wan, M. Koo (2003). *Transmural heterogeneity of calcium handling in canine*, Circ. Res. 92: 668-675.

[74] J. Lee, B. Smaill, N. Smith (2006). *Hodgkin-Huxley type ion channel characterization: An improved method of voltage clamp experiment parameter estimation*, J. Theor. Biol. 242: 123-134.

[75] I. J. LeGrice, B. H. Smaill, L. Z. Chai, S. G. Edgar, J. B. Gavin, P. J. Hunter (1995), *Laminar structure of the heart: ventricular myocyte arrangement and connective tissue architecture in the dog*, Am. J. Physiol. Heart Circ. Physiol. 269: H571-H582.

[76] G. R. Li, C. P. Lau, A. Ducharme, J. C. Tardif, S. Nattel (2002). *Transmural action potential and ionic current remodeling in ventricles of failing canine hearts*, Am. J. Physiol. Heart Circ. Physiol. 283: H1031-H1041.

[77] J. Li and O. B. Widlund (2006). *BDDC algorithms for incompressible Stokes equations*, SIAM J. Numer. Anal. 44(6): 2432-2455.

[78] J. Li and O. B. Widlund (2007). *On the use of inexact subdomain solvers for BDDC algorithms*, Comp. Meth. Appl. Mech. Eng. 196(8): 1415-1428.

[79] J. Li and O. B. Widlund (2006). *FETI-DP, BDDC, and block Cholesky methods*, Internat. J. Numer. Methods Engrg., 66: 250-271.

[80] J. Li and X. Tu (2009). *Convergence analysis of a balancing domain decomposition method for solving a class of indefinite linear systems*, Numer. Linear Algebra Appl., 16: 745-773.

[81] L. M. Livshitz, Y. Rudy (2007). *Regulation of Ca^{2+} and electrical alternans in cardiac myocytes: role of CAMKII and repolarizing currents*, Am. J. Physiol. Heart Circ. Physiol. 292: H2854-H2866.

[82] D. W. Liu, G. A. Gintant, C. Antzelevitch (1993). *Ionic bases for electrophysiological distinctions among epicardial, midmyocardial, and endocardial myocytes from the free wall of the canine left ventricle*, Circ. Res. 72: 671-687.

[83] D. W. Liu, C. Antzelevitch (1995). *Characteristics of the delayed rectifier current (I_Kr and I_Ks) in canine ventricular epicardial, midmyocardial, and endocardial Myocytes. A weaker IKs contributes to the longer action potential of the M cell*, Circ. Res. 76: 351-365.

[84] M. M. Loeve (1955). *Probability Theory*. Van Nostrand, New Jersey.

[85] E. N. Lorenz (1956). *Empirical orthogonal eigenfunctions and statistical weather prediction*. Technical report, MIT Report, Department of Meteorology, Cambridge, MA.

[86] V. A. Maltseev, N. Silverman, H. N. Sabbah, A. I. Undrovinas (2007). *Chronic heart failure slows late sodium current in human and canine ventricular myocytes: implications for repolarization variability*, Eur. J. Heart Fail. 9: 219-227.

[87] J. Mandel, C. Dohrmann and R. Tezaur (2005). *An algebraic theory for primal and dual substructuring methods by constraints*, Appl. Numer. Math. 54(2): 167-193.

[88] T. Mathew (2008). *Domain Decomposition Methods for the Numerical Solution of Partial Differential Equations*, Lecture Notes in Computational Science and Engineering, Springer.

[89] R. Markinovic, J. D. Jansen (2006). *Accelerating iterative solution methods using reduced-order models as solution predictors*, Int. J. Numer. Meth. Engng 68: 525-541

[90] L. S. Milescu, G. Akk, F. Sachs (2005). *Maximum likelihood estimation of ion channel kinetics from macroscopic currents*, Biophys. J. 88: 2494-2515.

[91] C. B. Moler, C. F. Van Loan (1978). *Nineteen dubious ways to compute the exponential of a matrix*, SIAM Rev. 20: 801-836.

[92] MUMPS home page: http://graal.ens-lyon.fr/MUMPS

[93] M. Munteanu, L. F. Pavarino and S. Scacchi (2009). *A scalable Newton-Krylov-Schwarz method for the bidomain reaction-diffusion system*, SIAM J. Sci. Comp. 5: 3861-3883.

[94] A. L. Muzikant, E. W. Hsu, P. D.Wolf and C. S. Henriquez (2002). *Region specific modeling of cardiac muscle: comparison of simulated and experimental potentials*. Ann. Biomed. Eng. 30: 867-883.

[95] E. Neher, B. Sakmann (1976). *Single-channel currents recorded from membrane of denervated frog muscle fibres*, Nature (Lond.) 260: 799-802.

[96] E. Neher, B. Sakmann (1992). *The patch clamp technique*, Sci. Am. 266:44-51.

[97] J. M. Nerbonne, R. S. Kass (2005). *Molecular physiology of cardiac repolarization*, Physiol. Rev. 85: 1205-1253.

[98] J. S. Neu, W. Krassowska (1993), *Homogeneization of syncytial tissues*, Crit. Rev. Biomed. Eng. 21: 137-199.

[99] Noble, D., Rudy, Y. (2001), *Models of cardiac ventricular action potentials: iterative interaction between experiment and simulation*, Phyl. Trans. R. Soc. Lond. A, 359: 1127-1142.

[100] Y. Notay (2005). *Algebraic multigrid and algebraic multilevel methods: a theoretical comparison*, Numer. Lin. Algebra Appl. 12: 419-451.

[101] T. Osaka, I. Kodama, N. Tsuboi, J. Toyama and K. Yamada (1987). *Effects of activation sequence and anisotropic cellular geometry on the repolarization phase of action potential of dog ventricular muscles*, Circulation 76: 226-236.

[102] P. Pathmanathan, O. M. Bernabeu, R. Bordas, J. Cooper, A. Garny, J. M. Pitt-Francis, J. P. Whiteley and D. J. Gavaghan (2010). *A numerical guide to the solution of the bidomain equations of cardiac electrophysiology*, Prog. Biophys. Mol. Biol. 102: 136-155.

[103] L. F. Pavarino (2007). *BDDC and FETI-DP preconditioners for spectral element discretizations*, Comput. Meth. Appl. Mech. Engrg., 196: 1380-1388.

[104] L. F. Pavarino and S. Scacchi (2008). *Multilevel additive Schwarz preconditioners for the bidomain reaction-diffusion system*, SIAM J. Sci. Comp. 31 (1): 420-445.

[105] L. F. Pavarino, O. B. Widlund and S. Zampini (2010). *BDDC preconditioners for spectral element discretizations of almost incompressible elasticity in three dimensions*, SIAM J. Sci. Comp. Accepted for pubblication.

[106] M. Pennacchio and V. Simoncini (2002). *Efficient algebraic solution of reaction diffusion systems for the cardiac excitation process*. J. Comput. Appl. Math. 145: 49-70.

[107] M. Pennacchio, G. Savarè, P. Colli Franzone (2005), *Multiscale modeling for the bioelectric activity of the heart*, SIAM J. Math. Anal. 4: 1333-1370.

[108] M. Pennacchio and V. Simoncini (2009). *Algebraic multigrid preconditioners for the bidomain reaction-diffusion system*, Appl. Numer. Math. 59: 3033-3050.

[109] L. Priebe, D. J. Beuckelmann (1998). *Simulation study of cellular electric properties in heart failure*, Circ. Res. 82: 1206-1223.

[110] J. L. Puglisi, F. Wang, D. M. Bers (2004). *Modeling the isolated cardiac myocyte*, Progr. Biophys. Mol. Biol. 85: 163-178.

[111] A. J. Pullan, L. K. Cheng, L.M. Buist (2005). *Mathematically modelling the electrical activity of the heart*, World Scientific.

[112] Z. Qu and A. Garfinkel (1997). *An advanced algorithm for solving partial differential equation in cardiac conduction*. IEEE Trans. Biomed. Eng. 46 (9): 1166-1168.

[113] A. Quarteroni, A. Valli (1994). *Numerical Approximation of Partial Differential Equations*, Springer, Berlin.

[114] M. Reimann, V. Gurev, J.J. Rice (2009). *Computational modeling of cardica disease: potential for personalized medicine*, Personalized Medicine 6(1): 45-66.

[115] S. M. Ross (1996). *Stochastic Processes* (2nd ed), Wiley series in probability and mathematical statistics

[116] B. J. Roth (1991). *Action potential propagation in a thick strand of cardiac muscle*. Circ. Res. 68: 162-173.

[117] Y. Rudy, J. R. Silva (2006). *Computational biology in the study of cardiac ion channels and cell electrophysiology*, Quart. Rev. Biophys. 39: 57-116.

[118] J. W. Ruge and K. Stuben (1987). *Algebraic Multigrid (AMG)*, Multigrid Methods vol. 3 of Frontiers in Applied Mathematics, SIAM Philadelphia, 73-130.

[119] Y. Saad, M. Yeung, J. Erhel and G. Guyoumarch (2000), *A deflated version of the conjugate gradient algorithm*, SIAM J. Sci. Comp. 21(5): 1909-1926.

[120] F. B. Sachse (2004). *Computational Cardiology. Modeling of Anatomy, Electrophysiology, and mechanics*, LNCS 2966, Springer Verlag.

[121] S. Sanfelici (2002). *Convergence of the Galerkin approximation of a degenerate evolution problem in electrocardiology*. Numer. Meth. Part. Diff. Eq. 18 (2): 218-240.

[122] S. Scacchi (2007). *Multilevel Schwarz preconditioners for the bidomain system and applications to electrocardiology*, Ph. D. Thesis, Università degli studi di Pavia, Dipartimento di matematica.

[123] S. Scacchi (2008). *A hybrid multilevel Schwarz method for the bidomain model*, Comput. Methods Appl. Mech. Engrg. 197: 4051-4061.

[124] G. Seemann, F. B. Sachse , D. L. Wei, O. Dossel (2003). *Quantitative reconstruction of cardiac electro-mechanics in humanmyocardium: Regional heterogeneity*, J. Cardiovasc. Electrophysiol. 14

[125] L. Shamgar, L. Ma, N. Schmitt, Y. Haitin, A. Peretz, R. Wiener, J. Hirsch, O. Pongs, B. Attali (2006). *Calmodulin is essential for cardiac I_{Ks} channel gating and assembly: impaired function in Long-QT mutations*, Circ. Res. 98: 1055-1063.

[126] L. F. Shampine, M. W. Reichelt (1997). *The MATLAB ode suite*, SIAM J. Sci. Comp. 18: 1-22

[127] S. Sicouri, S. Moro, S. Litovsky, M. V. Elizari, C. Antzelevitch (1997). *Chronic amiodarone reduced transmural dispersion of repolarization in the canine heart*, J. Cardiovasc. Electrophysiol. 8: 1269-1279

[128] L. Sirovich (1987). *Turbulence and the dynamics of coherent structures, parts I-III*, Quart. Appl. Math. 45: 561-590.

[129] J. Smoller (1994). *Shock waves and reaction-diffusion equations*. Springer-Verlag, New York, Second ed.

[130] B. F. Smith, P. Bjorstad, and W. D. Gropp (1996). *Domain Decomposition: Parallel Multilevel Methods for Elliptic Partial Differential Equations*, Cambridge University Press.

[131] A. Soubret, G. Helmlinger, B. Dumotier, R. Bibas, A. Georgieva (2009). *Modeling and simulation of preclinical cardiac safety: towards an integrative framework*, Drug Metab. Pharamcokinet. 24(1): 76-90.

[132] J. Southern, J. Pitt-Francis, J. Whiteley, D. Stokeley, H. Kobashi, R. Nobes, Y. Kadooka and D. Gavaghan (2007). *Multiscale computational modelling in biology and physiology*, Progr. Biophys. Mol. Biol. 96: 60-89.

[133] J. Stoer and R. Bulirsch (2002). *Introduction to Numerical Analysis* (3rd ed.). Berlin, New York: Springer-Verlag.

[134] D. Streeter (1979), *Gross morphology and fiber geometry in the heart*, in R.M. Berne (Ed.), Handbook of physiology, vol. 1, Williams and Wilkins, p.61, sect 2.

[135] J. Sundnes, G. T. Lines and A. Tveito (2003). *Efficient solution of ordinary differential equations modeling electrical activity in cardiac cells*. Math. Biosci. 172: 55-72.

[136] J. Sundnes, G. T. Lines, X. Cai, B. F. Nielsen, K. A. Mardal, A. Tveito (2006). *Computing the electrical activity of the heart*, Springer.

[137] J. Sundnes, R. Artebrant, O. Skavhaug, A. Tveito (2009). *A second-order algorithm for solving dynamic cell membrane equations*, IEEE Trans. Biomed. Eng. 56(10): 2546-2548.

[138] X. Sun, H. S. Wang (2005). *Role of the transient outward current in shaping canine ventricular action potential: a dynamic clamp study*, J. Physiol. 564: 411-419.

[139] G. Szabo, N. Szentandrássy, T. Biro, B. I. Tóth, G. Czifra, J. Magyar, T. Banyasz, A. Varro, L. Kovacs, P. P. Nanasi (2005). *Asymmetrical distribution of ion channels in canine and human left-ventricular wall: epicardium versus midmyocardium*, Eur. J. Physiol. 450: 307-316.

[140] A. Toselli and O. B. Widlund (2005). *Domain Decomposiiton methods - Algorithms and theory*, Springer.

[141] X. Tu and J. Li (2008). *A balancing domain decomposition method by constraints for advection-diffusion problems*, Commun. Appl. Math. Comput. Sci., 3: 25-60.

[142] UMFPACK home page: http://www.cise.ufl.edu/research/sparse/umfpack

[143] C. R. Valdivia, W. W. Chu, J. Pu, J. D. Foell, R. A. Haworth, M. R. Wolff, T. J. Kamp, J. C. Makielski (2004). *Increased late sodium current in myocytes from a canine heart failure model and from failing human heart*, J. Mol. Cell. Cardio. 38: 475-483.

[144] N. G. Van Kampen (2004). *Stochastic Processes in Physics and Chemistry*, North-Holland.

[145] M. Veneroni (2006), *Reaction-diffusion systems for the macroscopic bidomain model of the cardiac electric field*, tech. report, I.M.A.T.I.-C.N.R.

[146] B. Victorri, A. Vinet, F. A. Roberge and J. P. Drouhard (1985). *Numerical integration in the reconstruction of cardiac action potentials using Hodgkin-Huxley type models*. Comp. Biomed. Res. 18: 10-23.

[147] E. Vigmond, R. Weber dos Santos, A.J. Prassl, M. Deo, G. Plank (2008) *Solvers for the cardiac bidomain equations* Progr. Biophys. Mol. Biol. 96: 3-18.

[148] P. C. Viswanathan, R. M. Shaw and Y. Rudy (1999). *Effects of IKr and IKs heterogeneity on action potential duration and its rate dependence: a simulation study*, Circulation 99: 2466-2474.

[149] H. S. Wang, I. S. Cohen (2003), *Calcium channel heterogeneity in canine left ventricular myocytes*, J. Physiol. 547: 825-833.

[150] L. Xiao, L. Zhang, W. Han, Z. Wang, S. Nattel (2006). *Sex-based transmural differences in cardiac repolarization and ionic-current properties in canine left ventricles*, Am. J. Physiol. Heart. Circ. Physiol. 291: H570-H580.

[151] W. Xiong, Y. Tian, D. DiSilvestre, G. F. Tomaselli (2005). *Transmural heterogeneity of NaCa exchange: evidence for differential expression in normal and failing hearts*, Circ. Res. 97: 207-209.

[152] G. X. Yan, W. Shimizu, C. Antzelevitch (1998). *Characteristics and distribution of M cells in arterially perfused canine left ventricular wedge preparations*, Circulation 98(18): 1921-1927.

[153] J. Zeng, K. R. Laurita, D. S. Rosenbaum, Y. Rudy (1995). *Two components of the delayed rectifier K^+ current in ventricular myocytes of the guinea pig type: theoretical formulation and their role in repolarization*, Circ. Res. 77:140-152.

[154] D. Zipes and J. Jalife (2009). *Cardiac Electrophysiology*, 5th ed., W. B. Sauders Co., Philadelphia.

[155] A. C. Zygmunt, R. J. Goodrow, C. Antzelevitch (2000). *INaCa contributes to electrical heterogeneity within the canine ventricle*, Am. J. Physiol. Heart Circ. Physiol. 278: H1671-H1678.

[156] A. C. Zygmunt, G. T. Eddlestone, G. P. Thomas, V. V. Nesterenko, C. Antzelevitch (2000). *Larger late sodium conductance in M cells contributes to electrical heterogeneity in canine ventricle*, Am. J. Physiol. Heart Circ. Physiol. 281: H689-H697.